TECHNISCHE UNIVERSITÄT MÜNCHEN
Lehrstuhl für Informationstechnische Regelung

Human interaction with a team of multiple cooperating robots

Dominik Manuel Sieber

Vollständiger Abdruck der von der Fakultät für Elektrotechnik und Informationstechnik der Technischen Universität München zur Erlangung des akademischen Grades eines

Doktor-Ingenieurs (Dr.-Ing.)

genehmigten Dissertation.

Vorsitzender: Prof. Dr.-Ing. Eckehard Steinbach

Prüfer der Dissertation:

1. Prof. Dr.-Ing. Sandra Hirche
2. Prof. dr. ir. Ming Cao

Die Dissertation wurde am 04.10.2016 bei der Technischen Universität München eingereicht und durch die Fakultät für Elektrotechnik und Informationstechnik am 28.07.2017 angenommen.

Foreword

This dissertation has emerged from five years of work at the Chair of Automatic Control Engineering (LSR) and later, at the newly founded Chair of Information-Oriented Control (ITR) at the Technische Universität München. It has so far been the greatest challenge in my life. The outcome of this thesis would not have been possible without a number of people giving me support and advice in different ways. I would like to thank all of them.

First and foremost, I would like to express my sincerest gratitude to Prof. Sandra Hirche for having given me the opportunity to conduct my research under her supervision, for her steady support in the scientifical ups and downs, and for providing me with an excellent research environment in which I could realize my ideas. Over the past few years, I have learned a lot from her. I would also like to thank Prof. Martin Buss because he was the first to encourage me to begin my research. In addition, I am very grateful for the kind support in nonscientific questions, which I received from the administrative teams of LSR and ITR.

My deepest thanks go to my former colleagues and now friends, Thomas Beckers and Dr. Jose Ramon Medina Hernandez for having always lifted my spirits during rough times and for their advise in difficult questions. Special thanks go to my long-term room mate Frederik Deroo for being such a pleasant and supportive personality and for all the joyful collaborations and discussions. I will especially miss that. Furthermore, I would like to thank my short-term room mate Selma Music for the pleasant collaboration in developing an architecture for cognitive adjustable team control, Timo Fritzsch, Sebastian Erhart, and Dr. Thomas Nierhoff for the fruitful discussions in the field of mobile multi-robot manipulation, Prof. Ayse Kücükyilmaz and Prof. Yuki Ueno for arriving at ITR as foreign researchers and later leaving as friends, Melanie Kimmel, Muriel Lang, and Andreas Lawitzky. All my other friends, thank you for your patience.

The thesis has also been influenced and supported by the excellent work of my students, especially by Paul Färber who contributed to the convergence analysis of controlled consensus protocols, by Alexander Kürzl and Alexander Kuhn through their contribution to the virtual experience of controlled consensus protocols, and by Jonas Umlauft through his valuable support in coupling dynamic movement primitives. Many thanks to all for the strong commitment.

Finally, I would like to thank my parents Sonja and Peter, my brother Konstantin, and last but most importantly my girlfriend Elena for their permanent encouragement and understanding during this ambitious time of my life.

Thank you all for broadening my mind in this challenging period.

Munich, September 2016 Dominik Sieber

Abstract

The interaction between a human and multiple cooperating robots bears highly significant relevance in many pivotal application domains. The employment of cooperative manipulators covers application areas ranging from a team of robots transporting a variable-sized payload to multiple robots clearing an unstructured path in search-and-rescue scenarios or collaboratively assembling facilities in hostile and complex places. The benefits of employing multiple manipulators for cooperatively manipulating a common object include increased payload capacity, expanded functionality, and increased dexterity with larger objects. Due to their complementary strengths robots will soon replace humans when it comes to repetitive or exhausting work while a human outperforms a robot in unknown situations when cognitive abilities are essential. As a consequence the interaction of a single human with a team of cooperative robots, which collaboratively manipulate an object, poses significant challenges such as the distributed robot control for cooperative object manipulation and the forward mapping from human input to object motion.

The present thesis explores the distributed control and human interaction aspects in the guidance of a cooperative manipulation task. We focus on the following relevant open challenges: First, a control design which optimally coordinates multiple robots in order to satisfy the input and state constraints at hand for a successful execution of the cooperative manipulation task. Second, the requirements and the performance of a human-robot interaction paradigm which enables the guidance of a cooperative manipulation task by a human operator while still preserving autonomous functionalities of the robot team in both theoretical facets and practical use. Third, the influence of the human operator on the individual (robotic) agents from a system theoretic point of view based on topological conditions which additionally and especially becomes appealing when considering the interaction with large-scale networks.

The major contributions of this thesis focus on the previously mentioned challenges. Regarding distributed robot control enabling cooperative manipulation we introduce (i) an optimal control problem which combines the classical quadratic cost function with a relaxed formation constraint in terms of an additional biquadratic penalty term and (ii) the coordination of individually generated dynamic movement primitives by a formation-preserving feedback for each primitive. To guide a cooperative manipulation task we propose a formation-based approach to map the human input to the motion of the object cooperatively manipulated by multiple manipulators where the human can be interpreted as the leader in a leader-follower formation with the robotic manipulators being the followers. In contrast to classical methods we further introduce fundamental insights into the controllability of leader-follower networks by establishing novel topological characterizations of the uncontrollable subspace based on particular clustering of the underlying interaction graph. All presented methods and approaches provide generic contributions in the field of human-robots-interaction which can in particular be employed for but are not generally limited to the guidance of a cooperative manipulation task by a single human operator. In this regard, this thesis complements not only the existing theoretical contributions on cooperative robotic manipulation and human network interaction but additionally highlights the practical use of the methodologies in extensive experimental studies with multiple anthropomorphic mobile robots throughout this work.

Zusammenfassung

Der Interaktion zwischen einem Menschen und mehreren kooperierenden Robotern wird eine beachtliche, zukunftsträchtige Bedeutung in vielfältigen Bereichen zugeschrieben. Als Beispiel kann der Transport verschiedenartiger Ladegüter oder die gemeinscchaftliche Montage von Anlagen genannt werden. Auf Grund einer vergrößerten Nutzlast, einer gesteigerten Flexibilität und einer erhöhten Geschicklichkeit bei großen Objekten während der gemeinsamen Objektmanipulation bringt der Einsatz kooperativer Roboter deutliche Vorteile mit sich. Angesichts ihrer komplementären Stärken werden Roboter Menschen immer stärker bei anstrengender, sich wiederholender Arbeit ersetzen, während Menschen Roboter auf Grund ihrer kognitiven Fähigkeiten in unbekannten Situationen übertreffen. Konsequenterweise birgt die Interaktion eines Menschen mit einem Roboterteam zur gemeinsamen Objektmanipulation große Herausforderungen, wie zum Beispiel eine verteilte Roboterregelung für die kooperative Manipulation und ein Vorwärtsmapping des Menschen auf die Objektbewegung.

Die vorliegende Arbeit erforscht die Aspekte der verteilten Regelung und der menschlichen Interaktion bei der Lenkung einer robotergesteuerten kooperativen Manipulationsaufgabe. Wir konzentrieren uns auf die folgenden bislang unerforschten Punkte: Erstens einen Reglerentwurf, der die einzelnen Roboter optimal koordiniert, sodass jeder Roboter die vorhandenen Gleichungsnebenbedingungen erfüllt und die kooperative Objektmanipulation gemeinsam erfolgreich bewältigt wird. Zweitens die Eigenschaften eines Mensch-Roboter-Interaktionsmechanismus, der die Lenkung einer robotergesteuerten kooperativen Manipulationsaufgabe durch einen Menschen ermöglicht und dabei dennoch die autonomen Funktionalitäten der Roboter bewahrt. Drittens der Einfluss des Menschen auf die individuellen (Roboter-)Agenten, basierend auf einer topologischen Betrachtung des Interaktionsgraphen, was insbesondere bei großen Netzwerken vielversprechend ist.

Der Hauptbeitrag dieser Arbeit beantwortet die offenen Forschungsthemen von oben. Hinsichtlich der verteilten Roboterregelung führen wir (i) ein Optimalsteuerungsproblem ein, das eine quadratische Kostenfunktion mit einer relaxierten Gleichungsnebenbedingung an die Roboterformation kombiniert und (ii) eine Koordination von individuell berechneten dynamischen Bewegungsprimitiven durch eine die Roboterformation erhaltende Zustandsrückführung ein. Um eine robotergesteuerte kooperative Manipulation zu lenken, schlagen wir einen formationsbasierten Ansatz vor, der die Eingabe des Menschen auf die Bewegung des Objekts. das durch mehrere Roboter manipuliert wird, abbildet. Der Mensch kann als Anführer eines Anführer-Verfolger-Ansatz in dieser Anordnung interpretiert werden. Im Gegensatz zu den klassischen Methoden erweitern wir die wesentlichen Erkenntnisse in der Steuerbarkeit des Consensus Protokolls, indem wir neuartige topologische Bedingungen basierend auf einem speziellen Clustering des Interaktionsgraphen herleiten. Diese führen dann zu nicht-steuerbaren Unterräumen im Protokoll. Alle in dieser Arbeit vorgestellten Methoden liefern einen allgemeingültigen Beitrag im Fachgebiet der Mensch-Roboter-Interaktion, der im Besonderen für die Lenkung einer robotergesteuerten kooperativen Manipulationsaufgabe verwendet werden kann, aber im Allgemeinen nicht darauf beschränkt ist. Diesbezüglich ergänzt diese Arbeit nicht nur die bestehende Literatur in den Fachgebieten der robotergesteuerten, kooperativen Manipulation und der Mensch-Netzwerk-Interaktion, sondern verdeutlicht auch noch deren praktische Relevanz durch umfangreiche Experimente mit mehreren mobilen, anthropomorphen Robotermanipulatoren.

Contents

Notations

Abbreviations

2D	two-dimensional
3D	three-dimensional
6D	six-dimensional
AEP	almost equitable partition
BFGS	Broyden-Fletcher–Goldfarb-Shanno
CoM	center of mass
DMP	dynamic movement primitive
DoF	degrees of freedom
EE	end effector
FMS	formation
IMP	impedance
LED	light emitting diode
LEP	leader-invariant almost equitable partition
LQR	linear quadratic regulator
LTI	linear time-invariant
LWPR	locally weighted projected regression
LWR	light-weight robot
PBH	Popov-Belevitch-Hautus
SVD	singular value decomposition
UAV	unmanned aerial vehicles
VR	virtual reality

Conventions

Scalars, Vectors, and Matrices

x	scalar
$\boldsymbol{x}$	vector
$\|\boldsymbol{x}\|$	absolute value of $\boldsymbol{x}$
$\|\|\boldsymbol{x}\|\|$	Euclidean norm of $\boldsymbol{x}$

X	matrix
$X^\intercal$	transpose of X
X^{-1}	inverse of X
$X^\dagger$	pseudoinverse of X
$\mathrm{range}(X)$	range of the matrix X
$\ker(X)$	null space of the matrix X
$\dim(X)$	dimension of the matrix X
$\mathrm{vec}(X)$	vectorization of the matrix X
$\mathrm{mat}(x)$	reshaping a vector x into a matrix
I_n	$n \times n$ identity matrix
$\mathbf{1}$	vector with ones of appropriate size
0	scalar/vector/matrix with zeros of appropriate size
$f(\cdot)$	scalar function
$\boldsymbol{f}(\cdot)$	vector function
$\mathscr{X}$	matrix related to overall dynamics, set
$\lvert\mathscr{X}\rvert$	Cardinality of the set $\mathscr{X}$
$\dot{x}, \ddot{x}$	first, second time derivative of x
$\bar{x}$	augmented or reduced variant of x
$\hat{x}$	average of x
$\boldsymbol{x}^*$	equilibrium of $\boldsymbol{x}$, trivial case of a partition (Chapter 5)
$A \oplus B$	Kronecker product
$\boldsymbol{a} * \boldsymbol{b}$	convolution operator

Number sets

$\mathscr{L}_2$	Space of piecewise continuous, square-integrable functions
$\mathbb{R}$	Set of real-valued number
$\mathbb{R}^+$	Set of non-negative real-valued number
$\mathbb{Z}$	Set of natural numbers including zero
$\mathbb{Z}^+$	Set of non-negative natural numbers

Subscripts and Superscripts

$(\cdot)_0$	initial time at $t = 0$
$(\cdot)_h$	associated with the human
$(\cdot)_i$	associated with agent/ robot i
$(\cdot)_{i,m}$	associated with the manipulator of robot i
$(\cdot)_{i,b}$	associated with the mobile base of robot i
$(\cdot)_{i,k}$	associated with the kth state of robot i
$(\cdot)_{ij}$	associated with the robot i w.r.t. robot j
$(\cdot)_j$	associated with agent/ robot j
$(\cdot)_L$	associated with the leader-invariant case
$(\cdot)_o$	associated with the object
$(\cdot)_w$	associated with the world frame
$(\cdot)_{\text{fms}}$	associated with the formation-based set-point generator
$(\cdot)_{\text{imp}}$	associated with the impedance-based interaction dynamics
$(\cdot)_{\text{tot}}$	associated with the overall system dynamics
$(\cdot)_{x,y}$	translational component in x,y-direction
$(\cdot)_\varphi$	rotational component
$(\cdot)^A$	associated with the analytical solution
$(\cdot)^c$	associated with the controllable subspace
$(\cdot)^{\hat{c}}$	associated with the uncontrollable subspace
$(\cdot)^d$	desired value
$(\cdot)^e$	associated with the environment
$(\cdot)^o$	associated with the orientation
$(\cdot)^p$	associated with the position
$(\cdot)^q$	associated with the quaternion
$(\cdot)^{\text{ext}}$	associated with the external wrenches
$(\cdot)^{\text{int}}$	associated with the internal wrenches
$(\cdot)^{\text{err}}$	associated with the error
$(\cdot)^{\text{obs}}$	associated with the obstacle
$(\cdot)^{\mathscr{K}}$	associated with the 6D stiffness
$(\cdot)^\Sigma$	associated with non-interacting wrenches
$(\cdot)^\parallel$	associated with the range of a space
$(\cdot)^\perp$	associated with the null-space/ an orthogonal subspace
$(\cdot)^\pi$	associated with the partition π.

Symbols

Unless otherwise denoted:

A	constraint coefficient matrix (Chapter 2), system matrix (Chapter 3, 4, 5)
b	constraint centripedal vector (Chapter 2),
$\boldsymbol{b}_{(\cdot)}$	input vector

$B_{(\cdot)}(\boldsymbol{\theta}_{(\cdot)})$	robot inertia matrix
$B_{(\cdot)}$	input matrix
$C_{(\cdot)}(\boldsymbol{\theta}_{(\cdot)})$	robot Coriolis and centrifugal matrix,
$C_{(\cdot)}$	cluster
$\boldsymbol{d}_{(\circ)(\bullet)}$	desired displacement between $(\circ)$ and $(\bullet)$
$d_{(\circ)(\bullet)}$	desired distance between $(\circ)$ and $(\bullet)$
$d_{(\cdot)}$	translational damping gain
$D_{(\cdot)}$	damping matrix
$\boldsymbol{e}_1, \boldsymbol{e}_2, \ldots, \boldsymbol{e}_n$	standard basis vectors in $\mathbb{R}^n$
$e_{(\cdot)}$	error component
$\mathscr{E}$	set of edges
$\boldsymbol{f}_{(\cdot)}$	force
$F_{(\cdot)}$	robot friction matrix
$\boldsymbol{g}$	gravity vector
$\boldsymbol{g}_{(\cdot)}(\boldsymbol{\theta}_{(\cdot)})$	robot gravity vector
G_i	partial grasp matrix of the ith agent
G	grasp matrix
$\boldsymbol{h}_{(\cdot)}$	$= [\boldsymbol{f}_{(\cdot)}^{\intercal}, \boldsymbol{t}_{(\cdot)}^{\intercal}]^{\intercal}$, wrench
$J_{(\cdot)}$	robot Jacobian
J_o	rotational object inertia
J	cost functional
$k_{(\cdot)}$	proportional gain
$K_{(\cdot)}$	stiffness matrix
K	feedback matrix
L	Lagrangian (Chapter 2), Laplacian (Chapter 4, 5)
$m_{(\cdot)}$	translational mass gain
$M_{(\cdot)}$	mass matrix
$N_{(\cdot)}$	neighbor of $(\cdot)$
N	number of robots/agents
$n_{(\cdot)}$	number of $(\cdot)$
n	number of joints
$\boldsymbol{p}_{(\cdot)}$	position
$\dot{\boldsymbol{p}}_{(\cdot)}$	translational velocity
$\boldsymbol{q}_{(\cdot)}$	$= [\nu_{(\cdot)}, \epsilon_{(\cdot)}^{\intercal}]^{\intercal}$, orientation in quaternion form
Q	positive weighting matrix
$Q_{(\cdot)}$	weighting matrix (Chapter 3), controllability matrix (Chapter 4, 5)
$p((\cdot))$	share of $(\cdot)$
P	characteristic matrix of a partition
$\boldsymbol{r}_{(\cdot)}$	grasp constraint vector
$R_{(\bullet)}^{(\cdot)}$	rotation matrix of $(\cdot)$ relative to $(\bullet)$
R	positive weighting matrix
$s_{(\cdot)}$	phase variable
$S(\cdot)$	skew-symmetric matrix operator defining the cross product
S	positive weighting matrix

t	time
$t_{(\cdot)}$	torque
$T_{(\cdot)}$	kinetic energy
T	final time (Chapter 3), similarity transformation (Chapter 4, 5)
$\boldsymbol{u}_{(\cdot)}$	input
$U(\boldsymbol{q})$	aid matrix for quaternion propagation defined in Eq. (2.5)
$\boldsymbol{\nu}_{(\cdot)}$	$= [\ \dot{\boldsymbol{p}}_{(\cdot)}^{\intercal}, \boldsymbol{\omega}_{(\cdot)}^{\intercal}]^{\intercal}$, twist as 6D manipulator velocity, eigenvector (Chapter 5)
ν	task-dependent feedback to human
$V_{(\cdot)}$	potential energy/ field/ Lyapunov candidate/ storage function
$\boldsymbol{x}_{(\cdot)}$	state
x	Cartesian position component
y	Cartesian position component
$\boldsymbol{z}$	state
$\alpha_{(\cdot)}$	weighting parameter
$\beta_{(\cdot)}$	weighting parameter
$\gamma_{(\cdot)}$	scalar step length (Section 5.3), weighting parameter (Section 3.4, 4)
Γ	weighting matrix
$\Gamma(\nu)$	set of neighbors of vertex ν
$\Gamma_{V_1}(\nu)$	set of neighbors of vertex ν within the vertex set V_1
$\delta_{(\cdot)}$	rotational damping gain (Chapter 2), weighting parameter (Chapter 3)
$\boldsymbol{\epsilon}_{(\cdot)}$	imaginary part of a quaternion
$\boldsymbol{\zeta}_{(\cdot)}$	state
$\boldsymbol{\theta}_{(\cdot)}$	robot joint configuration
$\kappa_{(\cdot)}$	rotational proportional gain (Chapter 2), weighting parameter (Chapter 3)
$\boldsymbol{\lambda}$	adjoint state
$\boldsymbol{\lambda}_{(\cdot)}$	eigenvalue
$\mu_{(\cdot)}$	rotational inertia gain
$\nu_{(\cdot)}$	real part of a quaternion, weighting parameter (Section 3.4)
$\boldsymbol{\xi}_{(\cdot)}$	$= [\boldsymbol{p}_{(\cdot)}^{\intercal}, \boldsymbol{q}_{(\cdot)}^{\intercal}]^{\intercal}$, pose
$\sigma(\cdot)$	set of eigenvalues of $(\cdot)$
$\Sigma_{(\cdot)}$	coordinate sytem frame
π	partition
$\rho_{(\cdot)}$	characteristic polynomial of $(\cdot)$, partition (Chapter 5)
$\boldsymbol{\tau}_{(\cdot)}$	robot actuation torque
$\tau_{(\cdot)}$	timing parameter
φ	rotational angle
$\chi_{(\cdot)}$	particular state
$\mathcal{V}$	set of vertices
$\boldsymbol{\omega}_{(\cdot)}$	angular velocity

List of Figures

List of Tables

1

Introduction

Conducting is the mighty and intricate art of supervising and directing a large instrumental ensemble such as an orchestra or a chorus. In an orchestra the conductor acts as a guide to the ensemble of musicians. He or she uses hand gestures to control e.g. the orchestra's tempo or the correct entry of various ensemble members. While obeying the conductor's signals the individual musicians of the orchestra still need to communicate nonverbally and arrange among themselves in order to deliver an outstanding performance to the audience. Comparable circumstances arise when robotic assistances enter our everyday's work and personal life in the near future: an exceptional and convincing performance of the robotic helpers is required so that robots can become universally and widely accepted. Then the intended role of the human is primarily to become the conductor or guide of a multitude of serving and facilitating robotic assistances. In order to likewise offer a convenient interaction between the human guide and the robots both cooperation and coordination between the individual robots is required.

Already today a large portion of the goods which are produced in factories is part of a fully automated assembly line. Following the overall advancements in the field of robotics the situations where the cooperation of multiple robots is required have gained in importance. The impact of cooperative robots in payload transportation for manufacturing and industrial applications cannot be overestimated. The benefits of employing multiple manipulators to manipulate a common object cooperatively include increased payload capacity, expanded functionality, and increased dexterity with larger objects. The employment of cooperative manipulators covers applications ranging from an assembly of robots transporting differently sized payloads in the absence of gantry cranes to a group of robots clearing an unstructured path in search-and-rescue scenarios. Similarly extra-terrestrial colonization efforts can clearly benefit from cooperative manipulation when mobile rovers equipped with manipulators can cooperatively assemble the facilities.

Out of all things necessary to successfully realize a cooperative manipulation task, robot control is the most relevant element. The constraints of a manipulation task which is accomplished by

an ensemble of multiple robots requires a tight coordination and cooperation of all participating robots. A cooperative manipulation task is considered to be successfully conducted when the multi-robot team jointly manipulates the object from an initial configuration to a final configuration without damaging the object, i.e. there is no significant deviation of the forces acting on the manipulated object from the desired forces. The first endeavors to synthesize a collective robot behavior for cooperative manipulation focus on a decentralized control scheme where each robot infers its desired motion/force control set-points from a global plan where no communication among the team members takes place. Each robot self-reliantly reacts to adaptations in the global plan but does not efficiently and cooperatively react in a distributed way to disturbances acting on a single robot. Advances in real-time inter-robot communication and in distributed control algorithms enable the development of distributed coordination controllers where the particular capabilities of the individual robots are exploited while achieving the common global objectives of cooperative manipulation. Recalling the image of an orchestra robot control in a cooperative manipulation task corresponds to the individuals professionally playing the particular instrument while the group collectively performs through nonverbal communication and arrangement.

It can be expected that due to their complementary strengths robots will replace humans to an even bigger extent in the future in particular when it comes to repetitive or exhausting work. Unlike in familiar situations, however, a human outperforms a robot in unknown situations where the human cognitive abilities are essential. Within the context of human robot interaction, most established controllers enable the human to only direct a single robot at a time and this solutions does not scale. The development of a user interface for controlling multiple robots robots presents a valuable prospect to bring a human in the control loop. One of the problems is that the number of robots a single operator can supervise is naturally limited by human attention and the human memory capacity. A cooperative manipulation task requires a single human operator to control a group of autonomous robotic agents without guiding each robot individually but directing the collective as a group. Recalling the image of the orchestra the human task is here to supervise and guide the collective of robots. Both cooperative robot manipulation algorithms and controlling a team of robots state significant challenges on their own, however an approach addressing both simultaneously is an extraordinarily challenging assignment.

We envision a human operator being the conductor of an ensemble of multiple mobile robots cooperatively manipulating an object. To achieve this vision, we acknowledge the importance of an efficient control mechanism to simultaneously guide multiple agents while autonomy is left with each robot. In order to motivate the relevance of the research topic the main challenges which are faced by the control design for guiding multiple robots in a cooperative manipulation task are summarized in the following.

1.1 Challenges

The control design for the guidance of a cooperative multi-robot manipulation task faces multiple challenges in the fields of robot control, human-machine interaction, and networked control systems. Some of the key issues studied in this thesis are summarized as follows:

Control design

A multi-robot cooperative manipulation task can be considered as a system consisting of multiple robots and an object to be manipulated. The particular members of the cooperating robot team are physically coupled through the object which imposes strict constraints on the control objectives. Using a team of robots for cooperatively manipulating an object drastically increases the complexity since the motions of all manipulators need to be coordinated. The behavior of the cooperative manipulator system is determined by the interaction of the manipulator dynamics which are typically multi-degree-of-freedom with nonlinear dynamics and the dynamics of the object to be manipulated. The interplay between manipulator control schemes and the interaction forces among the manipulators needs to be addressed in a successful implementation of a joint coordination strategy for cooperatively manipulating robots.

Human-machine interaction

In order to provide high-level instructions to the robots an interaction mechanism for the human operator is required where he/she can explicitly guide a cooperative multi-robot manipulation task. The human operator of such a complex system is provided with a large number of interaction possibilities to achieve the system goal efficiently and safely. Recent development in robotics makes it possible to automate many aspects of the manipulation task and masks the task from the operator in situations where relevant autonomous core functionalities are required such as not damaging the object regardless of the human command or collective obstacle avoidance in an unstructured environment. Among many others two fundamental issues have been identified in the interaction between a human and a group of robots: the choice of a suitable and natural way to simultaneously command multiple robots and providing appropriate feedback to the human operator.

Network synthesis

Traditionally, the cooperative manipulation of an object only lacks a handful of collaborating robots. The influence of the human operator on the particular robot dynamics is known to depend on both the number of acting robots and the interaction topology among the cooperating robots. When a handful robots develop into a large number of robots the complexity and the implication of the problem is significantly increased and the research problem transforms into a human-network interaction problem. Here, the influence of the human operator on particular network agents can be still explained using classical system theory. However, control theory provides no answer to what the relevance of the particular interaction between any two agents for the controllability of the system is. For such large-scale network system novel topological methods for characterizing and describing the influence of the human input on the individual agents are required.

1.2 Main Contribution and Outline

This thesis aims for fundamental issues in the guidance of a multi-robot cooperative manipulation task by a human operator. It studies the scientific questions of *"how to design a distributed control law which optimally coordinates multiple robots in order to accomplish the manipulation task*

cooperatively?", "what are the requirements of a human-robot interaction principle which enables the guidance of a cooperative manipulation task by a human operator while still preserving autonomous functions of the robot team?", "how does the number of (robotic) agents and the interaction topology among the (robotic) agents affect the influence of the human operator on particular robots and how can we characterize this effect by topological properties of the graph which represents the interaction topology of the system?" All these questions will be targeted in the domain of multi-robot cooperative manipulation and human-network interaction. Chapter 2 reviews related background on cooperative object manipulation by multiple robotic manipulators and establishes a model of the manipulated object and the dynamics of a robotic multi-arm system. The following chapters address the aforementioned problems of (i) control design for multi-robot cooperation, (ii) human-machine interaction, and (iii) network synthesis. To enable an effective cooperative manipulation task, Chapter 3 introduces novel methods for devising distributed controllers which employ formation control in the optimal control design or couple individually generated trajectories in order to achieve the desired global objective. Regarding human-machine interaction, a novel and innovative team control approach for the human guidance of a multi-robot cooperative manipulation task based on a leader-follower formation control is presented in Chapter 4. Leader-follower formation dynamics are advantageous for interfacing a cooperative manipulation task but they genuinely demonstrate their strengths when dealing with large-scale networks. Chapter 5 introduces fundamental insights on the relation between the interaction topology of a leader-follower formation and the particular coupling mechanisms. In addition, novel topological conditions based on graph partitioning for characterizing the influence of a single input on the particular following agents are presented. In the following, the major contributions within each chapter are outlined.

Chapter 2: Modeling of a Multi-Robot Cooperative Manipulation Task

In this chapter a force control scheme based on the commonly employed impedance control is introduced which is widely employed for cooperative multiple mobile manipulators. The coordination problem of the emerging kinematic tree structure built by mobile platform and two anthropomorphic manipulators is resolved by a decoupling technique in task space. A consistent modeling of the interaction dynamics consisting of the individual impedance-controlled manipulators and the manipulated object is presented at the object and the manipulator level. The presented model relies on the Gauss' principle of least constraint. Simultaneously we present an extensive formulation of the state and input constraints which are apparent in a cooperative manipulation task and whose violation leads to undesired and not motion-inducing forces called internal forces. Internal force analysis is considered as an evaluation criterion and the impact of the coordination schemes on the manipulation performance is demonstrated in an experimental study with four 7 degree of freedom manipulators on two mobile platforms. Some results of this chapter have been partly published previously in [1].

Chapter 3: Formation-based Coordination of Cooperative Robotic Manipulation

The main contributions of this chapter are distributed control approaches for cooperative manipulation tasks facilitated by a movement synchronizing control law and a suboptimal LQR-like control law for physically cooperating manipulators. The first approach regulates the multi-robot

system in an optimal fashion to a final configuration while maintaining its formation. To achieve the LQR-like control law, we formulate an optimal control problem which combines the classical quadratic cost function with a relaxed formation (rigidity) constraint in terms of an additional biquadratic penalty term. This relaxed rigidity constraint is justified by the use of impedance control, by which minor deviations from the rigidity constraint result in tolerable object stress. Because of the biquadratic term the LQR problem cannot be solved using standard methods, we propose an iterative descent method inspired. The second approach is based on formation control and coupled DMP-based trajectory planning. Here, DMPs generate individual manipulator trajectories to a desired final configuration, which is in agreement with the initial configuration of the multi-robot team. During the tracking phase, it may happen that individual DMPs violate the formation rigidity or disturbances occur on a single manipulator. The issue is circumvented in our approach by using a formation-preserving feedback for each DMP. Minor remaining deviations from the formation are accommodated by local impedance control laws in each manipulator such that they react compliantly to their environment. Both proposed control and trajectory generation approaches are evaluated in experiments and their robustness against perturbations and reduced internal forces on the object are demonstrated for cooperative manipulation and synchronized motion tasks. The results of this chapter have been partly published previously in [2, 3, 4]

Chapter 4: Human Interaction with a Multi-Robot Manipulation Task

The contribution of this chapter is a novel approach for the human guidance of a multi robot cooperative manipulation task. It is based on a leader-follower formation control approach. We discuss system equilibria and their stability and show that the human-guided set-point generator and the impedance-based multi-robot interaction dynamics are asymptotically stable for a human position command being the input. Particularly critical for internal forces is also the transient phase, where excessive forces can easily occur if the motion transients of the individual robots do not match. Therefore, we present a controllability analysis of the human-robot team interaction in a cooperative manipulation task. We investigate the controllable eigenmodes of the robot formation and show that it is beneficial during the transient phase when every robot can access the state information of the human leader. As a result the desired trajectories are in accordance with the object geometry during the transient phase and the desired internal force acts on the object. Based on these results we devise a control strategy for human-controlled formations of physically cooperating robots. If the human could control multiple robots independently in a cooperative manipulation task, the human can drive different robots independent from each other and is thus able to actively alter the distances between the robots. Hence there can occur a violation of the formation rigidity which results in undesired stress on the object. Furthermore, we present results of a pilot study in which vibrotactile feedback based on the formation state is applied to the human operator. The results of this chapter have been partly published previously in [5, 6].

Chapter 5: System Analysis of Interaction Dynamics through Graph Partitioning

The main contribution of this article is to provide novel topological conditions for uncontrollability in leader-follower consensus dynamics. Typically leader-invariant AEPs are consulted to describe the controllable subspace topologically. We approach the novel conditions as follows: First we mathematically indicate under which circumstances the uncontrollable subspace of a particular

interconnection graph is not completely characterized by leader-invariant AEPs. To identify the uncontrollable subspaces we make use of the fact that a 0−entry in an eigenvector of the Laplacian L or geometric multiplicity of the eigenvalues lead to an uncontrollable subspace. A particular special case of eigenvectors characterized by AEPs is an augmented class of Faria vectors which is related to the uncontrollable subspace of the controlled consensus problem. By doing so we can characterize an uncontrollable subspace of the controlled consensus problem and its corresponding eigenvalue. Based on these findings, we discuss under which conditions the selection of multiple leaders in a network leads to an uncontrollable subspace. Due to the duality of controllability and observability, the obtained results translate to the corresponding observability problem. The result of this article is approached by an extensive numerical investigation to obtain empirical results which uncontrollable subspaces can be characterized by the conditions presented in this article and not by leader-invariant AEPs. The numerical investigations consider a number of graphs with different graph size and a different number of edges. The numerical examples consolidate that the proposed conditions based on Faria vectors can topologically characterize a different part of the uncontrollable subspace than AEP condition under certain conditions and substantiate the importance of the novel topological conditions. The presented conditions provide a more complete picture which subspaces in a controlled consensus protocol are controllable and uncontrollable, respectively. The results of this chapter have been partly published previously in [7, 8].

2

Modeling of a Multi-Robot Cooperative Manipulation Task

2.1 Motivation

The cooperation and interaction of several mobile manipulators to achieve a common task is a popular research topic. A specific problem in the area is the cooperative manipulation of objects where several physically cooperating manipulators collaboratively transport an object from an initial to a final configuration. Some tasks are difficult or even impossible to get when a single robotic manipulator has to execute them. For example the manipulation of heavy or large objects requires the collaboration of several manipulators. Other relevant applications of cooperative manipulation are the assembly of multiple parts without employing individual fixtures or the manipulation of flexible objects where the objects feature extra degrees of freedom. A successful manipulation task is characterized by accurately manipulating the object without distortion along a desired trajectory. A motion coordination of the cooperating manipulators is required in order to reach the object's goal position and orientation and such that the stress acting on the object does not deviate too much from the desired stress. Using mobile manipulation here is exceptionally interesting since it substantially increases the workspace of all cooperating manipulators and extends the manipulation task to large-scale environments. Cooperative manipulation schemes aim to achieve a global control goal by conducting a group of manipulators resulting only from local control actions. Each manipulator interacts directly with the object and indirectly with the remaining manipulators through the object by the aforementioned local control action. In order to later devise coordination control strategies for the cooperating manipulators we now revise historical developments in cooperative manipulation.

2.2 Related Work

The research interest on the physical cooperation of multi-arm robots has emerged in the early 1970s [9, 10]. Already back then the importance of employing a force/compliance control scheme and using task-space control for the coordination of the manipulators in a tight physical coupling has been recognized. A compliant behavior of the cooperating manipulators w.r.t. the manipulated object was realized by utilizing the back-drivability of the actuators in [9]. In retrospect the results concerning cooperative manipulation can be mainly seen as preliminary.

A strong theoretical background on the cooperation of a multi-robot system is established in the 1980s [11]. In particular during that time the researcher defined a task vector which lies in the object to be manipulated [12] and derived multi-body dynamics of a closed kinematic chain which consisted of multiple cooperating robots and the object [13, 14]. The derivation of these techniques has enabled the application of more advanced control approaches in order to facilitate a multi-robot cooperative manipulation task.

Technological advances and theoretical results in hybrid motion/force control enabled two principal questions to be investigated in the 1990s: how can we simultaneously control both the trajectory of the object and the stress acting on the object by multiple robotic manipulators; and how can we exploit novel robot control techniques to render the cooperating manipulators compliant w.r.t. the object. In order to deal with the former challenge different techniques have been proposed which employ force decomposition schemes as studied in [15, 16, 17, 18]. Force optimization techniques have been exploited in studies of cooperative manipulation [19]. In particular, a unique and geometrical consistent mathematical model of the internal forces/torques acting on the manipulated is considered to be a major challenge. Without explicitly taking into account the dynamics of the collaborating robotic manipulators a general solution to internal forces is presented in [20]. The second research direction in the 1990s investigates how to render manipulators compliant w.r.t to the environment. Proposed control methods used in cooperative manipulation tasks range from motion and force control techniques [21], to adaptive control approaches [22, 23], or even joint-space control [24, 25]. In a tight physical coupling, impedance-based control schemes are considered favorable in manipulation tasks, since they specify the desired dynamics in analogy to a mechanical mass-spring-damper system. Impedance control [26] is widely applied for end effector control enforcing a relation between measured force and resulting motion. In cooperative manipulation tasks impedance control enables to actively render a desired robot behavior and to simultaneously determine an internal and external compliance by employing a structural control design approach [27]. Furthermore, it may also be used to define the desired dynamics of the manipulated object [28] which is subject to the forces acting on the attached end effectors. Distributing impedance-based control schemes among several cooperating manipulators is demonstrated to be preferable in [29] which also includes a stability analysis Both principal research questions of the 1990s, namely impedance control and internal force control, are brought together in [18] where an internal-force based impedance control scheme for cooperating manipulators is proposed. However, in [18] the impedance control scheme is only employed to regulate the internal force. A relevant and fundamental fact is neglected here that internal force actually arises from the rendered impedance-based system dynamics and so the impedance control parameters need to be considered in characterizing internal forces acting on the object. Just recently, this gap between the two main research directions from the 1990s has

been closed in [30] where a mathematical model for the internal force is derived studying the interaction dynamics of impedance-controlled manipulators in task space in order to finally reveal multi-body dynamics considering manipulator and object dynamics.

Research interests in cooperative manipulation around the 2000s mainly focus on expanding and extending the worskpace of a cooperative manipulation task by mobile platforms. Two major challenges in mobilizing cooperative manipulating robots are considered to be the variety of mobile platforms available, e.g. holonomic in contrast to non-holonomic or omnidirectional in contrast to conventual wheels and that the motion of the particular robots is always subject to a global reference system. By utilizing mobile bases for each cooperating robots the relative pose between any two manipulating robots is subject to motion, too. A collection of proposed mobile multi-robot manipulating systems with mobile bases is depicted in Figure 2.1. A pioneering research result is presented in [31] where a decentralized strategies for cooperative manipulation with mobile manipulator systems which are installed on a holonomic mobile base is proposed. Control schemes and motion planning algorithms for cooperative mobile manipulation tasks incorporating the non-holonomic mobile platforms are presented from various centralized perspectives in [32, 33, 34]. In [35] impedance controllers for the transportation of a large object is proposed by particularly locking and unlocking joints of the manipulators mounted on mobile platforms. Another simple but promising distributed approach for cooperative mobile manipulation is presented in [36, 37, 38]: To accomplish a cooperative physical manipulation task some control methods only consider rather simple mobile robots in order to enclosure the object collectively and then push the object collaboratively. From a centralized entity, cooperative optimal motion planning schemes are developed in [39] and the consequences of flexibility are outlined in [40]. In particular, [37] provides a convenient solution for tackling the issues that arise from the relative movement of the robots when using mobile platforms by aligning the individual robotic reference systems through data exchange. It remains open how to perform distributed control of the motion of a dual manipulator systems mounted on a single mobile platform in order to accomplish a successful cooperative manipulation task.

Just recently, around the 2010s novel technologies in force-/torque sensors bring impedance control back in the focus of cooperative manipulation research [41]. In particular, a comparison of object-level grasp controllers for dynamics cooperative manipulation tasks shows the supremacy of using distributed impedances for cooperative manipulation tasks from a practical point-of-view [42]. In addition, recent advances and novel methods in theoretical distributed network control find their path into the distributed control of multiple robotics systems. Their modes of operation are versatile: uncertainty in the kinematics of an individual manipulator and the closed kinematic chain built by two manipulators is addressed in [43] and [44, 45, 46]. Recent publications [47, 41] indicate the relevance and the expected benefits of distributed control architectures for dual-arm mobile manipulation tasks. Decentralized motion control approaches [48] and distributed estimation methods for unknown payloads [49, 50] are recently discussed in the literature.

To sum up now, the literature review in cooperative robotic manipulation suggests to employ a distributed impedance control in task-space in order to render each manipulator compliant w.r.t each other for a successful execution of the cooperative manipulation task. The workspace of each manipulators is to be extended with a mobile platform and the motion of the platform needs to be locally coupled with the impedance control in order to retain the local control actions. For

latter proposing distributed control methods a consistent system model with several fundamental theoretical results of the impedance-controlled cooperating manipulators and the object to be hold is derived in the upcoming sections.

2.3 Robot Dynamics and Control

First, we present the general dynamical model of a robot and revise a feedback linearization control law in order to realize a compliant behavior of the robot. Both models are introduced in order to present the assumptions which are considered throughout this work. In order to decouple the motion of the mobile platform from the manipulators we propose a decoupling approach for manipulator and mobile platform and conclude with an illustration of the resulting system architecture.

2.3.1 Robot Model and Control

For a detailed analysis of the interaction between the manipulators among each other through the object it is convenient to consider a robot behavior which is compliant. A model which highlights the interaction effects of a cooperative manipulation task in joint space are presented in [60, 61, 62, 63]. For a better understanding of the interaction between the manipulators through the object it is beneficial to refer to a operational space control scheme. However, the motion of the robot is generally described in generalized coordinates. Using for example a Lagrange formulation in order to describe the equation of motion of a robotic manipulator [64, 65, 66], the dynamic model of a manipulator with $n \in \mathbb{N}^+$ joints can be written as

$$B_i(\boldsymbol{\theta}_i)\ddot{\boldsymbol{\theta}}_i + C_i(\boldsymbol{\theta}_i, \dot{\boldsymbol{\theta}}_i)\dot{\boldsymbol{\theta}}_i + F_i\dot{\boldsymbol{\theta}}_i + \boldsymbol{g}_i(\boldsymbol{\theta}_i) = \boldsymbol{\tau}_i - J_i^{\mathsf{T}}(\boldsymbol{\theta}_i)\boldsymbol{h}_i^e, \tag{2.1}$$

where the generalized coordinates $\boldsymbol{\theta}_i \in \mathbb{R}^n$, $\dot{\boldsymbol{\theta}}_i \in \mathbb{R}^n$, and $\ddot{\boldsymbol{\theta}}_i \in \mathbb{R}^n$ are the joint position, joint velocity, and joint acceleration, respectively. Furthermore, $B_i(\boldsymbol{\theta}) \in \mathbb{R}^{n\times n}$ is the inertia matrix which is known to be always positive definite and symmetric. $C_i(\boldsymbol{\theta}_i, \dot{\boldsymbol{\theta}}_i)\dot{\boldsymbol{\theta}}_i \in \mathbb{R}^n$ refers to the centrifugal and Coriolis terms and $F_i\dot{\boldsymbol{\theta}}_i \in \mathbb{R}^n$ to the viscous friction torques. The gravity vector is given by $\boldsymbol{g}_i(\boldsymbol{\theta}_i) \in \mathbb{R}^n$. The actuation torques are denoted by $\boldsymbol{\tau}_i \in \mathbb{R}^n$. If the manipulators are in contact with the environment which is in our setup the object and the remaining manipulators then $J_i^{\mathsf{T}}(\boldsymbol{\theta}_i)\boldsymbol{h}_i^e \in \mathbb{R}^n$ are the interacting torques resulting from the contact forces $\boldsymbol{h}_i^e \in \mathbb{R}^6$ which are exerted on the environment by the manipulator's end-effector. The direct kinematics which accounts for the dependence of the operational-space task variable $\boldsymbol{\xi}_i$ from the joint positions $\boldsymbol{\theta}_i$ as

$$\boldsymbol{\xi}_i = \boldsymbol{k}(\boldsymbol{\theta}_i),$$

where $\boldsymbol{k}(\cdot)$ is a generally nonlinear vector function. The Jacobian $J_i(\boldsymbol{\theta}_i) \in \mathbb{R}^{6\times n}$ defines a mapping for the differential kinematics

$$\boldsymbol{v}_i = J_i(\boldsymbol{\theta}_i)\dot{\boldsymbol{\theta}}_i, \tag{2.2}$$

(a) (a)

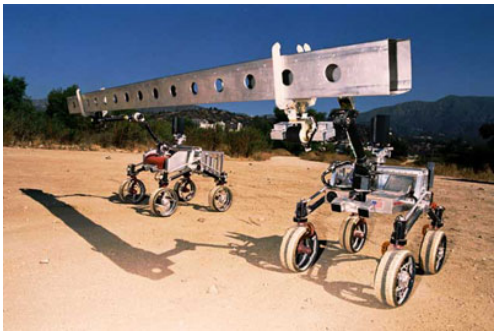

(b) (b)

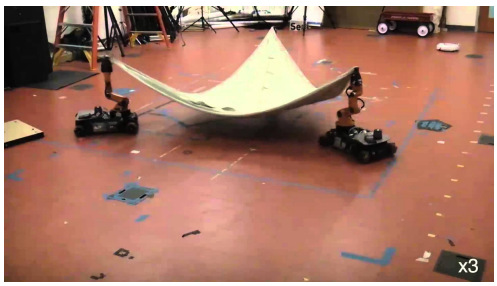

(c) (c)

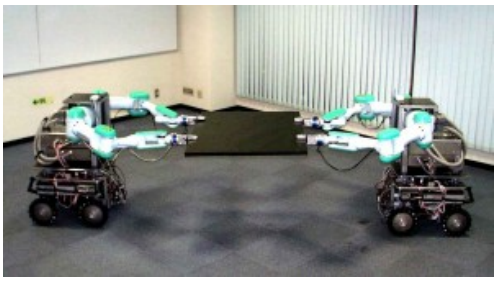

(d) (d)

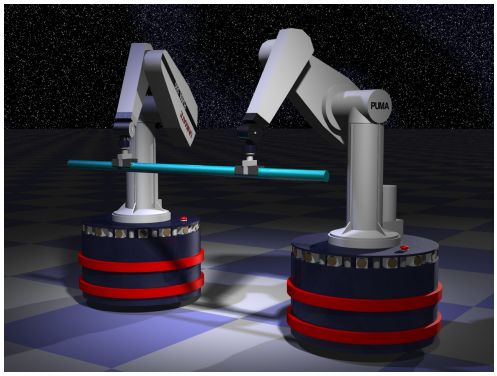

(e) (e)

(f) (f)

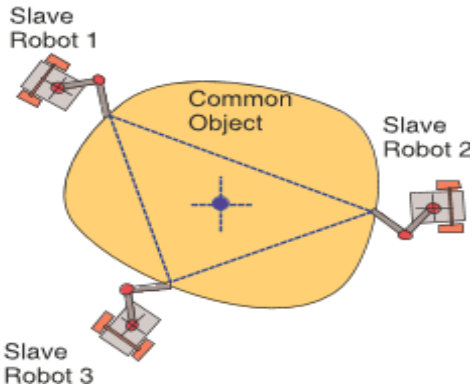

(g) (g)

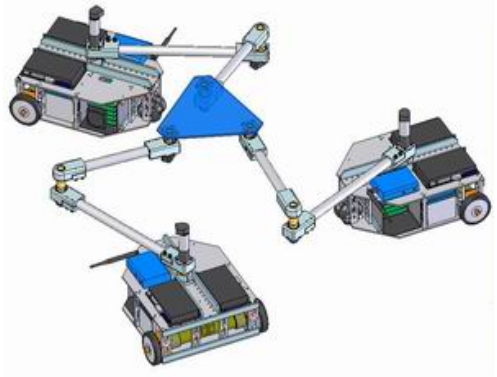

(h) (h)

Figure 2.1: Examples of cooperative mobile multi-robot manipulation systems: (a) Heterogeneous robotic systems in [32], (b) Planetary rover exploration in [51], (c) Manipulating deformable objects in [52], (d) Caster-like motion in [53], (e) Decentralized control in [54], (f) Distributed manipulation in [55], (g) Cooperative tele-manipulation in [56, 57], (h) Wheeled mobile robots in [58, 59].

between the joint velocities $\dot{\boldsymbol{\theta}}_i$ and the end-effector velocity $\boldsymbol{\nu}_i$. In line with the literature the twist $\boldsymbol{\nu}_i$ in operational space is defined by the end-effector's translational and angular velocity as $\boldsymbol{\nu}_i = \left[\dot{\boldsymbol{p}}_i^\intercal, \boldsymbol{\omega}_i^\intercal\right]^\intercal \in \mathbb{R}^6$. Depending on the representation of the orientational part of $\boldsymbol{\nu}_i$ the literature distinguishes between the analytical Jacobian J_i^A which references to the rotational velocity and the geometrical Jacobian J_i which references to the angular velocity. In order to allow minor deviations of the desired position trajectories from the constraints which are always apparent in a physical cooperation task and which can result e.g. from model and geometric uncertainties or external disturbances we propose to employ a impedance control scheme for each of the N manipulators here. We choose

$$\boldsymbol{\tau}_i = B_i(\boldsymbol{\theta}_i)\boldsymbol{y}_i + C_i(\boldsymbol{\theta}_i, \dot{\boldsymbol{\theta}}_i)\dot{\boldsymbol{\theta}}_i + F_i\dot{\boldsymbol{\theta}}_i + \boldsymbol{g}_i(\boldsymbol{\theta}_i) + J_i^\intercal(\boldsymbol{\theta}_i)\boldsymbol{h}_i^e, \tag{2.3}$$

where $\boldsymbol{\tau}_i$ generally accounts for different possible nonlinear control options through feedback linearization. The impedance control scheme can be attributed to a mechanical system with mass matrix M_i, damping matrix D_i, and stiffness matrix K_i. Hence, we impose the desired compliant and moving behaviours with freely tuneable and designable parameters M_i, D_i, and K_i and conceptually determine $\boldsymbol{y}_i$ to be

$$\boldsymbol{y}_i = J_i^{A^{-1}}(\boldsymbol{\theta}_i)M_i^{-1}\left(M_i\dot{\boldsymbol{\nu}}_i^d + D_i(\boldsymbol{\nu}_i - \boldsymbol{\nu}_i^d) + \boldsymbol{h}_i^{\mathscr{K}}(\boldsymbol{\xi}_i, \boldsymbol{\xi}_i^d) - M_i\dot{J}_i^A(\boldsymbol{\theta}_i, \dot{\boldsymbol{\theta}}_i)\dot{\boldsymbol{\theta}}_i - h_i + h_i^d\right).$$

Here, $\boldsymbol{\xi}_i = [\boldsymbol{p}_i^\intercal, \boldsymbol{q}_i^\intercal]$ denotes the pose and $\boldsymbol{h}_i = [\boldsymbol{f}_i^\intercal, \boldsymbol{t}_i^\intercal]^\intercal \in \mathbb{R}^6$ is the applied wrench to the i-th manipulator. The pose is split into the end-effector position $\boldsymbol{p}_i \in \mathbb{R}^3$ describing the translational part and the unit quaternion $\boldsymbol{q}_i = \left(\eta_i, \boldsymbol{\epsilon}_i^\intercal\right)^\intercal \in SO(3)$ describing the rotational part where $\eta_i \in \mathbb{R}$ is the real part and $\boldsymbol{\epsilon}_i \in \mathbb{R}^3$ is the imaginary part. Throughout this thesis all quaternions $\boldsymbol{q}_i$ are unit quaternions, i.e. the following relationship always holds

$$\boldsymbol{q}_i^\intercal\boldsymbol{q}_i = \eta_i^2 + \boldsymbol{\epsilon}_i^\intercal\boldsymbol{\epsilon}_i = 1.$$

The wrench $\boldsymbol{h}_i$ is split into forces and torques $\boldsymbol{f}_i, \boldsymbol{t}_i \in \mathbb{R}^3$. Furthermore, the desired manipulator pose is represented by $\boldsymbol{\xi}_i^d = [\boldsymbol{p}_i^d, \boldsymbol{q}_i^d]$ and the desired wrench by $\boldsymbol{h}_i^d$. The desired position $\boldsymbol{p}_i^d \in \mathbb{R}^3$ of the ith end-effector in task space is denoted as $\boldsymbol{p}_i^d = [p_{i,1}^d, p_{i,2}^d, p_{i,3}^d]$, where $p_{i,1}^d, p_{i,2}^d, p_{i,3}^d$ denote the components along each translational direction in Cartesian space. The desired orientation $\boldsymbol{q}_i^d \in \mathbb{S}^3$ is in a similar manner denoted as $\boldsymbol{q}_i^d = \left[\eta_i^d, \boldsymbol{\epsilon}_i^d\right]$, where η_i^d is the scalar part and $\boldsymbol{\epsilon}_i^d$ is the vector part of the quaternion. The compliance is represented by $M_i = \mathrm{diag}(m_i I_3, \mu_i I_3), D_i = \mathrm{diag}(d_i I_3, \delta_i I_3), K_i = \mathrm{diag}(k_i I_3, \kappa_i I_3) \in \mathbb{R}^{6\times 6}$ wich are the positive definite mass, damping, and stiffness matrices, respectively. Note that parameters M_i, D_i, and K_i can be freely chosen and tuned and they impose the desired dynamics on the system in both motion phases and contact phases. The translational behavior is determined by scalar values $m_i, d_i, k_i \in \mathbb{R}^+$ rendering an isotropic translational behavior. The rotational behavior is specified by the scalar parameters $\mu_i, \delta_i, \kappa_i \in \mathbb{R}^+$. A stiffness [67] in six degrees-of-freedom is given by

$$\boldsymbol{h}_i^{\mathscr{K}}(\boldsymbol{\xi}_i, \boldsymbol{\xi}_i^d) = \begin{bmatrix} \boldsymbol{f}_i^K \\ \boldsymbol{t}_i^\kappa \end{bmatrix} = \begin{bmatrix} k_i(\boldsymbol{p}_i - \boldsymbol{p}_i^d) \\ 2\kappa_i U(\boldsymbol{q}_i)^\intercal(\boldsymbol{q}_i - \boldsymbol{q}_i^d) \end{bmatrix}, \tag{2.4}$$

where the difference of current and desired orientation is defined as the imaginary part of the quaternion product $\boldsymbol{q}_i \cdot (\boldsymbol{q}_i^d)^{-1}$ and can be expressed as $U(\boldsymbol{q}_i)^\intercal(\boldsymbol{q}_i - \boldsymbol{q}_i^d)$. Here, the aid matrix

$U(\boldsymbol{q}_i) \in \mathbb{R}^{4\times 3}$ is defined as

$$U(\boldsymbol{q}_i) = \begin{pmatrix} -\boldsymbol{\epsilon}_i^\intercal \\ \eta_i I_3 + S(\boldsymbol{\epsilon}_i) \end{pmatrix}. \tag{2.5}$$

The operator $S(\cdot)$ is the skew-symmetric matrix operator defining the cross product, i.e. $S(\boldsymbol{a})\boldsymbol{b} = \boldsymbol{a} \times \boldsymbol{b}$. When using unit quaternions the aid matrix $U(\boldsymbol{q}_i)$ features the following relevant identities

$$U(\boldsymbol{q}_i)^\intercal U(\boldsymbol{q}_i) = I_3, \tag{2.6a}$$
$$U(\boldsymbol{q}_i) U(\boldsymbol{q}_i)^\intercal = I_4 - \boldsymbol{q}_i \boldsymbol{q}_i^\intercal, \text{ and} \tag{2.6b}$$
$$U(\boldsymbol{q}_i)^\intercal \boldsymbol{q}_i = 0. \tag{2.6c}$$

A proper conversion between the time derivative of the robot state $\dot{\boldsymbol{\xi}}_i$ and the twist $\boldsymbol{\nu}_i$ is given by

$$\boldsymbol{\nu}_i = \begin{bmatrix} I_3 & 0 \\ 0 & 2U(\boldsymbol{q}_i)^\intercal \end{bmatrix} \dot{\boldsymbol{\xi}}_i, \tag{2.7}$$

where the conversion can be compactly written with the help of the aid matrix $U(\boldsymbol{q}_i) \in \mathbb{R}^{4\times 3}$. In order to keep linearity and decoupling along the degrees of freedom, a force/torque sensor is required to measure the interaction force $\boldsymbol{h}_i$. Furthermore, the following assumptions regarding the sensor measurements and the system parameters are made.

Assumption 2.1. The measurements of the force $\boldsymbol{h_i}$ and the joint values $\boldsymbol{\theta}_i, \dot{\boldsymbol{\theta}}_i, \ddot{\boldsymbol{\theta}}_i$ are error-free. Furthermore, the terms $B_i(\boldsymbol{\theta}_i)$, $C_i(\boldsymbol{\theta}_i, \dot{\boldsymbol{\theta}}_i)$, $F_i\dot{\boldsymbol{\theta}}_i$, $\boldsymbol{g}_i(\boldsymbol{\theta}_i)$ of the robot dynamics system (2.1) and the Jacobians J_i and J_i^A in the differential kinematics (2.2) are exactly known.

The assumptions allow us to completely characterize the system dynamics by an active compliance where the system behavior is specified by the matrices M_i, D_i, K_i. Due to the use of impedance control, small uncertainties and deviations will not result in high internal forces exerted on the object. By inserting (2.3) in (2.1) we obtain a Cartesian impedance control [68] in operational space for each manipulator given by

$$M_i(\dot{\boldsymbol{\nu}}_i - \dot{\boldsymbol{\nu}}_i^d) + D_i(\boldsymbol{\nu}_i - \boldsymbol{\nu}_i^d) + \boldsymbol{h}_i^{\mathscr{K}}(\xi_i, \xi_i^d) = \boldsymbol{h}_i - \boldsymbol{h}_i^d. \tag{2.8}$$

In case of a free-space motion, i.e. $\boldsymbol{h}_i = 0$ and no desired force $\boldsymbol{h}_i^d = 0$, it is straightforward using Lyapunov theory [69] to show that the desired position converges as

$$\lim_{t\to\infty} \xi_i = \xi_i^d, \quad \lim_{t\to\infty} \boldsymbol{\nu}_i = \boldsymbol{\nu}_i^d, \quad \lim_{t\to\infty} \dot{\boldsymbol{\nu}}_i = \dot{\boldsymbol{\nu}}_i^d.$$

Note that the robotic manipulators can still be diverse, have different robot dynamics or hardware restrictions. By designing an appropriate nonlinear feedback control law the dynamics of the robot can be expressed as (2.8). Hence, the applied wrench to the environment, that will be in our case the object, does only depend on the tuneable impedance parameters M_i, D_i, and K_i and not on the actual robot dynamics. In the following analysis we want to avoid undesired effects such as different systematic convergence rates and oscillations which can arise from heterogenous or non-isotropic impedance parameters.

Assumption 2.2. The impedance parameters are isotropic in all dimension and for all manipulators, i.e. $m = m_i = m_j, d = d_i = d_j, k = k_i = k_j, \mu = \mu_i = \mu_j, \delta = \delta_i = \delta_j, \kappa = \kappa_i = \kappa_j \forall i, j$ which can for the translational case be compactly written as:

$$M = mI_{6N}, D = dI_{6N}, K = kI_{6N}. \tag{2.9}$$

For illustration we build up examples based on dynamical systems for the robots and the set-point generator which is finally employed in the experimental section.

Example 2.1. Let us consider a robot controlled by impedance-controlled manipulator dynamics (2.8). For the sake of exposition we illustrate the dynamics of (2.8) along one translational dimension as the translational dynamics are decoupled. We choose the scalar damping to be $d_i = 120$, the stiffness to be $k_i = 160$, the mass to be $m_i = 10$, and $f_i^d = 0$ yielding

$$10\ddot{p}_i + 120\dot{p}_i + 160p_i = 160p_i^d + f_i. \tag{2.10}$$

The initial position of the robot is $p_i(t_0) = 0$ and at $t = 1s$ the desired position p_i^d of each robot is set to 1. Between $t = 5s$ and $t = 7s$ an external force $f_i = -20N$ acts on the manipulator. The external force causes a deviation of the robot trajectory from the desired position p_i^d since the manipulator is rendered compliant w.r.t external forces. The trajectory of the manipulator controlled by (2.8) is depicted in Fig. 2.2.

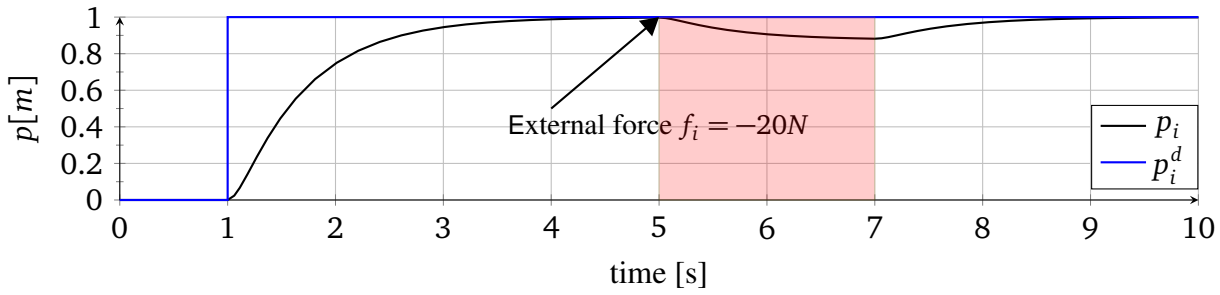

Figure 2.2: Robot trajectories p_i resulting from step response at $t = 1s$. Deviation of the trajectory from the desired position results from an external force $f_i = -20N$ between $t = 5s$ and $t = 7s$.

2.3.2 Mobile Platform Control

Up to now the mobile platform is treated as additional degrees of freedom in the specific manipulator model (2.1). This is well-suited method when the dynamics of a torque-controlled mobile base is present. Then, the system of manipulator and base is a redundant system which can be treated as a unified dynamical system, see e.g. [70, 71]. However, a decomposition of the manipulator motion and mobile base motion by compensating the base motion is preferred for mobile base which provide precise configuration measurements but have only limited tracking and actuation capabilities [72]. As is usually the case this is true for most available robotic platforms

and especially also for all mobile bases which are used in the experimental sections throughout this thesis. For the platform control design we adopt a strategy similar to [31] in which the increased redundancy is resolved by minimizing a cost function in the manipulator's null-space. As highlighted in [70], a heavy basis is usually characterized by a rather slow and coarse dynamics in contrast to the fast and accurate dynamics of a lightweight manipulators. The slow and coarse dynamics of the mobile platform mainly result from a delayed or imprecise wheel actuation. In our setup we have such a mobile platform onto which two light-weight robotic manipulators are mounted. Therefore, the generalized coordinate $\boldsymbol{\theta}_i$ of the i-th manipulator is decomposed into

$$\boldsymbol{\theta}_i = \begin{bmatrix} \boldsymbol{\theta}_{i,m} \\ \boldsymbol{\theta}_{i,b} \end{bmatrix},$$

where $\boldsymbol{\theta}_{i,m}$ denotes the coordinates of the robotic manipulator and $\boldsymbol{\theta}_{i,b}$ the joint vector of the mobile base. An analogous decomposition is performed for the j-th manipulator attached to the same mobile platform. The dynamics of the (light-weight) robots whose equation of motion is described by the generalized coordinates $\boldsymbol{\theta}_{i,m}$ and $\boldsymbol{\theta}_{j,m}$ is modeled using (2.1). However, often the dynamics of the mobile platform with $\boldsymbol{\theta}_{i=j,b}$ cannot be characterized by the second-order dynamics (2.1) and need to be simplified as

$$\dot{\boldsymbol{\theta}}_{i=j,b} = \boldsymbol{u}_{i=j,b}, \tag{2.11}$$

where $\boldsymbol{\theta}_{i=j,b}$ is the joint vector of the mobile platform onto which the i-th and j-th manipulator are mounted and $\boldsymbol{u}_{i=j,b}$ is the corresponding velocity-based input to the platform. Furthermore, $\boldsymbol{\theta}_{i=j,b}$ coincides with the Cartesian pose of the platform in the world frame which is given by

$$\boldsymbol{\theta}_{i=j,b} = \begin{bmatrix} x_i \\ y_i \\ \varphi_i \end{bmatrix}.$$

Using these definitions the differential kinematics of the anthropomorphic structure where two manipulators are attached to a single mobile base can be written as

$$\begin{bmatrix} \boldsymbol{v}_i \\ \boldsymbol{v}_j \end{bmatrix} = \underbrace{\begin{bmatrix} J_{i,m}(\boldsymbol{\theta}_i) & 0 & J_{i,b}(\boldsymbol{\theta}_i) \\ 0 & J_{j,m}(\boldsymbol{\theta}_j) & J_{j,b}(\boldsymbol{\theta}_j) \end{bmatrix}}_{J(\boldsymbol{\theta}_i, \boldsymbol{\theta}_j)} \begin{bmatrix} \dot{\boldsymbol{\theta}}_{i,m} \\ \dot{\boldsymbol{\theta}}_{j,m} \\ \dot{\boldsymbol{\theta}}_{i=j,b} \end{bmatrix},$$

where $J_{i,m}$, $J_{j,m}$ and $J_{i=j,b}$ denote the Jacobian of the i-th, the j-th manipulator, and the common mobile platform, respectively. When decoupling the mobile platform from the manipulators, most disturbances are efficiently compensated before propagating to the end-effector level. The presented control effectively decouples the manipulator end-effector poses $\boldsymbol{\xi}_i$ and $\boldsymbol{\xi}_j$ from the base configuration $\boldsymbol{\theta}_{i=j,b}$. In addition, we avoid the computationally expensive calculation of the pseudo-inverse $J(\boldsymbol{\theta}_i, \boldsymbol{\theta}_j)^\dagger$.

To achieve the desired decoupling we adopt an approach similar to [31] but formulate the displacement of the end-effector frames with respect to the mobile base frame in task space instead of in joint space. The desired relative platform position with respect to the end-effector

poses ξ_i and ξ_j is expressed in terms of an error between the actual geometric average $\bar{\xi}_{ij}$ of both poses and a desired translational and rotational offset $[d_x, d_y, d_\varphi]$. We are now ready to define the error as

$$\begin{bmatrix} e_x \\ e_y \\ e_\varphi \end{bmatrix} = \begin{bmatrix} \frac{1}{2}\boldsymbol{e}_1^\intercal(\xi_i + \xi_j) - d_x \\ \frac{1}{2}\boldsymbol{e}_2^\intercal(\xi_i + \xi_j) - d_y \\ \text{atan2}(\boldsymbol{e}_1^\intercal(\xi_i - \xi_j), \boldsymbol{e}_2^\intercal(\xi_i - \xi_j)) - d_\varphi \end{bmatrix},$$

where $\boldsymbol{e}_1$ and $\boldsymbol{e}_2$ are the unit principal vectors used to extract the x- and y-components of the respective vector expressed in the base frame and atan2 is the function to calculate the arctangent of two parameters uniquely. The introduced variables are illustrated in Fig. 2.3.

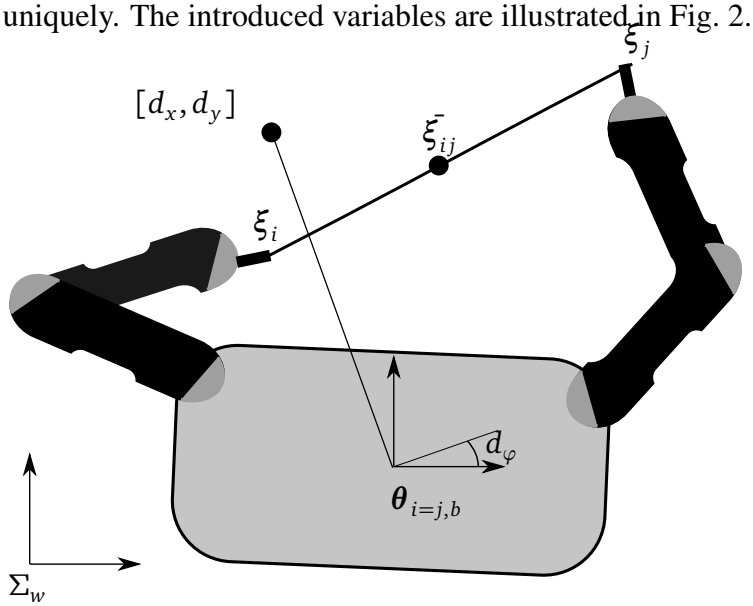

Figure 2.3: Illustration of the desired displacement offset between two manipulators and the mobile platform.

Subsequently the error term is employed with a proportional gain as the velocity control input $\boldsymbol{u}_{i=j,b}$ in (2.11) for the mobile platform as

$$\dot{\boldsymbol{\theta}}_{i=j,b} = -\text{diag}(k_x, k_y, k_\varphi) \begin{bmatrix} e_x \\ e_y \\ e_\varphi \end{bmatrix}, \tag{2.12}$$

where $k_x, k_y, k_\varphi \in \mathbb{R}^+$ are positive, scalar gains. In order to achieve the desired decoupling of manipulator and platform, the induced platform motion (2.12) is compensated by adding the reverse velocity signal to the desired end-effector trajectories $\boldsymbol{v}_i^d$ and $\boldsymbol{v}_j^d$ in the impedance dynamics (2.8) in terms of

$$\boldsymbol{v}_i^d = \hat{\boldsymbol{v}}_i^d - J_{i,b}(\boldsymbol{\theta}_i)\dot{\boldsymbol{\theta}}_{i=j,b} \text{ and } \boldsymbol{v}_j^d = \hat{\boldsymbol{v}}_j^d - J_{j,b}(\boldsymbol{\theta}_j)\dot{\boldsymbol{\theta}}_{i=j,b}, \tag{2.13}$$

where the matrix $J_{i,b}(\boldsymbol{\theta}_i), J_{j,b}(\boldsymbol{\theta}_j) \in \mathbb{R}^{6\times 3}$ maps the 3 DoF motion of the platform onto the 6 DoF motion of manipulators. Note here that based on $\boldsymbol{v}_i^d$ in (2.13) each manipulator is also able to compute $\boldsymbol{\xi}_i^d$ and $\dot{\boldsymbol{v}}_i^d$ by proper integration/derivation of the desired velocity for a more efficient decoupling of the manipulator motion from the base motion. $\hat{\boldsymbol{v}}_i^d$ and $\hat{\boldsymbol{v}}_j^d$ are the extrinsic reference

velocity inputs for the manipulator i and j, respectively. Here, $\hat{\boldsymbol{v}}_i^d$ is the velocity reference and the pose and acceleration references are consequently denoted by $\hat{\boldsymbol{\xi}}_i^d$ and $\dot{\hat{\boldsymbol{v}}}_i^d$.

This procedure allows to steer the mobile platform hierarchically by performing desired end-effector trajectories and dragging the platform to desired offset between end-effectors and mobile platform in Equation (2.12). The resulting control architecture is depicted exemplarily for two manipulators mounted on the same mobile platform in Fig. 2.4. Varying end-effector positions

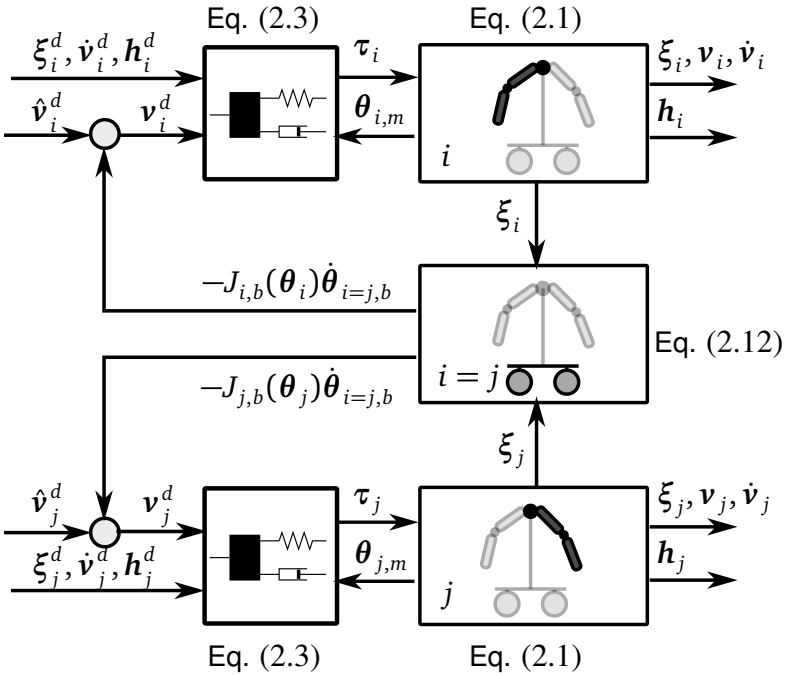

Figure 2.4: Schematic overview of the cooperative mobile manipulation control architecture.

will induce a platform motion in order to minimize the error function defined in (2.12). While tracking the computed end-effector trajectory, the measured end-effector forces are employed for evaluating the distributed impedance equations (2.8). Note that from here on we use $\hat{\boldsymbol{v}}_i^d$ and $\boldsymbol{v}_i^d$ likewise.

2.3.3 Object Dynamics

After introducing the manipulator dynamics we are now ready to state the equation of motion of the manipulated object. It can be derived by Lagrangian mechanics using object's kinetic and potential energy as

$$T_o = \frac{1}{2}\boldsymbol{v}_o^\intercal M_o \boldsymbol{v}_o \quad \text{and} \quad V_o = m_o[\boldsymbol{g}^\intercal,\ 0]\boldsymbol{\xi}_o, \tag{2.14}$$

where $M_o = \mathrm{diag}(m_o I_3, J_o)$ and $m_o \in \mathbb{R}^+$ is the mass and $J_o \in \mathbb{R}^{3\times3}$ is the inertia of the object. The gravity vector is denoted by $\boldsymbol{g}$. By evaluating the Lagrangian $L_o = T_o - V_o$ of the object

$$\frac{d}{dt}\frac{\partial L_o}{\partial \boldsymbol{v}_o} + \frac{\partial L_o}{\partial \boldsymbol{\xi}_o} = \boldsymbol{f}_o, \tag{2.15}$$

we finally result in

$$M_o \dot{\boldsymbol{\nu}}_o + \begin{bmatrix} \mathbf{0} & \mathbf{0} \\ \mathbf{0} & S(\boldsymbol{\omega}_o) J_o \end{bmatrix} \boldsymbol{\nu}_o + \begin{bmatrix} -m_o \boldsymbol{g} \\ \mathbf{0} \end{bmatrix} = \boldsymbol{h}_o, \tag{2.16}$$

where $\boldsymbol{h}_o$ is the effective force acting on the object resulting from the interaction with in our case the manipulators or generally the environment.

2.4 Cooperative Manipulation Task

In this work we consider a cooperative manipulation task where multiple manipulators rigidly grasp an object and the desired positions of the cooperating robots are explicitly guided by a position control mechanism. The objective is to guide a cooperatively manipulated object starting from an initial configuration to a goal configuration by an external command. In a cooperative manipulation autonomous functionalities of the physically cooperating robots are required. Such functionalities make it possible that no excessive force is exerted on the object or that there is a cooperative mechanism to avoid obstacles. Given the setting introduced in the previous chapters the control problem of a cooperative manipulation task consists of fulfilling the following objective [73].

Definition 2.1. The objective of a cooperative manipulation task is given by

$$\lim_{t \to \infty} \xi_o(t) \to \xi_o^d(t),$$

where $\xi_o^d(t) \in \mathbb{R}^6$ is the desired trajectory of the object and

$$\lim_{t \to \infty} \boldsymbol{h}_i(t) \to \boldsymbol{h}_i^d(t),$$

where $\boldsymbol{h}_i^d \in \mathbb{R}^{6N}$ are the desired manipulator wrenches acting on the object.

Note that in our setup $\xi_o^d(t)$ describes the trajectory of the object which consists of a path of waypoint over time. For each point in time t the corresponding waypoint ξ_o^d is known and so the motion is more strictly defined or in other words the motion of the object is described by less degree-of-freedom. By having less degree-of-freedom we circumvent some challenges from pure path planning problems where only the waypoints are given such as the following of a path with unbounded curvatures and crossing points.

To achieve cooperation we employ a system model used for the physically-coupled cooperative multi-robot team based on a formation-based approach. For the description of the overall system dynamics, a virtual coordinate system is attached to each end-effector denoted by Σ_i and to the manipulated object denoted by Σ_o. To mathematically describe the model more compactly and to focus on the human influence later we assume that all coordinate systems Σ_i and Σ_o are aligned and equally rotated w.r.t. the world frame Σ_w as

$$R_o^i = I_3,$$

where R_o^i is a rotation matrix from end-effector frame Σ_i to object frame Σ_o. If yet the particular coordinate systems of robots are not aligned, we assume that each robot knows its own rotation in the world frame Σ_w such that all robots move in a coordinated way in the world frame Σ_w. Just recently, the importance of defining the reference systems appropriately is highlighted and extensively discussed in [74]. The general setup with physically cooperating manipulators is depicted in Fig. 2.5.

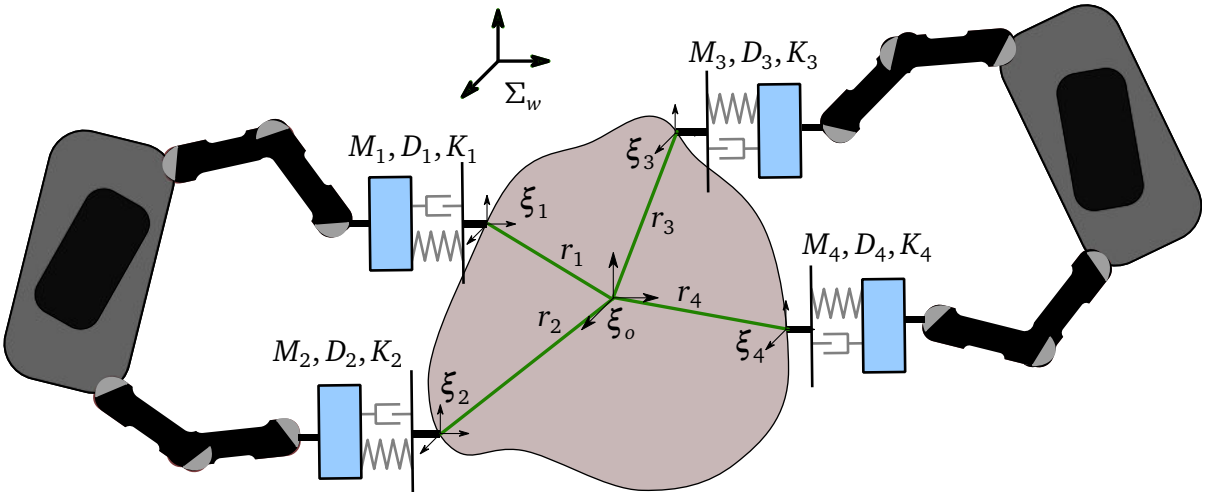

Figure 2.5: Four impedance controlled manipulators are rigidly connected to the object. To control the object trajectory and the desired internal forces acting on the object the particular set-points of the mass-spring-damper systems need to be generated.

2.4.1 Kinematic Constraints in Cooperative Manipulation Task

We consider a cooperative manipulation task where the manipulated object is rigid and the robotic end-effectors are rigidly connected to the object. Due to that we can express the position $\boldsymbol{p}_i$ of the ith robot as a function of the distance to the object center and the quaternion $\boldsymbol{q}_i$ as

$$\xi_i = \begin{bmatrix} \boldsymbol{p}_i \\ \boldsymbol{q}_i \end{bmatrix} = \begin{bmatrix} \boldsymbol{p}_o + \boldsymbol{r}_i \\ \boldsymbol{q}_o \end{bmatrix}, \tag{2.17}$$

where the displacement $\boldsymbol{r}_i = R_o(\boldsymbol{q}_o)^o\boldsymbol{r}_i$ indicates the relative displacement between the object frame and the end-effector frame and $R_o(\boldsymbol{q}_o) \in \mathbb{R}^{3\times3}$ is a rotation matrix from world frame to object frame. Rigidly connected end-effectors yield a constant displacement in the object frame as ${}^o\boldsymbol{r}_i = \text{const}$.

Assumption 2.3. We assume the object frame Σ_o is in the center of all manipulator frames Σ_i.

This assumption is not strong as the location of the object frame can be freely chosen by the system designer. Yet this assumption gives us the following equality condition for the relative displacements:

$$\sum_i {}^o\boldsymbol{r}_i = \sum_i \boldsymbol{r}_i = \boldsymbol{0}. \tag{2.18}$$

Following the argumentation of [30] the constraints of a cooperation manipulation task (2.17) are differentiated w.r.t. time as

$$\boldsymbol{\nu}_i = \begin{bmatrix} \dot{\boldsymbol{p}}_i \\ \boldsymbol{\omega}_i \end{bmatrix} = \begin{bmatrix} \dot{\boldsymbol{p}}_o + S(\boldsymbol{r}_i)^\intercal \boldsymbol{\omega}_o \\ \boldsymbol{\omega}_o \end{bmatrix} = G_i(\boldsymbol{r}_i)^\intercal \boldsymbol{\nu}_o \quad \text{and} \tag{2.19}$$

$$\dot{\boldsymbol{\nu}}_i = \begin{bmatrix} \ddot{\boldsymbol{p}}_i \\ \dot{\boldsymbol{\omega}}_i \end{bmatrix} = \begin{bmatrix} \ddot{\boldsymbol{p}}_o + S(\boldsymbol{r}_i)^\intercal \dot{\boldsymbol{\omega}}_o + S(\boldsymbol{\omega}_o)^2 \boldsymbol{r}_i \\ \dot{\boldsymbol{\omega}}_o \end{bmatrix} = G_i(\boldsymbol{r}_i)^\intercal \dot{\boldsymbol{\nu}}_o + \begin{bmatrix} S(\boldsymbol{\omega}_o)^2 \boldsymbol{r}_i \\ 0 \end{bmatrix}, \tag{2.20}$$

where the matrix $G_i(\boldsymbol{r}_i) \in \mathbb{R}^{6\times 6}$ is a submatrix of the grasp matrix $G \in \mathbb{R}^{6x6N}$ which is defined by

$$G = [G_1, G_2, \ldots, G_N] \text{ where } G_i = \begin{bmatrix} I_3 & 0 \\ S(\boldsymbol{r}_i) & I_3 \end{bmatrix}. \tag{2.21}$$

We are now ready to compactly rewrite the constrained acceleration condition (2.20) for all manipulators i as

$$A \begin{bmatrix} \dot{\boldsymbol{\nu}}_o \\ \dot{\boldsymbol{\nu}} \end{bmatrix} = \boldsymbol{b}, \tag{2.22}$$

where $\dot{\boldsymbol{\nu}} = \left[\dot{\boldsymbol{\nu}}_1^\intercal, \ldots, \dot{\boldsymbol{\nu}}_N^\intercal\right]^\intercal \in \mathbb{R}^{6N}$ are the concatenated accelerations of the manipulator poses. The constraint matrix $A \in \mathbb{R}^{6N\times 6(N+1)}$ and the centripetal terms $\boldsymbol{b} \in \mathbb{R}^{6N}$ are then given by

$$A = \begin{bmatrix} -G^\intercal & I_{6N} \end{bmatrix} \quad \text{and} \quad b = \begin{bmatrix} S(\boldsymbol{\omega}_o)^2 \boldsymbol{r}_1 \\ 0 \\ \vdots \\ S(\boldsymbol{\omega}_o)^2 \boldsymbol{r}_N \\ 0 \end{bmatrix}, \tag{2.23}$$

which we employ to express the constrained dynamics of object and manipulators in the upcoming section.

2.4.2 Constrained Dynamics of Cooperating Manipulators and Object

In this section we derive the joint system model of object and impedance controlled manipulators which are driven by distributed set-points. Based on (2.22) a general and consistent model for the multi-robot interaction dynamics for impedance-controlled manipulators is recently presented in [30] which is based on the Gauss' principle of least constraint. In order to cope with the constrained motion of the robotic manipulators the non-interaction wrenches of the object $\boldsymbol{h}_o^\Sigma \in \mathbb{R}^6$ and the manipulators $\boldsymbol{h}^\Sigma = \left[\boldsymbol{h}_1^\Sigma, \ldots, \boldsymbol{h}_N^\Sigma\right] \in \mathbb{R}^{6N}$ are projected by a linear transformation onto the interaction wrenches of the object $\boldsymbol{h}_o \in \mathbb{R}^6$ and of the manipulators $\boldsymbol{h} \in \mathbb{R}^{6N}$ in which the cooperative manipulation constraints are satisfied:

$$\begin{bmatrix} \boldsymbol{h}_o \\ \boldsymbol{h} \end{bmatrix} = A^\intercal \left(A\bar{M}^{-1}A^\intercal\right)^{-1} \left(\boldsymbol{b} - A\bar{M}^{-1} \begin{bmatrix} \boldsymbol{h}_o^\Sigma \\ \boldsymbol{h}^\Sigma \end{bmatrix}\right), \tag{2.24}$$

where $\bar{M} = \operatorname{diag}(M_o, M_1, \ldots, M_N)$ is a block-diagonal matrix of all mass matrices. Here, $\boldsymbol{h}_o^\Sigma$ and $\boldsymbol{h}_i^\Sigma$ are the inputs of the manipulators dynamics (2.8) and the object dynamics (2.16), respectively

and are given by

$$\boldsymbol{h}_o^{\Sigma} = -\begin{bmatrix} \mathbf{0} & \mathbf{0} \\ \mathbf{0} & S(\boldsymbol{\omega}_o)J_o \end{bmatrix}\boldsymbol{\nu}_o - \begin{bmatrix} -m_o\boldsymbol{g} \\ \mathbf{0} \end{bmatrix} \text{ and} \tag{2.25}$$

$$\boldsymbol{h}_i^{\Sigma} = M_i\dot{\boldsymbol{\nu}}_i^d - D_i(\boldsymbol{\nu}_i - \boldsymbol{\nu}_i^d) - \boldsymbol{h}_i^{\mathscr{K}}(\xi_i, \xi_i^d) - \boldsymbol{h}_i^d. \tag{2.26}$$

Furthermore, $\boldsymbol{h}_o$ is the interaction wrench acting on the object. Let now be $M = \operatorname{diag}(M_1, \ldots, M_N)$. By employing $Q = (M^{-1} + G^{\intercal}M_o^{-1}G)^{-1}$ and (2.23) the interaction wrench (2.24) of $\boldsymbol{h}_o$ is given by

$$\boldsymbol{h}_o = -GQG^{\intercal}M_o^{-1}\boldsymbol{h}_o^{\Sigma} + GQM^{-1}\boldsymbol{h}^{\Sigma} - GQ\boldsymbol{b}.$$

We are now ready to model the overall system dynamics consisting of multiple manipulators and the object by replacing $\boldsymbol{h}_o$ and $\boldsymbol{h}_o^{\Sigma}$ in the object dynamics (2.16) as:

$$M_o\dot{\boldsymbol{\nu}}_o = (I_6 - GQG^{\intercal}M_o^{-1})\boldsymbol{h}_o^{\Sigma} + GQM^{-1}\boldsymbol{h}^{\Sigma} - GQ\boldsymbol{b}. \tag{2.27}$$

After application of Woodbury and Searle matrix identities which is omitted here for space reasons the constrained object dynamics (2.27) can be expressed as

$$(M_o + \sum G_iM_iG_i^{\intercal})\dot{\boldsymbol{\nu}}_o = \boldsymbol{h}_o^{\Sigma} + \sum_i G_i\boldsymbol{h}_i^{\Sigma} - GM\boldsymbol{b}. \tag{2.28}$$

Finally, we substitute (2.23), (2.25), and (2.26) in (2.28). Here, we set $\sum_i G_i\boldsymbol{h}_i^d = [-m_o\boldsymbol{g}^{\intercal}, 0]^{\intercal}$ to account for the gravity force of the object as described similarly in [75] in order to result in the overall system dynamics given by

$$\mathscr{M}\dot{\boldsymbol{\nu}}_o + \mathscr{D}\boldsymbol{\nu}_o + \mathscr{C}_o\boldsymbol{\nu}_o + \mathscr{K}_o\xi_o = \sum_i \mathscr{K}_i\xi_i^d + \sum_i \mathscr{D}_i\boldsymbol{\nu}_i^d + \sum_i \mathscr{M}_i\dot{\boldsymbol{\nu}}_i^d + \tilde{\boldsymbol{h}}_o, \tag{2.29}$$

where $\tilde{\boldsymbol{h}}_o$ is an external disturbance and the apparent inertia $\mathscr{M}$,$\mathscr{M}_i$, damping $\mathscr{D}$,$\mathscr{D}_i$, coriolis-centripetal matrix $\mathscr{C}_o$, and the stiffness $\mathscr{K}_o, \mathscr{K}_i$ result in

$$\mathscr{M} = \begin{bmatrix} (m_o + \sum m_i)I_3 & 0 \\ 0 & J_o + \sum \mu_i I_3 + m_i S(\boldsymbol{r}_i)S(\boldsymbol{r}_i)^{\intercal} \end{bmatrix},$$

$$\mathscr{D} = \begin{bmatrix} \sum_i d_i I_3 & 0 \\ 0 & \sum \delta_i + d_i S(\boldsymbol{r}_i)S(\boldsymbol{r}_i)^{\intercal} \end{bmatrix},$$

$$\mathscr{C}_o = \begin{bmatrix} 0 & \sum m_i S(\boldsymbol{\omega_o})S(\boldsymbol{r}_i)^{\intercal} \\ 0 & S(\boldsymbol{\omega_o})J_o + \sum m_i S(\boldsymbol{r}_i)S(\boldsymbol{\omega_o})S(\boldsymbol{r}_i)^{\intercal} \end{bmatrix},$$

$$\mathscr{K}_o = \begin{bmatrix} \sum_i k_i I_3 & 0 \\ 0 & \sum_i \kappa_i U(q_o)^{\intercal} \end{bmatrix},$$

$$\mathscr{K}_i = \begin{bmatrix} k_i I_3 & 0 \\ k_i S(\boldsymbol{r}_i) & \kappa_i U(q_o)^{\intercal} \end{bmatrix},$$

$$\mathscr{D}_i = \begin{bmatrix} d_i I_3 & 0 \\ d_i S(\boldsymbol{r}_i) & \delta_i I_3 \end{bmatrix}, \text{ and } \mathscr{M}_i = \begin{bmatrix} m_i I_3 & 0 \\ m_i S(\boldsymbol{r}_i) & \mu_i I_3 \end{bmatrix}.$$

Here, the off-diagonal entries $\sum m_i S(\boldsymbol{r}_i)^\intercal, \sum m_i S(\boldsymbol{r}_i)$ in $\mathscr{M}$, $\sum_i d_i S(\boldsymbol{r}_i), \sum d_i S(\boldsymbol{r}_i)^\intercal$ in $\mathscr{D}$, and $k_i S(\boldsymbol{r}_i)^\intercal$ in $\mathscr{K}_o$ vanish due to Assumtions 2.2 and 2.3. Note that for the equation of motion (2.29) we obtain a centralized equation of motion for the object pose $\boldsymbol{\xi}_o$ which is driven by decentralized set-point inputs $\mathscr{K}_i \boldsymbol{\xi}_i^d$, $\mathscr{D}_i \boldsymbol{\nu}_i^d$, and $\mathscr{M}_i \dot{\boldsymbol{\nu}}_i^d$ from each attached cooperating manipulator.

2.4.3 Internal Forces in Cooperative Manipulation Task

Internal forces arise due to the interaction between the cooperating robotic manipulators and lie by definition in the null space of the grasp matrix G [17]. Given the measured end-effector forces $\boldsymbol{h}_i$ the internal force $\boldsymbol{h}_i^{\text{int}} \in \mathbb{R}^6$ which induce no motion of the object are generally computed via

$$\begin{bmatrix} \boldsymbol{h}_1^{\text{int}} \\ \vdots \\ \boldsymbol{h}_N^{\text{int}} \end{bmatrix} = \left(I_{6N} - G^\dagger G\right) \begin{bmatrix} \boldsymbol{h}_1 \\ \vdots \\ \boldsymbol{h}_N \end{bmatrix}, \tag{2.30}$$

wherein $G^\dagger$ is a particular ("no-squeeze") pseudo-inverse of the grasp matrix G. This setting is especially appropriate for position-controlled manipulators which accurately drive to a particular position and do not react compliantly. However, in our presented approach the impedance-controlled manipulators (2.8) are compliant w.r.t the environment through the measurement of the force $\boldsymbol{h}_i$. Since the measured forces are already used in our system dynamics we are able to employ the particular robot dynamics in the definition and the computation of the internal forces.

Such a definition of internal forces in an impedance-based control scheme is presented in [30] where the robotic end-effectors are a rigid formation which exchange wrenches through the object to maintain the rigid formation. Internal forces can be here interpreted as formation-maintaining forces which arise from a deviation between the actual formation and a desired rigid formation which is described as the distances from the reference agent i to all the other agents j. Hence, the object frame Σ_o is shifted into one particular agent i so that one of the cooperating manipulators, denoted by $\boldsymbol{p}_i$, is the reference for all the other manipulators, denoted by $\boldsymbol{p}_j$. Employing (2.17) for two manipulators i and j the desired displacement $\boldsymbol{d}_{ij}$ between any pair i and j is given by

$$\boldsymbol{p}_i - \boldsymbol{p}_j = \boldsymbol{d}_{ij} = \boldsymbol{r}_i - \boldsymbol{r}_j, \tag{2.31}$$

for which the rotation of the object $R_o(\boldsymbol{q}_o)$ is required in the world frame. The rotational constraint of the manipulators between two frames i and j is present in a cooperative manipulation and can be expressed using quaternion formalism as follows

$$\boldsymbol{q}_i = \boldsymbol{q}_j. \tag{2.32}$$

For the sake of exposition let now be $i = 1$ and $j = 2, \ldots, N$. Derivating (2.31) and (2.32) twice

w.r.t time yields a modified constraint matrix

$$\bar{A} = \begin{bmatrix} -G^{\intercal}(\boldsymbol{d}_1) & I_{6(N-1)} \end{bmatrix} \quad \text{and} \quad \bar{\boldsymbol{b}} = \begin{bmatrix} S(\boldsymbol{\omega}_o)^2 \boldsymbol{d}_{12} \\ 0 \\ \vdots \\ S(\boldsymbol{\omega}_o)^2 \boldsymbol{d}_{1N} \\ 0 \end{bmatrix},$$

where $\boldsymbol{d}_1 = [\boldsymbol{d}_{12}, \ldots, \boldsymbol{d}_{1N}]$. An explicit solution for the internal force $\boldsymbol{h}^{\text{int}}$ based on the modified constraint matrix $\bar{A}$ is presented generally in [76] and for the multi-robot interaction in [30] as

$$\boldsymbol{h}^{\text{int}} = M^{\frac{1}{2}} (\bar{A} M^{-\frac{1}{2}})^{\dagger} (\bar{\boldsymbol{b}} - \bar{A} M^{-1} \boldsymbol{h}^{\Sigma}), \tag{2.33}$$

where $M = \text{diag}(M_1, M_2, \ldots, M_N)$ is the overall mass matrix of all manipulators and the entries of $\boldsymbol{h}^{\Sigma}$ are given in (2.26). Note here that the desired set-points ξ_i^d need to be generated for each physically cooperating robot. It is obvious that decentralized inputs ξ_i^d can cause an violation of the constraint (2.31) and (2.32) and can thus result in an internal force.

At this stage we are mostly interested how the set-points ξ^d, the set-velocities $\boldsymbol{\nu}^d$, and the set-accelerations $\dot{\boldsymbol{\nu}}^d$ need to be generated such that there is no internal force $\boldsymbol{h}^{\text{int}} = \boldsymbol{0}$. In order to solely investigate the effect of specific set-points on the appearance of internal forces $\boldsymbol{h}^{\text{int}}$ we neglect the effect of the desired forces, i.e. $\boldsymbol{h}_i^d = 0$. Consequenctly, we use $\boldsymbol{h}^{\Sigma}$ as defined in (2.26) for the internal forces $\boldsymbol{h}^{\text{int}}$ (2.33) which are generated by distributed set-points (2.4) given by

$$\boldsymbol{h}^{\text{int}} = M^{\frac{1}{2}} (\bar{A} M^{-\frac{1}{2}})^{\dagger} \left(\bar{\boldsymbol{b}} - \bar{A} M^{-1} \left(M \dot{\boldsymbol{\nu}}^d - D(\boldsymbol{\nu} - \boldsymbol{\nu}^d) - \boldsymbol{h}^{\mathcal{K}}(\xi, \xi^d) \right) \right),$$

where $\boldsymbol{\nu}^d, \dot{\boldsymbol{\nu}}^d \in \mathbb{R}^{6N}$ are the concatenated desired velocities and accelerations. As now $\boldsymbol{\nu} = G^{\intercal} \boldsymbol{\nu}_o$ and as both M and D commute with all matrices due to Assumption 2.2 and as a straightforward computation yields $\bar{A} G^{\intercal} = 0$ the internal wrench $\boldsymbol{h}^{\text{int}}$ can be simplified to

$$\boldsymbol{h}^{\text{int}} = M^{\frac{1}{2}} (\bar{A} M^{-\frac{1}{2}})^{\dagger} \left(\bar{\boldsymbol{b}} - \bar{A} \dot{\boldsymbol{\nu}}^d - M^{-1} D \bar{A} \boldsymbol{\nu}^d + M^{-1} \bar{A} \boldsymbol{h}^{\mathcal{K}}(\xi, \xi^d) \right).$$

By now employing $\boldsymbol{\nu}^d = G^{\intercal} \boldsymbol{\nu}_o^d$ similar to Eq. (2.19) and $\dot{\boldsymbol{\nu}}^d = G^{\intercal} \dot{\boldsymbol{\nu}}_o^d + \boldsymbol{b}$ similar to (2.20) for a desired velocity $\boldsymbol{\nu}_o^d$ and a desired acceleration $\dot{\boldsymbol{\nu}}_o^d$, respectively. These are the desired velocity and acceleration inputs $\boldsymbol{\nu}^d$ and $\dot{\boldsymbol{\nu}}^d$ which do not induce any undesired internal force. By using the facts $\bar{A}\boldsymbol{b} = \bar{\boldsymbol{b}}$ and $\bar{A} G^{\intercal} = 0$ the internal wrench is given by

$$\boldsymbol{h}^{\text{int}} = M^{\frac{1}{2}} (\bar{A} M^{-\frac{1}{2}})^{\dagger} M^{-1} \bar{A} \underbrace{\begin{bmatrix} k(\boldsymbol{p}_1 - \boldsymbol{p}_1^d) \\ -2\kappa U(\boldsymbol{q}_1)^{\intercal} \boldsymbol{q}_1^d \\ \vdots \\ k(\boldsymbol{p}_N - \boldsymbol{p}_N^d) \\ -2\kappa U(\boldsymbol{q}_N)^{\intercal} \boldsymbol{q}_N^d \end{bmatrix}}_{\boldsymbol{h}^{\mathcal{K}}(\xi, \xi^d)}. \tag{2.34}$$

Evaluating any two equations i and j of $\bar{A}M^{-1}\boldsymbol{h}^{\Sigma}$ the internal wrench (2.34) yields

$$\begin{aligned}\boldsymbol{f}_i^{\text{int}} &= -k(\boldsymbol{p}_i - \boldsymbol{p}_i^d) - S(\boldsymbol{d}_{ij})2\kappa U(\boldsymbol{q}_i)^{\intercal}\boldsymbol{q}_i^d + k(\boldsymbol{p}_j - \boldsymbol{p}_j^d) \text{ and}\\ \boldsymbol{\tau}_i^{\text{int}} &= 2\kappa U(\boldsymbol{q}_i)^{\intercal}\boldsymbol{q}_i^d - 2\kappa U(\boldsymbol{q}_j)^{\intercal}\boldsymbol{q}_j^d.\end{aligned}$$

When we consider the rotational constraint (2.32) it is obvious that the internal torque $\boldsymbol{\tau}_i^{\text{int}} = 0$ only if $\boldsymbol{q}_i^d = \boldsymbol{q}_j^d$. For the internal force we result in $\boldsymbol{f}_i^{\text{int}} = 0$ if the current orientation $\boldsymbol{q}_i$ matches the desired one as $\boldsymbol{q}_i = \boldsymbol{q}_i^d$ and if $\boldsymbol{p}_i^d - \boldsymbol{p}_j^d = \boldsymbol{d}_{ij}$. For the latter result we employed (2.31) for the current set-points $\boldsymbol{p}_i, \boldsymbol{p}_j$. In conclusion the desired property of the trajectory generator is to always satisfy the constraints (2.31) and (2.32) concerning the robotic positions $\boldsymbol{p}_i, \boldsymbol{p}_j$ and orientations $\boldsymbol{q}_i, \boldsymbol{q}_j$ also for the desired set-point pairs $\boldsymbol{p}_i^d, \boldsymbol{p}_j^d$ and $\boldsymbol{q}_i^d, \boldsymbol{q}_j^d$ as follows:

$$\boldsymbol{p}_i^d - \boldsymbol{p}_j^d = \boldsymbol{d}_{ij} \text{ and} \tag{2.35}$$

$$\boldsymbol{q}_i^d = \boldsymbol{q}_j^d. \tag{2.36}$$

In the upcoming chapter we present an approach which generates desired-set points $\boldsymbol{p}_i^d$ distributedly while satisfying the constraint (2.35) and (2.36). Note that a distributed method requires an exchange of the desired positions among the robots by communication.

A special case is present for the modified constraint matrix $\bar{A}$ when we only consider translational motions and the constraint matrix is then given by

$$\bar{\bar{A}} = \begin{bmatrix} 1 & I_{3(N-1)} \end{bmatrix},$$

where $\bar{\bar{A}} \in \mathbb{R}^{3N\times 3N}$ and $1 \in \mathbb{R}^{3N\times 3}$ is a matrix with ones. Under the isotropic impedance parameters (2.9) we get a more specific result for the internal forces (2.33) which is given by

$$\boldsymbol{f}^{\text{int}} = (\sqrt{m})^2\bar{\bar{A}}^{\dagger}\bar{\bar{A}}\frac{1}{m}k\left(\boldsymbol{p} - \boldsymbol{p}^d\right) = k\bar{\bar{A}}^{\dagger}\bar{\bar{A}}\boldsymbol{e}, \tag{2.37}$$

where we define $\boldsymbol{e} = \boldsymbol{p} - \boldsymbol{p}^d$ and the matrix $\bar{\bar{A}}^{\dagger}\bar{\bar{A}} \in \mathbb{R}^{3N\times 3N}$ is given by

$$\bar{\bar{A}}^{\dagger}\bar{\bar{A}} = \begin{pmatrix} \frac{N-1}{N}I_3 & -\frac{1}{N}I_3 & \cdots & -\frac{1}{N}I_3 \\ -\frac{1}{N}I_3 & \frac{N-1}{N}I_3 & \cdots & -\frac{1}{N}I_3 \\ & \vdots & \ddots & \\ -\frac{1}{N}I_3 & -\frac{1}{N}I_3 & \cdots & \frac{N-1}{N}I_3 \end{pmatrix}.$$

By employing the average of the particular error state $\hat{\boldsymbol{e}} = \frac{1}{N}\left[\sum \boldsymbol{e}_i{}^{\intercal}, \sum \boldsymbol{e}_i{}^{\intercal}, \ldots, \sum \boldsymbol{e}_i{}^{\intercal}\right]^{\intercal}$ we can simplify (2.37) as

$$\boldsymbol{f}^{\text{int}} = k(\boldsymbol{e} - \hat{\boldsymbol{e}}). \tag{2.38}$$

The interpretation of (2.38) is that an internal force, $\boldsymbol{f}^{\text{int}} \neq 0$, acts on the object if the particular robot inputs $\boldsymbol{e}$ are not equal to the averaged system input $\hat{\boldsymbol{e}}$: $\boldsymbol{e} \neq \hat{\boldsymbol{e}}$. An internal force $\boldsymbol{f}^{\text{int}} \neq 0$ acts on the object, which is mostly undesired in a cooperative manipulation task. In this article we set the desired force to zero in order to simplify the argumentation. However, the principle approach

also holds for non-zero internal force. Hence, to avoid an internal force, $\boldsymbol{f}^{\text{int}} = 0$, all inputs $\boldsymbol{e}$ need to be equal: $\boldsymbol{e}_i = \boldsymbol{e}_j = \frac{1}{N}\sum \boldsymbol{e}_i$. We now want to illustrate the occurrence of internal forces based on the previous example.

Example 2.2. We continue here with the previously defined Example 2.1. An object is manipulated by three manipulators of which each features the dynamics defined (2.10). The mass of object is $m_o = 1$ and the initial position is $p_o(t_0) = 0$. The particular impedance-controlled manipulator dynamics (2.10) yield an overall dynamics given by

$$31\ddot{p}_o + 360\dot{p}_o + 480p_o = \sum_{i=1}^{3} 160p_i^d + \tilde{f}_o. \tag{2.39}$$

At $t = 1s$ the set-points are driven from $\boldsymbol{p}^d = [0,0,0]^\intercal$ to $\boldsymbol{p}^d = [0.9,1,1.1]^\intercal$. The motion of the object follows the desired position 0 to $\hat{\boldsymbol{p}}^d = 1$, yet there is an internal force (2.38) as acting on the object as depicted in Fig 2.6. The occasion for the internal force is a deviation of the particular desired positions p_1^d, p_3^d from p_2^d from wich we can also infer that the particular set-points p_1^d, p_3^d, p_2^d diverge from the average $\hat{\boldsymbol{p}}^d$ in the transient phase.

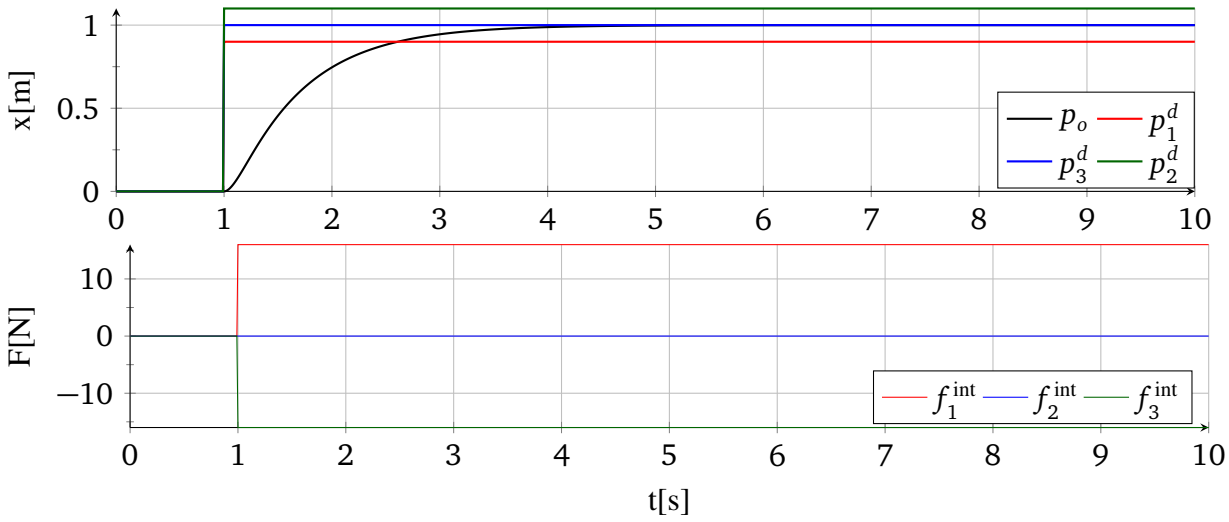

Figure 2.6: Object trajectory p_o resulting from distributed robot set-points p_1^d, p_3^d, p_2^d. Deviation of the set-points results in an internal force $f_i^{\text{int}} \neq 0$.

After discussing the occurrence of internal force in a cooperative manipulation task, we now want to discuss the effect of the human input on particular set-points $\boldsymbol{p}_i^d$.

2.5 Experimental Validation

In order to evaluate the presented control scheme and to perform a demonstration on two heterogeneous, dual-arm mobile robots, we conducted a full-scale experiment in our laboratory.

2.5.1 Mobile Robot Platforms

The first of two robots used for the experimental evaluation consists of two 7 DoF robotic manipulators [77] with incremental encoders capturing the joint angles. Due to the use of incremental encoders this manipulator type is susceptible to kinematic uncertainties. The second robot is equipped with two commercially available *KUKA LWR 4+* manipulators [78]. Both dual-arm manipulators are front-mounted on top of a rigid torso as depicted in Fig. 2.7. The workspace of the robotic manipulators is extended by a four-wheeled omni-directional mobile platform. The movement of object and robots were captured with an infrared 3D-motion tracking system (*PTI VisualEyez II VZ4000*). Further details on the robots and on the motion tracking system can be found in Appendix C.

We are now ready to provide some important findings and insights regarding the scalability of the approach. Note that from a theoretical point of view, the approach scales quite good as every additional robot comes along with corresponding system dynamics (2.1). Hence, the particular manipulator dynamics are incorporated in the overall multi-robot dynamics (2.29) and the particular set-points for the additional robot are computed analogously to the remaining robotic set-points. However, from a practical point of view, the scaling of the approach has room for improvement. As soon as a single robotic manipulator fails due to e.g. hardware issues or limitations, this failure frequently initiates a chain reaction resulting in additional robots to fail or stop the manipulation task. When robotic prototypes are used as in our setup, each additional robot employed in the experiment increases the chance of a failed experimental run. This issue can be overcome by employing a proper lifecycle or activity management throughout all involved cooperating robots.

2.5.2 Experimental Results

The manipulated object consists of a reinforced aluminum frame with handholds for the robots. The rigid frame has a length of $l_0 = 1.20m$, a width of $w_0 = 0.80m$ and a total weight of $m_0 = 3.2$ kg. The grasp geometry $\boldsymbol{r}_i$ is known to each manipulator during the task execution. For the manipulation task, the impedance control loops of the end-effectors $i = 1 \ldots 4$ in (2.8) are tuned according to the following values:

$$M_i = \begin{bmatrix} 6\, I_3 \text{ kg} & 0_3 \\ 0_3 & 0.5\, I_3 \text{ kg m}^2 \end{bmatrix},$$
$$D_i = \begin{bmatrix} 200\, I_3 \text{ Ns/m} & 0_3 \\ 0_3 & 10\, I_3 \text{ Nm s/rad} \end{bmatrix},$$
$$K_i = \begin{bmatrix} 200\, I_3 \text{ N/m} & 0_3 \\ 0_3 & 100\, I_3 \text{ N/m} \end{bmatrix}.$$

Dynamic forces are neglected due to low velocities and accelerations during the transportation phase. As a consequence, the left-hand side of the object dynamics (2.16) reduces to $-m_o \boldsymbol{g}^o$. The gravitational forces of the object mass are assumed to be equally distributed among the manipulators and are statically compensated. The chosen object trajectory is a pure translation in the x-y-plane, starting at the origin and describing the number “8” as illustrated by the red graph

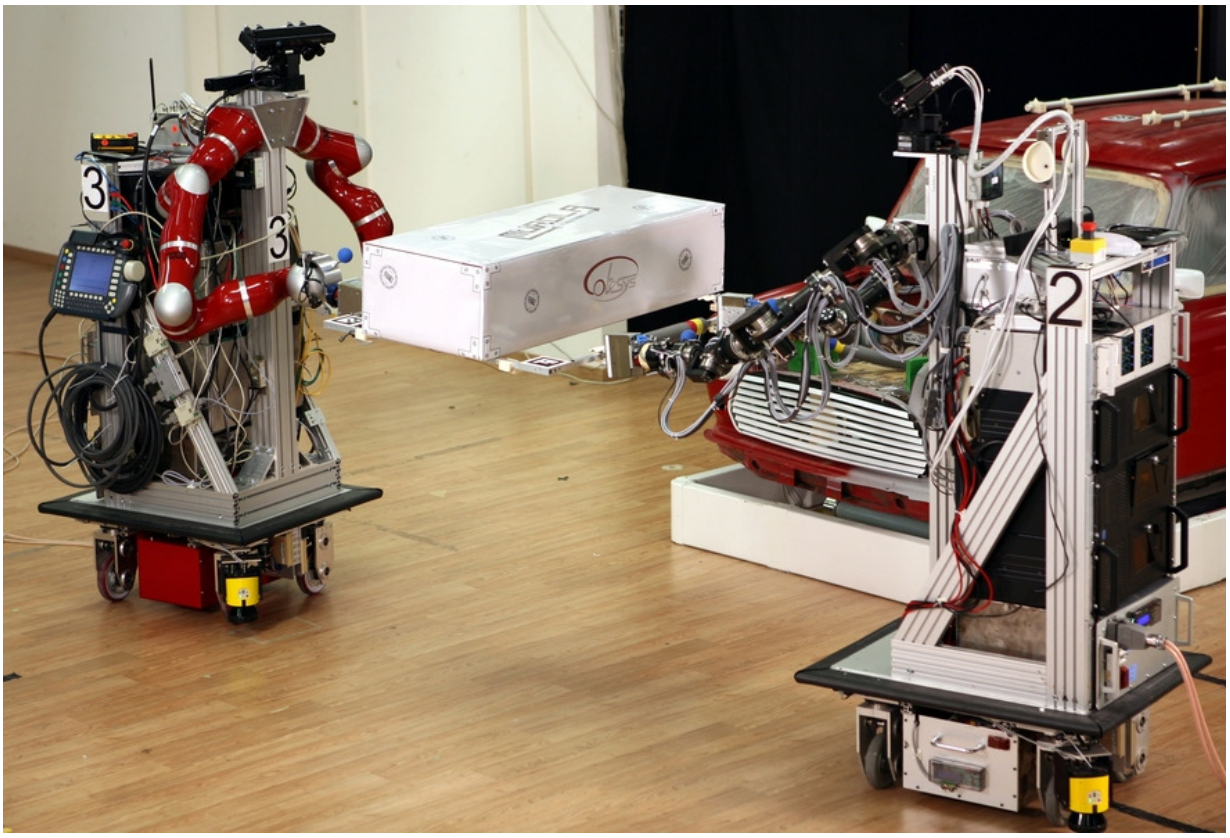

Figure 2.7: Anthropomorphic mobile robots transporting an object cooperatively.

in Fig. 2.8.

The maximum displacement of $1.0m$ for the given trajectory is sufficient to illustrate the benefits of the control architecture and the effects relevant to uncertain kinematic parameters. The grasp points of the four involved end-effectors are identified as

$$\boldsymbol{p}_1(t_0) = \begin{pmatrix} 0.39m \\ -0.24m \\ 0m \end{pmatrix}, \; \boldsymbol{p}_2(t_0) = \begin{pmatrix} 0.39m \\ 0.24m \\ 0m \end{pmatrix} \boldsymbol{p}_3(t_0) = \begin{pmatrix} -0.39m \\ -0.28m \\ 0m \end{pmatrix}, \; \boldsymbol{p}_4(t_0) = \begin{pmatrix} -0.39m \\ 0.28m \\ 0m \end{pmatrix}.$$

The estimated orientation of the end-effectors is

$$\boldsymbol{q}_1(t_0) = \boldsymbol{q}_2(t_0) = \boldsymbol{q}_3(t_0) = \boldsymbol{q}_4(t_0) = \begin{pmatrix} 1 \\ 0 \\ 0 \\ 0 \end{pmatrix}.$$

given as unit quaternions with the upper entry denoting the scalar component. The end-effector force signals are recorded and the internal force component is extracted according to Eq. (2.30). The force signals are filtered by a moving average filter with a window size of $T_{ma} = 300\text{ms}$. For the purpose of a clear presentation only the force signals of the opposed end-effectors $i = \{1, 4\}$ are plotted in Fig. 2.9.

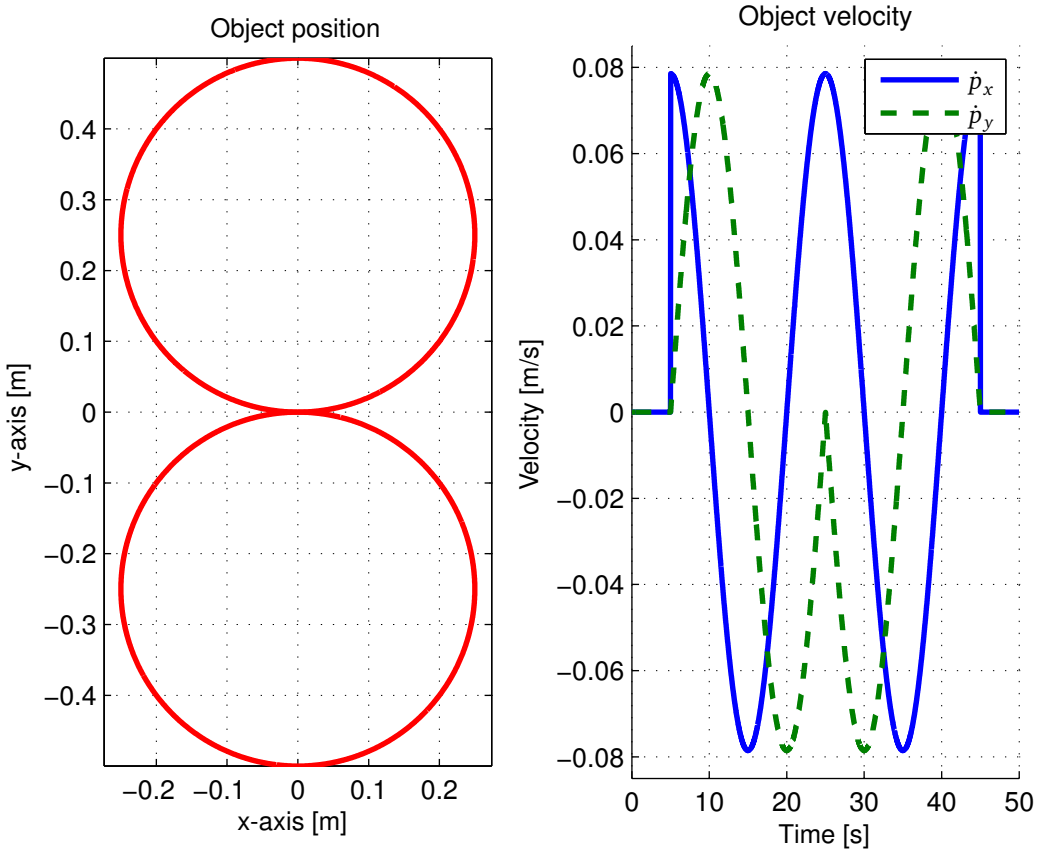

Figure 2.8: Desired object trajectory for the mobile manipulation task.

While performing the manipulation task we decouple the motion of manipulators and mobile platform as described in Sec. 2.3.2. The applied stress acting on the object remains satisfactory small. However we still observe the impact of the non-ideal platform steering which is caused by the motion decoupling. At time instants $t = 15s$ and $t = 36s$ we observe peaks in the force signals depicted in Fig 2.9 which arise from the necessary but uncompensated wheel-turning action at the reversal points of the trajectory. The remaining fluctuations of the force measurements apparent in both end-effector signals are caused by the interaction of the four impedance-controlled end-effectors. The distinct offset of $\boldsymbol{f}_4^{\text{int}}$ is caused by an initial tension when closing the gripper fingers.

In a second run, the estimated grasp orientation of the fourth gripper is intentionally biased by a rotation of 5 degrees about the z-axis. This value is considered as a worst-case estimation of the kinematic uncertainty when grasping the object autonomously with a local visual servoing routine. The resulting grasp orientation is therefore

$$\boldsymbol{q}_4^{\text{biased}} = \begin{pmatrix} 0.999 \\ 0 \\ 0 \\ 0.0436 \end{pmatrix}.$$

This choice will generate a divergent trajectory for the fourth end-effector with respect to the

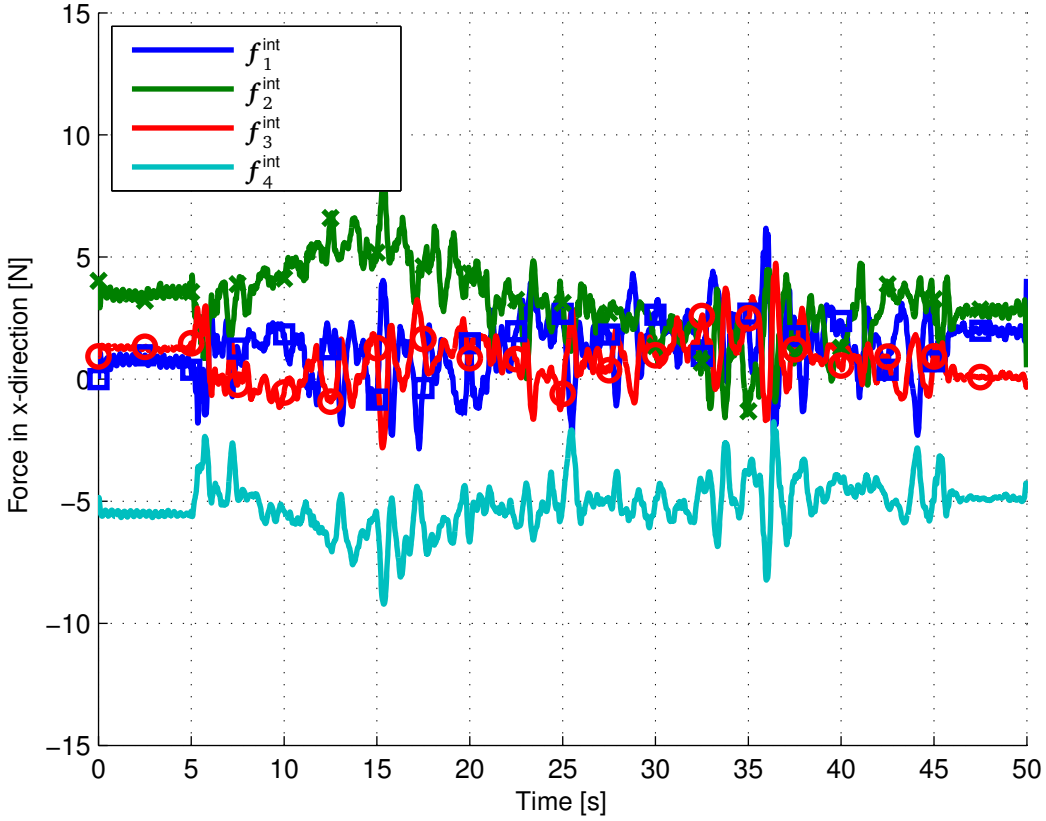

Figure 2.9: Internal force for unbiased grasp parameters.

desired object trajectory as depicted by the black dashed line in the left subplot of Fig. 2.8. During the upper loop of the 8, the trajectory of the biased end-effector diverges approximately 0.02m in x-direction due to the initial rotational offset. The end-effector force signals for $i = \{1, 4\}$ and the biased end-effector parameter is plotted in Fig. 2.10.

The force signal $\boldsymbol{f}_4^{\text{int}}$ of the biased end-effector exhibits the undesired amplitude as expected due to the biased initial grasp. Again we notice some force peaks at the reversal points of the trajectory due to the non-ideal platform motion. The remaining force signals $\boldsymbol{f}_i^{\text{int}}$ for $i = \{1, 2, 3\}$ share the applied stress with converse signs. The violation of the compatible trajectory in y-direction remains small for the chosen trajectory. For non-periodic manipulation trajectories the observed decrease of the internal stress does not apply. Instead the error induced by uncertain kinematics will accumulate, induce further stress on the object and limit thus the actually usable workspace of the cooperative manipulation system as a function of the admissible force magnitude. The design of a non-differential feedback control schemes to overcome this inconvenience is subject of the upcoming chapter.

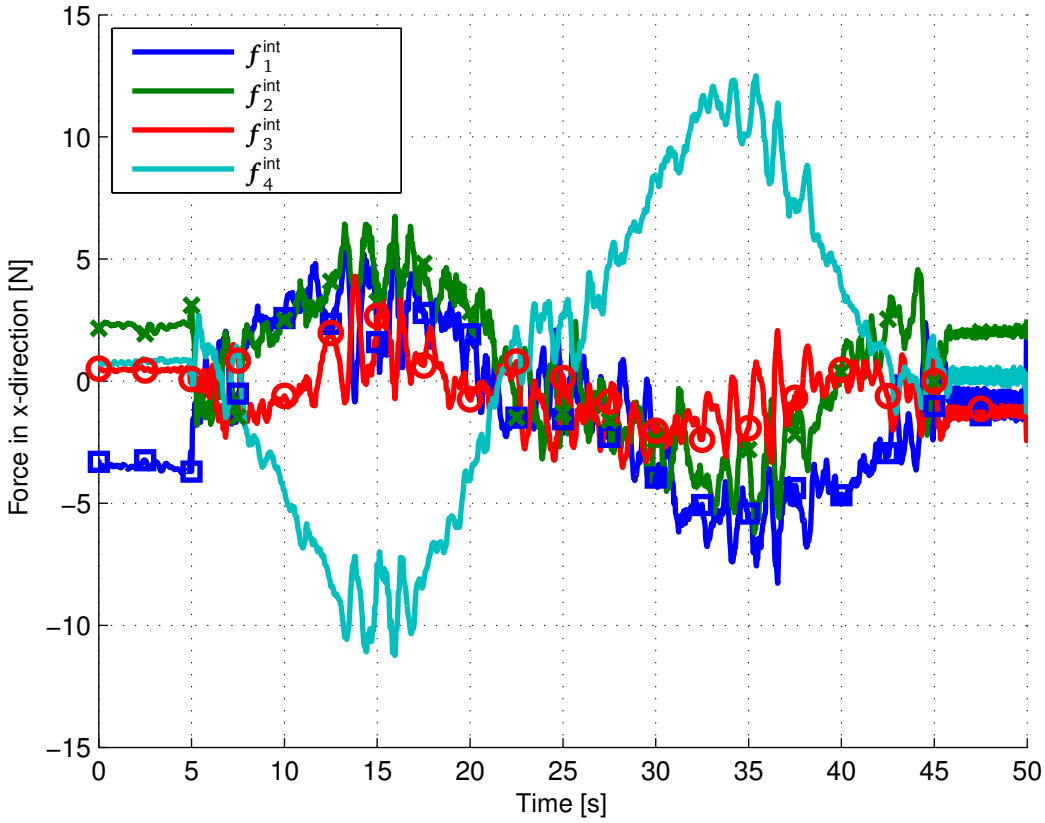

Figure 2.10: Internal force for biased grasp parameters.

2.6 Summary

In this chapter we studied the dynamical system model of a cooperative manipulation task performed by multiple robotic manipulators. Therefore, in Section 2.3 the dynamical systems of the individual components which are manipulator model, mobile platform, and the object dynamics are introduced. To successfully conduct a cooperative manipulation task we are in line with the literature and render the actions of the robotic system which is composed of two anthropomorphic manipulators and a mobile base compliant by a feedback linearization of the nonlinear robot dynamics and we decouple the manipulator motion and the mobile base motion. Based on the definition of a cooperative manipulation task introduced in Chapter 2.4 the presence of strict input and state constraints is discussed when the object is rigidly grasped by multiple manipulators. These constraints are necessary to derive a unified and general nonlinear dynamical model of an object manipulated by multiple compliant manipulators. The result of this analytical derivation is an equation of motion for the centralized object state which is in our case driven by multiple decentralized system inputs which are injected by the individual manipulators. If the decentralized robotic inputs violate the previously mentioned kinematic constraints an internal stress is exerted on the object. In Chapter 2.5 the proposed control design is proven a valid and systematic model for enabling cooperative manipulation in a prototypical scenario in which four full-sized, anthropomorphic robots are effectively coordinated in order to transport a payload

from an initial to a final configuration. More sophisticated approaches which coordinate the manipulators are introduced in the upcoming chapter.

3

Formation-based Coordination of Cooperative Robotic Manipulation

3.1 Motivation

Physical cooperation of robotic manipulators turns out to be a recurring challenge in a wide variety of tasks such as joint object manipulation and synchronized handover tasks. Cooperative object manipulation tasks are on hand when the scope of a single manipulator is exceeded. This happens for example when heavy and bulky objects need to be transported. As it is highlighted in the previous chapter a manipulation task which is cooperatively accomplished by a team of multiple robots can be characterized by a centralized system model which is excited by different and distributed robotic inputs. If the robot inputs satisfy the kinematic constraints of a cooperative manipulation task, then the internal forces acting on the objects are significantly reduced. In order to achieve a successful object manipulation, a flexible, robust, and distributed control and task execution mechanism is required here which coordinates the robot inputs effectively and efficiently. Note that a control architecture is called distributed if there is no central coordinating entity, i.e. each manipulator has its own local controller which may communicate with other local controllers to achieve the overall control goal. Communication among cooperating robots is crucial in order to eventually embed cooperating multi-robot teams in our everyday life where a wide range of disturbances can occur and the robots have to mutually react to those disturbances. The control scheme for coordinating the robotic inputs requires two main features: First, a goal regulation which drives the robotic system inputs to a final configuration, preferably in an optimal fashion or by imitating complex motor actions, and second, an inter-robot coordination such that the overall system consisting of multiple distributed impedance-controlled manipulators does not damage the transported object.

3.2 Related Work

Different control approaches have been proposed for cooperative manipulation [79]. A popular approach consists of distributing the impedances to multiple cooperating manipulators in closed contact which extends the capabilities of the robot team in transportation and contact tasks, see for example [80, 1, 35]. Those approaches decouple the path planning from the control, i.e. individual trajectories are planned for each robotic manipulator taking into account the object geometry and grasp points [54, 81]. A straightforward solution to the path planning problem requires a feedforward planning of individual trajectories for each manipulator by considering grasp points and the object geometry. If feedback is missing in the path planning and in the task execution, a feedforward approach is always very sensitive to the initial configuration, the model accuracy, and in particular to external disturbances from the environment [82].

By using a centralized planner the motion of all cooperating robot members can be planned simultaneously addressing state and input constraints. However, due to the apparent state constraints among other things a centralized planner only scales very poorly with increasing number of team members, generalized coordinates, and constraints [82]. Behavior-based motion-planning approaches for a coordination of a team of robots focus on the entanglement of the multiple team member by fragmenting the high-level goal into straightforward task assignments with simple controllers. The convenience of decentralizing the tasks requires less communication among the robots and still the emergent team performance is against expectation satisfying [83, 84]. Yet a methodical procedure to system engineering and incorporating a desired team performance and behavior is widely known to be a very tough challenge here.

Also related to the robot coordination problem are methods in formation control of mobile robots, where usually no manipulation and no physical cooperation is considered. [85, 86, 87, 88]. Depicted in Figure 3.1 is the gallery of various formation-based robots which are coordinated by a formation control paradigm. Surveys [89, 90, 91] of several approaches for the coordination of a robotic formation are discussed in the literature. Favorable methods for coordinating and abstracting the particular robots range from leader-follower approaches [92], to virtual structures [93], and virtual leaders [94]. In addition, formation control models can facilitate prescribed formation maneuvers based on parameters [95] and are capable of incorporating team feedback [96]. Due to these flexibilities and the ability to scale with increasing system complexity we adopt formation control for cooperative manipulation in the following chapters. Regarding the coupling between the particular robots the formation control problem can be differentiated between a distance-based, displacement-based, and position-based approach [89]. In position-based control the particular robotic agents sense their position in a global reference system and actively steer their own state to the desired one in order to establish a desired formation. In a displacement-based approach the robots need to know the orientation of the world coordinate system, but not their positions in the world coordinate system. The displacement-based formation is defined by desired displacements between the agents and the resulting formations are invariant to translations. The displacement-based approach requires less advanced communication capabilities and less complex interaction topologies between the cooperating agents when compared to the distance-based approach. The distance-based formation is defined by desired distances between the agents and then the resulting formation is invariant to both translations and rotations. In comparison to a distance-based approach, where the coupling is bearing-like along all dimensions

in $\mathbb{R}^3$, in a displacement-based approach more advanced sensing capabilities are required but the requirements on the interaction topology are less. All formation-based approaches are suitable for outdoor applications by using appropriate sensing technologies such as GPS or a compass. Since position-based formation control has proven to be difficult for precise formation control, we neglect it and focus on displacement-based and distance-based approaches in the upcoming chapter. In [85] a formation control problem is presented for agents with integrator dynamics using a positive definite function, which they employ for the leader-follower approach in mobile robots. Using the rigidity constraint in the control design phase for the interaction with larger networks a leader-follower network is studied in [86]. Controlling and maintaining triangular formations for mobile autonomous agents is studied in [87, 88].

In terms of distance-based formation control a formation rigidity constraint which is embedded and relaxed in an LQR-like optimal control problem is introduced in Chapter 5.3. However, the approach only considers the maintenance of the rigidity constraint and is not suitable for establishing formations and synchronized movements. Often, it is crucial to develop desired complex motor actions which are performed by the individual robots. Primitive-based control is used to generate trajectories out of several primitives which encode simple and stereotypical motions [97, 98]. A powerful tool for representing discrete and periodic trajectories are Dynamic Movement Primitives (DMPs) developed in [99] and [100]. DMPs are mainly used for imitation and learning tasks of a single manipulator and are therefore useful for representing and generating human-like movements. Coupling dynamic motor primitives is investigated for cooperative manipulation in Chapter 3.4. Besides for bimanual tasks with force feedback in [101] this has not been considered in-depth in the literature. At least, we present in Chapter 3.5 a displacement-based formation control approach which facilitates both goal regulation and desired internal force control.

3.3 Optimal Feedback Control under Relaxed Constraints

This section introduces a reduced state-space model for interconnected cooperative multi-robot teams, which is employed as model for the iterative optimal control design. Those reductions and assumptions are necessary to apply an iterative control design. A feedback control law is then derived for this system that drives the robot team from an initial configurations to a final configuration.

3.3.1 Multi-Robot Cooperation - A State Space Model

Consider a cooperative team of interacting robots $i = 1, \ldots, N$, each one evolving according to the inverse dynamic feedback-linearized impedance control as defined in Eq. (2.8). For the i-th manipulator, the position $\boldsymbol{p}_i$ of the end-effector frame Σ_i is expressed in a world coordinate system Σ_w. For this approach we only consider translational movements for the various end-effectors, i.e. either an unactuated joints along the orientations is mounted on each end-effector or the rotational stiffness, damping, and mass are tuned in order to render a gravity compensation effect for all rotational motions. Note that although the rotational motion of the particular robots is not actively controlled the object can still be rotated. Since an impedance control enforces a compliance of the manipulator with respect to its environment, it is widely used in manipulation tasks by

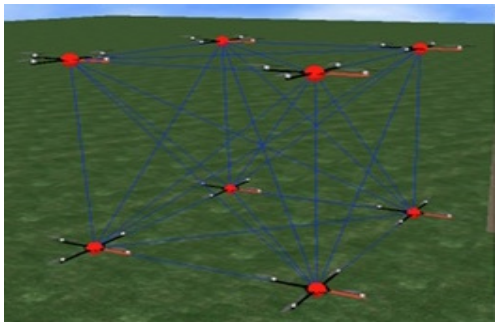

(a) (a)

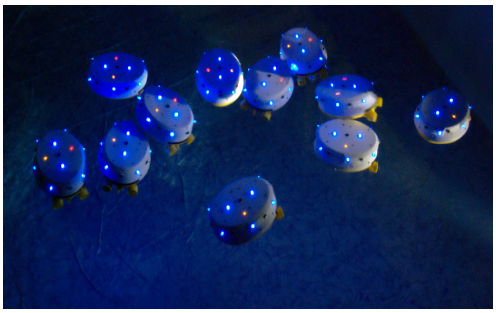

(b) (b)

(c) (c)

(d) (d)

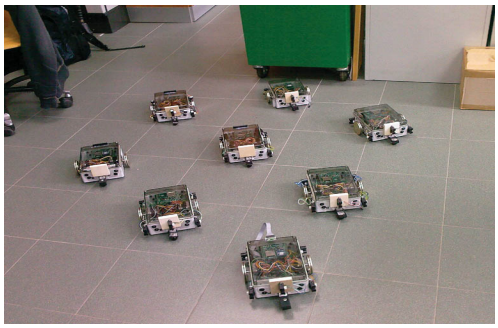

(e) (e)

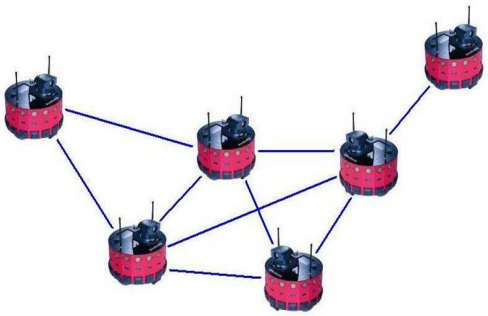

(f) (f)

(g) (g)

(h) (h)

Figure 3.1: Examples of multi-robot formation setups: (a) Time-varying topology fur UAVs [102], (b) Underwater collective movement principles [103] (c) Decentralized capture by mobile robots [104], (d) Cooperative localization of mobile robots [105], (e) Agreement on common reference frame [106], (f) Locally interacting mobile robots [107], (g) Cooperative throwing and catching [108], (h) Autonomous self-assembly for task execution [109].

establishing the desired position $\boldsymbol{p}_i^d$ and velocity $\dot{\boldsymbol{p}}_i^d$. Accordingly, the system dynamics for one manipulator evolve according to

$$M_i\ddot{\boldsymbol{p}}_i + D_i\left(\dot{\boldsymbol{p}}_i - \dot{\boldsymbol{p}}_i^d\right) + K_i\left(\boldsymbol{p}_i - \boldsymbol{p}_i^d\right) = \boldsymbol{f}_i - \boldsymbol{f}_i^d, \tag{3.1}$$

where the positive definite matrices M_i, D_i, and $K_i \in \mathbb{R}^{3\times3}$ are the inertia, damping, and stiffness constituting the motion control scheme w.r.t. the control inputs: the desired force $\boldsymbol{f}_i^d$ and the desired velocity $\dot{\boldsymbol{p}}_i^d$, where the desired position $\boldsymbol{p}_i^d$ is inferred via integration. Further, $\boldsymbol{f}_i \in \mathbb{R}^n$ denotes the resulting force. For a single robotic manipulator, this force $\boldsymbol{f}_i$ arises from its contact with the environment. However, since cooperating manipulators are in contact through the object, an internal force among the physically cooperating manipulators can occur.

Partition of $\boldsymbol{f}_i$

In general, the end-effector force $\boldsymbol{f}_i$ is composed of the rigid-body dynamics $\boldsymbol{f}_i^{\text{motion}}$ which result from the motion of the object and thereby depends on $\boldsymbol{h}_o$ defined in Eq. (2.16), the external force $\boldsymbol{f}_i^{\text{ext}}$ which results from interaction with the environment (e.g. objects or interacting humans), and the internal force $\boldsymbol{f}_i^{\text{int}}$ which results from the interaction among the cooperating robots, i.e.

$$\boldsymbol{f}_i = \boldsymbol{f}_i^{\text{motion}} + \boldsymbol{f}_i^{\text{ext}} + \boldsymbol{f}_i^{\text{int}}. \tag{3.2}$$

The resulting force $\boldsymbol{f}_i - \boldsymbol{f}_i^d$ exciting the system in (3.1) can be decoupled from the object motion $\boldsymbol{f}_i^{\text{motion}}(\boldsymbol{h}_o)$ by setting $\boldsymbol{f}_i^d = \boldsymbol{f}_i^{\text{motion}}$. Hence, the rigid body dynamics $\boldsymbol{f}_i^{\text{motion}}$ and so $\boldsymbol{h}_o$ defined in Eq. (2.16) is suppressed in the impedance (3.1). This is reasonable, since a compliance resultant from the dynamics of the object leads to a permanent undesired position deviation of the multi-robot team, e.g. the object mass pulls down the manipulators. The external force $\boldsymbol{f}_i^{\text{ext}}$ can originate from an undesired obstacle or from a human input in direct physical contact with the object or with a single manipulator. For the sake of clarity we make the following assumptions.

Assumption 3.1. As we will be mainly concerned with the tracking performance in this section, we assume that at the initial time t_0 all current and desired positions are equal, $\boldsymbol{p}_i(t_0) = \boldsymbol{p}_i^d(t_0)$. Initial configurations $\boldsymbol{p}_i^d(t_0)$ are chosen reasonable to have no internal stress at the beginning. This is necessary since an internal stress at initial time can to an induced movement of the robotic manipulators, which is undesired for maintaining formation. An appropriate choice of the grasp points $\boldsymbol{p}_i(t_0), \boldsymbol{p}_i^d(t_0)$ is the easiest way to circumvent this.

Assumption 3.2. There is no external force, $\boldsymbol{f}^{\text{ext}} = 0$, and the exact object dynamic model (2.16) is known and can be used as feedforward term given by $\boldsymbol{f}_i^d = \boldsymbol{f}_i^{\text{motion}}(\boldsymbol{h}_o)$.

Assumption 3.3. For simplicity, we assume that the influence of damping D_i and inertia M_i are negligible for the internal forces in (2.33). The multi-robot team moves at moderate velocities as we assume here, that the distributed impedances are in a quasi-equilibrium state and act thereby primarily via its stiffness K_i. The influence of damping D_i and inertia M_i is negligible with this assumption, which strongly simplifies the cooperative robot model.

With these assumptions the internal force can be completely characterized by Eq. (2.38) arising from the difference between desired manipulator position and the arithmetic mean of all set-points.

When we establish the internal force model, we obtain the ith internal force partition by evaluating the result (2.38) row-wise as

$$\boldsymbol{f}_i^{\text{int}} = K_i(\boldsymbol{p}_i - \boldsymbol{p}_i^d - \frac{1}{N}\sum_{j=1}^{N}(\boldsymbol{p}_j - \boldsymbol{p}_j^d)), \tag{3.3}$$

where terms involving M_i and D_i vanish due to the previously made assumptions. Note here that the opposite sign in (3.3) in comparison with (2.38) appears due to Newton's third law which states there will always be a wrench with opposite sign be acting on the manipulator.

Cooperative Impedance Control

Connecting the results (3.1), (3.2), and (3.3) with Assumptions 3.1- 3.3, we obtain

$$M_i\ddot{\boldsymbol{p}}_i + D_i\left(\dot{\boldsymbol{p}}_i - \dot{\boldsymbol{p}}_i^d\right) + K_i\left(\boldsymbol{p}_i - \int_{t_0}^{t_e}\dot{\boldsymbol{p}}_i^d \mathrm{d}\tau\right) = K_i\left(\boldsymbol{p}_i - \int_{t_0}^{t_e}\dot{\boldsymbol{p}}_i^d \mathrm{d}\tau - \frac{1}{N}\sum_{j=1}^{N}\left(\boldsymbol{p}_j - \int_{t_0}^{t_e}\dot{\boldsymbol{p}}_j^d \mathrm{d}\tau\right)\right).$$

Remark 3.1. In most impedance control models a new state is introduced for $\left(\boldsymbol{p}_i - \int_{t_0}^{t_e}\dot{\boldsymbol{p}}_i^d \mathrm{d}\tau\right)$ in order to reduce the degree of the system. For cooperative manipulation, we cannot apply this argument because the minimal state space representation involves both absolute and relative positions. Therefore, the system degree of one manipulator remains 3.

Let $\boldsymbol{x}_i = \left[(\int_{t_0}^{t}\dot{\boldsymbol{p}}_i^d \mathrm{d}\tau)^\intercal, \boldsymbol{p}_i^\intercal, \dot{\boldsymbol{p}}_i^\intercal\right]^\intercal$ be the system state and $\boldsymbol{u}_i = \dot{\boldsymbol{p}}_i^d$ be the control input. Then a state space model for a single manipulator in cooperation results in

$$\dot{\boldsymbol{x}}_i = A_{ii}\boldsymbol{x}_i + B_{ii}\boldsymbol{u}_i + \sum_{j\in\{1,\dots,N\}\setminus\{i\}} A_{ij}\boldsymbol{x}_j, \tag{3.4}$$

with

$$A_{ii} = \begin{pmatrix} 0 & 0 & 0 \\ 0 & 0 & 1 \\ \frac{1}{N}M_i^{-1}K_i & -\frac{1}{N}M_i^{-1}K_i & -M_i^{-1}D_i \end{pmatrix},$$

$$A_{ij} = \begin{pmatrix} 0 & 0 & 0 \\ 0 & 0 & 0 \\ \frac{1}{N}M_i^{-1}K_i & -\frac{1}{N}M_i^{-1}K_i & 0 \end{pmatrix},$$

$$B_{ii} = \begin{pmatrix} 1 \\ 0 \\ M_i^{-1}D_i \end{pmatrix},$$

where A_{ii} is the system matrix of a single manipulator i, B_{ii} is its input matrix, and A_{ij} represents the physical coupling from manipulator j to manipulator i. After deriving the system dynamics for a multi-robot cooperative system, we obtain a standard LTI sytem.

$$\dot{\boldsymbol{x}} = A\boldsymbol{x} + B\boldsymbol{u}, \tag{3.5}$$

with the aggregated state vector $\boldsymbol{x} = \left[\boldsymbol{x}_1^\intercal, \ldots, \boldsymbol{x}_N^\intercal\right]^\intercal$ and the aggregated input vector $\boldsymbol{u} = \left[\boldsymbol{u}_1^\intercal, \ldots, \boldsymbol{u}_N^\intercal\right]^\intercal$. The total system is written as $A = \left[A_{ij}\right]$ and $B = \mathrm{diag}(B_{11}, \ldots, B_{NN})$.

3.3.2 Control Goals in Multi-Robot Manipulation Task

In this section we describe the control goal considered in this thesis. We want to design a linear state feedback controller $\boldsymbol{u} = -K\boldsymbol{x}$ which optimally drives a formation of interconnected manipulators described by the system dynamics (3.5) from an initial condition $\boldsymbol{x}_0$ to a desired end point $\boldsymbol{x}^{\mathrm{goal}}$ while maintaining the initial formation. In the following we describe the cost functional of our LQR-like optimal control problem and how the desired rigidity is relaxed.

In order to achieve goal regulation to the goal $\boldsymbol{x}^{\mathrm{goal}}$, we employ the standard transformation of our state $\boldsymbol{x}$ into

$$\tilde{\boldsymbol{x}} = \boldsymbol{x} - \boldsymbol{x}^{\mathrm{goal}}. \tag{3.6}$$

Then, we can formulate the LQR cost functional which gives a controller driving to the end point in an optimal fashion as

$$J = \tilde{\boldsymbol{x}}^\intercal(T)S\tilde{\boldsymbol{x}}(T) + \int_0^T \tilde{\boldsymbol{x}}^\intercal(t)Q\tilde{\boldsymbol{x}}(t) + \boldsymbol{u}^\intercal(t)R\boldsymbol{u}(t)\mathrm{d}t, \tag{3.7}$$

where S, Q (positive semi-definite), and R (positive definite) are weighting matrices expressing the desired performance. The weighting matrices need to be positive (semi-)definite in order to guarantee a minimum with the corresponding minimum cost finitely bounded from below.

Next, we define the formation and how we can integrate the desired distances between the robot positions into the cost functional. The formation is described by a static set of edges $\mathscr{E}$ with cardinality $||\mathscr{E}||$ between the manipulators such that the virtual structure of the formation is rigid during the movement phase. By virtual structure, we mean that the robots should maintain and keep their formation regardless of any direct mechanical coupling. The desired distance between any two robot position in the formation is described by an edge function $\boldsymbol{f}(\boldsymbol{x}) = \left(\ldots, \|\boldsymbol{p}_i - \boldsymbol{p}_j\|, \ldots\right) \in \mathbb{R}^{\|\mathscr{E}\|}$ which is required to satisfy $\boldsymbol{f}(\boldsymbol{x}) = \boldsymbol{d}$. Identical to (3.4) and (3.5), the state variable $\boldsymbol{x}$ is concenated by $\boldsymbol{x}_i$ and also contains the manipulator positions $\boldsymbol{p}_i$. Here, $\boldsymbol{d} = \left(\ldots, \|\boldsymbol{d}_{ij}\|, \ldots\right)$ is the desired rigid distance vector between all manipulators, and constant if rigidity is achieved. The desired rigid distance vector is given by the Euclidean norm of the cooperative manipulation constraint defined in (2.31). Differentiating $\boldsymbol{f}$ w.r.t time leads to

$$\left(\boldsymbol{p}_i - \boldsymbol{p}_j\right)^\intercal \left(\dot{\boldsymbol{p}}_i - \dot{\boldsymbol{p}}_j\right) = 0 \quad \forall (i,j) \in \mathscr{E}. \tag{3.8}$$

The geometrical interpretation of (3.8) is that the difference in position between two linked manipulators is orthogonal to the difference in velocity. This equation represents our second

control goal of maintaining formation rigidity. Due to Assumption 3.1 it is sufficient to maintain the formation instead of establishing it. In order to include the rigidity condition (3.8) into our LQR cost functional (3.7), we transform it into a quadratic term of the states. Thus (3.8) is written as $\boldsymbol{x}_{i,j}^{\intercal} Q_{ij} \boldsymbol{x}_{i,j}$ with $\boldsymbol{x}_{i,j} = [\boldsymbol{x}_i^{\intercal}, \boldsymbol{x}_j^{\intercal}]^{\intercal}$ by defining the blocks

$$[q_{ii}] = \left[q_{jj}\right] = \begin{pmatrix} 0 & 0 & 0 \\ 0 & 0 & \frac{1}{2} I_n \\ 0 & \frac{1}{2} I_n & 0 \end{pmatrix} \forall (i,j) \in \mathscr{E},$$

$$\left[q_{ij}\right] = \left[q_{ji}\right] = \begin{pmatrix} 0 & 0 & 0 \\ 0 & 0 & -\frac{1}{2} I_n \\ 0 & -\frac{1}{2} I_n & 0 \end{pmatrix} \forall (i,j) \in \mathscr{E}.$$

The resultant matrix $Q_{ij} = \left[\begin{smallmatrix} q_{ii} & q_{ij} \\ q_{ji} & q_{jj} \end{smallmatrix}\right]$ is symmetric but indefinite and thus it cannot be employed in a standard LQR problem directly. Since the equality constraint described in Eq. (3.8) can be violated in both directions, the indefiniteness of $\boldsymbol{x}_{i,j}^{\intercal} Q_{ij} \boldsymbol{x}_{i,j}$ is obvious, and its apparent global minimum is $-\infty$. The biquadratic term $(\boldsymbol{x}_{i,j}^{\intercal} Q_{ij} \boldsymbol{x}_{i,j})^2$ on the other hand has a minimum of 0, and is thus suitable to be included in an optimization to ensure relaxed rigidity. In other words, minimizing $(\boldsymbol{x}_{i,j}^{\intercal} Q_{ij} \boldsymbol{x}_{i,j})^2$ for all $(i,j) \in \mathscr{E}$ relaxes the equality constraint (3.8) into a minimization problem. Relaxation means that the resulting controller does not guarantee exact satisfaction of Eq. (3.8) for all times, but for appropriate weighting matrices, the controller design leads to values that are at least close to zero. Proper partitioning allows writing $(\boldsymbol{x}_{i,j}^{\intercal} Q_{ij} \boldsymbol{x}_{i,j})^2$ as

$$(\boldsymbol{x}^{\intercal} Q_k \boldsymbol{x})^2 \;\forall\; k \in \{1, ..., ||\mathscr{E}||\}\,. \tag{3.9}$$

While the control design objective of goal regulation requires the transformation to the coordinates $\tilde{\boldsymbol{x}}$ from (3.6), it is important to note that the relaxed rigidity condition (3.9) still needs to be satisfied in the original coordinate system $\boldsymbol{x}$. In order to combine both coordinate systems in the same cost functional we introduce an augmented state vector

$$\hat{\boldsymbol{x}} = \left(\tilde{\boldsymbol{x}}^{\intercal}, 1\right)^{\intercal}.$$

With this state vector, we reformulate the relaxed rigidity condition (3.9) into

$$\begin{aligned} &(\boldsymbol{x}^{\intercal} Q_k \boldsymbol{x})^2 \;\forall\; k \in \{1, ..., ||\mathscr{E}||\} \\ &= \left(\begin{pmatrix} \tilde{\boldsymbol{x}} \\ 1 \end{pmatrix}^{\intercal} \begin{pmatrix} Q_k & Q_k \boldsymbol{x}^{\text{goal}} \\ \boldsymbol{x}^{\text{goal}\intercal} Q_k & \boldsymbol{x}^{\text{goal}\intercal} Q_k \boldsymbol{x}^{\text{goal}} \end{pmatrix} \begin{pmatrix} \tilde{\boldsymbol{x}} \\ 1 \end{pmatrix}\right)^2 = \left(\hat{\boldsymbol{x}}^{\intercal} \hat{Q}_k \hat{\boldsymbol{x}}\right)^2 \;\forall\; k \in \{1, ..., ||\mathscr{E}||\}\,. \end{aligned} \tag{3.10}$$

We can now combine all of the terms into one cost functional and restate our control goal. The goal of our optimal control problem is to find a controller $\boldsymbol{u} = -\hat{K}\hat{\boldsymbol{x}}$ with structure $\hat{K} = [K, 0]$ in order to minimize the following cost functional

$$J = \hat{\boldsymbol{x}}(T)^{\intercal} \hat{S} \hat{\boldsymbol{x}}(T) + \int_0^T \sum_{k=1}^{||\mathscr{E}||} \left(\hat{\boldsymbol{x}}^{\intercal}(t) \hat{q}_k \hat{Q}_k \hat{\boldsymbol{x}}(t)\right)^2 + \boldsymbol{u}^{\intercal}(t) R \boldsymbol{u}(t) + \hat{\boldsymbol{x}}^{\intercal} \hat{Q} \hat{\boldsymbol{x}} \,\mathrm{d}t, \tag{3.11}$$

where $\hat{S}$ and $\hat{Q}$ have the structure $\hat{S} = \mathrm{diag}(S, 0)$ and $\hat{Q} = \mathrm{diag}(Q, 0)$ in order not to penalize the additional 1-state, $\hat{Q}_k$ is given in (3.10) and $\hat{q}_k$ is a positive scalar weighting factor. The term $\hat{\boldsymbol{x}}(T)^\intercal \hat{S} \hat{\boldsymbol{x}}(T)$ represents the penalty term resulting from the distance between $\boldsymbol{x}$ and $\boldsymbol{x}^{\mathrm{goal}}$ for the final time T. Control input constraints are indirectly realized by $\boldsymbol{u}^\intercal(t) R \boldsymbol{u}(t)$. This cost functional represents our combined control goals of maintained formation by the term $\sum_{k=1}^{||\mathscr{E}||} \left(\hat{\boldsymbol{x}}^\intercal(t) \hat{Q}_k \hat{\boldsymbol{x}}(t)\right)^2$, and goal regulation by the term $\hat{\boldsymbol{x}}^\intercal \hat{Q} \hat{\boldsymbol{x}}$. The zero column in $\hat{K}$ is necessary to discard the augmented 1-state.

3.3.3 Optimal Control Design

In this section, we present two algorithms to achieve our control goal described by the cost functional (3.11). Furthermore, an idea is presented to alleviate the local character of the resulting control law.

Gradient descent method using adjoint states

In this subsection we describe a solution algorithm to determine a suboptimal feedback to minimize the biquadratic cost functional (3.11), inspired by the results in [110]. While there is a linear relationship in the standard LQR problem between the primal states $\hat{\boldsymbol{x}}$ and the adjoint states $\hat{\boldsymbol{\lambda}}$ given by $\hat{\boldsymbol{\lambda}}(t) = P \hat{\boldsymbol{x}}(t)$, allowing for the solution to use a Riccati equation for the matrix P, this is not the case here. Because of the biquadratic term in the cost functional we are forced to use an alternative method based on simulated trajectories which is explained in the following.

Given the biquadratic cost functional (3.11) we want to iteratively determine the optimal state-feedback law. The corresponding Lagrangian function of the problem is

$$\begin{aligned} L =& \hat{\boldsymbol{x}}(T)^\intercal \hat{S} \hat{\boldsymbol{x}}(T) + \int_0^T \sum_{k=1}^{||\mathscr{E}||} \left(\hat{\boldsymbol{x}}^\intercal(t) \hat{q}_k \hat{Q}_k \hat{\boldsymbol{x}}(t)\right)^2 + \hat{\boldsymbol{x}}^\intercal \hat{Q} \hat{\boldsymbol{x}} \\ &+ \hat{\boldsymbol{\lambda}}^\intercal(t)(\dot{\hat{\boldsymbol{x}}}(t) - (\hat{A} - \hat{B}\hat{K})\hat{\boldsymbol{x}}(t)) + \hat{\boldsymbol{x}}^\intercal(t) \hat{K}^\intercal R \hat{K} \hat{\boldsymbol{x}}(t) \mathrm{d}t + \hat{\boldsymbol{\mu}}(\hat{\boldsymbol{x}}(0) - \hat{\boldsymbol{x}}_0), \end{aligned} \tag{3.12}$$

where $\hat{A} = \mathrm{diag}(A, 0)$ and $\hat{B} = [B^\intercal, 0^\intercal]^\intercal$. Partial integration of (3.12) gives

$$\begin{aligned} L =& \hat{\boldsymbol{x}}(T)^\intercal \hat{S} \hat{\boldsymbol{x}}(T) + \int_0^T \sum_{k=1}^{||\mathscr{E}||} \left(\hat{\boldsymbol{x}}^\intercal(t) \hat{q}_k \hat{Q}_k \hat{\boldsymbol{x}}(t)\right)^2 + \hat{\boldsymbol{x}}^\intercal(t) \hat{K}^\intercal R \hat{K} \hat{\boldsymbol{x}}(t) + \hat{\boldsymbol{x}}^\intercal \hat{Q} \hat{\boldsymbol{x}} - \hat{\boldsymbol{x}}^\intercal(t) \dot{\hat{\boldsymbol{\lambda}}}(t) \\ &- \hat{\boldsymbol{x}}^\intercal(t)(\hat{A} - \hat{B}\hat{K})^\intercal \hat{\boldsymbol{\lambda}}(t) \mathrm{d}t + \left[\hat{\boldsymbol{\lambda}}(t)^\intercal \hat{\boldsymbol{x}}(t)\right]_0^\intercal + \hat{\boldsymbol{\mu}}^\intercal(\hat{\boldsymbol{x}}(0) - \hat{\boldsymbol{x}}_0). \end{aligned}$$

We can derive equations for the adjoint state through the optimality condition $\frac{\partial L}{\partial \hat{\boldsymbol{x}}} = 0$. This gives

$$\begin{aligned} \dot{\hat{\boldsymbol{\lambda}}}(t) =& (\hat{A} - \hat{B}\hat{K})^\intercal \hat{\boldsymbol{\lambda}}(t) - 2\hat{K}^\intercal R \hat{K} \hat{\boldsymbol{x}}(t) - 2\hat{Q}\hat{\boldsymbol{x}}(t) - 4 \sum_{k=1}^{||\mathscr{E}||} (\hat{\boldsymbol{x}}^\intercal(t) \hat{q}_k \hat{Q}_k \hat{\boldsymbol{x}}(t)) \hat{q}_k \hat{Q}_k \hat{\boldsymbol{x}}(t), \\ \hat{\boldsymbol{\lambda}}(T) =& -2\hat{S}\hat{\boldsymbol{x}}(T), \quad \hat{\boldsymbol{\mu}} = -\hat{\boldsymbol{\lambda}}(0). \end{aligned}$$

The last equation gives justification that $\hat{\boldsymbol{\lambda}}(0)$ is free.

Proposition 3.1. *The gradient of the cost functional with respect to the feedback matrix $\hat{K}$ is*

$$\nabla_{\hat{K}} J = \int_0^T 2R\hat{K}\hat{\boldsymbol{x}}(t)\hat{\boldsymbol{x}}^\intercal(t) + B^\intercal\hat{\boldsymbol{\lambda}}(t)\hat{\boldsymbol{x}}^\intercal(t)\mathrm{d}t. \tag{3.14}$$

Proof. The gradient is determined from the Lagrange function. We get

$$\begin{aligned}\nabla_{\hat{K}} J \bullet H &= \int_0^T 2\hat{\boldsymbol{x}}^\intercal(t)H^\intercal R\hat{K}\hat{\boldsymbol{x}}(t) + \hat{\boldsymbol{x}}^\intercal(t)H^\intercal B^\intercal\hat{\boldsymbol{\lambda}}(t)\mathrm{d}t \\ &= \int_0^T 2R\hat{K}\hat{\boldsymbol{x}}(t)\hat{\boldsymbol{x}}^\intercal(t) + B^\intercal\hat{\boldsymbol{\lambda}}(t)\hat{\boldsymbol{x}}^\intercal(t)\mathrm{d}t \bullet H,\end{aligned}$$

where H is a variation in $\hat{K}$, and where $\bullet$ denotes the Frobenius inner product. □

The feedback matrix is then iteratively determined using the following algorithm.

Algorithm 1.

1. Simulate the states $\hat{\boldsymbol{x}}(t)$ for the finite horizon T.
2. Simulate the adjoint states $\hat{\boldsymbol{\lambda}}(t)$ for the same horizon according to (3.13).
3. Compute the gradient according to (3.14).
4. Update the feedback matrix

   $$\hat{K}^{(k+1)} = \hat{K}^{(k)} - \gamma_k \nabla_{\hat{K}} J^{(k)},$$

   where γ_k is a scalar step length.
5. If $\left|\frac{J^{(k)} - J^{(k-1)}}{J^{(k-1)}}\right| < \epsilon$, stop. Otherwise, increase k and go back to step 1.

The choice of the step size γ_k is important for the speed of convergence. A popular method is to choose a step size satisfying the Wolfe conditions [111] given by

$$\begin{aligned}J(\hat{K} + \gamma_k \mathrm{mat}(\boldsymbol{s}_k)) - J(\hat{K}) &\leq \gamma_k c_1 (\mathrm{vec}(\nabla_{\hat{K}} J))^\intercal \boldsymbol{s}_k, \\ (\mathrm{vec}(\nabla_{\hat{K}+\gamma_k \boldsymbol{s}_k} J))^\intercal \boldsymbol{s}_k &\geq c_2 (\mathrm{vec}(\nabla_{\hat{K}} J))^\intercal \boldsymbol{s}_k,\end{aligned} \tag{3.15}$$

where $c_1 \in (0, 1)$ and $c_2 \in (c_1, 1)$. For Algorithm 1, the search direction $\boldsymbol{s}_k$ is given by the vectorization of the negative gradient, i.e. $\boldsymbol{s}_k = -\mathrm{vec}(\nabla_{\hat{K}} J)$. An alternative step size for Algorithm 1 is the Barzilai-Borwein step size [112] which uses information of the previous step and is given as

$$\gamma_k = \frac{(\Delta\mathrm{vec}(\hat{K}))^\intercal (\Delta\mathrm{vec}(\hat{K}))}{(\Delta\mathrm{vec}(\hat{K}))^\intercal (\Delta\mathrm{vec}(\nabla_{\hat{K}} J))^\intercal}, \tag{3.16}$$

where $\Delta\mathrm{vec}(\hat{K}) = \mathrm{vec}(K^{(k)}) - \mathrm{vec}(\hat{K}^{(k-1)})$ and $\Delta\mathrm{vec}(\nabla_{\hat{K}} J) = \mathrm{vec}((\nabla_{\hat{K}} J)^{(k)}) - \mathrm{vec}((\nabla_{\hat{K}} J)^{(k-1)})$.

Minimization via BFGS method

The downside of Algorithm 1 presented in the previous section is that gradient methods generally converge slowly. However, the availability of the gradient according to (3.14) allows us to use more advanced optimization methods, like the Quasi-Newton Broyden-Fletcher-Goldfarb-Shanno (BFGS) method [113]. That means that instead of the negative gradient we use the following search direction

$$\boldsymbol{s}_k = -D_k \mathrm{vec}(\nabla_{\hat{K}^{(k)}} J),$$

where D_k approximates the inverse of the Hessian matrix.

We obtain the following algorithm.

Algorithm 2.

1. Choose $c_1, c_2 \in \mathbb{R}$, $\hat{K}_0 \in \mathbb{R}^{m\times n}$. Pick a positive definite matrix $D_0 \in \mathbb{R}^{mn\times mn}$, e.g. $D_0 = I_{mn}$.
2. Compute the search direction $\boldsymbol{s}_k$ as

   $$\boldsymbol{s}_k = -D_k \mathrm{vec}(\nabla_{\hat{K}} J),$$

   where the gradient $\nabla_{\hat{K}} J$ is given by to (3.14).
3. Compute the step size γ_k according to the Wolfe conditions (3.15).
4. Update the feedback matrix

   $$\hat{K}^{(k+1)} = \hat{K}^{(k)} + \gamma_k \mathrm{mat}(\boldsymbol{s}_k).$$

5. Set $\boldsymbol{p}_k = \mathrm{vec}(\hat{K}^{(k+1)}) - \mathrm{vec}(\hat{K}^{(k)})$ and $\boldsymbol{q}_k = (\mathrm{vec}(\nabla_{\hat{K}^{(k+1)}} J)) - (\mathrm{vec}(\nabla_{\hat{K}^{(k)}} J))$. Update D_k as

   $$D_{k+1} = D_k + \frac{(\boldsymbol{p}_k - D_k\boldsymbol{q}_k)\boldsymbol{p}_k^\intercal + \boldsymbol{p}_k(\boldsymbol{p}_k - D_k\boldsymbol{q}_k)^\intercal}{\boldsymbol{p}_k^\intercal \boldsymbol{q}_k} - \frac{(\boldsymbol{p}_k - D_k\boldsymbol{q}_k)^\intercal \boldsymbol{q}_k}{(\boldsymbol{p}_k^\intercal \boldsymbol{q}_k)^2}\boldsymbol{p}_k\boldsymbol{p}_k^\intercal.$$

6. If $\left|\frac{J^{(k)} - J^{(k-1)}}{J^{(k-1)}}\right| < \epsilon$, stop. Otherwise, increase k and go back to step 1.

Remark 3.2. Even though the two algorithms should lead to the same control law with the same cost this is not always the case. We attribute this to the nonconvexity of the cost functional causing the algorithms to converge to different local minima caused by the differences in search directions and step sizes. Also note that because the optimization problem has a finite horizon, the resulting control law is not guaranteed to be stabilizing for $t \to \infty$.

Averaging over the initial configuration x_0

One possible problem concerning the resulting feedback matrices of Algorithms 1 and 2 is that they are optimized w.r.t. to one specific initial configuration x_0. In practice however, the initial configuration might not be known in advance or might be slightly disturbed from the assumed one. In order to circumvent this problem, we propose to average over several initial configurations for

the simulated trajectories to obtain a control law that performs well for an area. The algorithms principally remain unchanged except for the gradient which is now given by

$$\nabla_{\hat{K}} J = \frac{1}{n_{\text{samples}}} \left(\sum_{i=1}^{n_{\text{samples}}} \int_0^T 2R\hat{K}\hat{\boldsymbol{x}}_i(t)\hat{\boldsymbol{x}}_i^\intercal(t) + B^\intercal \hat{\boldsymbol{\lambda}}_i(t)\hat{\boldsymbol{x}}_i^\intercal(t)\mathrm{d}t \right),$$

where $\hat{\boldsymbol{x}}_i(t)$ and $\hat{\boldsymbol{\lambda}}_i(t)$ are the trajectories resulting from the ith initial configuration, and n_{samples} is the number of selected initial configurations, see [110] for more details.

Remark 3.3. While this extension enlarges the area of possible initial configurations, this does not lead to a globally optimal control law. In fact, our numerical investigations show that initial configurations that are not considered directly in the design may lead to undesirable performance. This is also later shown in the example in Section 3.3.4.

3.3.4 Numerical Investigation

This section validate the control design algorithm.

Comparison between the presented algorithms

In this subsection we want to compare the computational performance between Algorithm 1 using the Barzilai-Borwein step size (3.16) and Algorithm 2. As a system, we consider three physically interconnected robots with system dynamics described by (3.5), all with identical parameters $M_i = I_3$, $D_i = 2\sqrt{3}I_3$ and $K_i = 3I_3$. Since each system has nine states, we have a total system dimension of 27. As a comparison scenario we move an initial triangle on the edges of the rectangle marked by the four crosses in Figure 3.2 in steps of length 0.5, resulting in 40 different starting points. The weighting matrices are chosen as $\bar{q}_k = 5$, $R = I_9$, $\hat{Q} = \mathrm{diag}(I_{27}, 0)$, $S = \mathrm{diag}(I_{27}, 0)$ with a horizon of 40. The optimization algorithms stop when the change in cost between iterations is less than 10^{-3}. The results of the comparison are summarized in Table 3.1. We see that the number of iterations is comparable for both algorithms. The fact that the number of iterations is lower for the gradient method is counter-intuitive and might be due to the fact that different local minima are found by the two algorithms. We observed in our investigations that even though both algorithms may achieve almost comparable costs, the actual resulting control matrices might be completely different. While the gradient descent algorithm has advantages in the computation time, the BFGS algorithm always achieves lower cost. The longer computation time of the BFGS algorithm for the same number of iterations is due to the step size computation according to the Wolfe conditions (3.15) which takes considerably longer than the computation of the Barzilai-Borwein step size. However, the average achieved cost and the median number of iterations is not significantly affected by the choice of the step size, Wolfe condition or Barzila-Borwein step size.

Note that for some categories we chose the median instead of the average because the BFGS algorithm produces some outliers that are not representative for its overall performance. In conclusion, if computational time is not an issue, the BFGS algorithm should be preferred because of the lower achieved cost.

Tabular 3.1: Comparison between Algorithms 1 and 2.

	Algorithm 1	Algorithm 2
Median number of iterations	184	191
Average achieved cost	82.09	75.92
Median computation time [s]	59.1	142.4
Average cost decrease by BFGS	-	9.2%
Median cost decrease by BFGS	-	8.1%

Illustrating numerical example

In this subsection we want to illustrate the result of Algorithm 2 with averaging over the initial configuration x_0. The system parameters are identical to the previous subsection. As weighting matrices we choose $R = 5I_9$, $S = \text{diag}(10I_{27}, 0)$, $\hat{q}_k = 100$ and $\hat{Q} = \text{diag}(0.1I_{27}, 0)$ because we want to emphasize maintaining of the formation. The optimization horizon is 40 seconds. The optimization algorithm stops when the change in cost between iterations is less than 10^{-3}. For the design, we pick 4 different initial configurations. The coordinates of the center points of the respective triangles are given in Table 3.2 and are marked as gray crosses in Figure 3.2. In the simulations the goal is to move the triangle formation of the three interconnected robots from four different initial configurations to a desired end point. These four initial configurations and the end point are also given in the table. Three of the initial configurations belong to the area surrounded by the four points used in the design, with two of them used directly in the design, while the fourth point is outside the area.

Figure 3.2 shows the resulting movements from all four initial configurations. We can see that the control design works well for all three points inside the area because the desired end point is reached and all the intermediate steps also show the initial formation. This shows that the relaxed rigidity condition is satisfied by the control design and the control law achieves all of its goals. For the point outside the area the desired end point is still reached but it can clearly be seen that the formation is violated in the intermediate steps because the formation stretches in all directions. This illustrates that the optimized control law has a local character and is not guaranteed to work well away from the initial configurations used during the optimization.

Remark 3.4. A phenomenon we observed during our numerical investigations is that while the classical LQR problem is invariant to scaling in the cost functional, meaning that the control law for Q and R is identical as the control law for cQ and cR with $c > 0 \in \mathbb{R}$, this is not the case here. Finding the exact reason will be part of future work.

Comparison with open loop input

In this subsection we compare the performance of the resulting feedback matrix from Algorithm 2 with an open loop input obtained with the Matlab function `fminunc`. The test scenario is the movement of a formation of three robots with identical system parameters as in Section 3.3.4. The open loop case corresponds to the generation of desired trajectories which are tracked by the impedance control law. The shape is a triangle with an initial center point $(0, 0)$. The desired end formation is a triangle with center point $(\frac{\sqrt{3}}{6}, 2.5)$ which is rotated by $-\frac{\pi}{2}$. We choose the

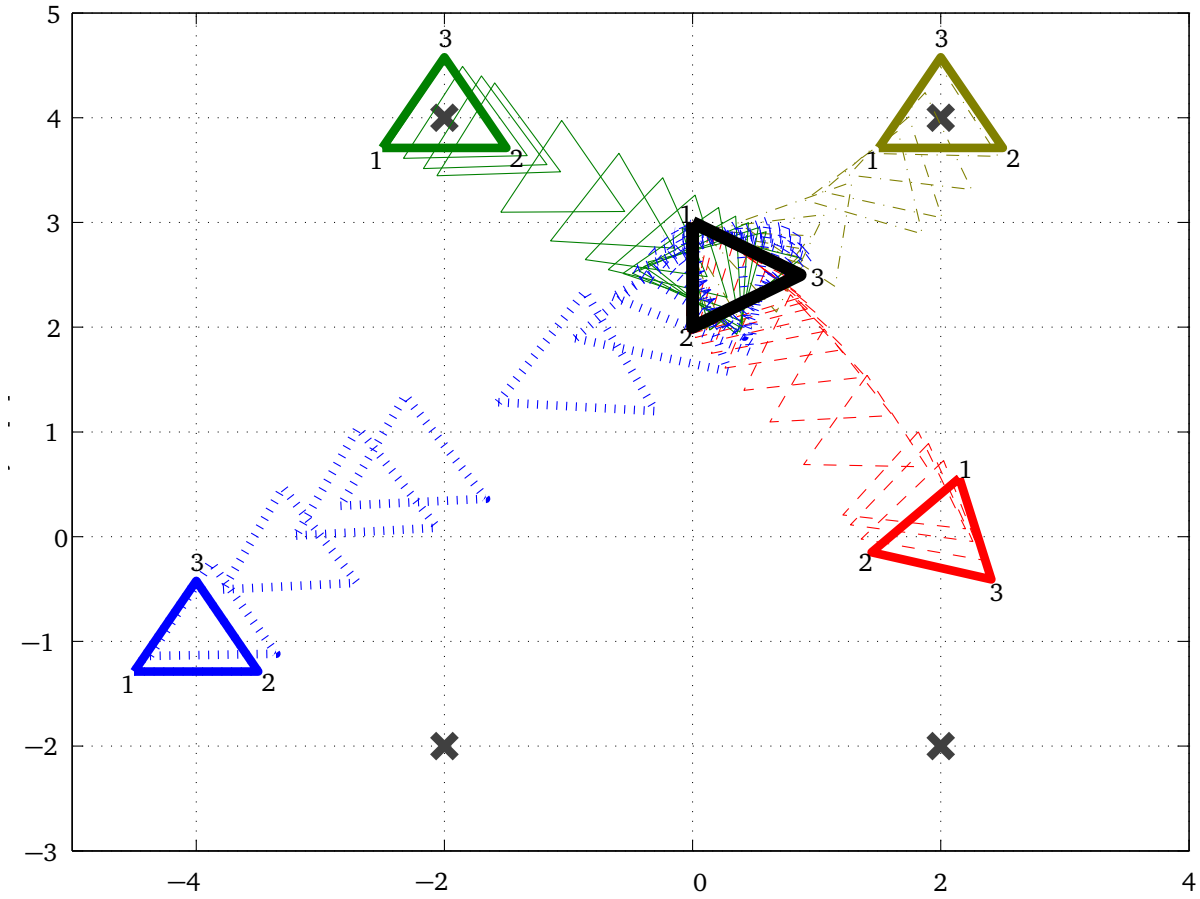

Figure 3.2: Three mobile robots drive from four different initial configurations (red dashed, yellow dashed dotted, green solid, blue dashed) to a common goal while trying to maintain the formation. Bold colored triangles illustrate the initial robot configuration, the bold black triangle is the final configuration. The blue triangle clearly loses formation because the shape of the triangle stretches during the movement, while the other three triangles maintain their shape.

weighting matrices $Q_k = 40I_{27}$, $R = 5I_9$, $S = \mathrm{diag}(10I_{27}, 0)$ and $\hat{Q} = \mathrm{diag}(10^{-2}I_{27}, 0)$, with the horizon 20.

The presented Algorithm 2 leads to a feedback control law which achieves the cost 11.13 after 958 iterations and 1543 seconds of computation time. The open loop trajectory is able to achieve a lower cost of 7.92 which is clear by the additional degree of freedom in the input signal but the computation time is much higher (117021 seconds $\approx$ 1.35 days). Besides computation time the feedback clearly has advantages when disturbances or uncertainties are considered.

3.3.5 Experimental Validation

To evaluate the control performance and to demonstrate the applicability of the proposed control scheme, a full-scale experiment is conducted. Our presented results show the benefits of the proposed controller approach by variations of the initial conditions and its reduction of internal forces.

Tabular 3.2: Starting and end points for visualizing example.

Phase	Center Point
Design	$x_1(t_0) = [2, -2, 0]$
Design	$x_2(t_0) = [2, 4, 0]$
Design	$x_3(t_0) = [-2, 4, 0]$
Design	$x_4(t_0) = [-2, -2, 0]$
Simulation	$x_1(t_0) = [2, 0, 0]$
Simulation	$x_2(t_0) = [2, 4, 0]$
Simulation	$x_3(t_0) = [-2, 4, 0]$
Simulation	$x_4(t_0) = [-4, -1, 0]$
Design & Simulation	$\boldsymbol{x}^{\text{goal}} = (\frac{\sqrt{3}}{6}, 2.5)$

Experimental Setup

The experimental setup consists of two commercially available *KUKA LWR 4+* (light-weight robot), which are mounted on a mobile platform. Since both manipulators are assembled on top of the same mobile platform, we circumvent the challenge of distributed robotic base frames, kinematic uncertainties, and communication uncertainties such as time delay and packet loss. Further details on the robots can be found in Appendix C. A workspace extension of both robotic manipulators is accomplished as described in Sec. 2.3.2 similar to the approach presented in [1]. A Cartesian impedance (3.1) is implemented and then both measured forces and M_i, D_i, and K_i are rotated into the world frame Σ_w. Both end-effector's Cartesian positions are captured by a *QualiSys* motion capture system at a frequency of 350 Hz from which we also obtain the transformation R_w^o. Further details on the Qualisys motion capture system can be found in Appendix C.

Experimental Design

Due to the decoupling of linear motions, we only consider translational motions for each manipulator. An unactuated revolute joint along yaw is mounted on each end-effector, such that the whole system can rotate while the manipulators move translational. Rotational motion of a manipulator hold the object orthogonal to its boundary for collision avoidance between manipulator and object. The impedance parameters are set to $M_{1,2} = 10I_3$, $D_{1,2} = 80I_3$, and $K_{1,2} = 120I_3$ for both manipulators. Five possible initial values are chosen around $\boldsymbol{x}_0 = [1.769, 2.08, 1, 1.769, 2.08, 1, 0, 0, 0, 1.769, 1.52, 1, 1.769, 1.52, 1, 0, 0, 0]^\intercal$, with the relative manipulator distance 0.56m . The goal configuration for both manipulators is set in accordance with Assumption 3.1 to $\boldsymbol{x}_e = [-1.08, -0.95, 1, -1.08, -0.95, 1, 0, 0, 0, -0.52, -0.95, 1, -0.52, -0.95, 1, 0, 0, 0]^\intercal$, and the manipulators at the final configuration are depicted in Fig. 3.3. The optimization parameters are chosen as $\hat{q}_k = 1000$, $Q = 0.01I_{18}$, $R = 20I_9$, and $S = 1I_{18}$.

Measurement of the system states for the feedback control law $\boldsymbol{u} = -\hat{K}\hat{\boldsymbol{x}}$ is performed such that for $\int_{t_0}^{t} \dot{\boldsymbol{p}}_{i,d} \mathrm{d}\tau$, $\dot{\boldsymbol{p}}_i^d$ is integrated in the controller and initial value $\dot{\boldsymbol{p}}_i^d(t_0)$ is defined by the motion capture system. The manipulator end-effector position $\boldsymbol{p}_i$ is captured and $\dot{\boldsymbol{p}}_i$ is its time

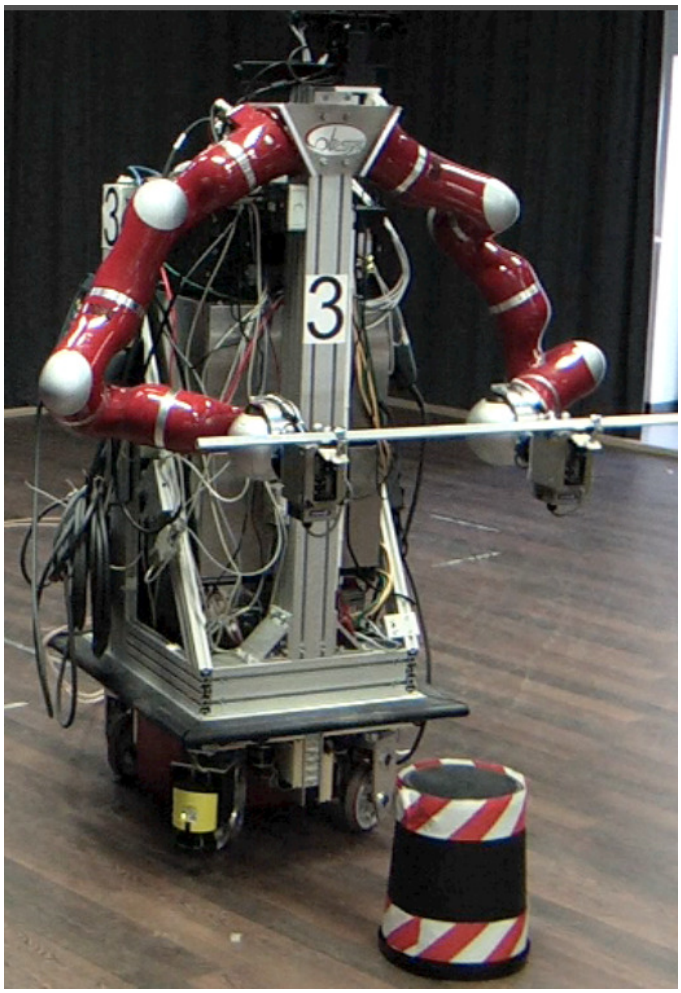

Figure 3.3: Two robotic manipulators hold a bar and reach a given goal configuration, whose centroid projection on the ground is marked by a striped object. Note that the two manipulators are independently controlled; the mounting on a single mobile platform prevents effects from kinematic and calibration uncertainties in the experiments.

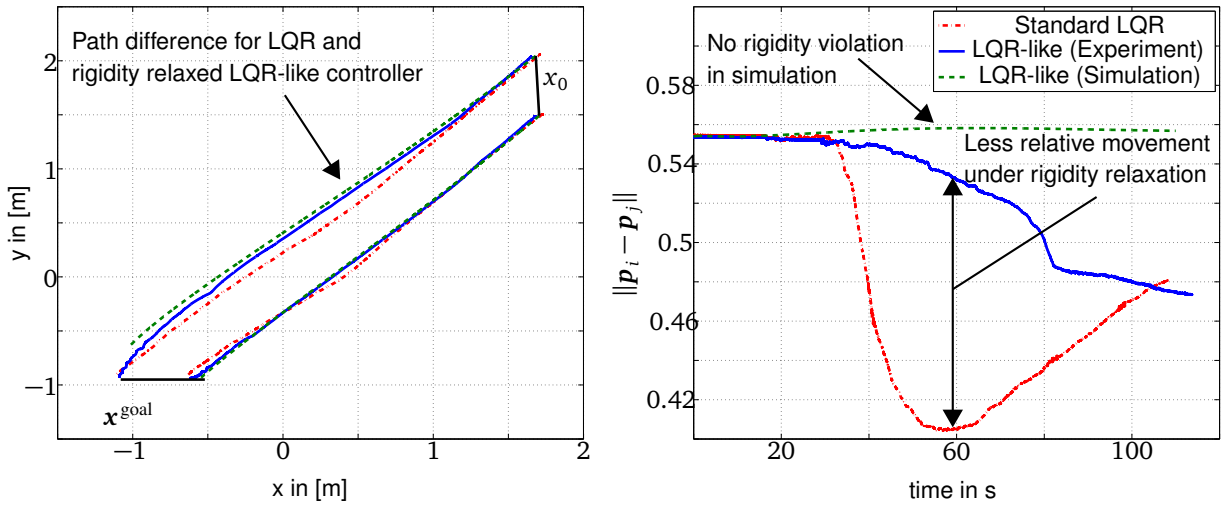

Figure 3.4: Multi robot trajectories for standard LQR, biquadratic LQR-like problem in simulation and full-scale experiment without bar.

derivative.

With these parameters, we conduct an experiment in our laboratory and compare the results to a controller derived by the standard LQR implementation `lqr` of *MATLAB/Simulink* with the weighting matrizes $Q = 1$, $R = 1000$ in accordance with cost function (3.7). The experimental result discussed later are obtained from a typical run, i.e. not from the aggregation of repeated experiments. In our experience the difference between two runs converging from equal $\boldsymbol{x}_0$ to $\boldsymbol{x}_e$ is only marginal.

Results: Manipulators without Rigid Link

In the first experiment, the robotic manipulators are driven to the final configuration without any rigid object in between the manipulators. In this scenario, we want to investigate if the multi-robot team maintains the formation in the experiment. Fig. 3.4 on the right shows the manipulator path from top view. The multi-robot team controller under rigidity relaxation according to (3.11) in a full-scale experiment is depicted in blue solid, the multi-robot team controller under LQR-like rigidity relaxation in simulation is depicted in green dashed, and the standard LQR controlled system according to (3.7) in red dashed-dotted. A good match between simulation and experiment is achieved in this setup. Both controllers regulate the multi-robot setup to the desired final configuration $\boldsymbol{x}^{goal}$. However, half way to the goal there is a deviation between the rigidity-relaxed LQR-like and standard LQR. Our rigidity-relaxed controller approaches the goal configuration not in a direct way, but it maintains its formation. Since our controller takes the formation explicitly into account, it achieves far better results for multi-robot cooperation compared to a problem setup without rigidity constraints.

Results: Manipulators with Rigid Link

In addition to the previous results a rigid link in terms of a bar is fixed to the manipulators in order to evaluate the occurring internal forces. Internal forces are calculating by means of (2.30).

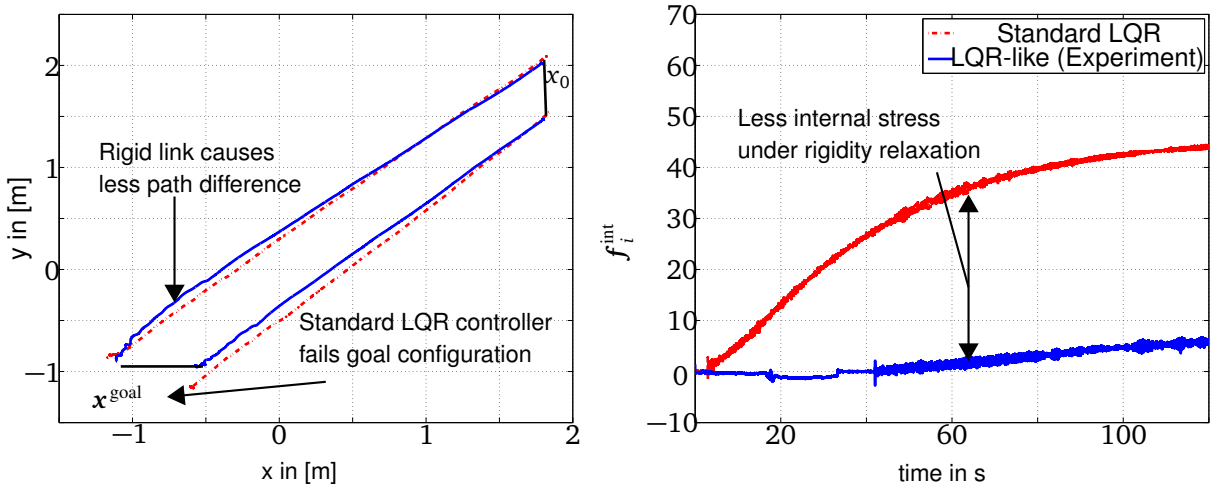

Figure 3.5: Multi robot trajectories for standard LQR, biquadratic LQR-like problem in simulation and full-scale experiment with bar and internal force f_i^{int}.

In Fig. 3.5 the LQR controlled system under rigidity relaxation according to (3.11) is depicted in solid blue line, the system controlled by standard LQR according to (3.7) is depicted in a dashed red line. A difference in both paths occurs, however it is not as strong as in the previous section due to the rigidity of the bar. However, the standard LQR controlled system is unable to attain the goal configuration. We assume that this is due to the rigid link which causes high effort in a rotation of the object.

Additionally, the internal force f_i^{int} along the rigid link, the only virtual linkage in a bimanual robot team, is analyzed, see Fig. 3.5. Internal forces on the object are heavily reduced with a suboptimal controller under rigidity constraints. In the full-scale experiment, a light chattering of the robotic manipulator occurred due to a non-perfect following of the platform. We assume that this causes the formation violation between the two manipulator end-effector positions for the real-world scenario compared to the simulation results on the right side of Fig. 3.4.

3.4 Coupling Dynamic Movement Primitives (DMPs) for Synchronized Movements

In this section an approach is presented to couple generalized motor actions in order to accomplish a cooperative manipulation task. As movement primitive-based control of robotic manipulators is used to generalize individual stereotypical motions it is challenging to interconnect the movement primitives in order to ultimately satisfy the formation constraints at hand. So compared to the previous sections we investigate here how to additionally *establish and preserve* the formation between manipulators resulting from geometric constraints in physical object manipulation or the synchronization of movements. In order to accommodate for minor deviations of the desired position trajectories from the formation constraints we propose to employ impedance control as described in Chapter 2 here. Note here that again only the translational movements of the impedance control laws are actively controlled since the later proposed coupling between the DMPs is based on a distance-based formation control approach. Distance-based formation control

is invariant to rotations and so we can impose a rotation on the object without actively controlling the rotations of the manipulators. For the rotational motion of the end-effector we either mount unactuated joints along the orientations on each end-effector or the rotational stiffness, damping, and mass are tuned such that we attain a gravity compensation-like motion for all rotational end-effector motions.

3.4.1 DMP - a Tool for Generalized Trajectory Presentation

DMPs provide a generalized trajectory generation framework for generating both discrete and periodic movements of a robotic manipulator. DMPs are able to steer desired set-points $\boldsymbol{p}_i^d$ from an initial position $\boldsymbol{p}_i^d(t_0)$ to a goal position $\boldsymbol{p}_i^{\text{goal}}$. DMPs can represent complex movements and are capable of incorporating state feedback in real-time [114]. The following attractor dynamic ensures that the solution of the attractive dynamical system, the trajectory $\boldsymbol{p}_i^d(t)$, converges towards the goal $\boldsymbol{p}_i^{\text{goal}}$ [115]

$$\tau \dot{\boldsymbol{z}}_i = \alpha_i(\beta_i(\boldsymbol{p}_i^{\text{goal}} - \boldsymbol{p}_i^d) - \boldsymbol{z}_i) + \boldsymbol{f}_i(s_i), \tag{3.17}$$

$$\tau \dot{\boldsymbol{p}}_i^d = \boldsymbol{z}_i, \tag{3.18}$$

where the nonlinearity $\boldsymbol{f}_i(s)$ is defined as

$$\boldsymbol{f}_i(s_i) = \frac{\sum_{k=1}^{W} w_k \Psi_k(s_i)}{\sum_{k=1}^{W} \Psi_k(s_i)} s_i, \; \Psi_k(s_i) = \exp\left(-h_k (s_i - b_k)^2\right), \tag{3.19}$$

where w_k, b_k, h_k are the weights, the centers and the radii, respectively, of the radial basis function distributed along the trajectory. Those parameters are determined during the learning process using Locally Weighted Projection Regression (LWPR) [116]. The number of basis functions W is also determined by LWPR. The parameters $\alpha_i, \beta_i > 0$ are adjusted prior to the learning process. To speed the movement up or slow it down the timing parameter $\tau > 0$ is set before the execution of the movement. A phase variable s_i is introduced in (3.19) instead of the time t to obtain an implicit dependency of $\boldsymbol{f}_i(s_i)$ on time [115]. By definition the dynamics of the phase variable s_i evolves according to a canonical system given by

$$\tau \dot{s}_i = -\gamma s_i, \qquad \gamma > 0. \tag{3.20}$$

The advantage of using the phase variable s_i instead of explicit time is that we are able to modify the evolution of time by appropriately adapting (3.20) during execution [115]. Thus by decelerating the canonical system, the execution of the steering function $\boldsymbol{f}_i(s_i)$ is slowed down and the speed of the robot motion can be reduced when necessary, e.g. in case of disturbances. Obviously, we have $s_i \to 0$ as $t \to \infty$ and therefore the nonlinear function $\boldsymbol{f}_i(s_i)$ defined in (3.19) converges to zero as time increases. Thus, the equilibrium point of the point attractor system (3.17) and (3.18) is asymptotically stable and it is given by

$$\begin{bmatrix} \boldsymbol{z}^* & \boldsymbol{p}_i^{d*} \end{bmatrix} = \begin{bmatrix} \boldsymbol{0} & \boldsymbol{p}_i^{\text{goal}} \end{bmatrix}.$$

As a result trajectories of the desired set-point $\boldsymbol{p}_i^d(t)$ generated by DMPs ensure the discrete movement from the initial point $\boldsymbol{p}_i^d(t_0)$ to the goal $\boldsymbol{p}_i^{\text{goal}}$. Furthermore, we can also employ DMPs to generate trajectories for periodic movements. In contrast to discrete movements the steering function $\boldsymbol{f}_i$ will not approach zero because it is a weighted sum of periodic functions $\Gamma_k(\phi_i)$ multiplied by the amplitude r of the oscillation as

$$\boldsymbol{f}_i(\phi_i) = \frac{\sum_{k=1}^{W} w_k \Gamma_k(\phi_i)}{\sum_{k=1}^{W} \Gamma_k(\phi_i)} r, \Gamma_k(\phi_i) = \exp\left(-h_k\left(cos(\phi_i - b_k) - 1\right)\right).$$

The function $\boldsymbol{f}_i(\phi_i)$ is used to modify the dynamics of the basic second-order system (3.17) and (3.18) similar to [117]. Rewriting (3.17) and (3.18) where the frequency of the oscillation is given by $\Omega = 1/\tau$ yields

$$\begin{aligned} \dot{\boldsymbol{z}}_i &= \Omega(\alpha_i(\beta_i(\boldsymbol{p}_i^{\text{goal}} - \boldsymbol{p}_i^d) - \boldsymbol{z}_i) + \boldsymbol{f}_i(\phi_i)), \\ \dot{\boldsymbol{p}}_i^d &= \Omega \boldsymbol{z}_i. \end{aligned}$$

For periodical movements, the phase variable ϕ_i increases constantly as opposed to s_i and is given by

$$\dot{\phi}_i = \Omega.$$

To ensure that the DMP-generated trajectories match the geometry of the object a formation control feedback is introduced for each DMP to mirror the physical linkage.

3.4.2 Feedback Control of DMPs for Cooperative Manipulation

The goal is to introduce a novel approach which generates cooperative and coordinated movements of N manipulators in a n-dimensional workspace by a DMP-based formation control approach. For the proposed control law, rotational motions of each manipulator are not actively controlled and are thus neglected so that the DMPs are represented by decoupled dynamics for each Cartesian degree of freedom (DoF). Note that we can still rotate the object without actively controlling the manipulator orientations.

For generating the set-points for each robotic manipulator we use a single point attractive system (3.17), (3.18) and one canonical system (3.20). Here, $\boldsymbol{p}_i^d$ denotes the set-point of the manipulator i which is the input to the impedance-controlled manipulator dynamics (3.1). The set-points of all manipulators are concatenated into $\boldsymbol{p}^d = [\boldsymbol{p}_1^{d\intercal}, \ldots, \boldsymbol{p}_N^{d\intercal}]^\intercal$. The desired trajectory $\boldsymbol{p}^d, \dot{\boldsymbol{p}}^d$ which are generated by N DMPs and tracked by the impedance-based control law (3.1) requires to satisfy the constraint (2.35) among the cooperating manipulators. Note that (2.35) defines the desired displacement between any two manipulators. Applying the Euclidean norm for (2.35) yields a desired distance between any two manipulators given by

$$\|\boldsymbol{p}_i^d - \boldsymbol{p}_i^d\| = d_{ij}, \tag{3.21}$$

where $d_{ij} = \|\boldsymbol{d}_{ij}\| \in \mathbb{R}$ is the desired distance. The goal configuration $\boldsymbol{p}^{\text{goal}}$ is an accordingly concatenated vector. Since each DMP only knows its own state, we establish a communication

link between neighboring DMPs and employ a cooperative term to modify the individual states. A DMP is denoted as a neighbor of another DMP if rigidity of the formation requires a desired distance to be maintained. Here, each DMP relies on the relative position to its neighbors and is attractive to the desired formation even under external disturbances. The graph representing the communication structure among the systems of DMPs which is formulated by the neighboring set is chosen such that rigidity of the formation is guaranteed, preferably using a minimum number of neighbors. For more details on formation rigidity the reader is referred to [118].

In order to employ DMPs in a cooperative manipulation task the ability of DMPs to react to the movements of other manipulators is important. To facilitate this a feedback term for cooperation is introduced for DMPs. Our approach is inspired by [99] where DMPs are enhanced to react to external perturbations. According to [114] the point attractive system (3.17) and (3.18) can be augmented to incorporate real-time feedback as follows

$$\begin{aligned}\tau\dot{\boldsymbol{z}} &= \alpha_i(\beta_i(\boldsymbol{p}_i^{\text{goal}} - \boldsymbol{p}_i^d) - \boldsymbol{z}_i) + \boldsymbol{f}_i(s_i),\\ \tau\dot{\boldsymbol{p}}_i^d &= \boldsymbol{z} + \alpha^{\text{err}}(\boldsymbol{p}_i - \boldsymbol{p}_i^d),\end{aligned}$$

where $\boldsymbol{p}_i$ denotes the actual measured position of the ith manipulator and $\boldsymbol{p}_i^d$ is the desired position. The slowing of the phase variable s_i until the error is reduced is a key feature of this approach. Note that the phase variable s_i directly controls the steering function $\boldsymbol{f}_i(s_i)$, which also decelerates proceeding until the error is compensated. According to [117] the canonical system is augmented to

$$\tau\dot{s}_i = -\frac{\gamma s_i}{1 + \gamma^{\text{err}}(\|\boldsymbol{p}_i - \boldsymbol{p}_i^d\|^2)}.$$

In the following we propose to replace the error term by a feedback term which establishes the desired distances among the robots by a formation control law. Here, a deviation of the relative distance between the set-points of any two neighbors $\|\boldsymbol{p}_i^d - \boldsymbol{p}_j^d\|$ from the desired distance d_{ij} is interpreted as an error term and is compensated before further proceeding to the goal. The point attractive system and the canonical system of manipulator i is reformulated as

$$\tau\dot{\boldsymbol{z}}_i = \alpha_i(\beta_i(\boldsymbol{p}_i^{\text{goal}} - \boldsymbol{p}_i^d) - \boldsymbol{z}_i) + \boldsymbol{f}_i(s_i), \tag{3.22}$$

$$\tau\dot{\boldsymbol{p}}_i^d = \boldsymbol{z}_i + \kappa_i \boldsymbol{c}_i(\boldsymbol{p}^d), \tag{3.23}$$

$$\tau\dot{s}_i = -\frac{\gamma_i s_i}{1 + \eta_i \|\boldsymbol{c}_i(\boldsymbol{p}^d)\|^2}, \tag{3.24}$$

where η_i and κ_i are both positive weighting parameters for the cooperation term $\boldsymbol{c}_i(\boldsymbol{p}^d)$ which is defined as follows. A common approach to ensure (3.21) is a formation control approach using an Artificial Potential Field (APF) which achieves a desired distance d_{ij} between two agents i and j [33]. Often a quadratic potential field $V_{ij}\left(\|\boldsymbol{p}_i^d - \boldsymbol{p}_j^d\|\right)$ is considered which has its global minimum at the desired distance d_{ij} as follows

$$V_{ij}\left(\|\boldsymbol{p}_i^d - \boldsymbol{p}_j^d\|\right) = \frac{1}{2}\left(\|\boldsymbol{p}_i^d - \boldsymbol{p}_j^d\| - d_{ij}\right)^2.$$

For the cooperation term we use the gradient of the potential field for formation control as

$$\begin{aligned} \boldsymbol{c}_i(\boldsymbol{p}^d) = &= -\sum_{j\in N_i} \delta_{ij} \frac{\partial V_{ij}\left(\|\boldsymbol{p}_i^d - \boldsymbol{p}_j^d\|\right)}{\partial \boldsymbol{p}_i^d} \\ &= -\sum_{j\in N_i} \delta_{ij} \frac{\boldsymbol{p}_i^d - \boldsymbol{p}_j^d}{\|\boldsymbol{p}_i^d - \boldsymbol{p}_j^d\|}(\|\boldsymbol{p}_i^d - \boldsymbol{p}_j^d\| - d_{ij}), \end{aligned} \tag{3.25}$$

where δ_{ij} is a positive parameter that is used to adjust the speed of convergence to the desired formation. Under this control law all agents converge to the desired formation [86].

Thus, the cooperation term is zero if the desired distances to all neighbors are maintained and (3.22), (3.23), (3.24) are equivalent to the original DMPs from (3.17) , (3.18) and (3.20), respectively. In case $\boldsymbol{c}_i(\boldsymbol{p}^d)$ increases the canonical system is decelerated and the steering function is delayed. Through $\boldsymbol{c}_i(\boldsymbol{p}^d) \neq \boldsymbol{0}$, an additional acceleration on the point attractive system is acting, which tends to restore the desired distance.

By choosing the parameters η_i and κ_i such that $\eta_i, \kappa_i \gg 1, \forall i$, we ensure an improved maintenance of the formation which comes at a cost of a stretched convergence time to reach the goal $\boldsymbol{p}_i^{\text{goal}}$. If the inter-robot distances diverge from the desired ones, a larger η_i decelerates the canonical systems and consequently the execution of the steering functions. Increasing κ_i enables a prompt reaction of the point attractive systems to disturbances of the desired inter-robot distances. Given this enhancement, DMPs are applicable for a cooperative manipulation task or the generation of synchronized periodic movement. A task plan provides the goal configurations $\boldsymbol{p}^{\text{goal}}$ and the inter-robot distances d_{ij} determined by the object geometry. The individual desired trajectories are generated by DMPs and then tracked by the impedance. A cooperative feedback term is introduced to enforce the desired distance by a formation control law.

Equilibria and Domain of Attraction

As the point attracting system (3.22) and (3.23) and the canonical system (3.24) are modified we investigate the equilibria of the attractor landscape of the augmented system. Analogously to the argumentation in [99], the stability properties of the canonical system are preserved, i.e. the equilibrium $s_i^* = 0$ of (3.24) is asymptotically stable and derived from

$$\tau \dot{s}_i^* = -\frac{\gamma_i s_i^*}{1 + \eta_i \|\boldsymbol{c}_i(\boldsymbol{p}^{d*})\|^2} \stackrel{!}{=} 0 \rightarrow s_i^* = 0 \ \forall i,$$

where we implicitly assume that $\|c_i(\boldsymbol{p}^d)\| \neq \infty$. Recalling the definition of the nonlinear function $\boldsymbol{f}_i(s_i)$ in (3.19), it is obvious that $\boldsymbol{f}_i(s_i) \rightarrow 0$ for $s_i \rightarrow 0$. Hence, the equilibrium point of systems (3.22) and (3.23) is derived using

$$\tau \dot{\boldsymbol{z}}_i^* = \alpha_i(\beta_i(\boldsymbol{p}_i^{\text{goal}} - \boldsymbol{p}_i^{d*}) - \boldsymbol{z}_i^*) \stackrel{!}{=} 0, \tag{3.26}$$

$$\tau \dot{\boldsymbol{p}}_i^{d*} = \boldsymbol{z}_i^* + \kappa_i \boldsymbol{c}_i(\boldsymbol{p}^{d*}) \stackrel{!}{=} 0. \tag{3.27}$$

From (3.27) we conclude that $\boldsymbol{z}_i^* = -\kappa_i \boldsymbol{c}_i(\boldsymbol{p}^{d*})$. Using this for $\boldsymbol{z}_i^*$ in (3.26) we obtain the following equilibria

$$\boldsymbol{p}_i^{d^*} = \boldsymbol{p}_i^{\text{goal}} + \frac{\kappa_i}{\beta_i}\boldsymbol{c}_i(\boldsymbol{p}^{d^*}) \;\; \forall i. \tag{3.28}$$

For illustration we the equilibria for $N = 2$ agents are computed. The computation of the equilibria for $N > 2$ agents from (3.28) is performed in a similar fashion. For the sake of simplicity of the subsequent analysis we assume $\beta_i = \kappa_i = 1$ and $\delta_{ij} = 1, \forall i, j$. Using $d_{12} = d_{21} = \|\boldsymbol{p}_1^{\text{goal}} - \boldsymbol{p}_2^{\text{goal}}\|$, (3.28) results in $\boldsymbol{p}_1^{d^*} = \boldsymbol{p}_1^{\text{goal}} - (\boldsymbol{p}_1^{d^*} - \boldsymbol{p}_2^{d^*})\left(1 - \frac{\|\boldsymbol{p}_1^{\text{goal}} - \boldsymbol{p}_2^{\text{goal}}\|}{\|\boldsymbol{p}_1^{d^*} - \boldsymbol{p}_2^{d^*}\|}\right)$ and $\boldsymbol{p}_2^{d^*} = \boldsymbol{p}_2^{\text{goal}} - (\boldsymbol{p}_2^{d^*} - \boldsymbol{p}_1^{d^*})\left(1 - \frac{\|\boldsymbol{p}_1^{\text{goal}} - \boldsymbol{p}_2^{\text{goal}}\|}{\|\boldsymbol{p}_2^{d^*} - \boldsymbol{p}_1^{d^*}\|}\right)$. As a result we obtain the desired equilibrium

$$\boldsymbol{p}_1^{d^*} = \boldsymbol{p}_1^{\text{goal}}, \quad \boldsymbol{p}_2^{d^*} = \boldsymbol{p}_2^{\text{goal}},$$

and an undesired equilibrium

$$\boldsymbol{p}_1^{d^*} = \boldsymbol{p}_2^{\text{goal}} + \frac{1}{3}\left(\boldsymbol{p}_1^{\text{goal}} - \boldsymbol{p}_2^{\text{goal}}\right), \quad \boldsymbol{p}_2^{d^*} = \boldsymbol{p}_2^{\text{goal}} + \frac{2}{3}\left(\boldsymbol{p}_1^{\text{goal}} - \boldsymbol{p}_2^{\text{goal}}\right).$$

In the desired equilibrium the agents have attained their goal positions $\boldsymbol{p}_1^{\text{goal}}$ and $\boldsymbol{p}_2^{\text{goal}}$ which are formation consistent. In the undesired equilibrium the agents do not reach their goal positions and do not maintain the formation. The undesired equilibrium is approached if the two vector fields of goal attraction $\boldsymbol{p}_i^{d^*} - \boldsymbol{p}_i^{\text{goal}}$ and cooperation term $\frac{\kappa_i}{\beta_i}\boldsymbol{c}_i(\boldsymbol{p}^{d^*})$ cancel each other out, which is illustrated in the top row of Fig. 3.6. A cancellation is possible if the vectors are linearly dependent

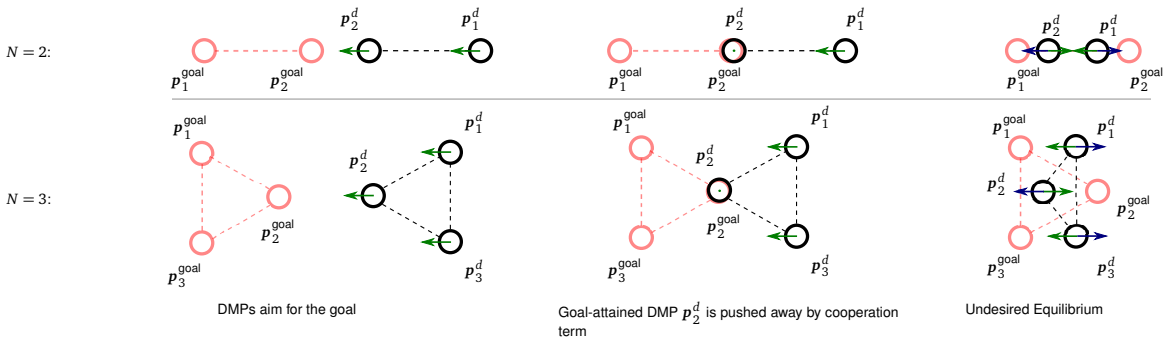

Figure 3.6: Top: Two manipulator set-points $\boldsymbol{p}_1^d, \boldsymbol{p}_2^d$ approach the goal configurations $\boldsymbol{p}_1^{\text{goal}}, \boldsymbol{p}_2^{\text{goal}}$ along the domain of attraction in opposite sequence to the goals. In the middle column, manipulator $\boldsymbol{p}_2^d$ reaches its goal position $\boldsymbol{p}_2^{\text{goal}}$ first, but $\boldsymbol{p}_1^d$ endeavors to reach goal $\boldsymbol{p}_1^{\text{goal}}$ which is $2d_{12}$ away. Due to the virtual coupling force of the cooperation term, $\boldsymbol{p}_1^d$ gets pushed away until both manipulators reach the undesired equilibrium in balance. Bottom: One undesired equilibrium for three manipulators .

and point in opposite directions. This explanation also provides an intuitive understanding of the domain of attraction of the undesired equilibrium. The domain of attraction describes the subspace, from which the agents start and can end up in an undesired equilibrium. In example

above with two agents the domain of attraction of the undesired equilibrium is given by a a line through the goal configurations with both agents being in switched configuration (compared to the goal positions). Note that for a larger number of agents the domain of attraction of the undesired equilibrium is complicated than a line. For practical application the undesired equilibrium is largely irrelevant as small perturbations allow the agents to escape this domain. For $N = 3$ one undesired equilibrium is illustrated in the bottom row of Fig. 3.6. In case of more agents the approach is similar, however the undesired equilibria and their domain of attraction is more complicated to compute; its formal analysis is still part of ongoing research.

3.4.3 Experimental Validation

Experimental Setup

The experimental setup consists of two commercially available KUKA LWR 4+ (light-weight robot), see Fig. 3.3. Both manipulators are assembled on top of the same mobile platform in order to avoid issues such as communication and kinematic uncertainties. Further details on the robots can be found in Appendix C. A Cartesian impedance control scheme (2.8) is employed to ensure compliance of the end-effectors. Both Cartesian positions are captured by a QualiSys motion capture system at a frequency of 350 Hz. Further details on the Qualisys motion capture system can be found in Appendix C. A workspace extension by a mobile platform of both robotic manipulators is accomplished according to the approach presented in Sec. 2.3.2 similar to [1]. The manipulator motion and the mobile platform motion are kinematically decoupled in task-space by employing an aritificial potential function. The experimental result discussed later are obtained from a typical run, i.e. not from a perfect or aggregated run. Except for occasional hardware failures the difference between two runs is only marginal in our experience. The parameters for DMPs are chosen equally for each manipulator in all dimensions as exhibited in Table 4.1 distinguished in discrete and periodic movements.

	Eq.	Discrete Movement	Periodic movement
Attractor system	(3.22)	$\alpha_i = 5,\ \beta_i = 0.01,\ \forall i$	
Canonical system	(3.24)	$\gamma_i = 0.01,\ \forall i$	
Time scaling	(3.23)	$\tau = 20\frac{1}{s}$	$\Omega = 1s$
Cooperation weight with cooperation	(3.23),(3.24)	$\eta_i = \kappa_i = 10$	$\eta_i = \kappa_i = 1$
Cooperation weight without cooperation	(3.23),(3.24)	$\eta_i = \kappa_i = 0,\ \forall i$	
Impedance parameters	(3.1)	$M = 10I_3, D = 120I_3, K = 160I_3$	

Tabular 3.3: Control parameters used in experiments.

Discrete Movement in Cooperative Manipulation

The objective of this first task is to demonstrate that cooperating DMPs maintain the formation in case of disturbances and compensate the deviations caused by other robotic manipulators. For this experiment, the robot performs a planar cooperative manipulation task with two end-effectors.

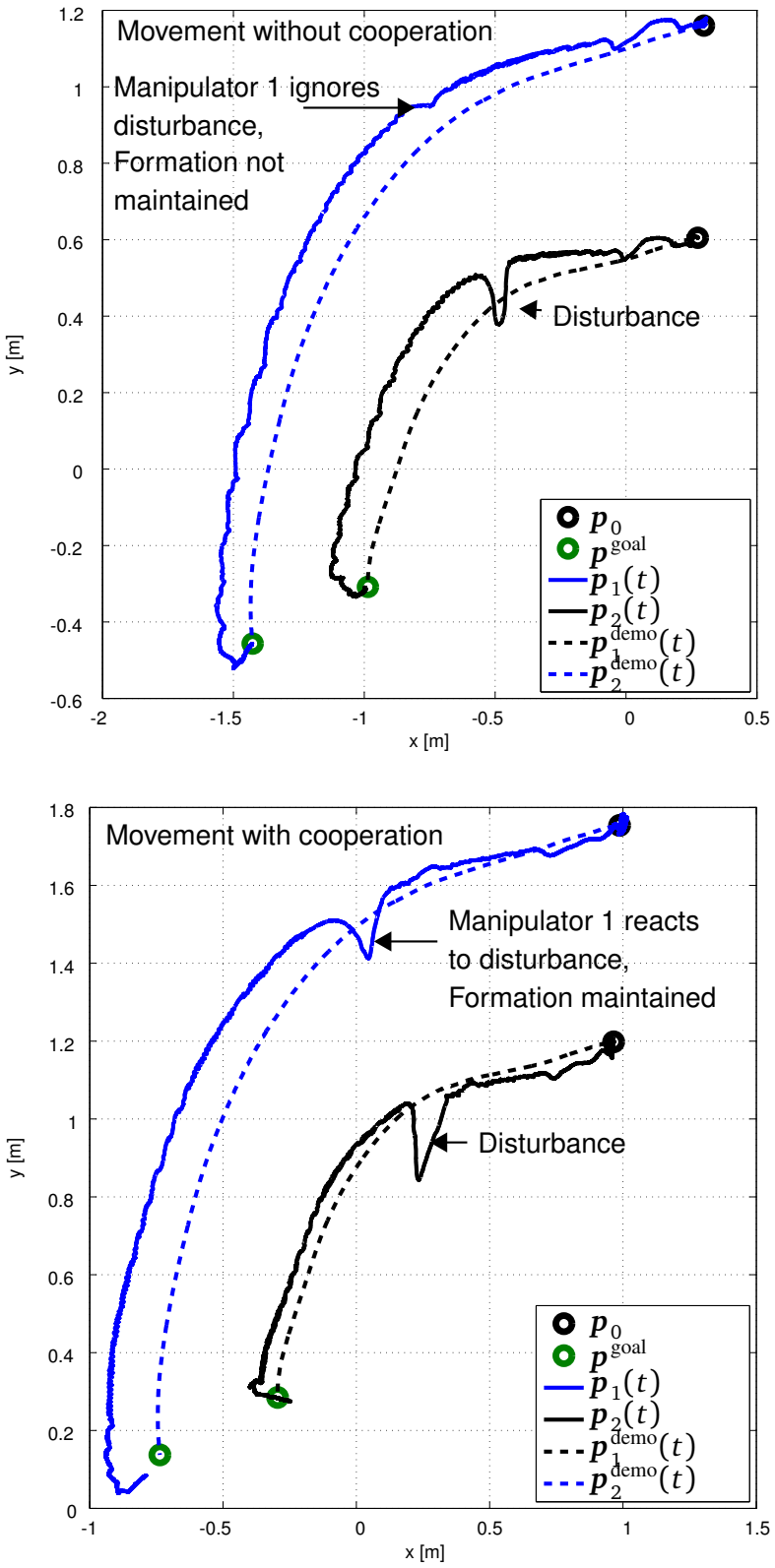

Figure 3.7: Multi-robot trajectories of the end-effectors in 2D space tracking a trajectory. Without cooperation a disturbance acting on one manipulator has no effect on the other. In cooperation both manipulators are virtually coupled.

The desired trajectory $\boldsymbol{p}^{\text{demo}}$ is generated from demonstrations by LWPR [116]. The task is to carry a beam from an initial to a final configuration, i.e. a discrete movement. In order to demonstrate the efficacy of our proposed approach, we remove the beam between the manipulators and identify the effect of cooperation without physical coupling. To visualize this effect more explicitly we employ the measured position $\boldsymbol{p}$ in (3.25) instead of the desired ones $\boldsymbol{p}^d$. During the movement a disturbance is imposed on one robotic manipulator by pushing against it. Due to the impedance control law the manipulator deviates from the desired trajectory $\boldsymbol{p}_2^d$. The results of this experiment are shown in Fig. 3.7. It is obvious that a disturbance acting on manipulator has no effect on the other one if cooperation feedback is turned off, i.e. $\eta_i = 0, \kappa_i = 0, \forall i$. When the cooperation feedback is turned on, i.e. $\eta \neq 0, \kappa \neq 0, \forall i$, the disturbance affects both manipulators instantaneously and simultaneously. As desired, the formation is restored by the cooperative DMP approach.

Motion Synchronization

The second experiment investigates the idea of cooperating DMPs for periodic movements. For this experiment both manipulators oscillate in phase with the same frequency and amplitude in one direction. During this experiment we turn the formation feedback on ($\eta_i \neq 0, \kappa_i \neq 0, \forall i$) and off ($\eta_i = 0, \kappa_i = 0, \forall i$) and observe the synchronization of two manipulators after being out of phase. We simulate a disturbance on one of the manipulators by fixing it manually for a short time. With this experiments, we demonstrate that disturbances acting on one of the manipulator also affect the trajectories of the other manipulator.

The results of this experiment with and without cooperation are shown in Fig. 3.8. After one cycle ($\approx 8s$) the cooperation is turned off and the two manipulators are drifting apart. At $t \approx 18s$ manipulator 1 is fixed at its current position manually, simulating a disturbance. After it is released at $t \approx 22s$ it keeps oscillating but the two manipulators are not in phase. So at $t \approx 26s$ the cooperation is turned on again and a both manipulators are synchronizing.

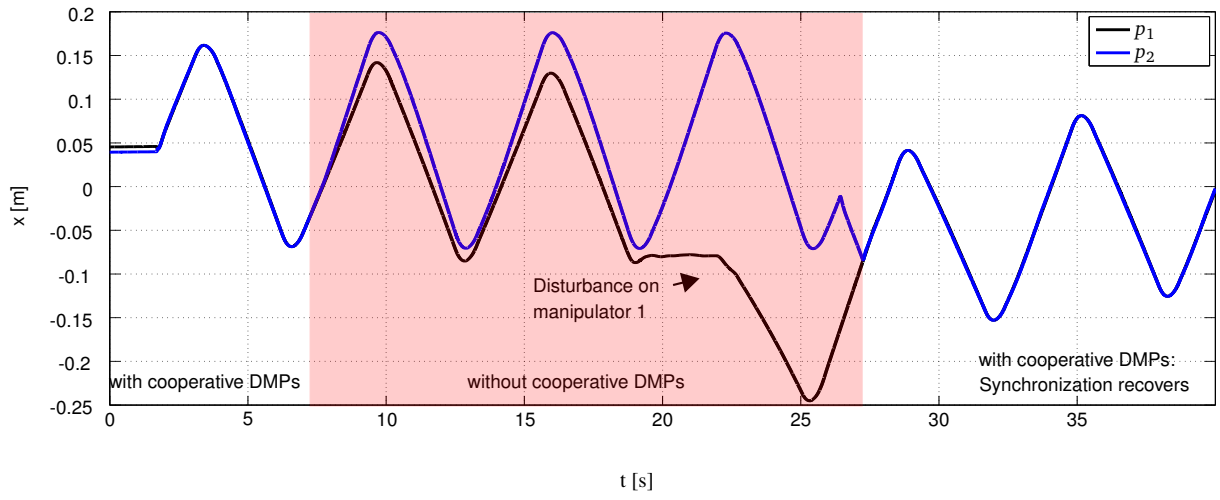

Figure 3.8: Synchronization of two manipulators performing a periodic movement.

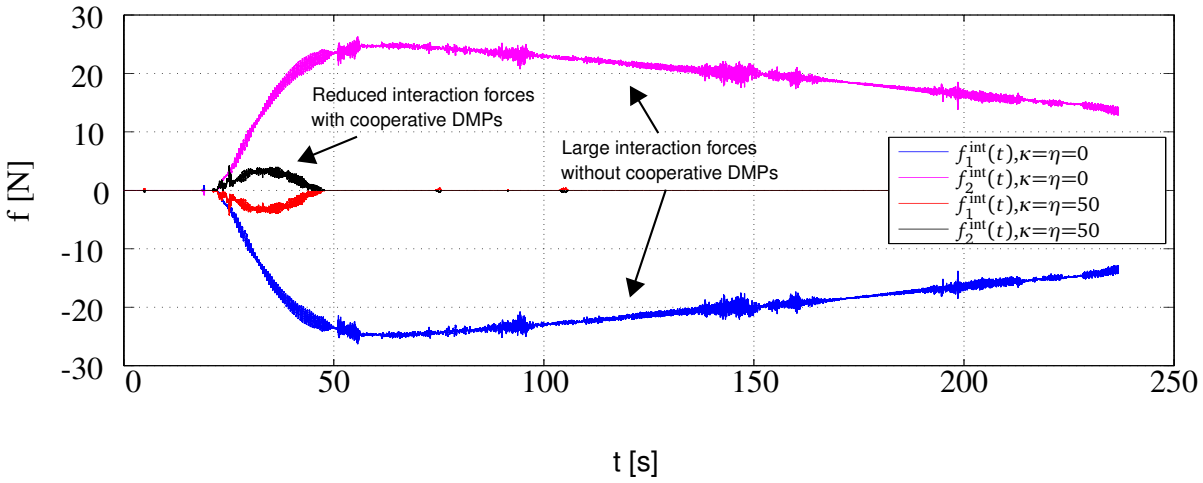

Figure 3.9: Internal forces are significantly reduced during a manipulation with cooperation.

Reducing internal forces

In a further experiment we show the reduction of internal forces acting on the object. In this experiment both manipulators follow a discrete movement. A beam is fixed but rotationally free at the manipulators. For the discrete movement individual trajectories are generated using DMPs which violate the formation constraint. Internal forces are calculating by means of (2.30).

Using DMPs without cooperation results in significant internal forces acting on the object because both manipulators follow trajectories that deviate from the desired formation. Due to impedance control the deviation causes a force on the object defined by (2.8). Using cooperative DMPs the trajectories are adjusted such that they match the desired formation. As desired, this results in reduction of forces acting on the object as shown in Fig. 3.9.

The approaches previously presented in Sections 3.3 and 3.4 employed a distance-based formation control law in order to coordinate the particular set-points. From now one we now focus on a displacement-based approach for cooperative manipulation.

3.5 Displacement-based Control for Cooperative Manipulation

From now on we employ a displacement-based approach to coordinate the particular end-effectors. A displacement-based coordination is not invariant to rotations, i.e. in order to control the rotation of the object we have to actively control both the translational and the rotational movement of each manipulator.

3.5.1 6 DoF Set-Point Generator for Multiple Manipulators

Here, the motion and accordingly the desired positions $\boldsymbol{p}_i^d$ for each of the N manipulators need to be in compliance with the geometry of the object as discussed before. Then the desired trajectories are called geometrically consistent with the object geometry. Translational and rotational inputs which are geometrically consistent are previously defined in (2.35) and (2.36).

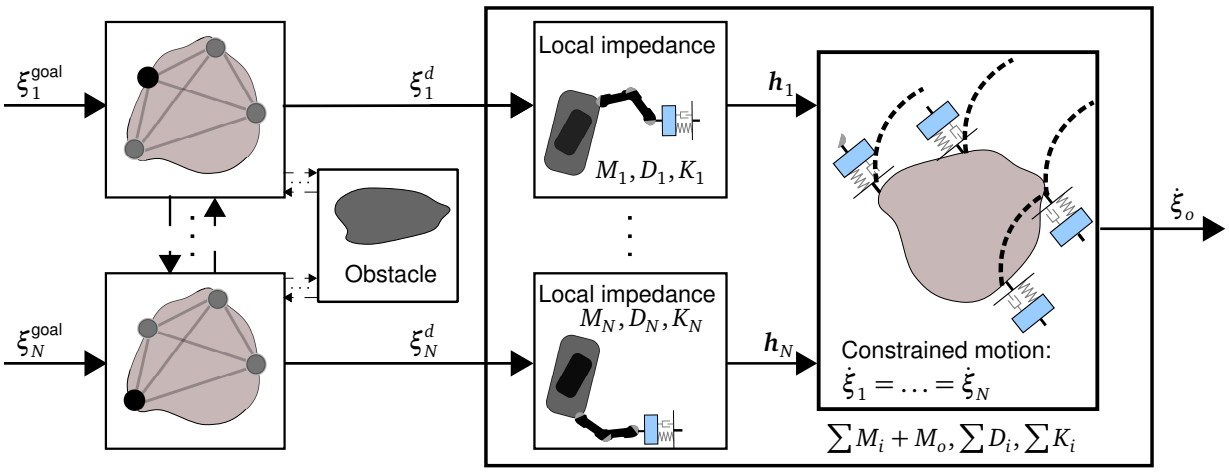

Figure 3.10: General control approach which facilitates a cooperative robotic manipulation task by means of a displacement-based coordination. The desired goal configuration ξ_i^{goal} clearly determines the desired poses ξ_i^d of impedance-controlled manipulators and influences the actual position ξ. Since the impedance-controlled manipulators are rigidly connected to the object, all of their positions move simultaneously: $\dot{\xi}_i = \dot{\xi}_j$. The position ξ_o of the cooperatively manipulated object is then specified by the interaction dynamics of multiple impedance-controlled manipulators.

The desired position $\boldsymbol{p}_i^d$ and the desired orientation $\boldsymbol{q}_i^d$ for the ith end-effector is the output of the formation control approach and by definition evolves according to

$$\begin{aligned} \dot{\boldsymbol{p}}_i^d &= \boldsymbol{u}_i, \\ \dot{\boldsymbol{q}}_i^d &= \frac{1}{2} U(\boldsymbol{q}_i^d)\boldsymbol{\omega}_i, \end{aligned} \tag{3.29}$$

where $\boldsymbol{u}_i \in \mathbb{R}^3$ is the translational system input. Here, $\frac{1}{2}U(\boldsymbol{q}_i^d)\boldsymbol{\omega}_i$ is the quaternion propagation as e.g. defined in [119] where the angular input is given by $\boldsymbol{\omega}_i$. Note here that for the translational motions of a manipulator, the dynamics $\dot{p}_{i,k}^d = u_{i,k}$ for each translational degree of freedom $k \in \{1,2,3\}$ is decoupled. In order to drive each manipulator to a desired final configuration $\xi_i^{\text{goal}} = \left[\boldsymbol{p}_i^{\text{goal}}, \boldsymbol{q}_i^{\text{goal}}\right]$ an feedback control law which considers the translational and rotational error between ξ_i^d and ξ_i^{goal} is required. Hence, we define the control law as

$$\begin{aligned} \boldsymbol{u}_i^{\text{goal}} &= -\left(\boldsymbol{p}_i^d - \boldsymbol{p}_i^{\text{goal}}\right), \\ \boldsymbol{\omega}_i^{\text{goal}} &= -U(\boldsymbol{q}_i^d)^{\intercal}\boldsymbol{q}_i^{\text{goal}}. \end{aligned}$$

Similarly, in order to account for the rigid formation which is to be maintained in a cooperative manipulation task we use (2.35) as a translational error term for the set-point of the ith manipulator w.r.t the jth manipulator as

$$\boldsymbol{e}_{ij}^p = \boldsymbol{p}_i^d - \boldsymbol{p}_j^d - \boldsymbol{d}_{ij}. \tag{3.30}$$

This formation is presented by a desired displacement $\boldsymbol{d}_{ij} = [d_{ij,1}, d_{ij,2}, d_{ij,3}]$ among the co-

operating manipulators i and j, which needs to be established and maintained throughout the complete task execution. Furthermore, the desired displacements $\boldsymbol{d}_{ij}$ have to be chosen to be *realizable* [120], i.e. there exist a $\boldsymbol{p}^{d*} = [\boldsymbol{p}_1^{d*}, \ldots, \boldsymbol{p}_N^{d*}] \in \mathbb{R}^{3N}$ such that $\boldsymbol{p}_i^{d*} - \boldsymbol{p}_j^{d*} = \boldsymbol{d}_{ij}, \ \forall(i,j)$. Note that the displacements are realizable when choosing them according to (2.35). Likewise the translational error term (3.30) a suitable orientation error for the unit quaternion representing the ith manipulator is given by

$$\boldsymbol{e}_{ij}^o = \eta_j^d \boldsymbol{\epsilon}_i^d - \eta_i^d \boldsymbol{\epsilon}_j^d - \boldsymbol{\epsilon}_i^d \times \boldsymbol{\epsilon}_j^d = -U(\boldsymbol{q}_i^d)^\intercal \boldsymbol{q}_j^d. \tag{3.31}$$

To minimize the translational error $\boldsymbol{e}_{ij}^p$ and the rotational error $\boldsymbol{e}_{ij}^o$ which is present between set-point i and any neighbor j we choose the input $\boldsymbol{u}_i$ of the translational movements to be $\boldsymbol{u}_i = \sum_{j \in N_i} \boldsymbol{e}_{ij}^p$ and the input $\boldsymbol{\omega}_i$ of the rotational movements to be $\boldsymbol{\omega}_i = \sum_{j \in N_i} \boldsymbol{e}_{ij}^o$. Hence, we can now formulate the feedback control law as follows

$$\boldsymbol{u}_i^{\text{fms}} = -\sum_{j \in N_i} \boldsymbol{e}_{ij}^p + S(\boldsymbol{d}_{io}) \boldsymbol{e}_{ij}^o, \tag{3.32}$$

$$\boldsymbol{\omega}_i^{\text{fms}} = -\sum_{j \in N_i} \boldsymbol{e}_{ij}^o, \tag{3.33}$$

where $S(\boldsymbol{d}_{io})\boldsymbol{e}_{ij}^o$ is the radial motion which is present for two set-points on a rigid body during a rotational motion. Note here that the displacement vector $\boldsymbol{d}_{io}$ determines the center of rotation. The desired displacement $\boldsymbol{d}_{ij}$ between i and j is transformed in the frame Σ_o as defined in (2.31). N_i describes the neighbors of agent i. In the following the set of neighborhood sets $\{N_1, \ldots, N_N\}$ is also called interaction topology.

Note that from a formation-control perspective, this approach is characterized as a displacement-based control approach [89] where the particular robots have to communicate the relative positions and quaternions to their neighbors. Under the control law (3.32) and (3.33) the desired robot positions and rotations converge to the desired formation only if the underlying interaction topology resulting from the N_is is connected or if there exists a spanning tree [89] which we address in the following assumption.

Assumption 3.4. The interaction graph describing the interaction topology is undirected and connected.

Remark 3.5. Graph theory is mostly used for large swarms with many agents. We will still employ this formalism here for the few agents as representation and standard results from graph theory can be carried over. Beneficially, by using the graph Laplacian matrix L, the latter proposed integration of the human into the formation can be expressed in a more convenient manner. The interested reader is referred to [90] and [121].

Remark 3.6. We propose to employ a formation control term to generate the desired manipulator trajectories $\boldsymbol{\xi}_i^d$. In general the multi-agent formation control can be differentiated between a distance-based, a displacement-based, and a position-based approach [89]. The displacement-based approach requires less advanced communication capabilities and less complex interaction topologies between the cooperating agents when compared to the distance-based approach. In a displacement-based approach the robots need to know the orientation of the world coordinate

system, but not their positions in the world coordinate system. For the sake of exposition we assume all desired positions $\boldsymbol{\xi}_i^d$ are expressed in a world coordinate system Σ_w which requires that each end-effector is aware of its rotation to that common reference frame. In comparison to a distance-based approach, where the coupling is bearing-like along all dimensions in $\mathbb{R}^3$, in a displacement-based approach more advanced sensing capabilities are required but the requirements on the interaction topology are less. All formation-based approaches are suitable for outdoor applications by using appropriate sensing technologies such as GPS or a compass.

Note here that the dynamical system (3.33) which determines the desired rotation $\dot{\boldsymbol{q}}_i^d$ only depends on the rotational error $\boldsymbol{e}_{ij}^o$. The dynamics of the translational set-point $\dot{\boldsymbol{p}}_i^d$ depend on the translational error $\boldsymbol{e}_{ij}^p$ itself but additionally they are influenced by the rotaional part $\boldsymbol{e}_{ij}^o$ due to the radial motion of the physically connected robots. Furthermore, we point out at this stage that the control laws (3.32) and (3.33) do not guarantee a so called collision avoidance [89] of the desired set-points among the manipulators. This is acceptable as a collision of two set-points results in no actual collision of the manipulators due to the rigid grasp. However, it violates the constraint (2.35) and therefore results in a corresponding internal force.

Now we are ready to discuss the benefits of employing the formation-based approaches (3.32) and (3.33) for generating the set-points $\boldsymbol{\xi}^d$ instead of using the kinematic relation between the ith end-effector and the object as for example defined in (2.19). Using (3.32) and (3.33) particular robotic set-points are able to react to other set-points. Hence, we are able to implicitly integrate autonomous and cognitive abilities in the particular robots in future work such as online reference adaptation or obstacle collision avoidance. Obstacle avoidance can for example be easily integrated for real-time applications in (3.32) by employing the gradient of a artificial potential field as proposed in [122] for each robot set-point as

$$U_i^{\text{obs}} = \begin{cases} \frac{1}{2}\left(\frac{1}{\|\boldsymbol{p}_i - \boldsymbol{p}_{\text{obs}}\|} - \frac{1}{d_i^{\text{obs}}}\right)^2 & \text{if } \|\boldsymbol{p}_i - \boldsymbol{p}_{\text{obs}}\| \leq d_i^{\text{obs}} \\ 0 & \text{if } \|\boldsymbol{p}_i - \boldsymbol{p}_{\text{obs}}\| > d_i^{\text{obs}}, \end{cases}$$

where $\|\boldsymbol{p}_i - \boldsymbol{p}_{\text{obs}}\|$ is the distance between the object position $\boldsymbol{p}_{\text{obs}} \in \mathbb{R}^3$ and the position $\boldsymbol{p}_i$ of robot i. Furthermore, $d_i^{\text{obs}} \in \mathbb{R}$ is the limit distance of the potential field influence. A control input which distributedly avoids obstacles is defined as

$$\boldsymbol{u}_i^{\text{obs}} = -\frac{\partial U_i^{\text{obs}}}{\partial \boldsymbol{p}_i}. \tag{3.34}$$

Addressing particular autonomous functionalities for each cooperating manipulator while still accomplishing the cooperative manipulation task is an interesting research question in this context. Using $\boldsymbol{u}_i = \boldsymbol{u}_i^{\text{goal}} + \boldsymbol{u}_i^{\text{fms}} + \boldsymbol{u}_i^{\text{obs}}$ for the total translational input and $\boldsymbol{\omega}_i = \boldsymbol{\omega}_i^{\text{goal}} + \boldsymbol{\omega}_i^{\text{fms}}$ for the total rotational input, the total set-point generator is given by

$$\begin{aligned} \dot{\boldsymbol{p}}_i^d &= -\left(\boldsymbol{p}_i^d - \boldsymbol{p}_i^{\text{goal}}\right) - \sum_{j \in N_i} \boldsymbol{e}_{ij}^p + S(\boldsymbol{d}_{io})\boldsymbol{e}_{ij}^o - \frac{\partial U_i^{\text{obs}}}{\partial \boldsymbol{p}_i}, \\ \dot{\boldsymbol{q}}_i^d &= -\frac{1}{2} U(\boldsymbol{q}_i^d) U(\boldsymbol{q}_i^d)^\intercal \boldsymbol{q}_i^{\text{goal}} - \sum_{j \in N_i} \frac{1}{2} U(\boldsymbol{q}_i^d) \boldsymbol{e}_{ij}^o, \end{aligned}$$

where the goal configuration ξ^{goal} is provided by an external task plan.

3.5.2 Numerical Investigation

In this subsection we want to illustrate the result of using the displacement based set-point generator for coordinating multiple manipulators. The goal of this numerical investigation is to demonstrate that a displacement-based set-point generator maintains the inter-robot distances in case of an additional obstacle avoidance task. For this investigation the $N = 4$ robots perform a planar cooperative manipulation task which includes an object rotation and an obstacle avoidance. There is a static object in the way of the robots around which the robots are required to drive simultaneously and efficiently. As a system we consider the initial end-effector poses $\xi_i(t_0)$ of the robotic manipulators to be

$$\xi_1(t_0) = [0.26, 1.2, 0, 1, 0, 0, 0], \quad \xi_2(t_0) = [0.26, 0.8, 0, 1, 0, 0, 0],$$
$$\xi_3(t_0) = [0.92, 0.8, 0, 1, 0, 0, 0], \quad \xi_4(t_0) = [0.92, 1.2, 0, 1, 0, 0, 0].$$

A global task plan provides particular goal configurations for each end-effector as

$$\xi_1^{\text{goal}} = \left[2.45, -1.24, 0, \frac{1}{\sqrt{2}}, 0, 0, -\frac{1}{\sqrt{2}}\right], \quad \xi_2^{\text{goal}} = \left[2.85, -1.24, 0, \frac{1}{\sqrt{2}}, 0, 0, -\frac{1}{\sqrt{2}}\right],$$
$$\xi_3^{\text{goal}} = \left[2.85, -0.58, 0, \frac{1}{\sqrt{2}}, 0, 0, -\frac{1}{\sqrt{2}}\right], \quad \xi_4^{\text{goal}} = \left[2.45, -0.58, 0, \frac{1}{\sqrt{2}}, 0, 0, -\frac{1}{\sqrt{2}}\right].$$

The position of the object is given by $\boldsymbol{p}_{\text{obs}} = [1.25, -0.25, 0]$ and the user-defined limit distance is given by $d_i^{\text{obs}} = 0.7$. The trajectory of the four manipulators in formation is depicted in Fig. 3.11. Due to the enhancement $\boldsymbol{u}_i^{\text{obs}}$ which is defined in (3.34), the particular set-points are able to perform a cooperative manipulation task and simultaneously avoid collision with the object. We can see that the control approach works well for all manipulators because the desired end points are reached, the obstacle is avoided and the manipulators maintain and restore their formation. In addition, due to state-feedback the cooperative avoidance is performed in real-time.

3.5.3 Internal Wrench Control

In a cooperative manipulation task the control of the internal forces is an elementary feature. In [30] an explicit description for resulting internal forces $\boldsymbol{h}^{\text{int}}$ is given by a projection of the set-points $\boldsymbol{p}_i^d$ and $\boldsymbol{q}_i^d$ onto the constraints which are defined in (2.23). In general, the desired internal wrench can be applied by using the following control signal in (2.33) as

$$\boldsymbol{h}^{\Sigma^*} = \boldsymbol{h}^{\Sigma} + \bar{A}^{\intercal}(\bar{A}M^{-1}\bar{A}^{\intercal})^{-1}(-\bar{A}M^{-1}\boldsymbol{h}^{\text{int},d} + \bar{b} - \bar{A}M^{-1}\boldsymbol{h}^{\Sigma}),$$

where $\boldsymbol{h}^{\text{int},d} \in \mathbb{R}^6$ denotes the desired internal force. Note here that substituting $\boldsymbol{h}^{\Sigma^*}$ for $\boldsymbol{h}^{\Sigma}$ in (2.33) straightforwardly shows that $\boldsymbol{h}^{\text{int}} = \boldsymbol{h}^{\text{int},d}$ and that the interaction dynamics (2.29) is not influenced by $\boldsymbol{h}^{\text{int},d}$. This has been proven in [30].

However by considering only translational movements and isotropic impedance parameters where $K = kI_N, D = dI_N, M = mI_N$ we can simplify the internal forces $\boldsymbol{f}^{\text{int}}$ following the

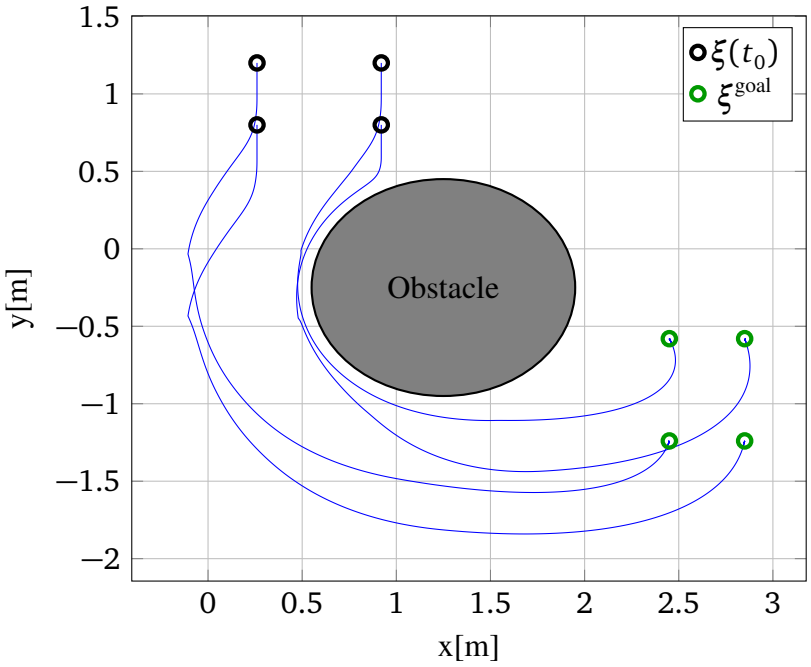

Figure 3.11: Four robotic set-points resembling a desired formation are driven from an initial configuration $\xi(t_0)$ to a desired final configuration ξ^{goal}. During the transit phase the set-points collectively avoid the collision with an obstacle.

argumentation from (2.38) as follows: $\boldsymbol{f}_i^{\text{int}} = k(\boldsymbol{e}_i - \bar{\boldsymbol{e}})$, where $\boldsymbol{e}_i = \boldsymbol{p}_i - \boldsymbol{p}_i^d$ and $\bar{\boldsymbol{e}}$ is the arithmetic mean of all $\boldsymbol{e}_i$: $\bar{\boldsymbol{e}} = \sum_{i=1}^{N} \frac{\boldsymbol{e}_i}{N}$. Often the task only requires to control a desired internal force acting on an object. In the following we introduce an approach to set a desired internal force $\boldsymbol{f}^{\text{int},d}$ with the set-point generator by altering the desired displacements $\boldsymbol{d}_{ij}$ among the physically cooperating robots. The idea here is to employ a desired displacements $\boldsymbol{d}_{ij}$ such that an desired internal force $\boldsymbol{f}_i^{\text{int},d}$ is present. Due to the definition of the internal force which is not motion-inducing force we have

$$\sum_{i=1}^{N} \boldsymbol{f}_i^{\text{int},d} = 0. \tag{3.35}$$

The general setup of multiple robots with varying inter-robot displacements is depicted in Fig. 3.12.

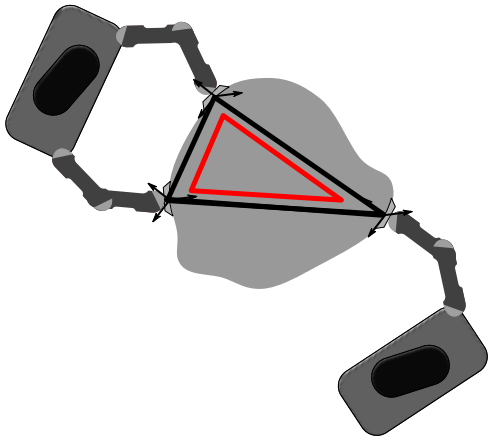

Figure 3.12: Multiple mobile robotic manipulators manipulating an object based on a formation-based set-point generator. The robot formation satisfies the geometrical dilation of the object and so no internal force acts on the object. (black formation). The displacement can be changed such that a desired internal force acts on the object based on the set-points (red formation).

The relationship between the desired robot set-point $\boldsymbol{p}_i^d$ and the desired object position $\boldsymbol{p}_o^d$ is defined by the desired displacements $\boldsymbol{d}_{io}$ between the object frame denoted by Σ_o and the particular robot Σ_i:

$$\boldsymbol{p}_i^d = \boldsymbol{p}_o^d + \boldsymbol{d}_{io},$$

where the displacements $\boldsymbol{d}_{io}$ are determined by freely choosing the frame Σ_o. Based Assumption 2.3 and the equality condition (2.18), we choose the displacements $\boldsymbol{d}_{io}$ as $\sum_{i=1}^{N} \boldsymbol{d}_{io} = 0$ All the remaining desired displacements d_{ij} where $i, j \in \{1, \ldots, N\}$ must be adapted such that the overall interaction topology is realizable, i.e. there exists a $\boldsymbol{p}^{d*}$ such that $\boldsymbol{p}_i^{d*} - \boldsymbol{p}_j^{d*} = \boldsymbol{d}_{ij}, \ \forall (i, j)$. Furthermore, if we now choose the displacement $\boldsymbol{d}_{io}$ as $\boldsymbol{d}_{io} = \boldsymbol{r}_i$ where $\boldsymbol{r}_i$ is defined in (2.17) the object geometry is satisfied by the desired set-points. Hence, for $\boldsymbol{e}_i = \bar{\boldsymbol{e}}$ and $\boldsymbol{d}_{io} = \boldsymbol{r}_i$ there is no internal force:

$$\boldsymbol{f}_i^{\text{int}} = k(\boldsymbol{e}_i - \sum_{i=1}^{N} \frac{\boldsymbol{e}_i}{N}) = k(\boldsymbol{p}_i - \boldsymbol{p}_i^d - \sum_{i=1}^{N} (\frac{\boldsymbol{p}_i - \boldsymbol{p}_i^d}{N})) = k(\boldsymbol{p}_o - \boldsymbol{p}_o^d + \boldsymbol{r}_i - \boldsymbol{d}_{io} - N\frac{\boldsymbol{p}_o - \boldsymbol{p}_o^d}{N}) = 0,$$

where we implicitly use the equality condition (2.18) for $\sum_{i=1}^{N} (\boldsymbol{r}_i - \boldsymbol{d}_{io}) = 0$ which is valid for any $\boldsymbol{r}_i$ and $\boldsymbol{d}_{io}$. We can now impose a desired internal force $\boldsymbol{f}_i^{\text{int},d}$ on the ith robot by setting displacement $\boldsymbol{d}_{ih}$ as follows

$$\boldsymbol{d}_{io} = \boldsymbol{r}_i - \frac{\boldsymbol{f}_i^{\text{int},d}}{k}. \tag{3.36}$$

By substituting (3.36) into (2.38) we yield the internal force as

$$\boldsymbol{f}_i^{\text{int}} = k(\boldsymbol{e} - \bar{\boldsymbol{e}}) = k(\boldsymbol{r}_i - \boldsymbol{d}_{io}) = \boldsymbol{f}_i^{\text{int},d},$$

which shows that we can explicitly control the internal forces acting on the object by setting the inter-robot distances between the set-points. We now want to illustrate the control of internal forces based on the previous examples.

Example 3.1. Let us consider three impedance-controlled robots with $k = 1500, d = 500, m = 100$. The desired displacements which satisfy the object geometry are given by $d_{1o} = 1, d_{2o} = 0, d_{3o} = -1$. At $t = 5s$ the goal is to impose a desired internal force $f_1^{\text{int}} = 150N, f_2^{\text{int}} = 0N, f_3^{\text{int}} = -150N$ which satisfies the condition for internal forces (3.35). We set the desired internal force by setting the displacement vectors to $d_{1o} = 1.1, d_{2o} = 0, d_{3o} = -1.1$. The trajectories and set-points are depicted in Fig. 3.13.

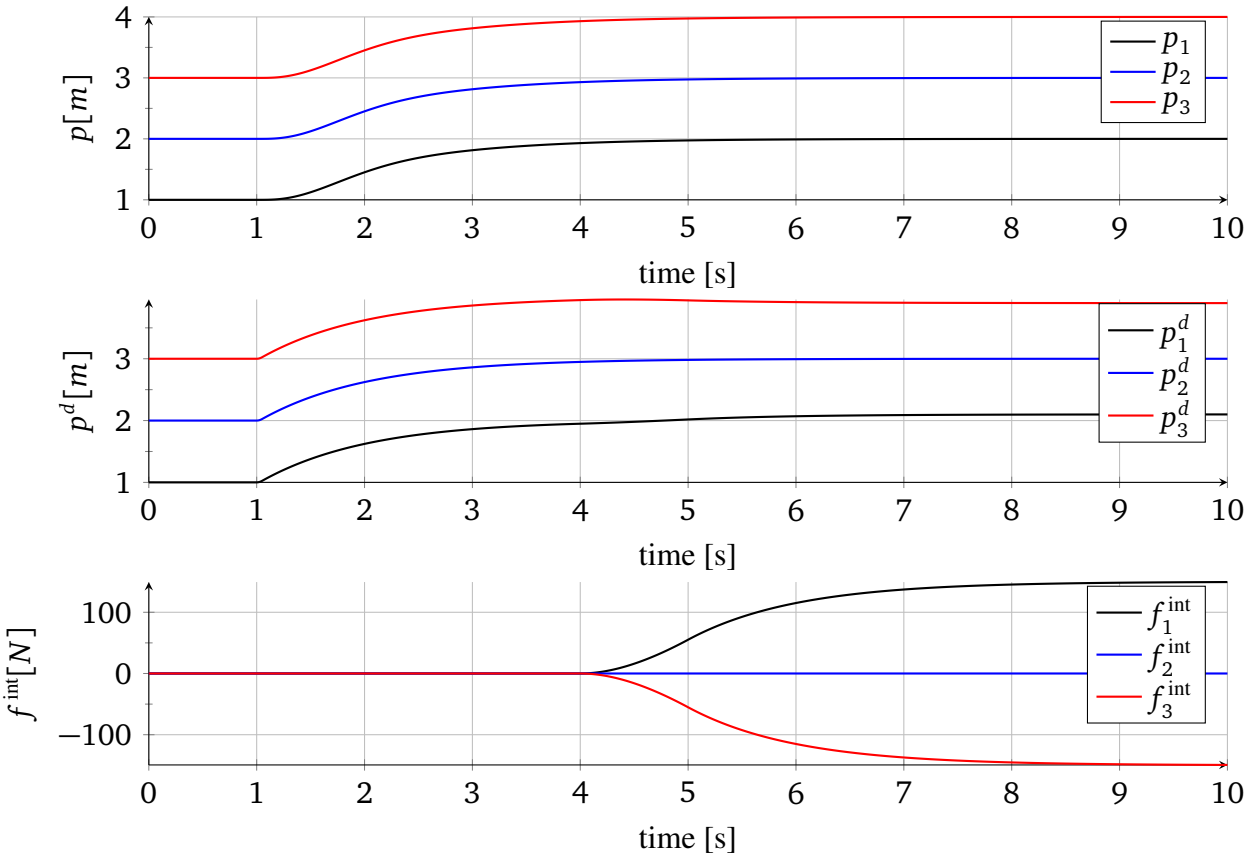

Figure 3.13: Robot trajectories p_i resulting from step response of p_i^{goal} at $t = 1s$. At $t = 4s$ the desired displacements are altered to obtain a desired internal force of $f_1^{\text{int},d} = 150$ and $f_3^{\text{int},d} = -150$.

3.6 Summary

This chapter introduces distributed formation control as a powerful tool for coordinating multiple manipulators which simultaneously conduct a cooperative robotic manipulation task. The methods' key aspect is to generate the particular robot set-points based on information exchange with the other cooperating robots such that the robot formation shape is in accordance with the geometry of the object to be manipulated. Due to this no excessive force is exerted on the object. In Section 3.3 an optimal feedback control design method coordinates the particular set-points based on a cost functional which also takes into account the robot formation based on a relaxation of the problem. For representing then both discrete and periodic motions in a cooperative manipulation task we employ movement primitives for the motion of particular robotic set-points and apply state feedback in real-time such that the ensemble of robot manipulators and object is coordinated effectively in Section 3.4. The approaches presented in Section 3.3- 3.4 consider the distance between a pair of robots in order to satisfy the kinematic constraints in a cooperative manipulation task and to establish the robot formation. Doing so is sufficient for successfully facilitating a cooperative manipulation task. However, the constraint is originally based on displacements and this fact is finally addressed in Section 3.5. In order to select one approach for the human guidance task in the next chapter we compare the different approaches in Tabular 3.4. All presented methods enable a simultaneous coordination of the robotic manipulators in order to effectively manipulate the object in 6D. Only in Section 3.3 the system dynamics are considered for trajectory generation from an optimal control point of view. However, due to the nonlinear nature of the cooperative manipulation task this approach has a tremendous computation time and is thus neglected for a reactive team guidance by a human operator. Furthermore, it is more difficult for a human to guide a distance-based formation since this approach is similar to controlling a vehicle with trailer or an "articulated vehicle" in 6D. As the selected method for the human guidance should also incorporate autonomous functions such as collision avoidance with obstacles we choose the 6D displacement-based set-point generator over the cooperative dynamic movement primitives.

Tabular 3.4: Comparison of the multi-robot coordination methods presented in Chapter 3

	Optimal Feedback Control	Cooperative Dynamic Movement Primitives	6D Set-Point Generator
Section	3.3	3.4	3.5
Object motion	6D	6D	6D
Cost function	yes	no	no
Obstacle avoidance	no	yes (not presented)	yes
Computation time	long	real-time	real-time
Formation type	distance	distance	displacement
End-effector motion	3D	3D	6D

4

Human Interaction with a Multi-Robot Manipulation Task

4.1 Motivation

While the physical cooperation of several manipulators, by which a common task is achieved, is a popular research topic in recent years [54, 1, 3], the interaction between a team of physically cooperating robots and humans has been far less explored. For manipulation tasks the cooperation of two or more partners is often crucial to enhance functionality and flexibility. This setting is particularly attractive as the multi-robot team typically outperforms the human at repetitive and exhausting tasks but not at cognitive reasoning in everyday tasks in unstructured environments. On the contrary, humans are very skilled in reasoning and decision making even in previously unknown situations. Therefore some attention has been dedicated to problem settings where a human acts as an operator of an automated complex system [123]. The interaction between a human and a group of robots poses two fundamental issues: i) the choice of a suitable and natural way to command multiple robots [124], and ii) providing the appropriate feedback to the human operator [102]. Largely unexplored is the question is how the human command should be mapped into the action space of the robots in a cooperative manipulation task which is mainly the topic of this chapter.

In this chapter we investigate the prototypical task where a single human operator controls a multi-robot cooperative manipulation task. We present a control scheme for a human to guide several robotic manipulators which cooperatively manipulate a common object to a final configuration. In a cooperative manipulation task it is essential that there is no significant deviation of the forces exerted on the manipulated object from the desired forces. Model uncertainties are always present and can be considered by rendering each manipulators compliant with an impedance control scheme in order to avoid high internal stress acting on the object. For each

cooperating robot particular robot set-points need to be generated which respect the kinematic coordination of the robots' motion and the human command. We formulate the coordination problem as a formation control framework in which set-points are distributedly generated for the robotic manipulators. Our work employs a human operator as the leader in a multi-robot manipulation task based on the widely-used leader-follower formation paradigm. The human operator is considered as part of the formation and controls the set-points of the particular robots with the movement of his/her hand, see Fig. 4.1. From a formation control point of view and based on the considerations in Chapter 3 we have to determine whether the human as leader interacts with a displacement-based formation or with a distance-based formation. Controlling a distance-based formation by a leader is very similar to controlling the motion of a trailer-car system by the motion of car. Two cases can be distinguished in the motion of the trailer-car system: the one, where the vehicle leads and pulls the trailer, is open loop stable as derived in [125]. In contrast, the other, where the trailer leads and is pushed, is open loop unstable and a controlling mechanism is required by the human driver. This is similar to balancing an inverted pendulum. The difference between the trailer-car system and the distance-based formation is that the car controls the trailer in two translational and one rotational DoF while the human controls the robotic formation in three translational and three rotational DoFs. This makes the distance-based formation guidance even more complex than controlling a trailer-car system and is inappropriate for an intuitive human-robot interaction paradigm due to the implicit inverted pendulum-like feedback control which needs to be performed by the human for a successful task execution. Hence, by exclusion we choose a displacement-based formation for the human guidance of a cooperative robotic manipulation task.

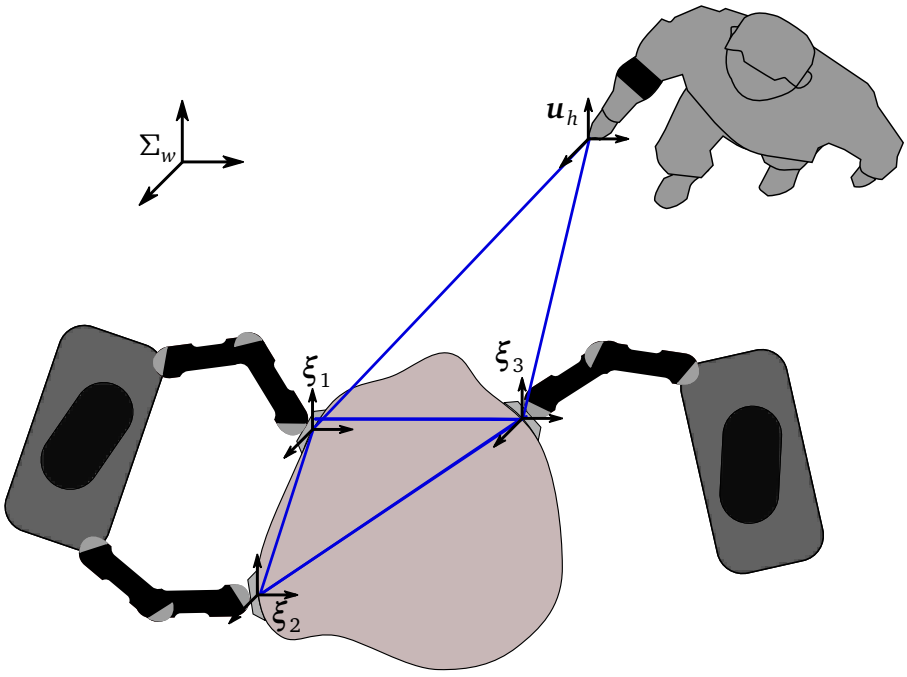

Figure 4.1: Three robotic manipulators perform a cooperative positioning task under a formation-preserving control law (blue lines). A human operator is the explicit leader of this formation and can control the robots distributedly.

4.2 Related work

The design of an interaction mechanisms to efficiently guide multiple robots is a very recent topic and only a limited amount of work is found in the literature. A gallery of various examples where a human operator interacts with a swarm of multiple robots is depicted in Fig. 4.2. Control of the overall behavior of multiple robots is explored in the context of multi-robot teleoperation [126, 127] where a group of slave robots is controlled by the human through a master robot. The main focus has been here on stability by exploiting passivity and the actual object manipulation is only incorporated by using a grasping shape function [56] without considering the apparent interaction dynamics which result from the constraints in a cooperative manipulation task [30]. Input constraints occur in a human-formation guidance setup when a group of non-holonomic mobile robots is to be guided [128]. For input constraints which are induced by the human input it is appealing to employ a visuo-haptic interaction mechanism for human-robot formation control which directly signalizes the constraints to the human operator [129, 130]. However, in a cooperative manipulation task the constraints are in addition also state constraints on the robotic states and the forward mapping has to ensure that these constraints are satisfied regardless of the human input. The choice of an appropriate input mechanisms plays an important role in guiding the multi-robot position. Examples are task-dependent graphical user interfaces for mobile handhelds [131] or gesture-based interfaces [132]. A specific research direction concerns the interaction of a single human with a swarm of multiple robots [133, 134, 135, 136]. A haptic interaction method for swarm interaction can improve the user experience by providing him an optimal location for interaction with a group of robots [137]. A characterization of the human influence on particular robots of a larger swarm is evaluated w.r.t. different network topologies based on a user study [138] by relating the individual influence to the controllability of a dynamical system. Yet no physical interaction is studied in those works and it remains unanswered what the relevance of the controllable and uncontrollable subspace in a cooperative manipulation task with physical coupling among the agents is. To sum up, all the aforementioned methods present interaction methods for a single user to control a group of robot but lack an explicit consideration of a physical coupling of the robots through the object. Hence, it remains open whether and how we can transfer the stability and controllability properties to a team of physically cooperating manipulators of which the motion is constrained due to the manipulated object.

All methods listed above have in common to employ position control. Position control is a mechanism by which the human operator controls the position of the robots directly. On the contrary, rate control maps human input on the velocity of the robots. For teleoperation applications in robotics [139] it is shown that position control usually outperforms rate control. Higher-order control approaches such as acceleration control including force control is usually considered more difficult by the human operator than controlling the position [140]. Hence, a position-based command can only interface the widely-used coordination of the cooperative robotic manipulators with a proper adaptation mechanism since this coordination method relies on the differential kinematics between object and cooperating manipulator velocity and depends on the grasp matrix [141, 142]. A position control scheme for multi-robot manipulation is present when employing an formation-based approach based on potential fields [143]. Without considering specific grasp points and without considering a human input formation control for

cooperative manipulation has been explored for mobile robots under the term caging [144, 37]. Additionally, by generating desired positions here instead of desired velocities as in the grasp matrix approach the drawbacks of differential approaches are avoided such as the accumulation of unbounded errors [145] which is previously discussed in the experimental evaluation in Section 2.5. To compensate for model uncertainties and external disturbances a centralized approach to control the internal force [20] for physically cooperating manipulators is widely used. To avoid central entity of internal force here a distribution of impedance-based control schemes [42, 146] among the manipulator is employed and it prevails the centralized approach by less inter-robot communication and reduced timing issues to exchange the measured forces among all cooperating manipulators.

4.3 Human Operator as Explicit Leader of Robotic Followers

The objective of this work is to let the human operator be the active member of the formation without being physically in touch with the manipulated object. To achieve this the desired displacements $\boldsymbol{d}_{ih}$ between the human and particular robots i have to be defined such that the virtual formation remains realizable. Therefore, the Cartesian pose $\boldsymbol{u}_h = \left[\boldsymbol{x}_h^\intercal, \boldsymbol{q}_h^\intercal\right]^\intercal \in \mathbb{R}^7$ of the human is required in the world frame Σ_w. In our task $\boldsymbol{x}_h$ is the position and $\boldsymbol{q}_h$ is the orientation of the human hand which can e.g. be distributedly sensed by the robot by a RGB-D camera.

For a compact formulation of the human-guided set-point system model we follow a standard argumentation used in formation analysis as e.g. done in [90] and transform the distributed set-points $\boldsymbol{p}_i^d$ into a particular point. A compact formulation of the 6 DoF set-point generator without goal regulation and without obstacle avoidance is given by

$$\dot{\boldsymbol{p}}_i^d = -\sum_{j\in N_i} \boldsymbol{e}_{ij}^p + S(\boldsymbol{d}_{ih})\boldsymbol{e}_{ij}^o, \tag{4.1}$$

$$\dot{\boldsymbol{q}}_i^d = -\sum_{j\in N_i} \frac{1}{2} U(\boldsymbol{q}_i^d)\boldsymbol{e}_{ij}^o, \tag{4.2}$$

where $S(\boldsymbol{d}_{ih})\boldsymbol{e}_{ij}^o$ is the radial motion which is present for two set-points on a rigid body during a rotational motion. Note here that the displacement vector $\boldsymbol{d}_{ih}$ determines the center of rotation. The desired displacement $\boldsymbol{d}_{ih}$ between the i and the human h is transformed in the frame Σ_o as similarly defined in (2.31). N_i describes the neighbors of agent i. In the following the set of neighborhood sets $\{N_1, \ldots, N_N, N_h\}$ is also called interaction topology. We choose the human frame Σ_h to be the center of rotation and transform the state of the ith robot into the center as

$$\boldsymbol{x}_i = \begin{bmatrix} \boldsymbol{x}_i^p \\ \boldsymbol{x}_i^q \end{bmatrix} = \begin{bmatrix} \boldsymbol{p}_i^d - \boldsymbol{d}_{ih} \\ \boldsymbol{q}_i^d \end{bmatrix}, \tag{4.3}$$

where $\boldsymbol{d}_{ih}$ is a displacement vector which satisfies $\boldsymbol{d}_{ij} = \boldsymbol{d}_{ih} - \boldsymbol{d}_{jh}$. For the sake of exposition we choose the constant displacement of the human input used in the transformation (4.3) to be $\boldsymbol{d}_{hh} = \boldsymbol{0}$ which acknowledges the human hand as center of rotation.

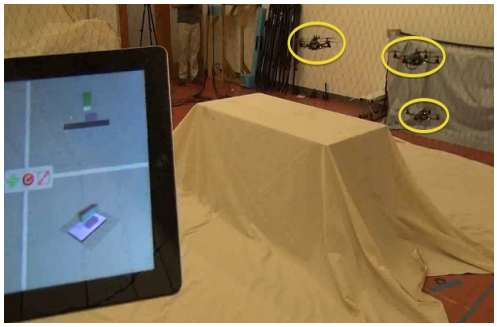

(a) (a)

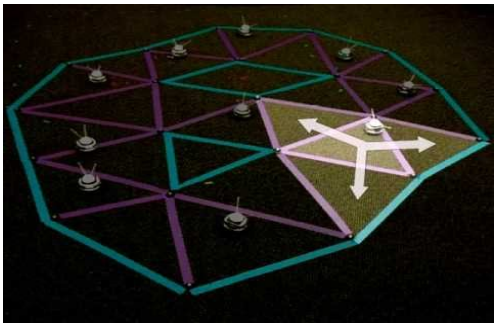

(b) (b)

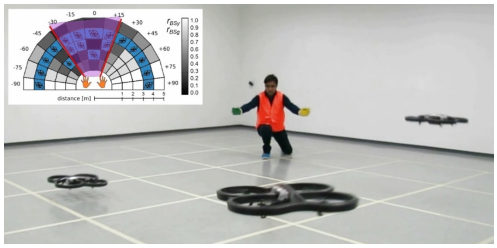

(c) (c)

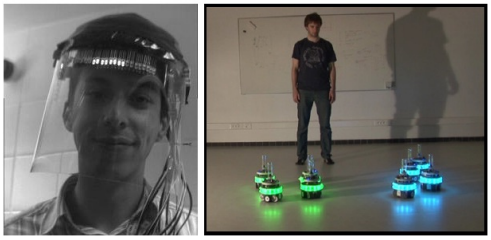

(d) (d)

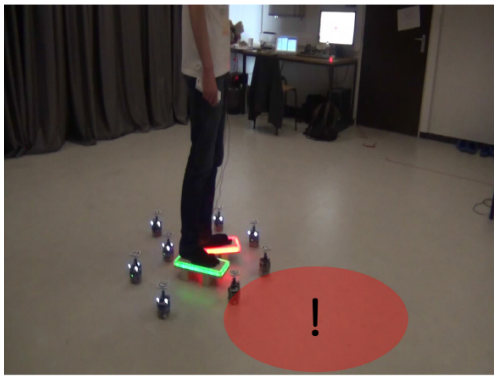

(e) (e)

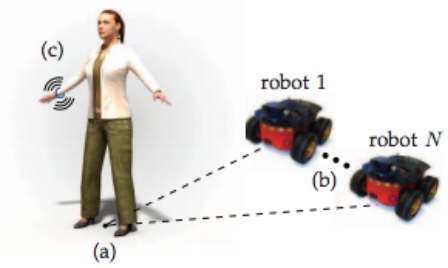

(f) (f)

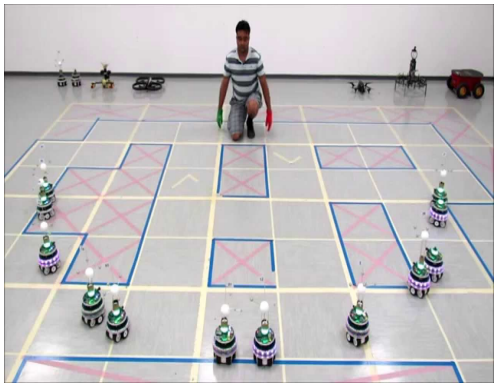

(g) (g)

(h) (h)

Figure 4.2: Examples of human-swarm interaction systems: (a) UAVs using multi-touch interface [131], (b) mobile robots using flow commands [134], (c) Quadrocopters using spatial gestures [147], (d) support of robot helper in fire fighting tasks [148, 149], (e) escorting robots [150], (f) human guidance with wearable haptics [130], (g) cooperative decision-making [151], (h) distributed framework design [152]

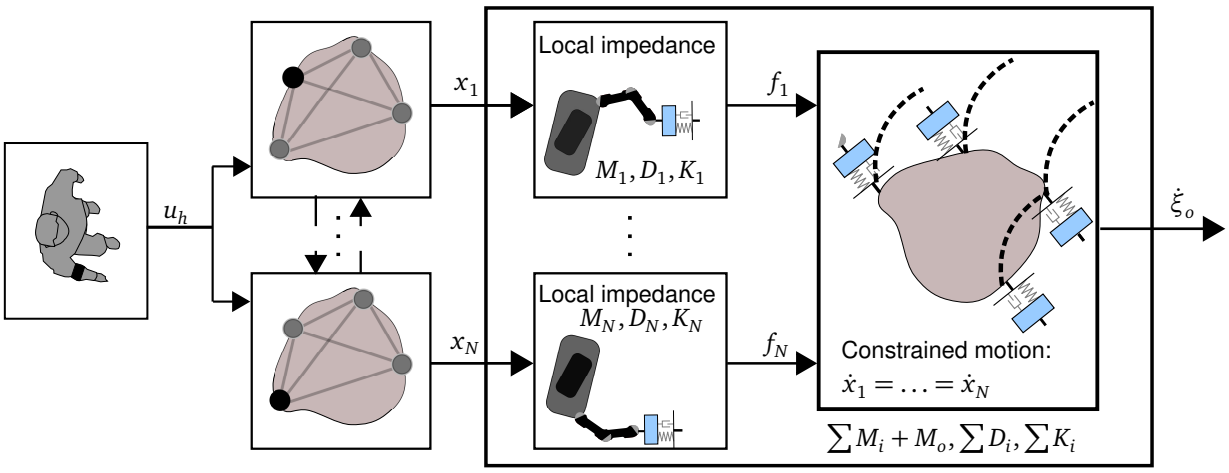

Figure 4.3: General control approach for the cooperative manipulation task guided by the human input u_h. The human input u_h clearly determines the transformed desired poses $\boldsymbol{x}$ of the impedance-controlled manipulators. Since the impedance-controlled manipulators are rigidly connected to the object, all of their positions move simultaneously: $\dot{\boldsymbol{x}}_i = \dot{\boldsymbol{x}}_j$. The pose ξ_o of the cooperatively manipulated object is then specified by the interaction dynamics of multiple impedance-controlled manipulators.

Hence, differentiating (4.3) w.r.t time yields the dynamics of set-point generator given by

$$\dot{\boldsymbol{x}}_i = \begin{bmatrix} \dot{\boldsymbol{p}}_i^d - \dot{\boldsymbol{d}}_{ih} \\ \dot{\boldsymbol{q}}_i^d \end{bmatrix} = \begin{bmatrix} -\sum_{j\in N_i} \boldsymbol{e}_{ij}^p + S(\boldsymbol{d}_{ih})\boldsymbol{e}_{ij}^o - S(\omega_i)\boldsymbol{d}_{ih} \\ -\sum_{j\in N_i} \frac{1}{2} U(\boldsymbol{q}_i^d)\boldsymbol{e}_{ij}^o \end{bmatrix} = \begin{bmatrix} -\sum_{j\in N_i} \boldsymbol{e}_{ij}^p \\ -\sum_{j\in N_i} \frac{1}{2} U(\boldsymbol{q}_i^d)\boldsymbol{e}_{ij}^o \end{bmatrix}, \quad (4.4)$$

where the rotational error $-\sum_{j\in N_i} S(\boldsymbol{d}_{ih})\boldsymbol{e}_{ij}^o$ and the time-derivative of the displacement vector $-S(\omega_i)\boldsymbol{d}_{ih}$ cancel out as $\omega_i = \sum_{j\in N_i} \boldsymbol{e}_{ij}^o$ and $S(\omega_i)\boldsymbol{d}_{ih} = -S(\boldsymbol{d}_{ih})\omega_i$. Hence, we observe that the transformation decouples the translational motion from the rotational one as $\boldsymbol{\omega}_i = \sum_{j\in N_i} \boldsymbol{e}_{ij}^o$. Since $\boldsymbol{e}_{ij}^p = (\boldsymbol{p}_i^d - \boldsymbol{d}_{ih}) - (\boldsymbol{p}_j^d - \boldsymbol{d}_{jh})$ and $\boldsymbol{e}_{ij}^o = U(\boldsymbol{q}_i^d)^\intercal(\boldsymbol{q}_i^d - \boldsymbol{q}_j^d)$ the dynamics (4.4) constitute a consensus protocol for the translational and rotational set-points. By also transforming the translational and rotational constraints (2.35) and (2.36) for the desired robot positions $\boldsymbol{p}^d$ and quaternions $\boldsymbol{q}^d$ with respect to any two i and j the constraint-satisfying desired positions are given by

$$\boldsymbol{x}_i = \boldsymbol{x}_j, \quad (4.5)$$

which defines the transformed version of the constraints (2.35) and (2.36). The general control approach of multiple impedance-controlled manipulators guided by a human operator is depicted in Fig. 4.3.

Partially following the argumentation in [153], we can compactly rewrite (4.4) using (2.6c) and (3.31). By doing so the human-extended dynamical system which involves the input of the

human is given by

$$\dot{\hat{\boldsymbol{x}}} = -\begin{bmatrix} L \otimes I_3 & 0 \\ 0 & \frac{1}{2}\bar{\mathscr{U}}(\boldsymbol{x}^q, \boldsymbol{q}_h)(L \otimes I_4) \end{bmatrix} \hat{\boldsymbol{x}}, \tag{4.6}$$

where L is the human-extended Laplacian matrix which can be decomposed as

$$L = -\left[\begin{array}{c|c} A_{\text{fms}} & \boldsymbol{b}_{\text{fms}} \\ \hline \boldsymbol{b}_{\text{fms}}^\intercal & \gamma \end{array}\right], \tag{4.7}$$

and $\hat{\boldsymbol{x}} = \left[\boldsymbol{x}^{p\intercal}, \boldsymbol{x}_h^\intercal, \boldsymbol{x}^{q\intercal}, \boldsymbol{q}_h^\intercal\right]^\intercal \in \mathbb{R}^{7(N+1)}$ is the concatenated pose and $\boldsymbol{x}^p = \left[\boldsymbol{x}_1^{p\intercal}, \ldots, \boldsymbol{x}_N^{p\intercal}\right]^\intercal \in \mathbb{R}^{3N}$ and $\boldsymbol{x}^q = \left[\boldsymbol{x}_1^{q\intercal}, \ldots, \boldsymbol{x}_N^{q\intercal}\right]^\intercal \in \mathbb{R}^{4N}$ is the concatenated position and quaternion vector. The human input $\boldsymbol{u}_h$ is appended to the concatenated robot states. The matrix $L \in \mathbb{R}^{N+1\times N+1}$ is the graph Laplacian. Furthermore, the matrix $\bar{\mathscr{U}}(\boldsymbol{x}^q, \boldsymbol{q}_h) \in \mathbb{R}^{4N\times 4N}$ is defined as $\bar{\mathscr{U}}(\boldsymbol{x}^q, \boldsymbol{q}_h) = \text{diag}(I_4 - \boldsymbol{x}_1^q \boldsymbol{x}_1^{q\intercal}, \ldots, I_4 - \boldsymbol{x}_N^q \boldsymbol{x}_N^{q\intercal}, I_4 - \boldsymbol{q}_h \boldsymbol{q}_h^\intercal)$.

Here, A_{fms} is the principal submatrix of L and reflects the influence of the cooperating robots on each other. Accordingly, $\boldsymbol{b}_{\text{fms}} \in \mathbb{R}^N$ represents the influence of the human leader on the team of robots. Similar to [138], $A_{\text{fms}} \in \mathbb{R}^{N\times N}$ and $\boldsymbol{b}_{\text{fms}} \in \mathbb{R}^N$ are the system and input matrices of the controlled consensus problem resulting from the graph Laplacian. It is generally known that 0 is an eigenvalue of L belonging to the eigenvector $\mathbf{1}$ [121]. Due to the decomposition (4.7) a relationship between A_{fms} and $\boldsymbol{b}_{\text{fms}}$ is then given by

$$A_{\text{fms}}\mathbf{1} = -\boldsymbol{b}_{\text{fms}}. \tag{4.8}$$

Here, $-L$ is known to be symmetric and negative semi-definite. Due to Cauchy's interlacing theorem, A_{fms} is then negative definite, i.e. all eigenvalues are negative as discussed in [90]. Both A_{fms} and $\boldsymbol{b}_{\text{fms}}$ result from the neighborhood topology of the formation control law. More precisely, $\boldsymbol{b}_{\text{fms}}$ contains entries with 1 and 0, where a 1-entry at the kth position indicates that the kth robot is a neighbor of the human. So $\boldsymbol{b}_{\text{fms}}$ is the direct representation of N_h as a vector as the k-entry of $\boldsymbol{b}_{\text{fms}}$ is 1 if $k \in N_h$. Hence, the desired state $\boldsymbol{x}_k$ of the kth robot is directly influenced by $\boldsymbol{u}_h$. This work has the following assumption for the interconnections represented by $\boldsymbol{b}_{\text{fms}}$.

Assumption 4.1. The vector $\boldsymbol{b}_{\text{fms}} \neq \mathbf{0}$ i.e. at least one of the N robotic manipulators has access to the human's constant input pose $\boldsymbol{u}_h$.

Yet as there is no direct physical contact between the human and the robot team, the human only imposes movements on the robot-formation by his/her arm movement. From a control theoretic perspective the human has only a directed influence on the states of the robot team. The opposite direction is not true as the team of cooperating robots has no direct influence on the human operator. Due to that the dynamics of the human motion (4.6) represented by $\dot{\boldsymbol{x}}_h = (\boldsymbol{b}_{\text{fms}}^\intercal \otimes I_3)\boldsymbol{x}^p + (\gamma \otimes I_3)\boldsymbol{x}_h$ and $\dot{\boldsymbol{q}}_h = \frac{1}{2}\mathscr{U}(\boldsymbol{q}_h)(\boldsymbol{b}_{\text{fms}}^\intercal \otimes I_4)\boldsymbol{q}^d + \frac{1}{2}\mathscr{U}(\boldsymbol{q}_h)(\gamma \otimes I_4)\boldsymbol{q}_h$ must be neglected in the system dynamics. The human-to-robots interaction is characterized by leader-follower consensus dynamics. The dynamical system representing the human influence on the

desired set-points is then given by

$$\dot{\boldsymbol{x}}^p = (A_{\text{fms}} \otimes I_3)\boldsymbol{x}^p + (\boldsymbol{b}_{\text{fms}} \otimes I_3)\boldsymbol{x}_h, \tag{4.9a}$$

$$\dot{\boldsymbol{x}}^q = \frac{1}{2}\mathscr{U}(\boldsymbol{x}^q)((A_{\text{fms}} \otimes I_4)\boldsymbol{x}^q + (\boldsymbol{b}_{\text{fms}} \otimes I_4)\boldsymbol{q}_h), \tag{4.9b}$$

where $\mathscr{U}(\boldsymbol{x}^q)$ is defined similar to $\bar{\mathscr{U}}(\boldsymbol{x}^q, \boldsymbol{q}_h)$ and can be simplified using (2.6b) as

$$\mathscr{U}(\boldsymbol{x}^q) = \text{diag}(I_4 - \boldsymbol{x}_1^q \boldsymbol{x}_1^{q\intercal}, \ldots, I_4 - \boldsymbol{x}_N^q \boldsymbol{x}_N^{q\intercal}).$$

Remark 4.1. In this work we focus on a direct and explicit interaction method where a human operator controls the robots non-physically by his/her arm movement. The proposed input $\boldsymbol{u}_h$ drives the cooperative manipulation task. For us providing $\boldsymbol{u}_h$ by a human arm movement is an example for a direct interaction method. We also imagine situations here where the input $\boldsymbol{u}_h$ is specified remotely by an appropriate input device as e.g. presented in [131]. The remaining results of this thesis still hold for such cases.

For illustration we present an example now.

Example 4.1. Assume now three equal robots of which the dynamics including the impedance parameters are defined in Example 2.1 and 2.2. For this example the general setup and the interaction topologies N_is which are required for the particular set-point generator (4.9) are depicted in Figure 4.1. Here we have $N_1 = \{2, 3, h\}$, $N_2 = \{1, 3\}$, $N_3 = \{1, 2, h\}$, and $N_h = \{1, 3\}$. The set-points x_1, x_2, x_3 are generated by (4.9) based on the human input x_h which results in the linearized dynamics given by

$$\begin{aligned}\dot{\boldsymbol{x}} &= A_{\text{fms}}\boldsymbol{x} + b_{\text{fms}}u \\ &= \begin{pmatrix} -3 & 1 & 1 \\ 1 & -2 & 1 \\ 1 & 1 & -3 \end{pmatrix}\begin{pmatrix} x_1 \\ x_2 \\ x_3 \end{pmatrix} + \begin{pmatrix} 1 \\ 0 \\ 1 \end{pmatrix} x_h.\end{aligned} \tag{4.10}$$

After stating the leader-follower dynamics for a human-robots team in formation, we are now ready to discuss the influence of the human input $\boldsymbol{u}_h$ on particular manipulator set-points $\boldsymbol{x}_i$ and its consequence for the occurrence of internal forces.

4.4 Human Influence on Particular Robotic Set-Points

The cooperative robots manipulate an object under a formation-preserving control law while a desired trajectory for the aggregated team of robots is provided to the robots by the human operator. Since we are at first interested in the evolution of the desired trajectories through the human input $\boldsymbol{u}_h$, we focus on the analysis of the formation-based set-point generator (4.9) in this section. When a human operator issues commands to a team of cooperative robots through the set-point generator (4.9), it is essential that all robots move in a coordinated way simultaneously, i.e. in formation, such that no undesired internal stress is applied to the object based on the human command $\boldsymbol{u}_h$. Hence, if the multi-robot cooperative team consists of more than two manipulators,

the question arises whether the human state $\boldsymbol{u}_h$ excites all robots simultaneously or if particular robots are excited independently from each other.

4.4.1 Internal Force During Transient Phase

We now have a closer look at if and in which way the distributed set-point generator (4.9) can induce an internal force. To investigate the occurrence of an internal force we revise the cases when there is no internal force induced which is given by the condition (4.5). There is no internal force induced if the set-points lie inside the subspace (4.5). Note that the constraint (4.5) is given for the desired robot states $\boldsymbol{x}_i$. If the constraint (4.5) holds for all robot pairs then all desired states $\boldsymbol{x}_i$ are equal. If all $\boldsymbol{x}_i \in \mathbb{R}^7$ are equal then the concatenated state for positions $\boldsymbol{x}^p$ can be compactly written using the set-builder notation as

$$\{\boldsymbol{x}^p \in \mathbb{R}^{3N} | \boldsymbol{x}^p = \left[\boldsymbol{x}_1^{p\intercal}, \ldots, \boldsymbol{x}_N^{p\intercal}\right]^\intercal \wedge \forall (i,j) : \boldsymbol{x}_i = \boldsymbol{x}_j \} = \\ \{\boldsymbol{x}^p \in \mathbb{R}^{3N} | \boldsymbol{x}^p = \mathbf{1} \otimes \boldsymbol{\chi}^p \},$$

and for rotations $\boldsymbol{x}^q$ as

$$\{\boldsymbol{x}^q \in \mathbb{R}^{4N} | \boldsymbol{x}^q = \mathbf{1} \otimes \boldsymbol{\chi}^q \},$$

where $\mathbf{1} \in \mathbb{R}^N$ denotes that the movement of the robots must be equal along a particular dimension. Furthermore, $\boldsymbol{\chi}^p \in \mathbb{R}^3$ and $\boldsymbol{\chi}^q \in \mathbb{R}^4$ are the free parameters which allow a separate scaling of the robots in the particular dimensions. Hence, the subspace of the desired set-points $\boldsymbol{x}$ and their time-derivatives $\dot{\boldsymbol{x}}$ in which no internal forces are induced is given by

$$\begin{aligned} \boldsymbol{x}^p &= \mathbf{1} \otimes \boldsymbol{\chi}^p, \quad \dot{\boldsymbol{x}}^p = \mathbf{1} \otimes \dot{\boldsymbol{\chi}}^p, \\ \boldsymbol{x}^q &= \mathbf{1} \otimes \boldsymbol{\chi}^q, \quad \dot{\boldsymbol{x}}^q = \mathbf{1} \otimes \dot{\boldsymbol{\chi}}^q, \end{aligned} \tag{4.11}$$

where the vector $\dot{\boldsymbol{\chi}} = [\dot{\boldsymbol{\chi}}^{p\intercal}, \dot{\boldsymbol{\chi}}^{q\intercal}]^\intercal$ is the time-derivative of $\boldsymbol{\chi} = [\boldsymbol{\chi}^{p\intercal}, \boldsymbol{\chi}^{q\intercal}]^\intercal$. We can now substitute (4.11) into (4.9) and reorder the system as follows

$$\Theta \begin{bmatrix} \mathbf{1} \otimes I_7 & -A_{\text{fms}} \mathbf{1} \otimes I_7 \end{bmatrix} \begin{bmatrix} \dot{\boldsymbol{\chi}} \\ \boldsymbol{\chi} \end{bmatrix} = \Theta \left[\boldsymbol{b}_{\text{fms}} \otimes I_7\right] \boldsymbol{u}_h, \tag{4.12}$$

where the matrix $\Theta \in \mathbb{R}^{6N \times 7N}$ is defined as $\Theta = \text{diag}(I_3, \ldots, I_3, U(\boldsymbol{x}_1^q)^\intercal, \ldots, U(\boldsymbol{x}_N^q)^\intercal)$. Here we result in a system of linear equations with unknowns $\dot{\boldsymbol{\chi}}$ and $\boldsymbol{\chi}$. The question remains open here whether we can find a solution that satisfies the system (4.12) w.r.t. the parameters $\dot{\boldsymbol{\chi}}$ and $\boldsymbol{\chi}$. Note here that the solution depends on the matrices $\boldsymbol{A}_{\text{fms}}$ and $\boldsymbol{b}_{\text{fms}}$ and not e.g. on rotational or translational motions. The solution is also independent from the matrix Θ as Θ is the same on both sides of (4.12). A straightforward approach to obtain the solution for $\dot{\boldsymbol{\chi}}$ and $\boldsymbol{\chi}$ is to pre-multiply (4.12) with a pseudo-inverse of $\Theta \begin{bmatrix} \mathbf{1} \otimes I_7 & -A_{\text{fms}} \mathbf{1} \otimes I_7 \end{bmatrix}$. However, the solution can be displayed more clearly and frankly if it is calculated as follows. In this work we rely on inspection of the columns $\mathbf{1} \otimes I_7$ and $-A_{\text{fms}} \mathbf{1} \otimes I_7$ in comparison with $[\boldsymbol{b}_{\text{fms}} \otimes I_7] \boldsymbol{u}_h$. We can rewrite the relationship $-A_{\text{fms}} \mathbf{1} \otimes I_7 = b_{\text{fms}} \otimes I_7$ given in (4.8). Due to that we know that (4.12) always has at least one solution since $-A_{\text{fms}} \mathbf{1} \otimes I_7$ constitutes the same subspace as $\boldsymbol{b}_{\text{fms}} \otimes I_7$.

We can identify two different cases for the solution of (4.12) by inspection: (a) for $\boldsymbol{b}_{\text{fms}} \neq \mathbf{1}$ the subspace formed by the first columns $\mathbf{1} \otimes I_7$ is independent from the subspace $\boldsymbol{b}_{\text{fms}} \otimes I_7$. Hence, by inspection we identify the solution of (4.12) to be $\dot{\boldsymbol{\chi}} = \mathbf{0}$ and $\boldsymbol{\chi} = \boldsymbol{u}_h$. The interpretation of this result is as follows: for $\boldsymbol{b}_{\text{fms}} \neq \mathbf{1}$ the operator does not induce an internal force for the static case $\boldsymbol{\chi}^* = \boldsymbol{u}_h$ and $\dot{\boldsymbol{\chi}}^* = \mathbf{0}$. Here, the desired set-points are in steady-state. However, as soon as the system states converge, i.e. $\dot{\boldsymbol{\chi}}^* \neq \mathbf{0}$, an internal force is induced. The states of a dynamical system converging to a steady state is called transient phase. Here, we result in a break-up of the formation during the transient phase of the dynamical system (4.9). Hence, in the transient phase the desired positions are not geometrically consistent with the object geometry any more; (b) for $\boldsymbol{b}_{\text{fms}} = \mathbf{1}$ each column of $\begin{bmatrix} \mathbf{1} \otimes I_7 & \boldsymbol{b}_{\text{fms}} \otimes I_7 \end{bmatrix}$ can be represented by $\boldsymbol{b}_{\text{fms}} \otimes I_7$. Hence, there exist infinitely many solutions for $\dot{\boldsymbol{\chi}}$ and $\boldsymbol{\chi}$ such that the human operator does not induce an internal force. We are now ready to state the final result relating the internal force and N_h.

Proposition 4.1. *There is no internal force* (2.33) *induced through the set-point generator* (4.9) *by* $\boldsymbol{u}_h$ *only if* $h \in N_i, \ \forall i \in \{1, \dots N\}$ *in* (4.1) *and* (4.2)*.*

Proof. If $h \in N_i, \ \forall i \in \{1, \dots N\}$ in (4.1) and (4.2), then the human input $\boldsymbol{u}_h$ is made accessible to all robots. If the human state can be accessed by all robots, we have $\boldsymbol{b}_{\text{fms}} = 1$. As discussed before in case of $\boldsymbol{b}_{\text{fms}} = 1$, the constraint of a cooperative manipulation (4.5) is satisfied in both steady-state and transient phase. If there is no divergence of the desired trajectories, i.e. (4.5) is satisfied, then there is no internal force acting on the object (2.33) which is caused by the input $\boldsymbol{u}_h$. □

Hence, all robotic followers in the formation should know the state of the human leader. The number of robots which can be independently influenced by the human obviously affects the subspace which is independently influenced by the human operator. The subspace which is independently influenced by the human operator is closely related to the controllability of a system. As previously commented for (4.12) the controllability question is the same for both translational and rotational movements. Due to that we restrict ourselves to the analysis of the matrix pair A_{fms} and $\boldsymbol{b}_{\text{fms}}$ in the following.

Remark 4.2. At first sight the consequence of Proposition 4.1 is unexpected from a formation-based perspective as it is only important that the human state is known by all robots. No information exchange between the robots is relevant in order to satisfy the constraints in the cooperative manipulation task. However, from a cooperative manipulation perspective this result is not surprising as we explain in the following. In a cooperative manipulation task a virtual point $\boldsymbol{\xi}_o$ is usually attached to the object's center of mass. Then, the grasp matrix G defined in (2.21) incorporates explicitly the kinematic parameters given by the displacements $\boldsymbol{r} = [\boldsymbol{r}_1^\intercal, \dots, \boldsymbol{r}_N^\intercal,]^\intercal$. G is then used order to generate desired velocities for the robotic manipulators $\dot{\boldsymbol{\xi}}^d$ based on the desired velocity of the virtual frame $\dot{\boldsymbol{\xi}}_o^d$ given by

$$\dot{\boldsymbol{\xi}}^d = G^\intercal \dot{\boldsymbol{\xi}}_o^d. \tag{4.13}$$

In $G^\intercal$ the virtual point $\boldsymbol{\xi}_o^d$ is also connected to all $\boldsymbol{\xi}_i^d$ to generate the desired velocities. If we now interpret the virtual point assigned to $\boldsymbol{\xi}_o^d$ as the leader then the requested interaction topology for both grasp matrix approach (4.13) and formation-based set-point generator (4.9) are similar. Note

here that the approach using the grasp matrix G actually defines a special case of our proposed set-point generator where the leader directly commands all followers and the system matrices are given by $A_{\text{fms}} = -I_N$ and $b_{\text{fms}} = \mathbf{1}$.

4.4.2 Human Shared Control of a Cooperative Manipulation Task

The influence of the human input on particular set-points plays a major role here and from a system theoretical perspective the influence of a input on system states is defined as a controllability characterization. Controllability in a leader-follower formation depends on the interaction topology and the interaction topology is defined by the neighbors N_is of the robots and human operator used in the gradient-descent control laws (4.1) and (4.2) in the formation. Although our leader-follower system (4.9) is defined for six dimensions in space, we investigate here only the controllability of one dimension which we justify as follows: the term $\otimes I_n$ including the Kronecker product extends the set-point generator to the multi-dimensional case. it is straightforward to show that the conclusions of the controllability analysis remain the same for single and multi-dimensional translation motion as the term $\otimes I_n$ creates a block diagonal matrix with the corresponding elements $A_{\text{fms}}, \boldsymbol{b}_{\text{fms}}$.

As discussed earlier for the rotational case in (4.12) the accessible subspace of the set-point generator (4.9) only depends on the matrix pair $(A_{\text{fms}}, \boldsymbol{b}_{\text{fms}})$ and not on the matrix Θ. As the matrix Θ ist used for mapping the input onto the subspace of quaternions and as the rank of Θ is always $3N$ we can neglect this matrix in the following analysis. As discussed in the previous section the influence of the human on the robotic set-points depends on the matrices $\boldsymbol{A}_{\text{fms}}$ and $\boldsymbol{b}_{\text{fms}}$ and not e.g. on rotational or translational motions. Hence, for analysing the shared control of a cooperative manipulation task we can simplify our system dynamics of (4.9) to

$$\dot{\boldsymbol{x}} = A_{\text{fms}}\boldsymbol{x} + \boldsymbol{b}_{\text{fms}}u, \tag{4.14}$$

where $\boldsymbol{x}$ characterizes one particular independently controllable states of $\boldsymbol{x}^p$ or $\boldsymbol{x}^q$ along one direction in space and u is the human input in that direction. Without loosing any insight into our problem this argumentation simplifies our analysis significantly.

In the controllability discussion we employ methods such as Kalman decomposition and eigenvalue analysis to interpret our results. The controllability matrix Q_{fms} of the matrix pair $(A_{\text{fms}}, \boldsymbol{b}_{\text{fms}})$ is defined as:

$$Q_{\text{fms}} = \begin{bmatrix} \boldsymbol{b}_{\text{fms}} & A_{\text{fms}}\boldsymbol{b}_{\text{fms}} & \dots & A_{\text{fms}}^{N-1}\boldsymbol{b}_{\text{fms}} \end{bmatrix}. \tag{4.15}$$

Here we focus on the analysis of the rank of Q_{fms} which characterizes the number of independently controllable states of $\boldsymbol{x}^p$ or $\boldsymbol{x}^q$ along one direction in space. If Q_{fms} is rank deficient the cooperating multi-robot system (4.14) can be decomposed into its controllable and uncontrollable part by the Kalman decomposition [154]. The similarity transformation of the Kalman decomposition is given by $T = \begin{bmatrix} Q_{\text{fms}}^{\parallel} \mid Q_{\text{fms}}^{\perp} \end{bmatrix}$, where $Q_{\text{fms}}^{\parallel} = \text{span}(Q_{\text{fms}}) \in \mathbb{R}^{N \times \text{rank}Q_{\text{fms}}}$ indicates the range of the controllable subspace and $Q_{\text{fms}}^{\perp} = \ker(Q_{\text{fms}}^{\intercal})$ the range of the uncontrollable subspace. Due to this

eigencomposition the similarity transformation results in

$$T^\intercal A_{\text{fms}} T = \begin{bmatrix} A^c_{\text{fms}} & 0 \\ 0 & A^{\hat{c}}_{\text{fms}} \end{bmatrix}, \quad T^\intercal \boldsymbol{b}_{\text{fms}} = \begin{bmatrix} \boldsymbol{b}^c_{\text{fms}} \\ 0 \end{bmatrix}, \\ \text{and} \begin{bmatrix} \boldsymbol{x}^c \\ \boldsymbol{x}^{\hat{c}} \end{bmatrix} = T^\intercal \boldsymbol{x}, \tag{4.16}$$

where c and $\hat{c}$ correspond to the controllable and uncontrollable parts of the robotic system and result in two decoupled subsystems. Due to the similarity transformation T the eigenvalues denoted as spectrum $\{\lambda_i^{A_{\text{fms}}}\}$ of A_{fms} and of $T^\intercal A_{\text{fms}} T$ are the same. The spectrum of A_{fms} is $\{\lambda_i^{A_{\text{fms}}}\} = \{\lambda_i^{A^c_{\text{fms}}}\} \cup \{\lambda_i^{A^{\hat{c}}_{\text{fms}}}\}$ where $\lambda_i^{A^c_{\text{fms}}}$ is the spectra of $A^c_{\text{fms}} \in \mathbb{R}^{\text{rank}Q_{\text{fms}} \times \text{rank}Q_{\text{fms}}}$ and $\lambda_i^{A^{\hat{c}}_{\text{fms}}}$ is the spectra of $A^{\hat{c}}_{\text{fms}} \in \mathbb{R}^{N-\text{rank}Q_{\text{fms}} \times N-\text{rank}Q_{\text{fms}}}$.

The derivation of the constraint (4.5) for $\boldsymbol{x}$ in (4.14) yields $\boldsymbol{x} \equiv \mathbf{1}$. The constraint can also be transformed into the space of controllable and uncontrollable states using the similarity transformation (4.16) as

$$T^\intercal \mathbf{1} = \begin{bmatrix} {Q^{\parallel}_{\text{fms}}}^\intercal \\ {Q^{\perp}_{\text{fms}}}^\intercal \end{bmatrix} \mathbf{1} = \begin{bmatrix} \boldsymbol{\nu}_k \\ \mathbf{0} \end{bmatrix}, \tag{4.17}$$

where the constraint-satisfying vector for the controllable subspace is given by $\boldsymbol{\nu}_k = {Q^{\parallel}_{\text{fms}}}^\intercal \mathbf{1} \in \mathbb{R}^{\text{rank}(Q_{\text{fms}})}$. Note that for the uncontrollable subspace ${Q^{\perp}_{\text{fms}}}^\intercal \mathbf{1}$ is always $\mathbf{0}$. We can show that by applying the relation (4.8) between A_{fms} and $\boldsymbol{b}_{\text{fms}}$ which results in $\mathbf{1} = -A^{-1}_{\text{fms}} \boldsymbol{b}_{\text{fms}}$. Since A_{fms} is negative definite it is invertible. The inverse A^{-1}_{fms} can be expressed using the Cayley-Hamilton theorem as

$$A^{-1}_{\text{fms}} = \frac{(-1)^{N-1}}{\det(A_{\text{fms}})}(A^{N-1}_{\text{fms}} + c_{N-1}A^{N-2}_{\text{fms}} + \ldots + c_1 I_N),$$

where c_k are the coefficients of the characteristic polynomial. As A^{-1}_{fms} is a linear combination of the matrices $I_N, \ldots A^{N-1}_{\text{fms}}$, the term $-A^{-1}_{\text{fms}}\boldsymbol{b}$ forms the same subspace as the controllability matrix Q_{fms} and its span $Q^{\parallel}_{\text{fms}}$ derived in (4.15). By definition $Q^{\perp}_{\text{fms}}$ is orthogonal $Q^{\parallel}_{\text{fms}}$ and so $-Q^{\perp}_{\text{fms}}A^{-1}_{\text{fms}}\boldsymbol{b} = \mathbf{0}$ always holds.

The meaning of the controllable subspace in case of a multi-robot formation remains unanswered until now, i.e. what is the resulting state after applying the transformation $T = \left[Q^{\parallel}_{\text{fms}} \mid Q^{\perp}_{\text{fms}}\right]$. In general, one has to analytically apply this similarity transformation to derive the controllable states $\boldsymbol{x}^c$ based on the robot state $\boldsymbol{x}$. It is known that the controllable states $\boldsymbol{x}^c$ depend on the interaction topology [86]. Due to the direct throughput of the human input $\boldsymbol{u}$ on its neighbors N_h through $\boldsymbol{b}_{\text{fms}}$ it is obvious that the human has at most influence on the robots in N_h. Hence, the state of robot $i \in N_h$ is directly influenced by the human through the distributed set-point generator (4.9). The neighbors of N_h again are thus only indirectly influenced by the propagation of the human input $\boldsymbol{u}$ based on the neighborhood relationships and the consensus protocol. Hence, we conclude that we change the human influence on the multi-robot team based on the underlying neighborhood topology. In the following we interpret the decomposition (4.16) from a shared control perspective where the uncontrollable subsystem is the autonomous robotic task and the controllable subsystem is the human task.

Autonomous Robotic Task

From a shared control perspective the uncontrollable subsystem

$$\dot{\boldsymbol{x}}^{\hat{c}} = A^{\hat{c}}_{\text{fms}} \boldsymbol{x}^{\hat{c}}, \tag{4.18}$$

can be interpreted as the autonomous sub-task of the overall robotic system. Uncontrollability means that the human has no influence on states $\boldsymbol{x}^{\hat{c}}$, i.e. the movement of the human hand has no effect on the transformed robot states. Since the human has no influence on the uncontrollable subsystem, the eigenmodes $\{\lambda_i^{A^{\hat{c}}_{\text{fms}}}\} \subset \{\lambda_i^{A_{\text{fms}}}\}$ are masked from the human. The uncontrollable subsystem $\dot{\boldsymbol{x}}^{\hat{c}} = A^{\hat{c}}_{\text{fms}} \boldsymbol{x}^{\hat{c}}$ is known [90] to be asymptotically stable, i.e. $\lim_{t\to\infty} \boldsymbol{x}^{\hat{c}} = \mathbf{0}$. As the system is asymptotically stable and as the initial condition can be freely chosen as $\boldsymbol{x}^{\hat{c}}(t_0) = 0$ we always have

$$\boldsymbol{x}^{\hat{c}} = \mathbf{0}. \tag{4.19}$$

We can now conclude that the uncontrollable states $\boldsymbol{x}^{\hat{c}}$ can be generally set to zero as defined in (4.19) and come up with the following proposition relating the internal force to the uncontrollable subsystem.

Proposition 4.2. *There is no internal force* (2.33) *induced by the uncontrollable system* (4.18).

Proof. As we can freely choose the initial condition for the set-point generator (4.9) to be $\boldsymbol{x}^{\hat{c}}(t_0) = 0$ and the uncontrollable subsystem (4.18) is asymptotically stable, the uncontrollable states are always 0 which is described in (4.19). Here, $\boldsymbol{x}^{\hat{c}} = \mathbf{0}$ means that the uncontrollable states $\boldsymbol{x}^{\hat{c}}$ lie in the same subspace as the constraint-satisfying vector derived in (4.17). Hence, the constraint for cooperative manipulation (4.5) is always satisfied. As the constraint (4.5) is satisfied for the uncontrollable system, we have $\boldsymbol{x} = \mathbf{1}$. Due to that no internal force (2.33) acts on the object caused by the uncontrollable subsystem. □

This result is desired as the human has no influence on the uncontrollable subsystem. However, it remains unanswered here wether the human input $\boldsymbol{u}$ on the controllable subsystem can cause an internal force .

Human Sub-task on the Manipulation Task

From a shared control perspective, the controllable subsystem

$$\dot{\boldsymbol{x}}^{c} = A^{c}_{\text{fms}} \boldsymbol{x}^{c} + \boldsymbol{b}^{c}_{\text{fms}} u, \tag{4.20}$$

can be interpreted as the sub-task of the human operator to the system. Before discussing the influence of the human on the particular robot states we first introduce a relation between $\text{rank}(Q_{\text{fms}})$ and the human input vector $\boldsymbol{b}_{\text{fms}}$. In particular we consider the case $\boldsymbol{b}_{\text{fms}} = 1$ which is the consequence of Prop. (4.1).

Proposition 4.3. *The single-leader controlled consensus protocol* (4.14) *has only one controllable eigenmode, i.e.* $\text{rank}(Q_{fms}) = 1$ *, if and only if* $\boldsymbol{b}_{fms} = \mathbf{1}$.

Proof. The proof of sufficiency assumes that $\boldsymbol{b}_{\text{fms}} = \mathbf{1}$. Since A_{fms} is the principal submatrix of the Laplacian $-L$ (4.7), the row sum of A_{fms} is -1. Hence, $A_{\text{fms}}\boldsymbol{b}_{\text{fms}} = -\mathbf{1}$. Iteratively, one can show that $A^k_{\text{fms}}\boldsymbol{b}_{\text{fms}} = (-1)^k\mathbf{1}$. Consequently, the controllability matrix $Q_{\text{fms}} = \left[\mathbf{1}, -\mathbf{1}, \mathbf{1}, \ldots, (-1)^{N-1}\mathbf{1}\right]$ has $\text{rank}(Q_{\text{fms}}) = 1$. As the controllability matrix describes the controllable subspace, we know that the leader can only control the average of all followers. For the proof of necessity, to have a single controllable eigenmode, $\text{rank}(Q_{\text{fms}}) = 1$ and so all columns of the controllability matrix Q_{fms} must be linearly dependent. Hence, there must exist an input vector $\boldsymbol{b}_{\text{fms}}$ such that $\boldsymbol{b}_{\text{fms}} = \chi A_{\text{fms}}\boldsymbol{b}_{\text{fms}}$, where $\chi \in \mathbb{R}$. By construction we always have $-A_{\text{fms}}\mathbf{1} = \boldsymbol{b}_{\text{fms}}$. Since A_{fms} is always regular [90], $\chi = -1$ and $\mathbf{b}_{\text{fms}} = \mathbf{1}$. For $A^2_{\text{fms}}\boldsymbol{b}_{\text{fms}}, \ldots, A^{N-1}_{\text{fms}}\boldsymbol{b}_{\text{fms}}$ this can be shown iteratively. □

For $\boldsymbol{b}_{\text{fms}} = \mathbf{1}$ the human leader is connected to all robots and so we have $N_h = \{1, \ldots, N\}$. For $\boldsymbol{b}_{\text{fms}} = \mathbf{1}$ we only have a single controllable mode which is the only interaction topology which satisfies the constraint (4.5). Hence, we propose that the human leader should only control a single eigenmode, i.e. $\text{rank}(Q_{\text{fms}}) = 1$. This result can also be interpreted by the controllable states $\boldsymbol{x}^c(t)$ which can be influenced by the human operator. For $\text{rank}(Q_{\text{fms}}) > 1$ the operator induces a violation of the constraint (4.5) in the transient phase of the desired trajectories $\boldsymbol{x}^c(t)$ by his movement $\boldsymbol{u}$.

This result is makes sense when we consider the eigenmodes which are influenced by the human. The human operator has only influence on the controllable eigenmodes $\lambda_i^{A^c}$ which correspond to the rates of convergence. The controllable state is concatenated and is labeled as $\boldsymbol{x}^c = \left[x^c_1, \ldots, x^c_{\text{rank}(Q_{\text{fms}})}\right]^\intercal$. The ith locally controllable state trajectory $x^c_i(t)$ of the robots evolves according to the solution of the ordinary differential equation given by

$$x^c_i = e^{\lambda_i^{A^c_{\text{fms}}} t} x^c_i(t_0) + \int_{t_0}^{t_1} e^{\lambda_i^{A^c_{\text{fms}}}(t-\tau)} b^c_{\text{fms,i}} u(\tau)\mathrm{d}\tau,$$

where $b^c_{\text{fms,i}}$ is the ith component of $\boldsymbol{b}^c_{\text{fms}}$. The resulting motion of the controllable subspace $\boldsymbol{x}_c$ always depends on the controllable eigenvalues of (4.14). For the controllable eigenvalues we come up with the following propositon.

Proposition 4.4. *All eigenvalues of the system matrix A^c_{fms} of the controllable subsystem* (4.20) *of the controlled consensus network* (4.14) *are distinct, i.e. $\lambda_i^{A^c_{fms}} \neq \lambda_{i+1}^{A^c_{fms}}$.*

Proof. Let us assume that the spectrum of A_{fms} has an eigenvalue with geometric multiplicity greater than one, i.e. $\lambda_i^{A_{\text{fms}}} = \lambda_{i+1}^{A_{\text{fms}}}$. Then we can always find a linear combination of the eigenvectors that produces a 0 entry at the position of the leader [90, Prop 10.3]. A 0 entry in the eigenvector at the position of the leader leads to an uncontrollable subspace [90]. Hence, all except one of the eigenvalues with geometric multiplicity greater than one can be in $\lambda_i^{A^c_{\text{fms}}}$. □

The eigenvalues $\lambda_i^{A^c_{\text{fms}}}$ of the controllable subsystem are always distinct from each other, i.e. $\forall i,\ \lambda_i^{A^c_{\text{fms}}} \neq \lambda_{i+1}^{A^c_{\text{fms}}}$. If there exist n different controllable eigenmodes for the human, then the human can locally control n different controllable states x^c_i. Since $\lambda_i^{A^c_{\text{fms}}} \neq \lambda_{i+1}^{A^c_{\text{fms}}}$, the human input

$u(t)$ drives the trajectories of the controllable states $\boldsymbol{x}_c(t)$ differently:

$$x_i^c(t) \neq x_j^c(t), \quad \forall i, j \text{ and } t \in [t_0, t_1]. \tag{4.21}$$

The local trajectories of the controllable states x_i^c are different in the transient phase due to (4.21) for $\operatorname{rank}(Q_{\text{fms}}) > 1$. If now the controllable state corresponds to a single robot or a cluster of robots, then the human operator can locally control those states independently. As the rate of convergence of the controllable system is different, the subsystems which are controllable by the human converge with different speeds and result in a violation of the constraint (4.5). We illustrate this in the following example.

Example 4.2. We continue here with the previously defined system dynamics from Example 2.1, 2.2 and 4.1. The controllability matrix Q_{fms} (4.15) of the set-point generator (4.10) from Example 4.1 reads as

$$Q_{\text{fms}} = \begin{pmatrix} 1 & -2 & 6 \\ 0 & 2 & -8 \\ 1 & -2 & 6 \end{pmatrix}.$$

By inspection of the rows we can directly see that the first and third row of Q_{fms} are equal and so $\operatorname{rank}(Q_{\text{fms}}) = 2$. We have $\operatorname{rank}(Q_{\text{fms}}) > 1$ as $N_h \neq \{1, 2, 3\}$ which results in an internal force as derived in Proposition 4.1. In contrast to Example 4.1 we do now change the interaction topology to be $N_h = \{1, 2, 3\}$ and $N_2 = \{1, 3, h\}$ in order to follow the consequence of Proposition 4.1 and result in the system dynamics for the set-point generator given by

$$\begin{aligned} \dot{\boldsymbol{x}} &= A_{\text{fms}}\boldsymbol{x} + b_{\text{fms}}u \\ &= \begin{pmatrix} -3 & 1 & 1 \\ 1 & \mathbf{-3} & 1 \\ 1 & 1 & -3 \end{pmatrix} \begin{pmatrix} x_1 \\ x_2 \\ x_3 \end{pmatrix} + \begin{pmatrix} 1 \\ \mathbf{1} \\ 1 \end{pmatrix} u. \end{aligned} \tag{4.22}$$

Note here that the difference entries between the examples (4.10) and (4.22) are highlighted bold. Using (4.22) as set-point generator there is no deviation of the set-points x_1, x_2, x_3 during the transient phase and no internal force f_i^{int} that acts on the object as depicted in Fig. 4.4.

4.4.3 Weighted Set-Point Generators to Reduce Internal Forces

In this section we present an approach how to significantly decrease internal stress acting on the object by introducing weights for formation-based set-point generator. The idea behind the weights is to increase remarkably the convergence rate of the desired-set points which are responsible for the internal force. Due to that the set-points converge faster and the internal force is considerably reduced. A major advantage of the weights is that no internal force occurs independent from which interaction topology is employed, i.e. there is no more demand which requires a human-to-all-robots topology for this.

By definition the particular set-point dynamics of the formation-based generator with weights

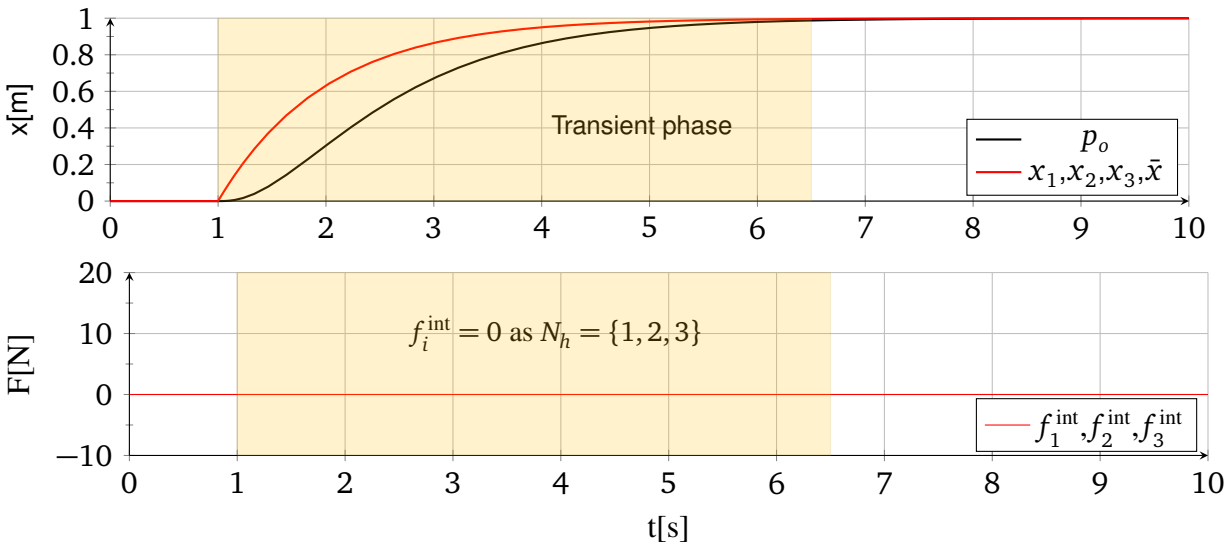

Figure 4.4: Object trajectory p_o resulting from distributedly generated robot set-points x_1, x_2, x_3. No deviation of the set-points in the transient between $t = 1s$ and $t = 6.5s$ and so there is no internal force $f_i^{\text{int}} = 0$.

evolve now according to

$$\dot{\boldsymbol{x}} = \Gamma u,$$

which denotes the weighted version of (3.29). Furthermore, $\Gamma = \text{diag}(\gamma_1, \ldots, \gamma_N)$ is a block-diagonal matrix with the entries being $\gamma_i > 0 \in \mathbb{R}$, Here, γ_i are scalar weights in order to allocate different speeds to different set-points. Following the previous argumentation we can rewrite our set-point generator dynamics as follows:

$$\dot{x} = \Gamma A_{\text{fms}} x + \Gamma b_{\text{fms}} u. \tag{4.23}$$

Before introducing a formal result which relates the weights γ_i to the internal force $\boldsymbol{h}^{\text{int}}$ we re-label our set-point generator (4.23). A re-labeling of the robots can be done without loss of generality and is performed here for the sake of exposition. Note here that all properties of the graph Laplacian remain since a re-labeling is just an isormophism of a graph and can thus be done without loss of generality. First we collect the states of all agents i belonging to the set N_h into the state $\tilde{\boldsymbol{x}}_2 \in \mathbb{R}^{\mathbf{1}^\intercal b_{\text{fms}}}$ where $\mathbf{1}^\intercal b_{\text{fms}}$ denotes the number of all direct neighbors. Analogously we put the states of all the remaining robots which are not in neighborhood N_h of the human into the state $\tilde{\boldsymbol{x}}_1 \in \mathbb{R}^{N - \mathbf{1}^\intercal b_{\text{fms}}}$. Furthermore, in our setup the weights are only different with respect to the previously defined two groups, i.e. the state $\tilde{\boldsymbol{x}}_1$ evolves with speed γ_1 and $\tilde{\boldsymbol{x}}_2$ evolves with γ_2. Hence, we have $\Gamma = \text{diag}(\gamma_1 I_{N - \mathbf{1}^\intercal b_{\text{fms}}}, \gamma_2 I_{\mathbf{1}^\intercal b_{\text{fms}}})$. By using that collocation for notation and by an appropriate decomposition of A_{fms} as

$$A_{\text{fms}} = \begin{bmatrix} A_{f1} & B_{f1} \\ B_{f1}^\intercal & A_{f2} \end{bmatrix},$$

we can rewrite (4.23) as follows:

$$\begin{bmatrix} \dot{\tilde{\boldsymbol{x}}}_1 \\ \dot{\tilde{\boldsymbol{x}}}_2 \end{bmatrix} = \begin{bmatrix} \gamma_1 A_{f1} & \gamma_1 B_{f1} \\ \gamma_2 B_{f1}^{\intercal} & \gamma_2 A_{f2} \end{bmatrix} \begin{bmatrix} \tilde{\boldsymbol{x}}_1 \\ \tilde{\boldsymbol{x}}_2 \end{bmatrix} + \begin{bmatrix} 0 \\ \gamma_2 \mathbf{1} \end{bmatrix} u, \tag{4.24}$$

where the states $\tilde{\boldsymbol{x}}_1$ are not directly influenced by the human input u. Based on this labeling we are now ready to formally state a relation between the weights γ_i and the internal force $\boldsymbol{h}^{\text{int}}$ which holds for any interaction topology.

Theorem 4.1. *The internal force $\boldsymbol{h}^{int} \to 0$ only if the weights γ_1 defined in the weighted set-point generator* (4.24) *are $\gamma_1 \to \infty$ for any interaction topology.*

Proof. We need to show now that for $\gamma_1 \to \infty$ we have $\boldsymbol{h}^{\text{int}} \to 0$. From (4.24), we know that there are two interconnected differential equations of which one dynamical system is without direct influence of the human given by

$$\dot{\tilde{\boldsymbol{x}}}_1 = \gamma_1 A_{f1} \tilde{\boldsymbol{x}}_1 + \gamma_1 B_{f1} \tilde{\boldsymbol{x}}_2, \tag{4.25}$$

and one dynamical system is with direct influence

$$\dot{\tilde{\boldsymbol{x}}}_2 = \gamma_2 A_{f2} \tilde{\boldsymbol{x}}_2 + \gamma_2 B_{f1}^{\intercal} \tilde{\boldsymbol{x}}_1 + \gamma_2 \mathbf{1} u. \tag{4.26}$$

Note here that this is not a decomposition into controllable and uncontrollable subspace as u still has indirect influence on $\tilde{\boldsymbol{x}}_2$ through $\tilde{\boldsymbol{x}}_1$. The equilibrium of (4.25) where $\dot{\tilde{\boldsymbol{x}}}_1 = 0$ is given by

$$\tilde{\boldsymbol{x}}_1(\infty) = -A_{f1}^{-1} B_{f1} \tilde{\boldsymbol{x}}_2.$$

An error between the state $\tilde{\boldsymbol{x}}_1$ and its equilibrium $\tilde{\boldsymbol{x}}_1(\infty)$ is defined by $\boldsymbol{e}_1 = \tilde{\boldsymbol{x}}_1 - \tilde{\boldsymbol{x}}_1(\infty)$ with which the error dynamics result in $\dot{\boldsymbol{e}}_1 = \gamma_1 A_{f1} \boldsymbol{e}_1$. For the absolute norm of the error $\boldsymbol{e}_1$ we can say that it converges with less or equal to the larger eigenvalue $\lambda_{\max}^{A_{f1}}$ of A_{f1} as

$$\boldsymbol{e}_1(t) = e^{(\gamma_1 A_{f1} t)} \boldsymbol{e}_1(t_o) \leq e^{(\gamma_1 \lambda_{\max}^{A_{f1}} t)} \boldsymbol{e}_1(t_o).$$

As $\lambda_{\max}^{A_{f1}} < 0$ and $\boldsymbol{e}_1(t_o)$ is bounded we have

$$\lim_{\gamma_1 \to \infty} \boldsymbol{e}_1(t) = 0, \tag{4.27}$$

due to which we can always express $\tilde{\boldsymbol{x}}_1$ by its equilibrium involving $\tilde{\boldsymbol{x}}_2$ as $\tilde{\boldsymbol{x}}_1 = -A_{f1}^{-1} B_{f1} \tilde{\boldsymbol{x}}_2$. We later show that $\boldsymbol{e}_1$ results in a violation of the constraint (4.5) which causes an internal $\boldsymbol{h}^{\text{int}} \neq 0$. We continue now by substituting the equilibrium $\tilde{\boldsymbol{x}}_1 = -A_{f1}^{-1} B_{f1} \tilde{\boldsymbol{x}}_2$ into (4.26) as

$$\dot{\tilde{\boldsymbol{x}}}_2 = \gamma_2 (A_{f2} - B_{f1}^{\intercal} A_{f1}^{-1} B_{f1}) \tilde{\boldsymbol{x}}_2 + \gamma_2 \mathbf{1} u. \tag{4.28}$$

To investigate the accessible subspace in which $\tilde{\boldsymbol{x}}_2$ can move we have a closer look at the

controllability matrix (4.15) and the controllable subspace of (4.28) defined by

$$Q_{\text{fms}} = \begin{bmatrix} \gamma_2 \mathbf{1} & \gamma_2^2 (A_{f2} - B_{f1}^{\intercal} A_{f1}^{-1} B_{f1}) \mathbf{1} \end{bmatrix} = \begin{bmatrix} \gamma_2 \mathbf{1} & \gamma_2^2 (A_{f2} \mathbf{1} + B_{f1}^{\intercal} \mathbf{1}) \end{bmatrix} = \begin{bmatrix} \gamma_2 \mathbf{1} & -\gamma_2^2 \mathbf{1} \end{bmatrix},$$

where we apply the relationships $\mathbf{1} = -A_{f1}^{-1} B_{f1} \mathbf{1}$ and $A_{f2} \mathbf{1} + B_{f1}^{\intercal} \mathbf{1} + \mathbf{1} = 0$. The relationships result from the decomposition (4.7) of A_{fms} in L and the fact that $L\mathbf{1} = \mathbf{0}$. Note here that the controllable subspace is $\mathbf{1}$, i.e. all entries of $\tilde{\boldsymbol{x}}_2$ are equal. By having equal entries in $\tilde{\boldsymbol{x}}_2$ we know that $\tilde{\boldsymbol{x}}_2 \in \tilde{x}_2^* \mathbf{1}$ where $\tilde{x}_2^* \in \mathbb{R}$ is a scaling factor. Due to that we know that all entries of $\tilde{\boldsymbol{x}}_2$ are equal. Hence, the constraint (4.5) is satisfied and no internal force $\boldsymbol{h}_{\text{int}}$ occurs here. We are now ready to show that $\boldsymbol{e}_1 \neq 0$ causes an internal force by substituting $\tilde{\boldsymbol{x}}_2 \in \tilde{x}_2^* \mathbf{1}$ and $\tilde{\boldsymbol{x}}_1 = -A_{f1}^{-1} B_{f1} \tilde{\boldsymbol{x}}_2$ into

$$\boldsymbol{e}_1 = \tilde{\boldsymbol{x}}_1 + A_{f1}^{-1} B_{f1} \tilde{\boldsymbol{x}}_2 = \tilde{\boldsymbol{x}}_1 + A_{f1}^{-1} B_{f1} \tilde{\boldsymbol{x}}_2^* \mathbf{1} = \tilde{\boldsymbol{x}}_1 - \tilde{\boldsymbol{x}}_2^* \mathbf{1},$$

where we can see that if $\tilde{\boldsymbol{x}}_1 - \tilde{x}_2^* \mathbf{1} \neq 0$ we have a difference between $\tilde{\boldsymbol{x}}_2$ and $\tilde{\boldsymbol{x}}_1$. Hence, by definition we have a difference between the states of the direct followers and the indirect followers. Due to that difference both $\tilde{\boldsymbol{x}}_1$ and $\tilde{\boldsymbol{x}}_2$ cannot be equal. Hence, for $\boldsymbol{e}_1 \neq 0$ the constraint (4.5) is violated which causes an internal force $\boldsymbol{h}_{\text{int}}$ acting on the object. However due to (4.27) we know that there is no internal force $\boldsymbol{h}^{\text{int}} \to 0$ induced by $\boldsymbol{e}_1 = 0$ as $\gamma_1 \to \infty$. □

Note that from a practical point of view it is impossible and preposterous to choose $\gamma_1 \to \infty$. However, it is often sufficient to choose γ_1 very large in comparison with γ_2. In this section we introduced weights for the set-point generator in order to significantly reduce the internal wrench acting on the object based on a controllability analysis. Controllability plays a major role in the system analysis of a human-guided multi-robot manipulation task. In the next step we discuss controllability of the multi-robot interaction dynamics and the controllability of the overall system consisting of set-point generator and interaction dynamcis.

4.5 Controllability of the Human-guided Cooperative Manipulation Task

The influence of the human input on particular set-points given by a controllability analysis gives us fundamental insight in the guidance of the set-points. We now extend this result by examining the human influence on both the particular robot set-points and the object motion by investigating the controllability of the impedance-based interaction dynamics (2.29) and the controllability of the overall system in serial connection. Note here that we follow the argumentation in Section 4.4 and discuss the controllability of (2.29) only for a single direction of space. Calculating the controllability of (2.29) with Lie algebra for the translational and rotational motions yields the same result as the simplified version addressing only one direction in space. However, in this analysis we focus on the controllability problem in one direction in space which can be presented more clearly as discussed in Section 4.4 in a similar fashion.

4.5.1 Controllability of the Impedance-based Multi-Robot Dynamics

A simplified version of multi-robot interaction dynamical system (2.29) in one direction under $\zeta = \left[p_o, \dot{p}_o\right]^\intercal \in \mathbb{R}^2$ reads as

$$\begin{aligned}\dot{\zeta} &= \begin{bmatrix} 0 & 1 \\ \Pi \sum_{i=1}^{N} k_i & \Pi \sum_{i=1}^{N} d_i \end{bmatrix} \zeta + \begin{bmatrix} 0 \\ \Pi \end{bmatrix} \boldsymbol{k}^\intercal \boldsymbol{x} \\ &= A_{\text{imp}} \zeta + \boldsymbol{b}_{\text{imp}} \boldsymbol{k}^\intercal \boldsymbol{x}, \end{aligned} \tag{4.29}$$

where $\Pi = -(m_o + \sum_{i=1}^{N} m_i)^{-1}$ and $\boldsymbol{k} = [k_1, \ldots, k_N]^\intercal$. Once again we employ (4.15) to derive the controllability matrix of the interaction dynamics given by

$$Q_{\text{imp}} = \begin{bmatrix} \boldsymbol{b}_{\text{imp}} & A_{\text{imp}} \boldsymbol{b}_{\text{imp}} \end{bmatrix} = \begin{bmatrix} 0 & \Pi^1 \\ \Pi^1 & \Pi^2 \sum_{i=1}^{N} d_i, \end{bmatrix},$$

where we can directly observe by inspection that $\text{rank}(Q_{\text{imp}}) = 2$ if $m_o < \infty, m_i < \infty$. So the interaction dynamics of cooperating distributed impedances under a rigid grasp are completely controllable for a single direction in space.

4.5.2 Controllability of the Guided Cooperative Manipulation Task

In this section we evaluate the controllability of the simplified versions of the set-point generator (4.14) and the interaction dynamics (4.29). The overall state $\boldsymbol{z}$ is then labeled as $\boldsymbol{z} = \left[\boldsymbol{x}^\intercal, \zeta^\intercal\right]^\intercal$. To evaluate the controllability of the serial concatenation we first have to evolve the complete system dynamics. For a single direction in space the series concatenation of the human-guided set-point generator (4.14) and the multi-robot interaction dynamics (4.29) results as

$$A_{\text{tot}} = \begin{bmatrix} A_{\text{fms}} & 0 \\ \boldsymbol{b}_{\text{imp}} \boldsymbol{k}^\intercal & A_{\text{imp}} \end{bmatrix}, \quad \boldsymbol{b}_{\text{tot}} = \begin{bmatrix} \boldsymbol{b}_{\text{fms}} \\ 0 \end{bmatrix}. \tag{4.30}$$

Evaluating the controllability condition (4.15) of the concatenated system (4.30) then results in

$$Q_{\text{tot}} = \begin{bmatrix} Q_1^* & \cdots & Q_i^* & \cdots & Q_{N+2}^* \\ Q_1^{**} & \cdots & Q_i^{**} & \cdots & Q_{N+2}^{**} \end{bmatrix}, \tag{4.31}$$

where the submatrices Q_i^*, Q_i^{**} of Q_{tot} are given as

$$Q_i^* = A_{\text{fms}}^{i-1} \boldsymbol{b}_{\text{fms}} \text{ if } i = 1, \ldots, N+2,$$

and

$$Q_i^{**} = \begin{cases} 0 & \text{if } i = 1 \\ \sum_{j=0}^{i-2} A_{\text{imp}}^{j} \boldsymbol{b}_{\text{imp}} \boldsymbol{k}^\intercal A_{\text{fms}}^{i-2-j} \boldsymbol{b}_{\text{fms}} & \text{if } i = 2, .., N+2. \end{cases}$$

The controllability of serial concatenation of dynamical systems is a rarely studied problem. In general, it is known [155] that the number of controllable states of the complete system is less or equal to the sum of controllable states of the particular systems:

$$\operatorname{rank}(Q_{\text{tot}}) \leq \operatorname{rank}(Q_{\text{fms}}) + \operatorname{rank}(Q_{\text{imp}}).$$

To avoid internal force acting on the object we introduced in Proposition 4.1 that the human input u is known by all robots and so the input vector reads as $\boldsymbol{b}_{\text{fms}} = \mathbf{1}$. Using $A_{\text{fms}}^k \boldsymbol{b}_{\text{fms}} = (-1)^k \mathbf{1}$ and $\boldsymbol{k}^\intercal \mathbf{1} = \sum_{i=1}^{N} k_i$, the overall controllability matrix (4.31) can then be simplified as

$$\begin{aligned} Q &= \begin{bmatrix} \mathbf{1} & -\mathbf{1} & \dots & (-1)^{N+2}\mathbf{1} \\ 0 & \boldsymbol{b}_{\text{imp}}\boldsymbol{k}^\intercal\mathbf{1} & \dots & \sum_{j=0}^{N-1} -1^{N-1-j} A_{\text{imp}}^j \boldsymbol{b}_{\text{imp}}\boldsymbol{k}^\intercal\mathbf{1} \end{bmatrix} \\ &= \begin{bmatrix} \mathbf{1} & -\mathbf{1} & \mathbf{1} & .. \\ 0 & \sum_{i=1}^{N} k_i \boldsymbol{b}_{\text{imp}} & \sum_{i=1}^{N} k_i (A_{\text{imp}}\boldsymbol{b}_{\text{imp}} - \boldsymbol{b}_{\text{imp}}) & .. \end{bmatrix}. \end{aligned} \tag{4.32}$$

As previously derived for $\boldsymbol{b}_{\text{fms}} = \mathbf{1}$ we have $\operatorname{rank}(Q_{\text{fms}}) = 1$ and $\operatorname{rank}(Q_{\text{imp}}) = 2$ is always valid. Hence, the rank of the concatenated system results as $\operatorname{rank}(Q) \leq 3$. In our proposed scheme, $\boldsymbol{b}_{\text{fms}} = \mathbf{1}$, we can observe that $\operatorname{rank}(Q_{\text{tot}}) = 3$ by only inspecting the first three columns of (4.32). From a theoretical perspective the human operator can independently influence the set-points of the multi-robot team $\boldsymbol{x}$, the object velocity $\dot{p}_o$, and the object position p_o in one particular direction in space.

However, for $\boldsymbol{b}_{\text{fms}} \neq \mathbf{1}$ a rank-deficiency of the controllability matrix Q can occur due to a special interplay of the impedance-based dynamics $A_{\text{imp}}/\boldsymbol{b}_{\text{imp}}$ and the set-point generator dynamics $A_{\text{fms}}/\boldsymbol{b}_{\text{fms}}$. The reason for this rank-deficiency is that the null-space of $Q^* = \left[Q_1^* \dots Q_i^* \dots Q_{N+2}^*\right]$ and the null-space of $Q^{**} = \left[Q_1^{**} \dots Q_i^{**} \dots Q_{N+2}^{**}\right]$ can intersect and so the intersecting space lies also in the null-space of Q. Then there can exist a vector

$$(r * s) \neq 0 \in \ker(Q^{*\intercal}) \cap \ker(Q^{**\intercal}),$$

which satisfies both $Q^*(r * s) = \mathbf{0}$ and $Q^{**}(r * s) = \mathbf{0}$. Consequently $r * s$ lies in the null-space of Q_{tot}, too.

To show such a rank-deficiency of Q we have a closer look at the first rows of Q as $Q^* = \left[I_N \dots A_{\text{fms}}^{i-1} \dots A_{\text{fms}}^{N+2}\right] \boldsymbol{b}_{\text{fms}}$. When analyzing the null-space of Q^* the Cayley-Hamilton theorem is helpful. The Cayley-Hamilton theorem states that A_{fms} satisfies its own characteristic equation $\rho_{A_{\text{fms}}}(A_{\text{fms}})$:

$$\rho_{A_{\text{fms}}}(A_{\text{fms}}) = r^\intercal \begin{bmatrix} I_N \\ A_{\text{fms}} \\ \vdots \\ A_{\text{fms}}^N \end{bmatrix} = 0, \tag{4.33}$$

where $r \in \mathbb{R}^N$ is the coefficient vector of the characteristic polynomial $\rho_{A_{\text{fms}}}(t)$ of order N

belonging to the system matrix A_{fms}. The roots A_{fms} of the polynomial $\rho_{A_{\text{fms}}}$ is invariant to a multiplication of $\rho_{A_{\text{fms}}}$ with any other polynomial $\sigma(t)$ of degree 2. Note here that the factor 2 accounts for the monomials A_{fms}^{N+1} and A_{fms}^{N+2} which are not present in (4.33) but in Q^*. The coefficient vector of $\sigma(t)$ is denoted by s. The multiplication of both polynomials $\rho(t)\sigma(t)$ is the convolution of the coefficient vectors $s * r$ where the operator $*$ denotes convolution. To account for the factors $I, A_{\text{fms}}, A_{\text{fms}}^2, \ldots, A_{\text{fms}}^{N+2}$ of Q_i^* we result in the multiplied characteristic polynomial as:

$$(r * s)^\intercal \begin{bmatrix} I_N \\ A_{\text{fms}} \\ \vdots \\ A_{\text{fms}}^N \\ A_{\text{fms}}^{N+2} \end{bmatrix} = 0.$$

Hence, there always exists a vector $r * s$ which is in the null-space of the first N rows of Q_{tot} given by

$$r * s \in \ker(\begin{bmatrix} \boldsymbol{b}_{\text{fms}} & A_{\text{fms}}\boldsymbol{b}_{\text{fms}} & \ldots & A_{\text{fms}}^{N+2}\boldsymbol{b}_{\text{fms}} \end{bmatrix}^\intercal),$$

which shows that the null-space of $\left[Q_1^*, \ldots, Q_{N+2}^*\right]$ has at least two free parameters which are constituted by the entries of vector s.

For the controllability submatrix Q^{**} the Cayley-Hamilton theorem is not applicable since the particular entries Q_i^{**} are sums of the matrix products with A_{fms} and A_{imp} where the powers of A_{fms} and A_{fms} are increasing and decreasing, respectively. We have to numerically determine the null-space $\ker(Q^{**\intercal})$ and check if $\ker(Q^{**\intercal})$ intersects with $\ker(Q^{*\intercal})$. A general method to determine intersecting null-spaces using a singular value decomposition is described in Appendix A based on the results in [156]. Note here that Q^{**} depends on A_{imp} and A_{imp} depends on the impedance parameters m, d, k. So particular impedance parameters m, d, k can cause that intersection and the rank-deficiency of Q_{tot}. If now under a specific interplay of $A_{\text{fms}}, A_{\text{imp}}, \boldsymbol{b}_{\text{imp}}$, the vector $(r * s)$ also lies in the null space of the last rows $\left[Q_1^{**}, \ldots, Q_{N+2}^{**}\right]$ of Q_{tot} then

$$(r * s)^\intercal \begin{bmatrix} 0 \\ \boldsymbol{b}_{\text{imp}}\boldsymbol{k}^\intercal\boldsymbol{b}_{\text{fms}} \\ \vdots \\ \sum_{j=0}^{N+2} A_{\text{imp}}^j \boldsymbol{b}_{\text{imp}}\boldsymbol{k}^\intercal (A_{\text{fms}})^{N-j}\boldsymbol{b}_{\text{fms}} \end{bmatrix} = 0.$$

Hence, $(r * s)$ lies in the null-space of Q_{tot} and so there is a rank-deficiency of the overall controllability matrix Q_{tot}. Under this special condition $\text{rank}(Q_{\text{tot}}) < \text{rank}(Q_{\text{fms}}) + \text{rank}(Q_{\text{imp}})$ and the human operator cannot control the set-points $\boldsymbol{x}$ and the object position $\boldsymbol{p}_o$ independently.

Example 4.3. We revise the set-point generator dynamics (4.10) from Example 4.1 here. The characteristic polynomial (4.33) of the linearized formation-based trajectory generation method (4.10) is $\rho_{A_{\text{fms}}}(t) = t^3 + 8t^2 + 18t + 8$ and $r = [1, 8, 18, 8]^\intercal$. The impedance parameter of the overall impedance dynamics concerning mass $\sum_{i=1}^{3} m_i + m_o = 31$ and stiffness $\sum_{i=1}^{3} k_i = 480$ are taken from

(2.39) in Example 2.2. The damping d is selected to be the free parameter to illustrate a potential rank-deficiency of Q_{tot}. Hence, the system matrices of impedance-based multi-robot cooperation (4.29) are given by

$$\dot{\zeta} = \begin{bmatrix} 0 & 1 \\ -\frac{480}{31} & -\frac{d}{31} \end{bmatrix} \zeta + \begin{bmatrix} 0 \\ -\frac{1}{31} \end{bmatrix} \boldsymbol{k}^{\mathsf{T}} \boldsymbol{x},$$

where $\zeta = [p_o, \dot{p}_o]^{\mathsf{T}}$. With $\boldsymbol{z} = [x_1, x_2, x_3, p_o, \dot{p}_o]^{\mathsf{T}}$, the concatenated system (4.30) is given by

$$\dot{\boldsymbol{z}} = \begin{bmatrix} -3 & 1 & 1 & 0 & 0 \\ 1 & -2 & 1 & 0 & 0 \\ 1 & 1 & -3 & 0 & 0 \\ 0 & 0 & 0 & 0 & 1 \\ -\frac{160}{31} & -\frac{160}{31} & -\frac{160}{31} & -\frac{480}{31} & -\frac{d}{31} \end{bmatrix} \boldsymbol{z} + \begin{bmatrix} 1 \\ 0 \\ 1 \\ 0 \\ 0 \end{bmatrix} u_h.$$

By evaluating the complete controllability matrix (4.31) for the system we observe that the rank of Q_{tot} is different as

$$\operatorname{rank}(Q_{\text{tot}}) = \begin{cases} 3 & \text{if } d = \frac{3762}{31} \vee d = \frac{9108}{31} \\ 4 & \text{if } d \neq \frac{3762}{31} \vee d \neq \frac{9108}{31}. \end{cases}$$

Based on numerical investigations, we assume that for N followers there are $N-1$ damping coefficients leading to that phenomena of rank-deficiency of Q_{tot}. As observed for three following robots there are two specific values of d which can lead to a rank-deficiency of Q_{tot}.

Since this rank-deficiency of Q_{tot} is just artificially induced by the interplay of the impedance-based (2.29) and the formation-based (4.9) dynamical system it has no effect on the internal force (2.33) which is only cased by the formation-based set-point generator. After discussing controllability properties of the guided cooperative manipulation task we are now ready to discuss the equilibria of the system dynamics, the stability of the equilibria, and the input-output behavior of the proposed interaction mechanism resulting from a human input in the next section.

4.6 Stability Analysis of the Human-guided Cooperative Manipulation Task

From a system theoretical perspective, the overall system is a serial concatenation of two dynamical systems: the formation control approach (4.9) which defines the input, namely the set-points ξ^d weighted by the total stiffness matrix $\mathscr{K}$, for the cooperative manipulation task dynamics (2.29). As the formation-based set-point generator only produces set-points ξ^d we set $\boldsymbol{v}_i^d = \dot{\boldsymbol{v}}_i^d = \boldsymbol{0}$ in (2.29). The signal flow plan of the overall structure is depicted as follows:

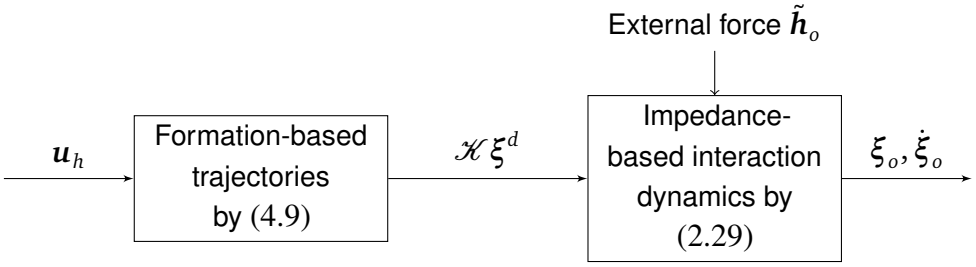

Note here that for the stability analysis we employ again the nonlinear dynamics (4.9) and (2.29) instead of their simplified linear versions (4.14) and (4.29). The reason is because the nonlinearity of the dynamical system leads to multiple equilibria and because it thus plays an important role when showing stability of the equilibria. First, we discuss the equilibria of the object which is approached based on a constant human input $\boldsymbol{u}_h$ and the distributed set-point generator. Subsequently, we provide an input-output model which relates the object velocity $\dot{\xi}_o$ of the impedance-based interaction dynamics to the human input $\boldsymbol{u}_h$.

4.6.1 Equilibria of the Cooperative Manipulation Task and Their Stability

In this section we investigate the Lyapunov stability of the overall system from a *constant* human input $\boldsymbol{u}_h$ to the output of the multi-robot cooperative manipulation task ξ_o. The equilibria of (4.9) and (2.29) are discussed separately since the equilibria of the human-guided set-point generator (4.9) and their stability are independent of (2.29). By doing so we can directly observe if the equilibria are in line with the constraints in a cooperative manipulation task. The equilibria of the impedance-based multi-robot dynamics (2.29) and their stability are then discussed both generally for any set-points and then in particular for the set-points equilibria generated by the human input in (4.9). As a result the separate discussion of the equilibria not only produces a more intelligible result but also provides us with more insights into the problem.

Equilibria and Stability of the Human-guided Set-point Generator

Given a specific human input $\boldsymbol{u}_h$ we are at first interested what the resultant desired set-points ξ^d are. In other words we are ready to derive the equilibiria of the set-point generator (4.9) and their stability properties. The stability of the set-point generator (4.9) for a constant human input $\boldsymbol{u}_h$ is analyzed in this section. Please note here at this stage that due to the use of quaternions $\boldsymbol{q}_i^d = \boldsymbol{q}_h$ and $\boldsymbol{q}_i^d = -\boldsymbol{q}_h$ stands for the same physical rotation. Hence, there exist two possible equilibria for the set-point generator which is formally stated in Proposition 4.5. In Proposition 4.6 we subsequently show that $\boldsymbol{q}_i^d = \boldsymbol{q}_h$ is the only stable equilibrium.

Proposition 4.5. *Under Assumptions 3.4 and 4.1 the human-guided set-point generator* (4.9) *has the following two equilibria, for all robotic manipulator* i*:*

$$\xi_i^d = \begin{pmatrix} \boldsymbol{p}_i^d \\ \boldsymbol{q}_i^d \end{pmatrix} = \begin{pmatrix} \boldsymbol{x}_h + \boldsymbol{d}_{ih} \\ \boldsymbol{q}_h \end{pmatrix}, \tag{4.34}$$

and

$$\xi_i^d = \begin{pmatrix} \boldsymbol{p}_i^d \\ \boldsymbol{q}_i^d \end{pmatrix} = \begin{pmatrix} \boldsymbol{x}_h + \boldsymbol{d}_{ih} \\ -\boldsymbol{q}_h \end{pmatrix}. \tag{4.35}$$

Proof. The equilibria of (4.9) clearly satisfy $\dot{\boldsymbol{x}}^p = \boldsymbol{0}$ and $\dot{\boldsymbol{x}}^q = \boldsymbol{0}$. We start with the rotational set-point generator for the desired robot orientations (4.9b) here as

$$\boldsymbol{0} = \frac{1}{2}\,\mathscr{U}(\boldsymbol{x}^q)\big((A_{\text{fms}} \otimes I_4)\boldsymbol{x}^q + (\boldsymbol{b}_{\text{fms}} \otimes I_4)\boldsymbol{q}_h\big), \tag{4.36}$$

where we substitute (4.8) for $\boldsymbol{b}_{\text{fms}}$ and employ $(A_{\text{fms}}\boldsymbol{1} \otimes I_4) = (A_{\text{fms}} \otimes I_4)(\boldsymbol{1} \otimes 1)$ to rewrite (4.36) as

$$\boldsymbol{0} = \frac{1}{2}\,\mathscr{U}(\boldsymbol{x}^q)(A_{\text{fms}} \otimes I_4)\big(\boldsymbol{x}^q - (\boldsymbol{1} \otimes \boldsymbol{q}_h)\big). \tag{4.37}$$

It is obvious that the trivial solution $\boldsymbol{x}^q = (\boldsymbol{1} \otimes \boldsymbol{q}_h)$ satisfies (4.37). Note here that $(A_{\text{fms}} \otimes I_4)$ is full-rank and the A_{fms} matrix has only integer entries. Hence, a solution of (4.37) can also lie in the null-space of the matrix $\mathscr{U}(\boldsymbol{x}^q)$ which is given by (2.6c). Due to that and the fact that the null-space must be an integer combination of $\boldsymbol{x}_i^q$ and $\boldsymbol{q}_h$ the solution of (4.37) is $\boldsymbol{q}_i^d = \boldsymbol{x}_i^q = \pm\boldsymbol{q}_h$. Consequently, we obtain the equilibria of the translational set-point generator (4.9a) by setting $\dot{\boldsymbol{x}}^p = 0$ as $\boldsymbol{0} = (A_{\text{fms}} \otimes I_3)\boldsymbol{x}^p + (\boldsymbol{b}_{\text{fms}} \otimes I_3)\boldsymbol{x}_h$ and the equilibria of (4.9a) are

$$\boldsymbol{x}^p = (-A_{\text{fms}}^{-1}\boldsymbol{b}_{\text{fms}} \otimes I_3)\boldsymbol{x}_h = \boldsymbol{1} \otimes \boldsymbol{x}_h,$$

where we use (4.3) to see that

$$\boldsymbol{p}_i^d = \boldsymbol{x}_h + \boldsymbol{d}_{ih},$$

which concludes our proof. □

We now define a set of robot set-points which only excludes the equilibrium (4.35) given by

$$\Omega_{\text{fms}} = \{\xi_i^d = \begin{pmatrix} \boldsymbol{p}_i^d \\ \boldsymbol{q}_i^d \end{pmatrix} | \boldsymbol{p}_i^d \in \mathbb{R}^3, \boldsymbol{q}_i^d \in SO(3) \cap \boldsymbol{q}_i^d \neq -\boldsymbol{q}_h\}.$$

At this point we are ready to state the stability of the set-point generator.

Proposition 4.6. *Let Assumptions 3.4 and 4.1 hold and let the initial states $\xi_i^d(t_o) \in \Omega_{fms}$. Then the equilibrium* (4.34) *of the human-guided set-point generator* (4.9) *is asymptotically stable.*

Proof. To show stability of set-point generator (4.9) we employ the following Lyapunov function candidate

$$V_{\text{fms}} = \frac{1}{2}\hat{\boldsymbol{x}}^\intercal(L \otimes I_7)\hat{\boldsymbol{x}}, \tag{4.38}$$

where the human-extended Laplacian matrix L is defined in (4.7). Note here that V_{fms} is positive definite and radially unbounded with respect to $\boldsymbol{x}_i - \boldsymbol{x}_j$ and $\boldsymbol{x}_i - \boldsymbol{u}_h$ for all $i \in N$ and $j \in N_i$. Using the fact that $\dot{\boldsymbol{u}}_h = \boldsymbol{0}$ the time-derivative of V is given by

$$\begin{aligned}\dot{V}_{\text{fms}} &= \hat{\boldsymbol{x}}^\intercal (L \otimes I_7)\dot{\hat{\boldsymbol{x}}} \\ &= \left[\boldsymbol{x}^{p\intercal}, \boldsymbol{x}_h^\intercal\right](L \otimes I_3)\begin{bmatrix} \dot{\boldsymbol{x}}^p \\ 0 \end{bmatrix} + \left[\boldsymbol{x}^{q\intercal}, \boldsymbol{q}_h^\intercal\right](L \otimes I_4)\begin{bmatrix} \dot{\boldsymbol{x}}^q \\ 0 \end{bmatrix} \\ &= -\dot{\boldsymbol{x}}^{p\intercal}\dot{\boldsymbol{x}}^p - \dot{\boldsymbol{x}}^{q\intercal}\dot{\boldsymbol{x}}^q \leq 0,\end{aligned}$$

where we employ (4.7) for the human-extended Laplacian L. Referring to Proposition 4.5 the set-point generator has two possible equilibria given by (4.34) and (4.35). Using (4.38) it is shown that the equilibrium (4.34) represents the minimum energy and any perturbation from (4.34) drives the system to (4.34). The proof is concluded by stating that $\xi_i^d(t)$ is bounded and the equilibrium (4.34) is the only point in Ω_{fms} where $\dot{V}_{\text{fms}} = 0$. Hence, due to LaSalle's invariance principle Ω_{fms} is the region of attraction in which the equilibrium (4.34) is asymptotically stable. Hence, (4.35) is unstable. □

Equilibria and Stability of the Impedance-based Multi-Robot Dynamics

Given distributed manipulator set-points ξ^d we are now interested in the resultant object pose ξ_o which are the equilibria of the interaction dynamics (2.29) and their stability properties. The stability of the impedance-based interaction dynamics (2.29) is analyzed by first deriving the equilibria generally in Proposition 4.7. In the following we discuss the particular implication of the proposed set-point generator (4.8) on the equilibria discussed in Proposition 4.7. We conclude this section by showing asymptotic stability of the interaction dynamics (2.29) under the proposed set-point generator (4.9) . Yet, before stating the equilibria of (2.29) we have to make clear that the potential solutions of a quaternion orientation error

$$U(\boldsymbol{q}_i)^\intercal \boldsymbol{q}_s = \boldsymbol{\tau}, \tag{4.39}$$

where $\boldsymbol{q}_i$ and $\boldsymbol{\tau}$ are known and $\boldsymbol{q}_s$ is the unknown quaternion are given by

$$\bar{\bar{\boldsymbol{q}}}_s = \bar{\boldsymbol{q}}_s + \alpha \boldsymbol{q}_i, \tag{4.40}$$

where $\bar{\boldsymbol{q}}_i$ is one particular solution of the underdetermined system of linear equations (4.39). Note here that in general there are infinitely many solutions. Yet we have to ensure that the solution $\bar{\bar{\boldsymbol{q}}}_i$ is also a unit quaternion by the scalar weight α which is then given by

$$\alpha = -\boldsymbol{q}_i^\intercal \bar{\boldsymbol{q}}_s \pm \sqrt{\boldsymbol{q}_i^\intercal \bar{\boldsymbol{q}}_s \boldsymbol{q}_i^\intercal \bar{\boldsymbol{q}}_s + (1 - \bar{\boldsymbol{q}}_s^\intercal \bar{\boldsymbol{q}}_s)}.$$

Hence, there exist always two solutions of (4.40) which are unit quaternions.

Proposition 4.7. *Let Assumptions 2.2 and 2.3 hold. Then the impedance-based multi-robot*

dynamics (2.29) *have the following equilibria*

$$\begin{pmatrix} \boldsymbol{v}_o \\ \boldsymbol{p}_o \\ \boldsymbol{q}_o \end{pmatrix} = \begin{pmatrix} \mathbf{0} \\ \frac{1}{N}\sum_i \boldsymbol{p}_i^d + \frac{1}{Nk}\tilde{\boldsymbol{f}}_o \\ \bar{\boldsymbol{q}}_o \end{pmatrix}, \tag{4.41}$$

where $\bar{\boldsymbol{q}}_o$ *is the solution of*

$$U(\sum_i \boldsymbol{q}_i^d)^\intercal q_o = \frac{1}{\kappa}\tilde{\boldsymbol{\tau}}_o + \frac{k}{\kappa}\sum_i S(\boldsymbol{r}_i)\boldsymbol{p}_i^d.$$

There are two rotational equilibria for (4.41) *due to* (4.40). .

Proof. The potential equilibria of (2.29) obviously satisfy $\boldsymbol{v}_o = \mathbf{0}$ and $\dot{\boldsymbol{v}}_o = \mathbf{0}$ which yields

$$\mathcal{K}_o \xi_o = \sum_i \mathcal{K}_i \xi_i^d + \tilde{\boldsymbol{h}}_o,$$

and in turn implies the particular equilibria of the positions and orientations as

$$\begin{aligned} \sum_i k_i \boldsymbol{p}_o &= \sum_i k_i \boldsymbol{p}_i^d + \tilde{\boldsymbol{f}}_o, \\ \mathbf{0} &= \sum_i k_i S(\boldsymbol{r}_i)^\intercal \boldsymbol{p}_i^d + \sum_i \kappa_i U(\boldsymbol{q}_o)^\intercal \boldsymbol{q}_i^d + \tilde{\boldsymbol{\tau}}_o. \end{aligned} \tag{4.42}$$

Solving (4.42) for $\boldsymbol{p}_o, \boldsymbol{q}_o$ and emplyoing Assumptions 2.2 and 2.3 yields (4.41). Due to (4.40) there are two rotational equilibria. □

Proposition 4.8. *Let Assumptions 2.2 and 2.3 hold and assume that there is no force disturbance* $\tilde{\boldsymbol{f}}_o = \mathbf{0}$*. Then the equilibria of the interaction dynamics* (2.29) *driven by the distributed set-point generator* (4.9) *are*

$$\begin{pmatrix} \boldsymbol{v}_o \\ \boldsymbol{p}_o \\ \boldsymbol{q}_o \end{pmatrix} = \begin{pmatrix} \mathbf{0} \\ \boldsymbol{x}_h + \frac{1}{N}\sum_i \boldsymbol{d}_{ih} \\ \boldsymbol{q}_h \end{pmatrix}, \tag{4.43}$$

and

$$\begin{pmatrix} \boldsymbol{v}_o \\ \boldsymbol{p}_o \\ \boldsymbol{q}_o \end{pmatrix} = \begin{pmatrix} \mathbf{0} \\ \boldsymbol{x}_h + \frac{1}{N}\sum_i \boldsymbol{d}_{ih} \\ -\boldsymbol{q}_h \end{pmatrix}. \tag{4.44}$$

Proof. The proof is the straightforward application of Propositions 4.5 and 4.8. We set $\tilde{\boldsymbol{f}}_o = \mathbf{0}$ and replace the particular set-points $\boldsymbol{p}_i^d$ in (4.41) by (4.34). Note here that $\sum_i k_i S(\boldsymbol{r}_i)^\intercal(\boldsymbol{x}_h + \boldsymbol{d}_{ih}) = \mathbf{0}$ due to Assumption 2.2 and $\boldsymbol{d}_{ih} = \boldsymbol{r}_i - \boldsymbol{r}_h$. □

We now define a set of object poses which only excludes the equilibrium (4.44) given by

$$\Omega_{\text{imp}} = \{ \begin{pmatrix} \boldsymbol{v}_o \\ \boldsymbol{p}_o \\ \boldsymbol{q}_o \end{pmatrix} | \boldsymbol{v}_o \in \mathbb{R}^6, \boldsymbol{p}_o \in \mathbb{R}^3, \boldsymbol{q}_o \in SO(3) \cap \boldsymbol{q}_o \neq -\boldsymbol{q}_h \}.$$

Proposition 4.9. *Let Assumptions 2.2 and 2.3 hold. Further, let* $\tilde{\boldsymbol{f}}_o = \boldsymbol{0}$ *and the initial state* $\left(\boldsymbol{v}_o^\intercal, \boldsymbol{p}_o^\intercal, \boldsymbol{q}_o^\intercal\right)^\intercal \in \Omega_{imp}$*. Then the equilibrium* (4.43) *is asymptotically stable. .*

Proof. To show stability of the interaction dynamics (2.29) we employ the following Lyapunov function candidate

$$V_{\text{imp}} = \frac{1}{2}\boldsymbol{v}_o^\intercal \mathscr{M} \boldsymbol{v}_o + (\xi_o - \xi_o^d)^\intercal \begin{bmatrix} \frac{1}{2}kI_3 & 0 \\ 0 & 2\kappa I_4 \end{bmatrix} (\xi_o - \xi_o^d),$$

which is positive definite and radially unbounded with regards to $\boldsymbol{v}_o$ and $(\xi_o - \xi_o^d)$ and due to the usage of the set-point generator (4.9) the desired object pose ξ_o^d is given by

$$\xi_o^d = \begin{pmatrix} \boldsymbol{x}_h + \frac{1}{N}\sum_i \boldsymbol{d}_{ih} \\ \boldsymbol{q}_h \end{pmatrix}.$$

Using (2.7), (2.29), (2.4) the time-derivative of V_{imp} is given by

$$\begin{aligned} \dot{V}_{\text{imp}} &= \frac{1}{2}\boldsymbol{v}_o^\intercal \dot{\mathscr{M}} \boldsymbol{v}_o + \boldsymbol{v}_o^\intercal \mathscr{M} \dot{\boldsymbol{v}}_o + \dot{\xi}_o^\intercal \begin{bmatrix} kI_3 & 0 \\ 0 & 4\kappa I_4 \end{bmatrix} (\xi_o - \xi_o^d) \\ &= \frac{1}{2}\boldsymbol{v}_o^\intercal (\dot{\mathscr{M}} - 2\mathscr{C}_o)\boldsymbol{v}_o - \boldsymbol{v}_o^\intercal \mathscr{D} \boldsymbol{v}_o + \boldsymbol{v}_o^\intercal \left(\begin{bmatrix} kI_3 & 0 \\ 0 & 2\kappa U(\boldsymbol{q}_o)^\intercal \end{bmatrix} \xi_o - \boldsymbol{h}_o^\kappa(\xi_o, \xi_o^d) \right) \\ &= -\boldsymbol{v}_o^\intercal \mathscr{D} \boldsymbol{v}_o \leq 0, \end{aligned}$$

where a straightforward calculation shows that $\frac{1}{2}\boldsymbol{v}_o^\intercal(\dot{\mathscr{M}} - 2\mathscr{C}_o)\boldsymbol{v}_o = 0$ which is a consequence of the Hamilton principle of conservation of energy. Note here that $\dot{V}_{\text{imp}}$ is negative semi-definite. We observe that the function candidate V_{imp} decreases as long as $\boldsymbol{v}_o \neq \boldsymbol{0}$. To find the equilibrium of (2.29), we have $\dot{V}_{\text{imp}} = 0$ and $\boldsymbol{v}_o = \boldsymbol{0}$ which rigorously shows that $\dot{V}_{\text{imp}} = 0$ only for (4.43) and (4.44). Since $\left(\boldsymbol{v}_o^\intercal(t), \boldsymbol{p}_o^\intercal(t), \boldsymbol{q}_o^\intercal(t)\right)^\intercal$ is bounded and the equilibrium (4.43) is the only point in Ω_{imp} where $\dot{V}_{\text{imp}} = 0$, (4.43) is asymptotically stable due to LaSalle's invariance principle. By investigating the minimum energy of V_{imp} it is shown that Ω_{imp} is the region of attraction for (4.43). Hence, any perturbation drives the system to (4.43). □

We are now ready to define a input/output relationship from a changing human input $\boldsymbol{u}_h$ to the cooperatively manipulated object velocity $\boldsymbol{v}_o$.

4.6.2 $\mathscr{L}_2$-stability of the Guided Cooperative Manipulation Task

A related approach which relates the interaction topology to stability in a leader-follower setup has been investigated under the term of leader-to-formation stability based on the notation of input-to-state stability [157]. The stability margins in [157] are tighter as they consider a specific

special interaction topologies where all cycles in the underlying graph are of order 3. In this section we now investigate the $\mathscr{L}_2$-stability of the overall system from a human input $\boldsymbol{u}_h$ to the output of the multi-robot cooperative manipulation task $\boldsymbol{\xi}_o$. For the sake of exposition we define the output $\boldsymbol{y}_{\text{fms}}$ of the set-point generator (4.9) to be the transformed set-points which are given by

$$\boldsymbol{y}_{\text{fms}} = \boldsymbol{x}. \tag{4.45}$$

Note that the output is $\boldsymbol{y}_{\text{fms}}$ not exactly the input $\boldsymbol{u}_{\text{imp}}$ of the impedance-based interaction dynamics (2.29). A *static* relation between the output $\boldsymbol{y}_{\text{fms}}$ and the input $\boldsymbol{u}_{\text{imp}}$ of the interaction dynamics (2.29) is given by

$$\boldsymbol{u}_{\text{imp}} = \sum_{i=1}^{N} \mathscr{K}_i \boldsymbol{\xi}_i^d = \mathscr{K} \boldsymbol{\xi}^d = \bar{\mathscr{K}}(\boldsymbol{x} + \boldsymbol{d}_h) = \bar{\mathscr{K}}(\boldsymbol{y}_{\text{fms}} + \boldsymbol{d}_h), \tag{4.46}$$

where $\mathscr{K} = [\mathscr{K}_1, \mathscr{K}_2, \dots \mathscr{K}_N]$ and $\boldsymbol{d_h} = \left[\boldsymbol{d}_{1h}^\intercal, \dots, \boldsymbol{d}_{Nh}^\intercal, \boldsymbol{0}^\intercal, \dots, \boldsymbol{0}^\intercal\right]^\intercal$. Furthermore, the matrix $\bar{\mathscr{K}}$ is a re-ordered variant of $\mathscr{K}$ which accounts for the fact that $\boldsymbol{\xi}^d$ and $\boldsymbol{x} = [\, \boldsymbol{x}^{p\intercal}, \boldsymbol{x}^{q\intercal}]^\intercal$ have different orders by means of positions and quaternions. Since we have already discussed the system equilibria by means of the object pose in the previous chapter we are now mostly concerned with the input-output stability from the distributed set-points to the object velocity. Knowing an approximated input-output relation between a human input and the object velocity is particularly interesting since the object velocity is directly associated with the manipulator velocity as discussed in (2.19) and the manipulator velocity is often absolutely constrained. Without exactly examining the nonlinear system dynamics we can then in advance decide whether a human input violates the manipulator velocity constraints. Since the focus of the cooperative manipulation task is on the velocity of the object from now on, we define the object velocity to be the system output. Hence, the output of the multi-robot cooperative manipulation task (2.29) is chosen to be the object velocity $\boldsymbol{v}_o$ given by

$$\boldsymbol{y}_{\text{imp}} = \boldsymbol{v}_o.$$

For a dynamical system $\mathscr{L}_2$-stability indicates that a "well-behaved" input into the system generates a "well-behaved" output and the system will then be considered a stable system [69]. Let $\|\boldsymbol{u}\|_{\mathscr{L}_2}$ be the $\mathscr{L}_2$-norm of a piecewise continuous, square-integrable functions

$$\|\boldsymbol{u}\|_{\mathscr{L}_2} = \sqrt{\int_0^\infty \boldsymbol{u}^\intercal(t)\boldsymbol{u}(t)dt} \; < \infty,$$

and the space is denoted by $\mathscr{L}_2^m$. The definition of $\mathscr{L}_2$-stability is the notion of bounded-input bounded-output stability. Furthermore, we define an extended space $\mathscr{L}_{2e}^m$ as

$$\mathscr{L}_{2e}^m = \{\boldsymbol{u} \;\mid\; \boldsymbol{u}_\tau \in \mathscr{L}_2^m, \forall \tau \in [0, \infty)\},$$

where $\boldsymbol{u}_\tau$ is a truncation of $\boldsymbol{u}$ defined by

$$\boldsymbol{u}_\tau = \begin{cases} \boldsymbol{u}(t) & 0 \leq t \leq \tau \\ \boldsymbol{0} & t > \tau. \end{cases}$$

The extended space $\mathscr{L}_{2e}^m$ enables us to consider unbounded "ever-growing" signals such as for example unit quaternions of which the norm is by definition always equal to one. Hence, a quaternion does not belong the space $\mathscr{L}_2^4$ but it belongs to the extended space $\mathscr{L}_{2e}^4$.

Definition 4.1 ([69])**.** A continuous function α: $[0, a) \rightarrow [0, \infty)$ is said to belong to class $\mathscr{K}$ if is is strictly increasing and $\alpha(0) = 0$.

Definition 4.2 ([69])**.** A system is said to be (small-signal) $\mathscr{L}_2$-stable if there a class $\mathscr{K}$ function α, defined on $[0, \infty)$, and a nonnegative constant β (and a positive constant r) such that between the input $\boldsymbol{u}_\tau \in \mathscr{L}_2$ and the output $\boldsymbol{y}_\tau \in \mathscr{L}_2$ the following inequality holds:

$$\|\boldsymbol{y}_\tau\|_{\mathscr{L}_2} \leq \alpha(\|\boldsymbol{u}_\tau\|_{\mathscr{L}_2}) + \beta, \quad \forall \boldsymbol{u}, \tau \in [0, \infty)(with \sup_{0 \leq t \leq \tau} \|\boldsymbol{u}\| \leq r).$$

It is said to be finite-gain $\mathscr{L}_2$-stable if there exist nonnegative constants γ and β such that

$$\|\boldsymbol{y}_\tau\|_{\mathscr{L}_2} \leq \gamma \|\boldsymbol{u}_\tau\|_{\mathscr{L}_2} + \beta.$$

To characterize input/output stability, we first derive the relation for the human-guided set-point generator (4.9) from human input to distributed set-points. Then the input/output for the distributed set-point to the object velocity of the impedance-based multi-robot dynamics (2.29) is discussed. Finally, we connect both results to show the input/output stability of the overall system.

$\mathscr{L}_2$-stability of the Human-guided Set-Point Generator

In order to argue about the system stability we first make an assumption about the human input $\boldsymbol{u}_h$.

Assumption 4.2. The human input $\boldsymbol{u}_h$ is $\boldsymbol{u}_h \in \mathscr{L}_{2e}$. This assumption is reasonable and justifiable for us since the (hand) position of the human operator is employed to guide the cooperative manipulation task here. Hence, the maximum operating range of providing a position $\boldsymbol{u}_h$ by the human operator is limited [158]. The position $\boldsymbol{u}_h$ on the human hand and the movement of the human body is bounded due to kinematics constraints occurrent in human physiology.

To show $\mathscr{L}_2$- stability of the human-guided set-point generator (4.9) with the output being $\boldsymbol{x}$ (4.45) we break the problem into finding first an $\mathscr{L}_2$-gain for the linear translational set-point generator (4.9a) with regards to the output $\boldsymbol{x}^p$ and then an $\mathscr{L}_2$ for the nonlinear rotational set-point generator (4.9b) with regards to the output $\boldsymbol{x}^q$. Subsequently we link both results. Hence, we are at first required to calculate the $\mathscr{L}_2$-gain for linear time-invariant systems which is defined in the following theorem taken from [69, Theorem 5.4]:

Theorem 4.2 ([69])**.** *Consider the linear time-invariant system*

$$\dot{\boldsymbol{x}} = A\boldsymbol{x} + B\boldsymbol{u},$$
$$\boldsymbol{y} = C\boldsymbol{x} + D\boldsymbol{u},$$

where A is Hurwitz. Let $G(s) = C(sI - A)^{-1}B + D$. Then, the $\mathscr{L}_2$-gain of the system is $sup_{\omega\in\mathbb{R}}\|G(jw)\|_2$.

Note here that for linear time-invariant system we are able to come up with an exact $\mathscr{L}_2$-gain as described in [69, Theorem 5.4]. Generally, one can only provide an upper bound on the gain. By applying this theorem to the translational set-point generator (4.9) with the output $\boldsymbol{x}^p$ defined in (4.45) we can show $\mathscr{L}_2$-stability in the following theorem.

Theorem 4.3. *The translation set-point generator dynamics* (4.9a) *with input $\boldsymbol{x}_h$ and output $\boldsymbol{x}^p$ defined in* (4.45) *is $\mathscr{L}_2$-stable with gain γ^p:*

$$\|\boldsymbol{x}^p\|_{\mathscr{L}_{2e}} \leq \gamma^p \|\boldsymbol{x}_h\|_{\mathscr{L}_{2e}}.$$

Proof. We apply Theorem 4.2 in the following. The human input $\boldsymbol{u}_h$ is assumed to be $\boldsymbol{u}_h \in \mathscr{L}_{2e}$. We have $A = A_{\text{fms}} \otimes I_3$, $B = \boldsymbol{b}_{fms} \otimes I_3$, $C = I_{3N}$, $D = 0$. The matrix A is Hurwitz since A_{fms} is a principal submatrix of the graph Laplacian $-L$ and all eigenvalues of $-L$ are nonpositive. The interlacing theorem about the spectra of principal matrices states that all eigenvalues of A_{fms} are negativ. Hence, the $\mathscr{L}_2$-gain is given by $\gamma^p = \sup_{\omega\in\mathbb{R}}\|G(jw)\|_2$. □

The rotational set-point generator (4.9b) is nonlinear by definition. However, for showing $\mathscr{L}_2$-stability we can use the fact that both input $\boldsymbol{q}_h$ and output $\boldsymbol{x}^q$ are unit quaternions.

Theorem 4.4. *The rotational set-point generator dynamics* (4.9b) *with input $\boldsymbol{q}_h$ and output $\boldsymbol{x}^q$ defined in* (4.45) *is $\mathscr{L}_2$-stable with gain γ^q:*

$$\|\boldsymbol{x}^q\|_{\mathscr{L}_{2e}} \leq \gamma^q \|\boldsymbol{q}_h\|_{\mathscr{L}_{2e}}. \tag{4.47}$$

Proof. The human input $\boldsymbol{q}_h$ is assumed to be $\boldsymbol{q}_h \in \mathscr{L}_{2e}$. By employing the unit quaternion property $\boldsymbol{q}_h^\intercal \boldsymbol{q}_h = 1$ the $\mathscr{L}_2$-norm of the input $\boldsymbol{q}_h$ is given as

$$\|\boldsymbol{q}_h\|_{\mathscr{L}_{2e}} = \sqrt{\int_0^\infty \boldsymbol{q}_h^\intercal(t)\boldsymbol{q}_h(t)dt} = \sqrt{\int_0^\infty 1dt}. \tag{4.48}$$

The output vector $\boldsymbol{x}^q$ is a concatenated vector of N unit quaternions $\boldsymbol{x}_1^q, \ldots, \boldsymbol{x}_N^q$ and so the

$\mathscr{L}_2$-norm is given by

$$\|\boldsymbol{x}^q\|_{\mathscr{L}_{2e}} = \sqrt{\int_0^\infty \boldsymbol{x}^{q\intercal}(t)\boldsymbol{x}^q(t)dt} = \sqrt{\int_0^\infty N dt} = \sqrt{N}\sqrt{\int_0^\infty 1 dt}. \tag{4.49}$$

By comparing (4.48) and (4.49) we can directly read the $\mathscr{L}_2$-gain as (4.47) where $\gamma^q = \sqrt{N}$. Note that the relation between (4.48) and (4.49) is actually an equality but we employ $\leq$ here in order to be consistent with the formalism of input-output stability. □

We now combine both formal statements in Theorem 4.3 and 4.4 as

$$\|\boldsymbol{x}\|_{\mathscr{L}_{2e}} = \left\| \begin{bmatrix} \boldsymbol{x}^p \\ \boldsymbol{x}^q \end{bmatrix} \right\|_{\mathscr{L}_{2e}} \leq \|\boldsymbol{x}^p\|_{\mathscr{L}_{2e}} + \|\boldsymbol{x}^q\|_{\mathscr{L}_{2e}} \leq \gamma^p \|\boldsymbol{x}_h\|_{\mathscr{L}_{2e}} + \gamma^q \|\boldsymbol{q}_h\|_{\mathscr{L}_{2e}}. \tag{4.50}$$

$\mathscr{L}_2$-Stability of the Impedance-based Multi-Robot Dynamics

The stability of the impedance-based interaction dynamics (2.29) is analyzed by first showing that the system is output strictly passiv. A system is said to be output strictly passive [69, Definition 6.3] if there exists a positive semi-definite function V such that

$$\boldsymbol{u}^\intercal \boldsymbol{y} \geq \dot{V} + \boldsymbol{y}^\intercal \boldsymbol{\rho}(\boldsymbol{y}),$$

and $\boldsymbol{y}^\intercal \boldsymbol{\rho}(\boldsymbol{y}) > 0, \ \ \forall \boldsymbol{y} \neq \boldsymbol{0}$. From output strictly passivity we can later infer $\mathscr{L}_2$-stability. We are now ready to state.

Theorem 4.5. *The dynamical system of impedance-based multi-robot dynamics* (2.29) *is output strictly passive for* $\tilde{\boldsymbol{h}}_o = \boldsymbol{\nu}_i^d = \dot{\boldsymbol{\nu}}_i^d = \boldsymbol{0}$ *with respect to the input* $\boldsymbol{u}_{imp} = \mathscr{K}\boldsymbol{\xi}_d$ *and the output* $\boldsymbol{y}_{imp} = \boldsymbol{\nu}_o$

Proof. We set $\boldsymbol{\nu}_i^d = \dot{\boldsymbol{\nu}}_i^d = \boldsymbol{0}$ in (2.29) as the formation-based set-point generator only generates the desired manipulator poses $\boldsymbol{\xi}_i^d$. We use the storage function

$$V = V_o + T_o + \sum_{i=1}^{N}(V_i + T_i), \tag{4.51}$$

where T_o, V_o are defined in (2.14) and T_i, V_i are defined as

$$T_i = \frac{1}{2}\boldsymbol{\nu}_i^\intercal M_i \boldsymbol{\nu}_i \quad \text{and} \quad V_i = \boldsymbol{\xi}_i^\intercal \begin{bmatrix} \frac{1}{2}kI_3 & 0 \\ 0 & 0 \end{bmatrix} \boldsymbol{\xi}_i,$$

in order to show that the system is output strictly passive. The storage function V is positive semi-definite as the potential energy terms T_o and T_i by definition positive definite. Furthermore, the kinetic energy terms V_o and V_i are positive semi-definite which then shows the positive

semi-definiteness of V. The time-derivative of V results with (2.7), (2.19), (2.20), and (2.29) as

$$\begin{aligned}\dot{V} &= \frac{1}{2}\boldsymbol{\nu}_o^\intercal \dot{\mathcal{M}}\boldsymbol{\nu}_o + \boldsymbol{\nu}_o^\intercal \mathcal{M}\dot{\boldsymbol{\nu}}_o + \sum_{i=1}^{N} \dot{\boldsymbol{\xi}}_i^\intercal \begin{bmatrix} kI_3 & 0 \\ 0 & 0 \end{bmatrix} \boldsymbol{\xi}_i \\ &= -\dot{\boldsymbol{\nu}}_o^\intercal \mathcal{D}\dot{\boldsymbol{\nu}}_o + \dot{\boldsymbol{\nu}}_o^\intercal \mathcal{K}\boldsymbol{\xi}^d \leq \dot{\boldsymbol{\nu}}_o^\intercal \mathcal{K}\boldsymbol{\xi}^d,\end{aligned}$$

where we simplify $\dot{V}$ similar to the considerations outlined in the proof of Prop. 4.9. Hence, we conclude that the system is output strictly passive. □

Remark 4.3. In Theorem 4.5 we neglect the external force given by $\tilde{\boldsymbol{h}}_o = \mathbf{0}$ in order to focus on the $\mathscr{L}_2$-stability of the interaction dynamics which arises merely from the input $\boldsymbol{u}_{\text{imp}} = \mathcal{K}\boldsymbol{\xi}^d$. However, one can analogously show output strictly passivity of (2.29) with the input $\boldsymbol{u}_{\text{imp}} = \mathcal{K}\boldsymbol{\xi}^d + \tilde{\boldsymbol{h}}_o$, too.

From output strictly passivity we can deduce $\mathscr{L}_2$-stability.

Lemma 4.1 ([69]). If the system $\dot{\boldsymbol{x}} = \boldsymbol{f}(t, \boldsymbol{x}, \boldsymbol{u})$, $\boldsymbol{y} = \boldsymbol{h}(t, \boldsymbol{x}, \boldsymbol{u})$ is output strictly passive with $\boldsymbol{u}^\intercal \boldsymbol{y} \geq \dot{V} + \kappa \boldsymbol{y}^\intercal \boldsymbol{y}$, for some $\kappa > 0$, then it is finite-gain $\mathscr{L}_2$-stable and its $\mathscr{L}_2$-gain is less than or equal to $\frac{1}{\kappa}$.

By applying Lemma 4.1 we are now ready to state the $\mathscr{L}_2$-stability of impedance-based multi-robot dynamics (2.29).

Theorem 4.6. *The impedance-based multi-robot dynamics* (2.29) *are finite-gain $\mathscr{L}_2$-stable with respect to the input $\boldsymbol{u}_{imp} = \mathcal{K}\boldsymbol{\xi}^d$ and the output $\boldsymbol{y}_{imp} = \boldsymbol{\nu}_o$, and the gain is less or equal to $\frac{1}{\lambda^{\mathcal{D}}_{max}}$. $\lambda^{\mathcal{D}}_{max}$ denotes the maximum eigenvalue of $\mathcal{D}$.*

Proof. We know that (2.29) is output strictly passive with $\boldsymbol{\nu}_o^\intercal \mathcal{K}\boldsymbol{\xi}^d \geq -\boldsymbol{\nu}_o^\intercal \mathcal{D}\boldsymbol{\nu}_o + \boldsymbol{\nu}_o^\intercal \mathcal{K}\boldsymbol{\xi}^d \geq -\lambda^{\mathcal{D}}_{\max}\boldsymbol{\nu}_o^\intercal \boldsymbol{\nu}_o + \boldsymbol{\nu}_o^\intercal \mathcal{K}\boldsymbol{\xi}^d$. Hence, due to Lemma 4.1 the system is also finite-gain $\mathscr{L}_2$-stable and the input-output relation can be defined with two nonnegative gains as:

$$\|\boldsymbol{\nu}_o\|_{\mathscr{L}_{2e}} \leq \gamma^{\text{imp}} \|\mathcal{K}\boldsymbol{\xi}^d\|_{\mathscr{L}_{2e}} + \beta^{\text{imp}}, \tag{4.52}$$

where $\gamma^{\text{imp}} = \frac{1}{\lambda^{\mathcal{D}}_{\max}}$ and $\beta^{\text{imp}} = \sqrt{\frac{2}{\lambda^{\mathcal{D}}_{\max}} V(\boldsymbol{\xi}(t_0))}$ as derived in [69]. $V(\cdot)$ is the storage function defined in (4.51). □

The $\mathscr{L}_2$-norm is often used to analyze the system, as a 2-norm can be naturally be interpreted as an energy-like measure. The $\mathscr{L}_2$-stability of the impedance-based interaction dynamics (2.29) is then formally stated in (4.52).

$\mathscr{L}_2$-Stability of the Guided Cooperative Manipulation Task

After seperately establishing the $\mathscr{L}_2$-stability of the human-guided set-point generator (4.9) and the impedance-based multi-robot dynamics (2.29) we are finally ready to state the $\mathscr{L}_2$-stability of the overall system. Before directly connecting the input output relations (4.50) and (4.52) we have to evaluate the $\mathscr{L}_2$-relation of $\boldsymbol{x}$ and $\boldsymbol{\xi}^d$ defined in (4.46) as

$$\|\boldsymbol{u}_{\text{imp}}\|_{\mathscr{L}_{2e}} = \|\mathcal{K}\boldsymbol{\xi}^d\| = \|\bar{\mathcal{K}}(\boldsymbol{x} + \boldsymbol{d}_h)\|_{\mathscr{L}_{2e}} \leq \gamma^{\mathcal{K}} \|\boldsymbol{x}\|_{\mathscr{L}_{2e}} + \beta^{\mathcal{K}},$$

where we have $\gamma^{\mathcal{K}} = \|\bar{\mathcal{K}}\|$. Note here that although $\gamma^{\mathcal{K}}$ actually depends on the quaternion $\boldsymbol{q}_o$, too. However, it has a finite gain due to the structure of the aid matrix $U(\boldsymbol{q}_o)$ which is defined in (2.5). Furthermore, we have $\beta^{\mathcal{K}} = \gamma^{\mathcal{K}}\|\boldsymbol{d}_{ih}\|$. Now we are ready to state the main result of input-output stability of the human-guided cooperative manipulation task.

Theorem 4.7. *The serial concatenation of human-guided set-point generator* (4.9) *and the impedance-based multi-robot dynamics* (2.29) *with the inputs* $\boldsymbol{u}_h = \left[\boldsymbol{x}_h^\intercal, \boldsymbol{q}_h^\intercal\right]^\intercal$ *and the output* $\boldsymbol{y} = \boldsymbol{v}_o$ *is finite-gain* $\mathcal{L}_2$*-stable.*

Proof. To show the bounded input and bounded output relationship of the input $\boldsymbol{u} = \boldsymbol{u}_h$ and the output $\boldsymbol{y} = \boldsymbol{v}_o$ we have to link the condition derived in (4.50) for the set-point generator and (4.52) for the multi-robot dynamics as

$$\begin{aligned}
\|\boldsymbol{v}_o\|_{\mathcal{L}_{2e}} &\leq \gamma^{\text{imp}}\|\mathcal{K}\boldsymbol{\xi}^d\|_{\mathcal{L}_{2e}} + \beta^{\text{imp}} \\
&\leq \gamma^{\text{imp}}\|\gamma^{\mathcal{K}}\|\boldsymbol{x}\ \|_{\mathcal{L}_{2e}} + \beta^{\mathcal{K}}\|_{\mathcal{L}_{2e}} + \beta^{\text{imp}} \\
&\leq \gamma^{\text{imp}}\gamma^{\mathcal{K}}\|\boldsymbol{x}\ \|_{\mathcal{L}_{2e}} + \gamma^{\text{imp}}\beta^{\mathcal{K}} + \beta^{\text{imp}} \\
&\leq \gamma^{\text{imp}}\gamma^{\mathcal{K}}\gamma^{p}\|\boldsymbol{x}_h\|_{\mathcal{L}_{2e}} + \gamma^{\text{imp}}\gamma^{\mathcal{K}}\gamma^{q}\|\boldsymbol{q}_h\|_{\mathcal{L}_{2e}} + \gamma^{\text{imp}}\beta^{\mathcal{K}} + \beta^{\text{imp}}.
\end{aligned} \tag{4.53}$$

We can observe that the input/output pair is $\mathcal{L}_2$-stable with the finite gains $\gamma^{\text{imp}}\gamma^{\mathcal{K}}\gamma^{p}$ and $\gamma^{\text{imp}}\gamma^{\mathcal{K}}\gamma^{q}$ and an offset $\gamma^{\text{imp}}\beta^{\mathcal{K}} + \beta^{\text{imp}} > 0$. □

In conclusion, the serial conatenation consisting of a human-guided set-point generator (4.9) and the multi-robot interaction dynamics (2.29) is bounded-input bounded-output stable. Hence, the velocity of the manipulated object is bounded which can be observed in condition (4.53). After establishing the stability between a human input $\boldsymbol{u}_h$ and the motion of the object $\boldsymbol{v}_o$ we are now ready to introduce a task-dependent feedback to the human operator and later evaluate the proposed interaction mechanism in a full-scale experiment.

4.7 Task-dependent Vibrotactile Feedback to the Human Operator

From a system theoretic point of view the shortcoming of a leader-follower dynamical systems is considered to be the lack of feedback to the leader from the followers. Due to the envisioned close interaction between human leader and robotic followers the human leader always receives *visual* feedback from the robot team. We additionally propose to provide a reality augmenting vibrotactile feedback to the human operator based on the multi-robot movement. When a human operator interacts with a team of robot, generally speaking he/she interacts with a redundant mechanical system. Here, the relevant elements of the mechanical system with which the human operator interacts are the task variable which are the end-effector poses $\boldsymbol{\xi}_i, \boldsymbol{\xi}_i^d$ of the robots and $\boldsymbol{\xi}_o$ of the object, and the generalized variables $\boldsymbol{\theta}_i$, which are the joint configuration of the particular end-effectors, and the differential relationship between generalized and task variables $J_i(\boldsymbol{\theta}_i)$ which are the Jacobian matrices of the particular robots. In general all those entities can be of interest for the human operator when interacting with a team of cooperating robots since they all are essential for accomplishing the cooperative robotic manipulation task. Yet, we argue that the

generalized variables $\boldsymbol{\theta}_i$ are already masked from the human operator by employing a task-space impedance control as defined in (2.8). Since the human operator only indirectly interacts with the generalized coordinates by the computed torque input (2.3) we categorize this kind of feedback to the human operator as subordinate feedback. The Jacobian matrix defined in (2.2) denotes the differential relation between generalized and task variables and it can be used to quantitatively measure the interaction of the human operator with the robots. For example it can provide the human operator with an optimal location of interaction as e.g. presented in [137]. Since our presented interaction paradigm between human and multi-robot team is defined in task-space through $\boldsymbol{\xi}_i, \boldsymbol{\xi}_i^d$ we argue that it is beneficial to feedback task-space variables to the human operator in our setup. The feedback which we propose is a task-dependent feedback that conceptualizes the human as a following agent. By doing so we display the transient phase of the robot formation to the human operator, i.e. we make the human aware when the multi-robot formation and the object are in motion. The aim of this feedback is to create a feeling of being in touch with the object to the human during the motion of the object.

4.7.1 Vibrotactile Cue During Transient Phase of the Set-Point Generator

The human-robot interaction paradigm as depicted in Fig. 4.1 envisions a free-space motion where the haptic channel of the human operator is not overloaded. Thus we propose to supplement a haptic feedback here. We avoid using the visual channel as we expect that this channel is already overloaded by the novel experience through the human-robot interaction approach. Furthermore, we avoid the audio channel as we want a direct addressing of the human operator without annoying other people around. Addtitionally, the haptic channel can be used to generate the sense of being in touch with the manipulated object, whereas our proposed approach is rather effortless for the human operator. In order not to restrict the workspace of the human by the haptic-feedback generating device as in the classical bilateral teleoperation, we employ wearable haptic technology here namely a vibrotactile cue. As the transfer of messages through a vibrotactile device is very limited [159], we only transfer a 1-dimensional scalar ν as feedback to the human. The role of the feedback is to signalize when the robot formation is in the transient phase resulting from a human input $\boldsymbol{u}_h$. The feedback signal to the human should cover the following features: intuitive, beneficial for human to accomplish the task, and based on distributed measurements from the robots. The feedback to the human is defined as

$$\nu = \sum_{i \in N} (\boldsymbol{u}_h - \boldsymbol{x}_i)^\intercal (\boldsymbol{u}_h - \boldsymbol{x}_i), \tag{4.54}$$

where the difference between the transformated desired setpoints $\boldsymbol{x}_i$ and the human input $\boldsymbol{u}_h$ are projected onto a single scalar ν by using the sum of squares as feedback to the human.

The interpretation of this signal ν is as follows. Since (4.9) is a dynamical system, an immediate change of the human input $\boldsymbol{u}_h$ always results in a transient phase of the robot followers $\boldsymbol{x}$. This transient phase is not caused by a delay, but by the propagation of $\boldsymbol{u}_h$ through (4.9a) and (4.9b). The time until the robots have reached its steady-state and have re-established the human-robot formation, i.e. $\forall i : \boldsymbol{x}_i = \boldsymbol{u}_h$ is called convergence time. This convergence time can be influenced e.g. by a suitable choice of γ_i in (4.23). As long as the robots are in the transition phase, i.e. $\exists i : \boldsymbol{x}_i \neq \boldsymbol{u}_h$, the desired formation is not established. So the signal is $\nu \neq 0$ and there is feedback

to the human depending on how far the robots are apart from the desired formation distance to the leader. If the desired formation is reached, $\forall i : \boldsymbol{x}_i = \boldsymbol{u}_h$, then $v = 0$ in (4.54) and no signal is transferred to the human. This is intuitive as it decreases the closer the robots are to their desired formation. The human operator as a leader clearly benefits from knowing when the robot team reaches its steady-state or when it is still in the transient phase.

As a single scalar v has to be transmitted by the vibrotactile feedback to the human, we decide to alter the frequency f_{vib} of the vibrotactile stimuli. Highest sensitivity of the stimuli for the human is achieved at frequencies up to 300 Hz [159]. Hence, we choose the transmitted frequencies to be $0 \dots f_{\max}$Hz, where 0 Hz means that the robots are in steady-state, $z = 0$, and $f_{\max}$ Hz corresponds to a maximal value $v_{\max}$ of v which is heuristically determined. A linear mapping between the feedback signal v and the vibrotactile frequency is given as

$$f_{\text{vib}} = \begin{cases} \alpha v & \text{if } \alpha v \leq f_{\max} \\ f_{\max} & \text{else,} \end{cases} \tag{4.55}$$

where $\alpha > 0$ is a scalar of appropriate unit. Using the Euclidean norm measure in (4.54) and employing a linear regression in (4.55) reflects a straightforward mapping of the distance to the desired formation and the vibrotactile cure here. More sophisticated solutions can involve a nonlinear mapping to account to provide more intensive feedback for situations when the formation is far apart from the desired one. A feedback to the human via a haptic channel is given by (4.54) and (4.55) which augments the user experience by means of wearable haptics.

4.8 Experiments

The goal of the experimental evaluation is to experimentally validate the previously established theoretical findings of the guidance of a cooperative manipulation task by a single human. We perform large-scale experiments to assess the behaviour of the manipulators in different human-robots formations. We analyze the resulting internal forces, the accuracy, and the sensitivity of the proposed guidance mechanism. In addition, we discuss the technical difficulties which we encountered.

4.8.1 Experimental Setup

In this section, behaviours of manipulators in different human robots formations are investigated. The general setup is depicted in Fig. 4.1. The outline of the human-guided set-point generator (4.9) and the impedance-based multi-robot dynamics (2.29) is already presented in the Examples 2.1-4.2. The differences between two formation scenarios are experimentally analyzed with respect to the motion of the manipulators and the internal force of the manipulated object. The experimental setup consists of three KUKA LWR 4, see Fig. 4.5. Further details on the robotic system can be found in Appendix C. A Cartesian impedance control scheme (2.8) is employed to ensure compliance of the end-effectors. For the sake of exposition we only consider one translational movement denoted by p_i and p_i^d for the manipulators $i = 1, 2, 3$ in this section without loosing any experimental insights, i.e. we uniformly set $\boldsymbol{q}_i = \boldsymbol{q}_i^d = \text{const}$. Here, $k = 3$ is the most convenient degree of freedom as the desired displacements $d_{ij,3} = 0$ and $d_{ih,3} = 0$ and so $p_i^d = x_i^p, \ \forall i$. A

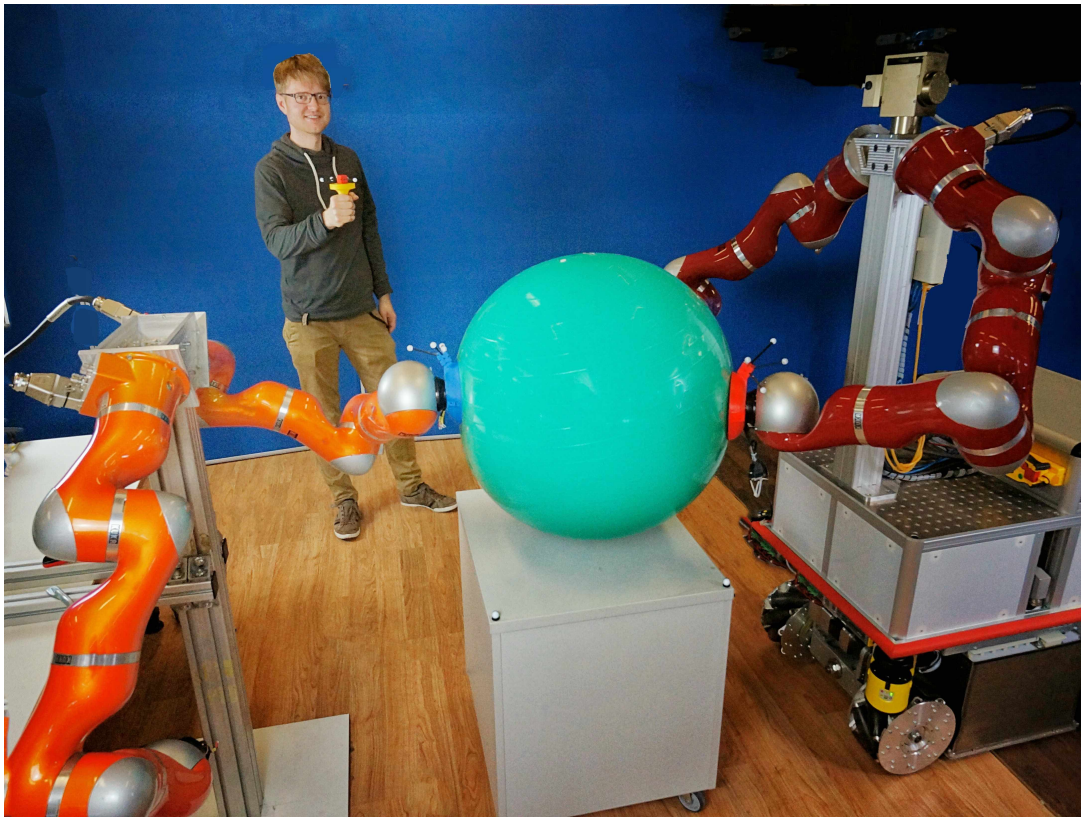

Figure 4.5: Human operator controls a group of robots which cooperatively manipulate an object.

workspace extension for all robotic manipulators by a mobile platform can be accomplished according to a potential function approach presented in [1]. In our experiments the object is an exercise ball with a diameter of 0.65 m and a weight of 1.159 kg which is maximally inflated to have a quasi-rigid object and the end-effectors are designed to obtain a quasi-rigid grasp of the object. The Cartesian positions $\boldsymbol{p}_1, \boldsymbol{p}_2, \boldsymbol{p}_3$ of the three robots and the Cartesian position $\boldsymbol{u}_h$ of the human operator's hand is captured by a passive-marker QualiSys motion capture system at a frequency of 200 Hz. Further details on the Qualisys motion capture system can be found in Appendix C. During the experiment, the human participant holds a marker-equipped handle in order to command the robot formation. A wearable vibrotactile wristband, developed at PERCRO lab to effectively deliver haptic stimuli at user's wrist, is used for giving feedback and providing cues to the human. Further details on the wristband can be found in Appendix (C). The parameters for the tasks are chosen equally for each manipulator in all dimensions for (2.8) as $M_i = 10I_3$, $D_i = 120I_3$, $K_i = 160I_3$. In order to evaluate different combinations of robotic neighbours and the importance of providing feedback to the human, three following scenarios are tested:

(a) No feedback to the human, $z = 0$, and the human neighbors as $N_h = \{2, 3\}$ and so $\boldsymbol{b}_{\text{fms}} = [0, 1, 1]^\intercal$

(b) No feedback to the human, $z = 0$, and the human neighbors as $N_h = \{1, 2, 3\}$ and so $\boldsymbol{b}_{\text{fms}} = [1, 1, 1]^\intercal$

(c) Feedback to the human provided by (4.54) & (4.55) and the human neighbors as $N_h = \{1, 2, 3\}$

	Eq.	Values of Parameters
Desired distance between manipulators	(3.25)	$\boldsymbol{d}_{12} = [0.4, 0, 0]$ m $\boldsymbol{d}_{23} = \boldsymbol{d}_{13} = [0.2, 0.615, 0]$ m
Desired distance between manipulators and human	(3.25)	$\boldsymbol{d}_{1h} = [1.2, 0.35, 0]$ m $\boldsymbol{d}_{2h} = [0.8, 0.35, 0]$ m $\boldsymbol{d}_{3h} = [1, 0.245, 0]$ m
Cooperation weight between manipulators	(3.25)	$\delta_{ij} = 1, \forall i, j$
Cooperation weight between manipulators and human	(3.25)	$\delta_{ih} = 2.5, \forall i$
Impedance parameters	(2.8)	$M = 10I_3$, $D = 120I_3$, $K = 160I_3$

Tabular 4.1: Control parameters used in experiments

The formations (a) and (b) are different with respect to the number of robots directly influenced by the human operator, i.e. by the number of controllable subspaces. The differences between the two formation scenarios are experimentally analyzed with respect to the manipulator motion and the internal force.

4.8.2 Technical Discussion

This section is a discussion of technical difficulties which we experienced during the experiments. The impedance parameters M_i, D_i, K_i of the individual robots are all selected heuristically since the robotic performance was initially well in the experiments. However, we can state the following observations: all impedance parameters are chosen isotropic and homogenous as discussed in Ass. 2.2 so that there are no undesired internal forces. To enable an isotropic parametrization of the impedance, the orientation of each robotic manipulator in a common world frame is measured by the Qualisys motion tracking system. In addition, the damping ratio $\zeta_i = \frac{d_i}{2\sqrt{m_i k_i}} = 1.5$ is chosen to be marginally larger than 1, so that the dynamics of the particular manipulators is overdamped and the steady state is reached in adequate time without oscillating.

Until Sec. 4.8 the manipulators are considered to *rigidly* grasp the *rigid* objects while now both the grasp and the object are only quasi-rigid. Both adaptations are necessary in the experiments because each LWR manipulator has only a maximum payload of 7 kg which is relatively low. Note for large objects usually used in cooperative manipulation this payload is drastically reduced to about $1-1.5$ kg due to large torques. The exercise ball is bulky and relatively light.

To compare conditions (a) and (b) the human input trajectory $\boldsymbol{u}_h$ is recorded for reproducibility of the experiment: the human operator moved the worn marker-equipped handle once from an initial to a final configuration, waited for about 1 second and then returned to the initial configuration. The duration of the trajectory $\boldsymbol{u}_h(t)$ is about $10s$ and the covered distance is about $0.5m$. The recorded trajectory $\boldsymbol{u}_h(t)$ is replayed to cope with the conditions (a) and (b) in an equal fashion.

All experimental results discussed in this section are obtained from a typical run, i.e. not from the aggregation of repeated experiments. Except for occasional hardware failures of one of the robotic systems there is no significant difference between any two runs. In our experience the difference between two runs driven by the same recorded trajectory $\boldsymbol{u}_h(t)$ is only marginal.

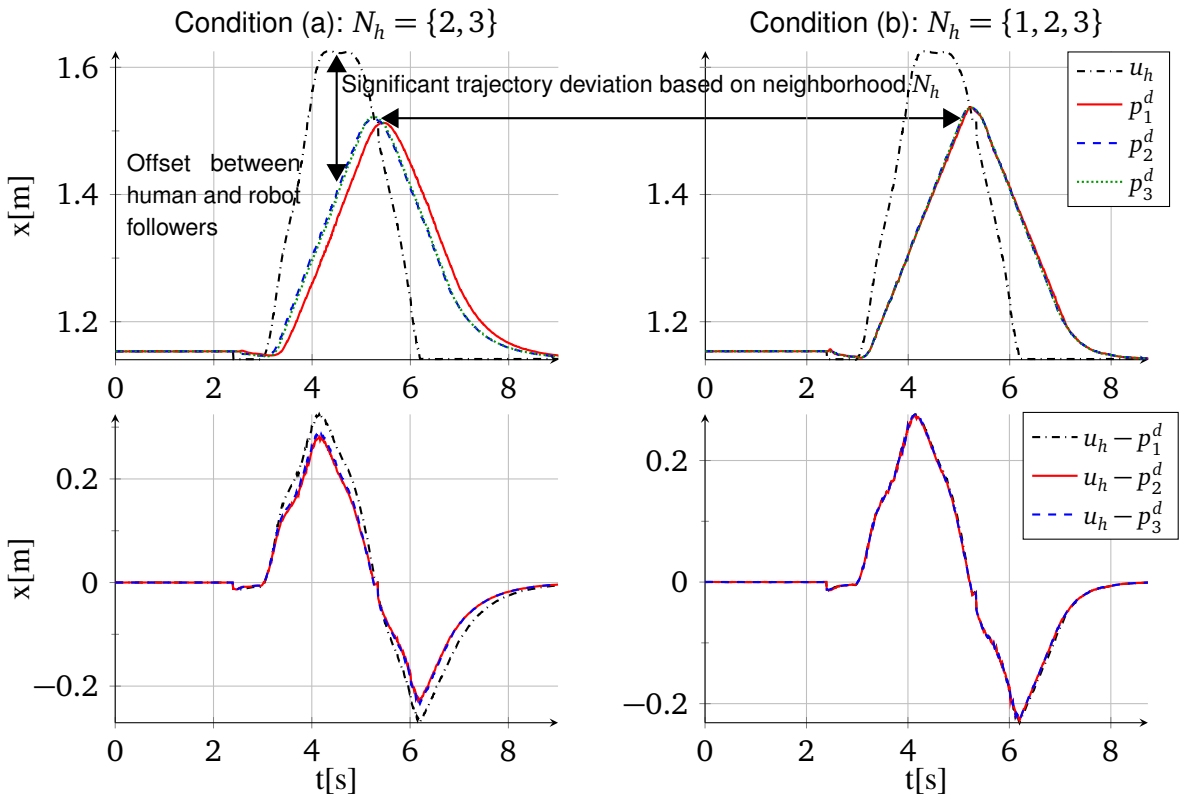

Figure 4.6: Three manipulator set-points p_1^d, p_2^d, p_3^d are controlled by the identical human input u_h under different neighborhoods N_h in condition (a) and (b). Different neighborhood topologies result in different controllable subspaces. Hence, the set-point p_i^d in one direction diverge due to different neighborhood $N_h = \{2,3\}$ (top left). For $N_h = \{1,2,3\}$ (top right) there is no deviation between the set-points. During the motion of the object there is a offset between human input u_h and the set-points p_i^d during the transient response. (bottom left for condition (a), bottom right for condition (b))

Hence, we neglect the comparison of multiple runs and focus on the findings resulting from a typical run.

4.8.3 Results and Discussion for the Set-point Generator

The dynamics of the human-guided set-point generator (4.9) are compared with the conditions (a) and (b). The conditions differ in the neighborhood set N_h of the human operator and so different controllable subspaces between (a) and (b) exist: by evaluating (4.16) for condition (a) we observe that there exist two controllable states $x_1^c = p_1^d$ and $x_2^c = \frac{1}{\sqrt{2}}(p_2^d + p_3^d)$ with different eigenvalues: $\lambda_1^{A_{\text{fms}}^c} = -3.41$ and $\lambda_2^{A_{\text{fms}}^c} = -0.5858$. Since there are two independently controllable subspaces for condition (a) with different eigenvalues of the subspaces, there can be significant deviation of the trajectory p_1^d compared to trajectories p_2^d and p_3^d as shown in Fig. 4.6. As the human operator has no influence on the uncontrollable subspace $x^{\hat{c}} = \frac{1}{\sqrt{2}}(p_2^d - p_3^d)$, both set-point trajectories p_2^d, p_3^d are equal as depicted on the top left side in Fig. 4.6.

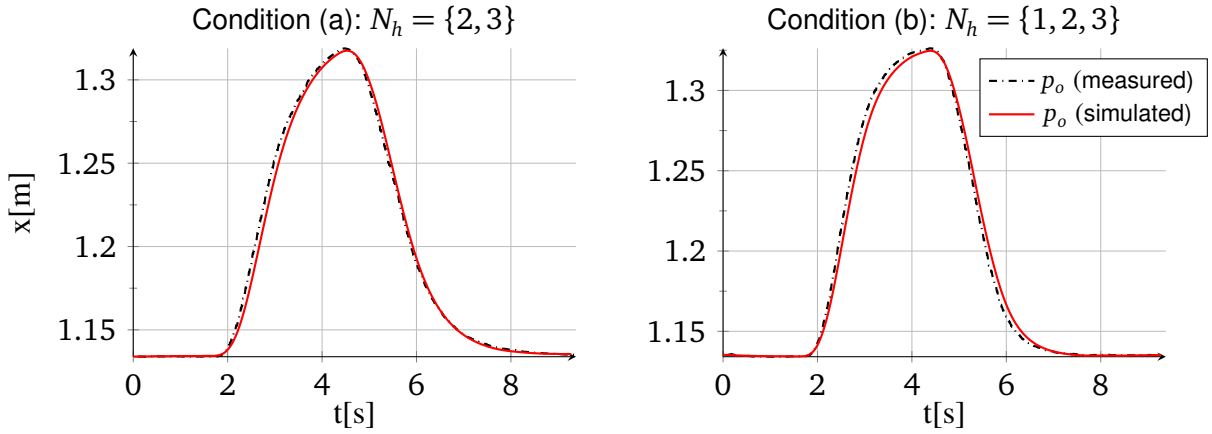

Figure 4.7: The object trajectory p_o driven by a human input u_h resulting from different scenario with condition (a) on the left and condition (b) on the right. For each condition the measured trajectory from the experiments is compared with a trajectory from a simulation.

For condition (b) the locally controllable subspace is the aggregated state $x^c = \frac{1}{\sqrt{3}}(p_1^d + p_2^d + p_3^d)$. Hence, the operator has only access to one controllable subsystem of the multi robot team which moves the desired position p_1^d, p_2^d, p_3^d simultaneously. This is in line with the Prop. 4.3. Due to that the set-point trajectories p_1, p_2, and p_3 are equal on the top right side in Fig. 4.6 and there is no breakup of the formation of set-points. By comparing the top left and top right subfigure in Fig. 4.6 we observe a significant trajectory deviation of p_1^d, p_2^d, and p_3^d based on the neighborhood N_h. Here, we conclude that the theoretical results from Eq. (4.12) and the subsequent Prop. 4.1 are validated in the experiments.

During the transient phase there is a offset between between the human input u_h and the manipulator set-points p_i^d for both conditions (a) and (b), i.e. the error term $u_h - p_i^d \neq 0$ for $\dot{u}_h \neq 0$ as depicted in the bottom left and right side in Fig. 4.6. For both conditions (a) and (b) the maximum positive offset is at approximately $t = 4.1$s and the maximum negative one is at $t = 6.1$s. The offsets can be described with the transient response of the dynamical system representing the human influence on desired set-points (4.9). Note that the the offset is relative to the settling time and we can tune the settling time with weights as described in (4.23). For $t > 8s$ the human input u_h is constant again and the offset converges to zero which experimentally demonstrates the stability of the system (4.9). The stability is theoretically derived in Section 4.6.

4.8.4 Results and Discussion for the Multi-robot Dynamics

The robotic manipulators grasp the object and the manipulator set-points are driven by (4.9) under the conditions (a) and (b) using the recorded human input u_h The effect of the different conditions (a) and (b) on the object trajectory p_o is as follows: by comparing the black and dashed line of the left and right side in Fig. 4.7 we observe no significant effect of the different neighbourhoods N_h on the object trajectory except that the object trajectory excited by the set-point generator in condition (b) converges slightly faster. We assume that this results from the direct influence of the human operator on all three set-points p_i^d simultaneously in condition (b).

Furthermore, we compare for both conditions the measured trajectory from the experiment (black, dashed line) with a simulated trajectory (red, solid line) resulting from the impedance-

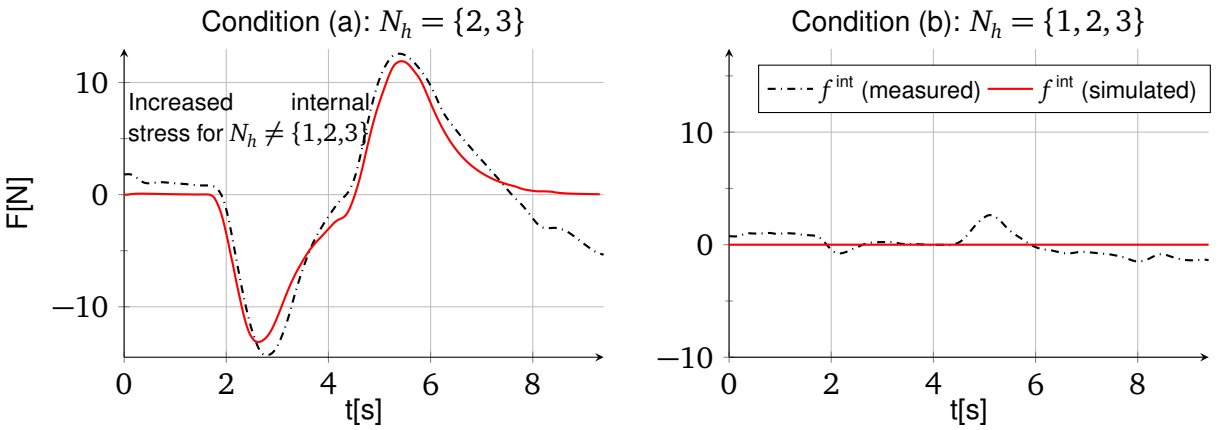

Figure 4.8: Internal force acting between manipulator 1 and 3 in direction $k = 3$ resulting from different scenarios with condition (a) on the left and condition (b) on the right. The internal force is significantly increased for condition (a) where $N_h \neq \{1,2,3\}$. For each condition the measured internal force from the experiments is compared with an internal force obtained from simulation.

based multi-robot dynamics (2.29) which is driven by the same set-point generator (4.9). The simulated set-point generator is excited by the identical recorded human input $\boldsymbol{u}_h$. There is a slight deviation between the measured and the simulated trajectory in Fig. 4.7 which we interpret as a consequence of deviating impedance parameters in theory and experiments. The reason for different impedance parameters can be explained by hardware variations. In total the measured and the simulated trajectory match well which validates the system model for a human-guided cooperative manipulation task, i.e. the series connection modelling of (4.9) and (2.29).

Since for condition (a) the deviation of the trajectory of p_1^d is not in compliance with the object geometry an increased measured internal force is acting on the object for this condition, see the black and dashed line on the left side in Fig. 4.8. For condition (b) with $N_h = \{1,2,3\}$ all manipulator set-points move simultaneously and the internal forces acting on the object are reduced as shown by the black and dashed line on the right side in Fig. 4.8. This experimental result is formally stated in Prop. 4.1. Again we compare the measured internal force from the experiment (black, dashed line) with a simulated internal force (red, solid line) resulting from the dynamics (4.9) and (2.34). For both conditions (a) and (b) the course of measured and simulated internal forces match well. However, a deviation between simulation and measurement is always present which is presumably caused by the force measuring hardware and the deviating impedance parameters as discussed in the previous paragraph. It is experimentally validated that the scenario (b), in which the leader controls only one subspace, results in manipulator motions without considerable deviations and the internal force is significantly reduced.

4.8.5 Results and Discussion of Wearable Feedback

A pilot study about wearable feedback to the human operator is conducted to demonstrate the successful implementation of the proposed interaction and feedback mechanism.

Design & Procedure

Three robots are controlled to establish a formation. The participants are told to put on the wearable wristband and to grasp the handle with their right hand. They are instructed to manipulate the object by moving the handle. The manipulation phase lasts for approximately 60 seconds. For the first 30 seconds no feedback is given to the participants (b1). After 30 seconds they are provided with feedback (c).

Participants

A total of 12 participants volunteered to take part in this study where they became the human leader in the multi-robot formation. All participants were right handed. The average age of the participants was 27.7 years at the time of testing, and 3 of them were female. 9 of them have previously worked with robots.

We use a visual analogue scale to assess the subjective experience of the human in terms of the safety, ease, likeness of guiding the robotic team. Furthermore, by swapping the feedback in conditions (b1) and (c) the preference of having the vibrotactile feedback to assist the guidance is evaluated. In (c) the human received vibrotactile feedback based on (4.54) and (4.55). In (b1) no feedback was transmitted. The data are normalized between $0-10$ where 10 being the positive experience, and are averaged across the participant. The results indicated that the participants experienced the guidance of the robotic team very safe with a mean score of 9.373 ± 0.590. Furthermore, a high score of ease (M = 9.003 ± 0.878) and likeness (M = 9.136 ± 1.121) in controlling the team are reported. The preference of using the vibrotactile feedback is reported slightly lower to the other subjective measures, scoring 7.567 ± 2.05. The analyses indicates that the user-centric guidance of robotic team is successfully implemented and vibrotactile feedback design based on the cooperative term (4.54) and (4.55) is preferred by the participants. Further investigation needs to elucidate wether the lower subjective appreciation of the vibrotactile feedback is due to the transmitted signal (4.54) or due to the mapping onto the vibrotactile outputs (4.55).

4.9 Summary

In this chapter we propose a control law and a feedback strategy for a cooperative robot team controlled by a single human in a cooperative robotic manipulation task under formation-based paradigms. The human operator is incorporated into the ensemble of cooperating robots by appointing him/her to be the leader of a virtual and artificial formation which generates the particular set-points in Section 4.3. Since we envision a contactless interaction and cooperation between human and the cooperating robots the robot team has no direkt influence on the human operator and so the operator becomes the explicit leader of the robotic formation-based set-point generator. A transformation of the robotic set-point states identifies the proposed formation-based set-point generator to be the widely-used leader-follower consensus protocol. In such a setup the influence of the leader on the followers or equivalently the controllability is of particular interest since an improper influence can result in trajectories of the robotic set-points which violate the cooperative manipulation task constraints and can consequently result in an undesired internal force acting on the object. By analyzing the controllability of the set-point generator

of such a human-robot formation we deduce that a one-to-all connection is beneficial for the manipulation task in Section 4.4. Section 4.5 clarifies that the influence of the human operator on the overall system which consists of the formation-based set-point generator and the multi-robot interaction dynamics is mainly dependent on the controllability of the set-point generator. Equilibria and their asymptotic stability in the overall system which is driven by the human input is investigated in Section 4.6. We show that the motion of the object being the output is $\mathscr{L}_2$-stable with respect to the human pose being the input to the overall system consisting of set-point generator and impedance-based interaction dynamics. From a control theoretic point of view the lack of feedback to the leader is considered to be a major drawback of leader-follower systems. Besides visual feedback which is present due to the close interaction paradigm we additionally suggest a task-dependent vibrotactile feedback to the human operator which augments the human experience during the interaction in Section 4.7. The effectiveness and quality of the virtual formation to guide a cooperative manipulation task is successfully demonstrated in experiments and a pilot study in Section 4.8.

5

System Analysis of Interaction Dynamics through Graph Partitioning

5.1 Motivation

One fascinating facet of the human-guided cooperative manipulation task is considered to be the dependence of the human influence on the interaction topology between the robots. This is even true for a relatively small group of robotic followers. A leader-follower setup with distributed interaction becomes more attractive for a large number of followers. Large-scale networked systems have moved into the focus of current research activities in the control community due to their many societally relevant applications such as environmental monitoring by mobile sensor nodes and vehicle/robot coordination in production, logistics and transport systems. Since constrained resources like communication capacities, computation complexities, and energy consumption need to be considered in such systems, a centralized control method is inappropriate here. Due to their scalability distributed control approaches are often preferable in such settings. The consensus problem is a widely studied canonical problem of distributed decision making, see e.g. [160]. The controlled consensus problem is a modification of the original setting in the sense that agents are selected to be controlled by an exogenous control input. The selected agents can be interpreted as leader nodes, while all others are follower nodes. Such dynamical systems are practically prominent as they can be adopted to effectively command and interact with quite a few adjustable, mobile manipulators in a cooperative manipulation task [5] or to model the opinion dynamics of a social network in the presence of stubborn beings [161]. Besides investigating the system properties like convergence of the system under the regime of such controlled agreement protocols, one specific research direction focuses on the controllability of the controlled agreement protocols. Controllability indicates if it is possible for the leader to drive the system states to any configuration in finite time [162, 163, 164]. The identification of the

uncontrollable subspace depending on the interaction graph and on the placement of the input nodes in the graph is an important problem which is studied within this chapter.

5.2 Related work

Controllability in the distributed coordination of a multi-agent system has recently been a compelling research topic. Traditionally, the controllability analysis of leader-follower formations can be distinguished between results based on algebraic graph properties [162] and results based on topological graph properties [165]. Algebraic graph properties provide necessary and sufficient conditions for system controllability in terms of Laplacian graph eigenvectors and eigenvalues. A remarkable conclusion is that the leader consensus network becomes uncontrollable if the eigenvector of the Laplacian has a zero-entry at the position of the leader [163, 90]. The algebraic properties for directed graphs are investigated by means of an alternative version of PageRank in [166]. Although the results on controllability of leader-follower formations based on algebraic graph theory are to the greatest possible extent complete in terms of necessary and sufficient conditions these conditions do not explain how the choice of the leader [167, 168] or the nearest neighbor interconnection [169] affects the system controllability. Especially for a network designer it is essential to be aware of the influence of the leader and the nearest neighbor interconnection on the system controllability.

Topological graph properties include the partitioning of the vertices in clusters and it is shown that particular partitions of the underlying network yield an upper and lower bound for the controllable subspace in terms of the distance partition and the maximal leader-invariant almost equitable partition, respectively[170]. The topological characterization in terms of graph clustering is used to describe to controllable subspace in terms of the maximal leader-invariant almost equitable partitions (LEP) [154, 171]. Almost equitable partitions are graph clusterings which are closely related to Laplacian eigenvectors [172] and can thus be used to interpret algebraic results as topological conditions [173]. In case of distance regular graphs both distance partition and the maximal leader-invariant almost equitable partition are equal and it is shown that the complete controllable subspace is completely characterized by topological properties [164]. The role of the agent dynamics and the network topology in the network controllability analysis is revealed here. In general for graphs which are not distance-regular the *complete* controllable subspace is not characterized by a particular partition. Describing the complete controllable subspace of controlled consensus networks based on topological properties is still an open issue [86, 174]. Recently, our work [8] partially characterizes the occurence of a gap between the algebraic and the topological characterization of the controllable subspace by exploiting Faria vectors [175]. Under specific neighboring circumstances two vertex sets with equal cardinality lead to Laplacian eigenvectors with entries $+1, -1, 0$, called Faria vector [176, 175]. Note that the previous results focus on the case of a fixed graph for the interaction topology. Different from those results, the controllability of leader-follower multi-agent systems under a switching interaction topology is studied in [177]. Sufficient conditions for the controllability of multi-agent systems where time delays are explicitly take into account are presented in [178]. Results on higher-order systems along this research direction can be found in [179, 180].

5.3 The Controlled Consensus Problem

Until the end of Section 5.3.1 we shortly revise the linear dynamics of the controlled consensus protocol and its controllability properties based on the Kalman condition in order to make this chapter self-contained. Since we have already discussed both in Sections 4.3 and 4.4 the mindful reader can continue to read with Section 5.3.2 without missing any insights by redefining $A = A_{\text{fms}}$ and $B = \boldsymbol{b}_{\text{fms}}$. For the remaining reader we consider in the following analysis a multi-agent system where each agent is labeled as $1, \dots, N+1$ and the set of all agents is denoted by $\mathcal{V}$. The state of agent i is identified by $x_i \in \mathbb{R}^d$ where d denotes its dimension. An agent j is called a neighbor $\mathcal{N}_i$ of agent i if agent i has knowledge about the state $x_j(t)$. The dynamics of each agent evolve according to the consensus equation

$$\dot{x}_i = \sum_{j \in \mathcal{N}_i} (x_j - x_i). \tag{5.1}$$

This system can also be characterized as a graph where each agent is represented by a vertex in $\mathcal{V} = \{v_1, \dots, v_{N+1}\}$. The neighboring relation between two agents i and j is represented by an edge in $\mathcal{E}_{ij}$ and the set of all edges $\mathcal{E} \subseteq \mathcal{V} \times \mathcal{V}$. The graph $\mathcal{G} = (\mathcal{V}, \mathcal{E})$ is assumed to be undirected and static. By concatenating the agent states in $\bar{x} = [x_1, \dots, x_{N+1}]$ and assuming $d = 1$ for simplicity of notation in this chapter, (5.1) can be compactly rewritten as

$$\dot{\bar{x}} = -L\bar{x},$$

where L denotes the graph Laplacian. We introduce a set $\mathcal{V}_l$ of the leader node and distinguish it from the set $\mathcal{V}_f$ of follower nodes with $\mathcal{V} = \mathcal{V}_f \bigcup \mathcal{V}_l$. We assume that the last node v_{N+1} corresponds to the leader and the first N nodes are the follower nodes (the labels can always be re-indexed such that this assumption is satisfied). Under this convention the graph Laplacian L is decomposed as

$$L = -\left[\begin{array}{c|c} A & B \\ \hline B^T & \gamma \end{array}\right], \tag{5.2}$$

where $A = A^T \in \mathbb{R}^{N \times N}$, $B \in \mathbb{R}^N$, and $\gamma \in \mathbb{R}$. By collecting all follower states into $x = [x_1, \dots, x_N]$ and using the leader node as input $u = [x_{N+1}]$, we formulate a standard LTI-system for the controlled system

$$\dot{x} = Ax + Bu. \tag{5.3}$$

Note that the edges belonging to the leader are directed ones here and hence the follower have no influence on the leader. From a controllability perspective there is no difference if the followers have influence on the leaders or not as one can always find a novel control law that cancels out the known B^T and γ [164].

Remark 5.1. For simplicity of exposition we restrict ourselves to a single leader node in the problem formulation and the description of leader-invariant AEPs similar to [86, 174, 154, 171, 163, 162]. One main contribution of this chapter is based on a conversion of established

algebraic conditions for controllability into topological conditions. Note that a vast majority of the conditions considering algebraic graph properties can only deal with the single leader case which then restricts the validity of the converted topological conditions for the single leader case, too. However, the proposed Faria vector condition for uncontrollability also extends to the multi-leader case as will be discussed later on.

5.3.1 Controllability Problem and Kalman Decomposition

The controllability matrix Q of the controlled consensus system (5.3) is given by

$$Q = \begin{bmatrix} B & AB & A^2B & \dots & A^{N-1}B \end{bmatrix}. \tag{5.4}$$

The question to be answered is whether the leader can drive the follower states to any arbitrary final configuration x^f, which is true if and only if $\operatorname{rank} Q = N$. For $\operatorname{rank} Q < N$ the uncontrollable subspace needs to be determined. Here, the structure within the matrices A and B is provided by the graph. From a controllability point of view there is no difference between the pair (A, B), the pair $(-A, -B)$.

An exact characterization of the controllable and uncontrollable subspace can be given based on algebraic properties. If Q is rank deficient the LTI-system (5.3) can be decomposed into its controllable and uncontrollable part by the Kalman decomposition [154]. In order to perform this Kalman decomposition by an orthonormal similarity transformation, the matrix $Q^{\|} = \operatorname{range}(Q) \in \mathbb{R}^{N \times \operatorname{rank} Q}$ is derived from the orthonormal image of the potentially rank-deficient controllability matrix Q. The similarity transformation is given by

$$T = \begin{bmatrix} Q^{\|} \mid Q^{\perp} \end{bmatrix},$$

where $Q^{\|} = \operatorname{range}(Q) \in \mathbb{R}^{N \times \operatorname{rank} Q}$ indicates the range of the controllable subspace and $Q^{\perp} = \ker(Q^{\intercal})$ the range of the uncontrollable subspace. This similarity transformation results in

$$T^T A T = \begin{bmatrix} A^c & 0 \\ 0 & A^{\hat{c}} \end{bmatrix}, \quad T^T B = \begin{bmatrix} B^c \\ 0 \end{bmatrix},$$
$$\text{and} \begin{bmatrix} x^c \\ x^{\hat{c}} \end{bmatrix} = T^{\intercal} x,$$

where c and $\hat{c}$ corresponds to the controllable and uncontrollable part and results in two decoupled subsystems

$$\begin{aligned} \dot{x}^c &= A_c x^c + B^c u^c \text{ and} \\ \dot{x}^{\hat{c}} &= A^{\hat{c}} x^{\hat{c}}. \end{aligned} \tag{5.5}$$

By definition the lower left block of $T^T A T$ must result in $0 \in \mathbb{R}^{\operatorname{rank} Q \times (N - \operatorname{rank} Q)}$ as x^c has by definition no influence on $x^{\hat{c}}$. Since $A = A^{\top}$, the upper right block also results as $0 \in \mathbb{R}^{(N - \operatorname{rank} Q) \times \operatorname{rank} Q}$ and hence x^c is unaffected by $x^{\hat{c}}$, too. The uncontrollable state vector is concatenated as follows: $x^{\hat{c}} = \begin{bmatrix} x_1^{\hat{c}}, \dots, x_{(N - \operatorname{rank}(Q))}^{\hat{c}} \end{bmatrix}$. Due to the similarity transformation T the eigenvalues denoted as spectrum $\sigma(A)$ of A and of $T^{\intercal} A T$ are the same. The spectrum of A is $\sigma(A) = \sigma(A^c) \cup \sigma(A^{\hat{c}})$ where

$\sigma(A^c)$ is the spectra of $A^c \in \mathbb{R}^{\text{rank}Q \times \text{rank}Q}$ and $\sigma(A^{\hat{c}})$ is the spectra of $A^{\hat{c}} =\in \mathbb{R}^{N-\text{rank}Q \times N-\text{rank}Q}$.

Remark 5.2. The uncontrollable part (5.5) is asymptotically stable in case of the controlled consensus problem. Since T represents a similarity transformation, the eigenvalues of A and $\begin{bmatrix} A^c & 0 \\ 0 & A^{\hat{c}} \end{bmatrix}$ remain the same. The eigenvalues of A are negative, which is a consequence of the spectra of the Laplacian L and that A is a principal submatrix of $-L$. Note that the spectra of L and $-L$ are $\sigma(-L) = -\sigma(L)$. See [181] for a detailed proof of this fact.

5.3.2 Necessary Conditions for Uncontrollability

In the following the controllability of the controlled consensus protocol is derived from its system theoretic properties. The system theoretic properties of the system (5.3) incorporate the algebraic properties of the underlying graph. The reason why we introduce the results considering the algebraic graph properties here at this point is to latter convert these conditions into topological properties. For an undirected graph $\mathcal{G}$ and a single input, a necessary and sufficient condition for the controllability of (5.3) is derived based on the eigenvalues of $-L$ and A [180, 163]. It is shown that system (5.3) is uncontrollable if a Laplacian eigenvector has a 0-entry at the $N+1$th element, where $N+1$ denotes the position of the leader. Due to the 0-entry at the leader position, the leader has no impact on this eigenmode which is formally stated as.

Proposition 5.1 ([90])**.** *Assume the system* (5.3) *with a single input to be uncontrollable. Then there exists an eigenvector of L that has a zero component on the index that corresponds to the input.*

Here, the Hautus criterion requires that $Av_A = \lambda v_A$ and $B^T v_A = 0$ are satisfied for each uncontrollable eigenmode. It is shown in [90] that v_A is a left eigenvector of A and $\begin{bmatrix} v_A^T, & 0 \end{bmatrix}$ is the left eigenvector of $-L$ associated with the common eigenvalue λ. Due to the symmetry of $-L$ and A, the left eigenvectors are equal to the right eigenvectors here.

Proposition 5.2 ([90])**.** *Consider the controlled consensus protocol* (5.3) *with a single input. If L has an eigenvalue with geometric multiplicity greater than one, then the system is uncontrollable.*

Note that Prop. 5.2 directly follows from Prop. 5.1. For example assume an eigenvalue of L with geometric multiplicity of two and the corresponding eigenvectors to be v_1 and v_2. By introducing the scalar $c \in \mathbb{R}$, the vector $v = v_1 + c\,v_2$ is also an eigenvector of L. As the scalar c can be freely chosen there is always a c which produces a 0- entry at the $N+1$th element. Hence, due to Prop. 5.1 the system is uncontrollable.

A conclusion of the Propositions 5.1 and 5.2 is to investigate the appearance of 0 elements in the eigenvectors of Laplacian and relate this to the uncontrollability of controlled agreement systems. Implicitly, the works of [170] and [154] make use of Prop. 5.1 to provide an upper bound on the controllable subspace which is the orthogonal complement to the uncontrollable subspace. Following a brief introduction of the main result of [170] and [154] in the upcoming section, we are able to argue why their results rather identifies the uncontrollable subspace than the controllable one. Subsequently, we provide new insights into the topological characterization of the uncontrollable subspace in a controlled agreement protocol.

5.3.3 Leader-invariant Almost Equitable Partitions

In large networks it is desirable to characterize the controllable and uncontrollable subspace by topological properties such as graph invariants or particular clusterings. A promising clustering which is used in this context are almost equitable partitions (AEP). [86, 154]. Note that in this context the terms *almost equitable partition* and *external equitable partition* are used equivalently in the literature. AEPs exploit the fact that certain follower agents tend to cluster and in general only the average of these agents can be controlled. Here, the clustering of nodes of a graph $\mathcal{G} = (\mathcal{V}, \mathcal{E})$ is defined by a partition map $\pi : \mathcal{V} \to \{C_1, \dots, C_k\}$, where $\pi(v_i)$ is the assigned cell for node i and k denotes the number of cells under the partition π. Consequently, an inverse operation $\pi^{-1}(C_i) = \{v_j \in \mathcal{V} | \pi(v_j) = C_i\}$ indicates the set of nodes belonging to cell C_i. The set of all clusters is defined as $\mathrm{dom}(\pi) = \{C_1, \dots, C_k\}$. The *node-to-cell degree* $\deg_\pi(v_i, C_j)$ indicates how many neighbors agent v_i has in cell C_j regarding the partition π. A clustering π of the nodes is called *almost equitable partition* (AEP) if, for all C_i, C_j, where $i \neq j$

$$\deg_\pi(v_k, C_j) = \deg_\pi(v_l, C_j), \text{ for all } v_k, v_l \in \pi^{-1}(C_i), \tag{5.6}$$

where the clustering considers all nodes inside a cell have the equal number of adjacent nodes in another neighboring cell. A characteristic matrix $P^\pi \in \mathbb{R}^{(N+1)\times k}$ is defined as

$$P^\pi = \left[p_{i,j}\right] = \begin{cases} 1 & \text{if } v_j \in C_i \\ 0 & \text{otherwise,} \end{cases} \tag{5.7}$$

where $p_{i,j}$ is the (i,j)th entry of the matrix P^π and so P^π represents a mapping from a cell to the belonging vertices. The k column vectors of the characteristic matrix P^π are called characteristic vector and denoted by p. Similar to the characteristic matrix we define a matrix $\bar{P}^\pi \in \mathbb{R}^{(N+1)\times(N+1-k)}$ as $\bar{P}^\pi \in \ker(P^{\pi\intercal})$ which is the orthogonal complement to the characteristic matrix P^π. Note here that $\bar{P}^\pi$ spans a basis for the null space of P^π with linearly independent columns. For the sake of completeness the column vectors of $\bar{P}^\pi$ are denoted by $\bar{p}_i$. For a particular characteristic matrix P^π given by an AEP, the computation of the orthogonal complement $\bar{P}^\pi$ is straightforward and uncomplicated. Since any vertex of the graph $\mathcal{G}$ can only be mapped to a single cell all characteristic vector p of P^π are orthogonal to each other and so $\bar{P}^\pi$ can be composed of vectors $\bar{p}$ of which each one is orthogonal to a column vector of the characteristic matrix P^π. As now the column vectors of P^π have equal components for all vertices belonging to a cell C_i and 0s otherwise, we can compute $\bar{P}^\pi$ from the differences between any two vertices in the cell C_i. Hence, we define $\bar{P}^\pi$ as

$$\bar{P}^\pi = \left[\bar{P}_1^\pi \;\; \dots \;\; \bar{P}_k^\pi\right], \tag{5.8}$$

where the submatrices $\bar{P}_i^\pi \in \mathbb{R}^{N\times(|C_i|-1)}$ are defined as

$$\bar{P}_i^\pi = [\bar{p}_j] = \begin{cases} \emptyset, & \text{if } |C_i| = 1 \\ e_k - e_l, & \text{otherwise for } j = 1, \dots, |C_i| - 1; \\ & \exists v_k \in \pi^{-1}(C_i), \\ & \forall v_l \in \pi^{-1}(C_i) \backslash \{v_k\}. \end{cases} \tag{5.9}$$

If $|C_i|$ vertices are mapped to the cell C_i there exist in total $|C_i|(|C_i|-1)/2$ of such differences between any two vertices. Note that we leave out here all cases with different signs, i.e. $e_i - e_j$ and $e_j - e_i$ form the same subspace. Due to the rank-nullity theorem, we know $\dim(\text{range}(P^\pi)) + \dim(\ker(P^{\pi\intercal})) = N + 1$. So only $|C_i| - 1$ of the $|C_i|(|C_i|-1)/2$ total differences have to be considered in order to arrange the null space of a particular column vector of the characteristic matrix P^π. For example suppose a characteristic vector p of P^π to be $p = e_j + e_k + e_l$ which represents a mapping of $|C_i| = 3$ vertices to a cell C_i. The straightforward and simple computation of possible vectors orthogonal to p neglecting the signs yields three different vectors: $e_j - e_k$, $e_j - e_l$, and $e_k - e_l$. For the construction of $\bar{P}^\pi$, only two of the three vectors, e.g. $e_j - e_k$ and $e_j - e_l$, are required here.

Remark 5.3. In [172] the almost equitable partitions are defined for simple undirected graphs. By using the out-degree Laplacian matrix L_{out} an almost equitable partitions can also be defined for weighted and directed graphs [182]. The conditions (5.6) apply for the out-degree of each vertex in the graph by summing up the weights as $d_{\text{out}}(v_k, C_j) = \sum_{l \in C_j} a_{kl}$, where a_{kl} is the weight between agent k and l, instead of $\deg_\pi(v_k, C_j)$.

Note here that for a particular graph there can exist multiple AEPs. All AEPs feature the following crucial property relating AEPs to the graph Laplacian L:

Lemma 5.1 ([172]). A partition π is called almost equitable if and only if the characteristic matrix $\text{range}(P^\pi)$ is L-invariant.

Suppose now that $\pi = (C_1, C_2, \ldots, C_k)$ is an almost equitable k-partition of a graph $\mathcal{G}$ with corresponding graph Laplacian L. Since now $\text{range}(P^\pi)$ is L-invariant, we know that the orthogonal complement $\text{range}(P^\pi)^\perp = \ker(P^{\pi\intercal})$ is $L^\intercal$-invariant. As we consider the graph $\mathcal{G}$ to be undirected, $L = L^\intercal$ and $\ker(P^{\pi\intercal})$ is L-invariant, too. Under the almost equitable k-partition π there are matrices $L^\pi \in \mathbb{R}^{k\times k}$ and $\bar{L}^\pi \in \mathbb{R}^{N+1-k\times N+1-k}$

$$LP^\pi = P^\pi L^\pi, \tag{5.10}$$
$$L\bar{P}^\pi = \bar{P}^\pi \bar{L}^\pi, \tag{5.11}$$

where $L^\pi = (P^{\pi\intercal}P^\pi)^{-1}P^{\pi\intercal}LP^\pi$ is called the generalized Laplacian matrix L^π in the literature. We now introduce the matrix $\bar{L}^\pi$ as complement generalized Laplacian matrix given by $L^\pi = (\bar{P}^{\pi\intercal}\bar{P}^\pi)^{-1}\bar{P}^{\pi\intercal}L\bar{P}^\pi$. Under the almost equitable k-partition π, the generalized Laplacian L^π represents a quotient graph $\mathcal{G}/\pi = (V_\pi, E_\pi, w_\pi)$ which is a weighted and directed graph whose nodes are $V_\pi = \text{dom}(\pi)$.

The next proposition is a direct consequence of Lemma 5.1 and the definition of L, P^π, and L^π, and it relates AEPs to the eigenvalues and eigenvectors of the graph Laplacian. It extends [172][Prop.3] to the case of orthogonal complement $\bar{P}^\pi$ of the characteristic matrix. By doing so we obtain a profound describtion how AEPs can describe the controllability of a controlled agreement protocol.

Proposition 5.3. *Let L be the Laplacian matrix of the graph $\mathcal{G}$. If $\pi = \{C_1, \ldots C_k\}$ is an almost equitable partition of $\mathcal{G}$, then the spectra $\sigma(L)$, $\sigma(L^\pi)$, $\sigma(\bar{L}^\pi)$ satisfy $\sigma(L) = \sigma(L^\pi) \cup \sigma(\bar{L}^\pi)$.*

Furthermore, then

$$\forall \lambda \in \sigma(L^\pi), \exists v \in \ker(L^\pi - \lambda I_{N+1}) \Leftrightarrow P^\pi v \in \ker(L - \lambda I_{N+1}),$$
$$\forall \lambda \in \sigma(\bar{L}^\pi), \exists v \in \ker(\bar{L}^\pi - \lambda I_{N+1}) \Leftrightarrow \bar{P}^\pi v \in \ker(L - \lambda I_{N+1}).$$

Proof. Assuming that L is the graph Laplacian of the graph $\mathcal{G}$ and $\pi = \{C_1, \ldots, C_k\}$ is an almost equitable k-partition, the matrices P^π and $\bar{P}^\pi$ are defined in (5.7) and (5.8). To see the similarity between the matrices L and $\mathrm{diag}(L^\pi, \bar{L}^\pi)$ transformed by the basis $\begin{bmatrix} P^\pi & \bar{P}^\pi \end{bmatrix}$ we compactly rewrite (5.10) and (5.11) as follows

$$\begin{bmatrix} P^\pi \bar{P}^\pi \end{bmatrix}^{-1} L \begin{bmatrix} P^\pi \bar{P}^\pi \end{bmatrix} = \begin{pmatrix} L^\pi & 0 \\ 0 & \bar{L}^\pi \end{pmatrix}.$$

Note here that due to the construction of P^π and $\bar{P}^\pi$, $\begin{bmatrix} P^\pi & \bar{P}^\pi \end{bmatrix}$ is full rank and invertible. The eigenvalues of the similar matrices L and $\mathrm{diag}(L^\pi, \bar{L}^\pi)$ are equal [156]: $\sigma(L) = \sigma(\mathrm{diag}(L^\pi, \bar{L}^\pi))$. Due to the block-diagonal structure of $\mathrm{diag}(L^\pi, \bar{L}^\pi)$ we have $\sigma(\mathrm{diag}(L^\pi, \bar{L}^\pi)) = \sigma(L^\pi) \cup \sigma(\bar{L}^\pi)$. The eigenvectors of L^π and $\bar{L}^\pi$ are transformed as

$$\begin{aligned} L^\pi v &= \lambda v, \\ P^\pi L^\pi v &= \lambda P^\pi v, \\ L P^\pi v &= \lambda P^\pi v, \end{aligned}$$

where we make use of the linear independence of the columns of P^π and the relation given by (5.10). The argumentation for $\bar{L}^\pi$ and $\bar{P}^\pi$ is conducted analogously which concludes this proof. □

This proposition is inspired by [172]. According to Proposition 5.3 the characteristic matrix P^π of an almost equitable partition and its orthogonal complement $\bar{P}^\pi$ influences the Laplacian eigenvectors. Hence, particular almost equitable partitions of graphs lead to invariant subspaces given by P^π or $\bar{P}^\pi$. For example a trivial cell, i.e. a cell that only contains a single vertex, directly affects $\bar{P}^\pi$ and the corresponding eigenvector. We formally state this as follows.

Proposition 5.4. *Let L be the Laplacian matrix of the graph $\mathcal{G}$ with N vertices. Suppose that there is an almost equitable k-partition $\pi = \{C_1, \ldots, C_i, \ldots, C_k\}$ in which the ith cell only contains a single vertex i.e. $\pi^{-1}(C_i) = v_k$. Then there exists an eigenvector of L that has a zero component on the kth index.*

Proof. Following the argumentation of Prop. 5.3 there is an eigenvector $\bar{P}^\pi v$ of L where the $\bar{P}^\pi$ is defined in (5.9). $\bar{P}^\pi$ is a linearly independent basis of the orthogonal complement to $\bar{P}^\pi$. We have $|C_i| = 1$ since the ith cell only contains a single vertex denoted by v_k. By construction (5.9) the k-th row of $\bar{P}^\pi$ is zero as $e_k^\intercal \bar{P}^\pi = \mathbf{0}^\intercal$. Hence, multiplying $\bar{P}^\pi$ with u always results in a zero entry at the kth index which concludes this proof. □

We revise now a result from the literature which relates the controllability of the single-leader controlled agreement protocol with the leader-invariant AEP. The *leader-invariant* AEP is defined

as a clustering where the leader node is in a trivial cell, i.e. $\pi^{-1}(\pi(v_{N+1})) = \{v_{N+1}\}$. Furthermore, a maximal AEP is denoted by $\pi^\star$, where *maximal* refers to the smallest possible number of cells. A key result from [171] states a necessary condition for the controllability of single-leader networks based on the topological property:

Proposition 5.5 ([171])**.** *A single leader network* (5.3) *is completely controllable only if $\mathcal{G}$ is connected and π^* is trivial, i.e. $\pi^{\star -1}(\pi^\star(v_i)) = \{v_i\}, \forall v_i \in \mathcal{V}$.*

The proof in [171] arguments that the range space of $Q^{\|}$ corresponds to the spanning set of the characteristic vectors p_i of the follower nodes yielding the following relation

$$Q^{\|} \subseteq \text{range}(P).$$

Consequently, the upper bound for the dimension of the controllable subspace of (5.3) is characterized in terms of an inequality as $\text{rank}(Q) \leq |\pi^\star| - 1$. Since this proposition lacks sufficiency, the complete controllable subspace cannot always be completely described by LEPs. As stated in [86] and [174], there exist trivial LEP for which the complete controllable subspace is still unknown.

Descriptively speaking the *leader-invariant*, maximal AEP π_L^* (LEP) is a rather good but not an exact characterization of the controllable subspace. Based on Prop. 5.3 and 5.4 we can now illustrate the consequence of using π_L^* for the uncontrollable subspace and not the controllable one as often done in the literature. By doing so we look at the controllability problem of the controlled consensus protocol from a different perspective. The reason why π_L^* is a good approximation is that the AEPs are leader-invariant and so one characteristic vector of the matrix $P^{\pi_L^*}$ is the standard basis vector e_{N+1}. Hence, due to the structure of $P^{\pi_L^*}$ its orthogonal complement $\bar{P}^{\pi_L^*}$ can only have zeros at all $N+1$th elements. Due to Prop. 5.3 we know that all eigenvectors u of the complement matrix $\bar{L}^\pi$ constitute also eigenvectors of the L given by $\bar{P}^\pi u$. As for the leader-invariant case $\bar{P}^\pi$ has only zeros at the position of the leader, the $N+1$th entry of $\bar{P}^\pi u$ is also zero as discussed in Prop. 5.4. Due to Prop. 5.1 we know that such a zero entry leads to an uncontrollable subspace and this renders all eigenvectors of $\bar{L}^\pi$ as uncontrollable ones. We note here that each almost equitable partition divides the eigenvalues of the graph Laplacian L into two subsets. The procedure of splitting eigenvalues into controllable and uncontrollable subspace is already discussed in Section 5.3.1. We link both transformations and come up with the following formal statement.

Proposition 5.6. *Let $\mathcal{G}$ be a graph with Laplacian L. $\bar{L}^\pi$ and $\bar{P}^\pi$ is defined as in Prop. 5.3 and the uncontrollable system matrix $A^{\bar{c}}$ is defined as in* (5.5)*. If $\pi_L = \{C_1, \ldots, C_k\}$ is an leader-invariant almost equitable partition, then*

$$\sigma(\bar{L}^\pi) \subseteq \sigma(A^{\bar{c}}),$$

and

$$|\sigma(\bar{L}^\pi)| \geq |\sigma(A^{\bar{c}})|.$$

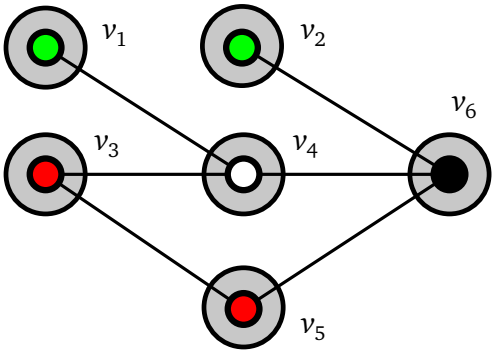

Figure 5.1: The leader is denoted as • and the partition π_l^* is denoted by the gray enclosures around the nodes. Here, $\pi_l^\star = \{\{v_1\},\{v_2\},\{v_3\},\{v_4\},\{v_5\},\{v_6\}\}$ is trivial, but $x^{\bar{c}} = -x_5 - x_3 + x_1 + x_2$ is uncontrollable. The signs of $x^{\bar{c}}$ are denoted by •/•.

Proof. Since $\bar{L}^\pi$ result from a similarity of L we know that $\sigma(\bar{L}^\pi) \subset \sigma(L)$. Furthermore, all uncontrollable eigenvalues of (5.3) are given by $\sigma(A^{\bar{c}}) \subset \sigma(A)$. By applying Prop. 5.1 for all uncontrollable eigenmodes we know that A and L share the uncontrollable eigenvalues, i.e. we also have $\sigma(A^{\bar{c}}) \subset \sigma(L)$. The sharing of common eigenvalues is also formally stated in e.g. [90, Lemma 10.4]. As π_L is a leader-invariant almost equitable partition, $\bar{P}^\pi$ has only zeros at the position of the leader. Hence, all eigenvector pairs which intersect $\bar{L}_\pi$ and L as defined in Prop. 5.3 are uncontrollable which follows from Prop. 5.1. Consequently, all corresponding eigenvalues $\sigma(\bar{L}^\pi)$ are uncontrollable ones, too. By definition all uncontrollable eigenvalues are contained in $\sigma(A^{\bar{c}})$ which concludes the proof. The inequality follows consequently. □

As π_L^* is maximal i.e. it refers to the fewest number of cells, the number of k is minimal. Due to that the matrix $\bar{P}^\pi$ which describes the uncontrollable subspace becomes larger. Still, there can exist more eigenvectors leading to an uncontrollable subspace which are not covered by partitions which are not leader-invariant. We will discuss the influence of leader-noninvariant partitions on the uncontrollable subspace in the following section. For illustration we consider the following well-known example from the literature [174].

Example 5.1. We consider the graph of the controlled consensus problem as illustrated in Fig. 5.1. Node 6 is the leader node, all other nodes are followers. The partition $\pi_l^\star$ is given by $\pi_l^\star = \{\{v_1\},\{v_2\},\{v_3\},\{v_4\},\{v_5\},\{v_6\}\}$, which is trivial. According to Proposition 5.5 we know that the controllable subspace is $\text{rank}(Q) \leq 5$. However, from the algebraic condition (5.4) we know that $\text{rank}(Q) = 4$ and from (5.5) we know that $x^{\bar{c}} = -x_5 - x_3 + x_1 + x_2$.

A novel method is required to characterize the uncontrollable subsystem as in Fig. 5.1.

5.4 Uncontrollability by Leader-Noninvariant Almost Equitable Partitions

The topological characterization of the uncontrollable subspaces in a controlled agreement protocol can to the greatest possible extent be described by leader-invariant almost equitable partitions. However, this condition for uncontrollability remains necessary until now. In the following section, we discuss how leader-noninvariant almost equitable can affect the uncontrollable subspace.

Before doing so we first revise [172, Prop. 4] which relates almost equitable bipartitions to integer eigenvalues and extend its result for the corresponding eigenvector as follows.

Proposition 5.7. *Let $\mathcal{G}$ be a graph with Laplacian matrix L. L^π and P^π is defined as in Prop. 5.3. If $\mathcal{G}$ has an almost equitable bipartition, i.e. a 2-partition, $\pi = \{C_1, C_2\}$ such that $\forall v_i \in C_1, deg_\pi(v_i, C_2) = \tau_2$ and $\forall v_j \in C_2, deg_\pi(v_j, C_1) = \tau_1$, then*

$$\lambda = deg_\pi(v_j, C_1) + deg_\pi(v_i, C_2) \in \sigma(L) \cap \sigma(L^\pi),$$

and

$$\exists v = P^\pi \begin{pmatrix} -\tau_2/\tau_1 \\ 1 \end{pmatrix} \in \ker(L - \lambda I_{N+1}).$$

Proof. According to the definition of π it follows that

$$L^\pi = \begin{pmatrix} \tau_2 & -\tau_2 \\ -\tau_1 & \tau_1 \end{pmatrix},$$

with the eigenvalues being $\sigma(L^\pi) = \{0, \lambda\}$ and the eigenvectors being $v = \mathbf{1}$ and $v = [-\tau_2/\tau_1, 1]^\intercal$. Therefore, by Prop. 5.3 the result follows. □

Following the argumentation of Prop 5.7, we come up with a proposition which relates an integer eigenvalue with a $N-1$-almost equitable partition. A $N-1$-almost equitable partition is a partition where all $N-2$ vertices are in a singleton cell except for two which are in a mutual cell.

Proposition 5.8. *Let $\mathcal{G}$ be a graph with Laplacian matrix L. $\bar{L}^\pi$ and $\bar{P}^\pi$ is defined as in Prop. 5.3. If $\mathcal{G}$ has an almost equitable $N-1$-partition $\pi = \{C_1, \dots, C_{N-1}\}$ and by definition the two-vertex-cell is $C_{N-1} = \{v_i, v_j\}$, then*

$$\lambda = \begin{cases} \deg(v_j) & \text{if } (i,j) \notin \mathcal{E} \\ \deg(v_j) + 1 & \text{if } (i,j) \in \mathcal{E}, \end{cases}$$

and

$$\exists v = e_i - e_j \in \ker(L - \lambda I_{N+1}).$$

Proof. According to the definition of π it follows that $\bar{P}^\pi = e_i - e_j \in \mathbb{R}^{N+1}$. Therefore, by Prop. (5.3) we know that $\bar{P}^\pi$ is an eigenvector of L. By evaluating $L\bar{P}^\pi = (\deg(v_i) + [l_{i,j}])e_i - (\deg(v_i) + [l_{j,i}])e_j$ we see that in the Laplacian matrix $l_{j,i} = 1$ if $(i,j) \in \mathcal{E}$ and $l_{j,i} = 0$ if $(i,j) \notin \mathcal{E}$. Hence, the result follows. □

Based on almost equitable partitions which are not necessarily leader-invariant we are now able to characterize eigenvalues of the Laplacian. A straightforward application of Prop. 5.8 formally describes an uncontrollable subspaces as

Proposition 5.9. *Let $\mathcal{G}$ be a graph with Laplacian matrix L. If $\mathcal{G}$ has an almost equitable $N-1$-partition $\pi = \{C_1, \dots, C_{N-1}\}$ and the leader vertex $v_l \notin C_{N-1}$ where C_{N-1} is the two-vertex-cell then controlled consensus protocol* (5.3) *is uncontrollable. The eigenvalue λ and the corresponding eigenvector v is defined as in Prop. 5.8. The uncontrollable eigenmode is then represented by the eigenvalue λ and the corresponding eigenvector v.*

Proof. The proof is a straighforward application of Propositions 5.8, 5.4, and 5.1. □

Note here that Prop. 5.9 is a special case of Prop. 5.5 where we additionally obtain the eigenvalue for an almost equitable $N-1$-partition. In the following we relate both Prop. 5.7 and 5.8 to the uncontrollability of the controlled consensus protocol.

5.4.1 Geometric Multiplicity and AEPs

In Proposition 5.2 uncontrollability is discussed which is caused by an eigenvalue of the Laplacian L with geometric multiplicity greater than one. Eigenvalues of L can also be identified by means of almost equitable partitions using Prop. 5.7 and 5.8. We are now ready to bring together both results and come up with the following formal statement.

Proposition 5.10. *Let $\mathcal{G}$ be a graph with Laplacian matrix L with $N > 2$ nodes. L^{π_i}, P^{π_i}, $\bar{L}^{\pi_i}$ and $\bar{P}^{\pi_i}$ is defined as in Prop. 5.3 where here the subscript accounts for two different almost equitable partitions $i \in 1, 2$. Suppose that there is*

(a) *an almost equitable bipartition π_1 with eigenvalue $\lambda_1 = \sigma(L^{\pi_1})\backslash 0$ of $\mathcal{G}$ as defined in Prop. 5.7 and an almost equitable bipartition π_2 of $\mathcal{G}$ with eigenvalue $\lambda_2 = \sigma(L^{\pi_2})\backslash 0$ as defined in Prop. 5.7 where $\pi_2 \neq \pi_1$* or

(b) *an almost equitable $N-1$ partition π_1 of $\mathcal{G}$ with eigenvalue $\lambda_1 = \sigma(\bar{L}^{\pi_1})$ as defined in Prop. 5.8 and an almost equitable $N-1$ partition π_2 of $\mathcal{G}$ with eigenvalue $\lambda_2 = \sigma(\bar{L}^{\pi_2})$ as defined in Prop. 5.8 where $\pi_2 \neq \pi_1$* or

(c) *an almost equitable bipartition π_1 with eigenvalue $\lambda_1 = \sigma(L^{\pi_1})\backslash 0$ of $\mathcal{G}$ as defined in Prop. 5.7 and an almost equitable $N-1$ partition π_2 of $\mathcal{G}$ with eigenvalue $\lambda_2 = \sigma(\bar{L}^{\pi_2})$ as defined in Prop. 5.8.*

If now $\lambda_1 = \lambda_2$, then the controlled consensus protocol (5.3) *is uncontrollable.*

Proof. The controlled consensus protocol (5.3) is uncontrollable for eigenvalues with geometric multiplicity greater than one. To prove the statement we have to show that the eigenvalues λ_1 and λ_2 described by conditions (a)-(c) have a geometric multiplicity greater than one. We know that $\lambda = \lambda_1 = \lambda_2$ and so the corresponding eigenvectors are

(a) $v_1 = P^{\pi_1}[-\lambda\ 1]^\intercal$ and $v_2 = P^{\pi_2}[-\lambda\ 1]^\intercal$ where $v_1 \neq v_2$ as $P^{\pi_1} \neq P^{\pi_2}$ following from $\pi_1 \neq \pi_2$ *or*

(b) $v_1 = \bar{P}^{\pi_1}$ and $v_2 = \bar{P}^{\pi_2}$ where $v_1 \neq v_2$ as $\bar{P}^{\pi_1} \neq \bar{P}^{\pi_2}$ which follows from $\pi_1 \neq \pi_2$ *or*

(c) $v_1 = P^{\pi_1}[-\lambda\ 1]^\intercal$ and $v_2 = \bar{P}^{\pi_2}$ where $v_1 \neq v_2$ as $P^{\pi_1}[-\lambda\ 1]^\intercal$ is a vector which has $|C_1|$ entries with $-\lambda$ and $|C_2|$ entries with 1. In contrast, $\bar{P}^{\pi_2}$ is a vector with just two elements $+1/-1$ different from 0. As now $N > 2$, v_1 and v_2 must be different.

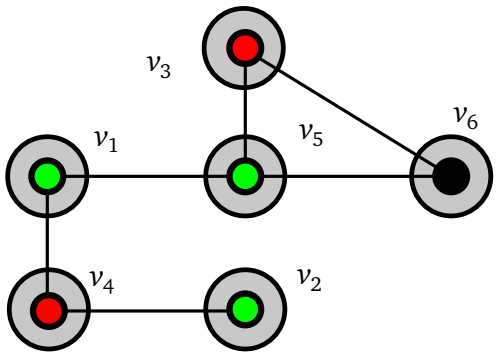

Figure 5.2: The leader is denoted as • and the partition π_l^* is denoted by the gray enclosures around the nodes. Here, $\pi_l^\star = \{\{v_1\},\{v_2\},\{v_3\},\{v_4\},\{v_5\},\{v_6\}\}$ is trivial, but $x^{\bar{c}} = 2x_4 + x_3 - x_1 - x_2 - x_5$ is uncontrollable. The signs of the elements in $x^{\bar{c}}$ are denoted by •/•.

As now $v_1 \neq v_2$ there is a eigenvalue which has a geometric multiplicity greater than one which makes (5.3) uncontrollable. □

The next example shows how Prop. 5.10 can be used to account for uncontrollable subspaces which are not covered by leader-invariant maximal almost equitable partitions.

Example 5.2. Consider the graph $\mathcal{G}$ depicted in Fig. 5.2 which is taken from literature [8]. It has a trivial leader-invariant AEP. However, the uncontrollable subspace can be computed as $x^{\bar{c}} = 2x_4 + x_3 - x_1 - x_2 - x_5$ where the 4th vertex is double weighted here. We can explain $x^{\bar{c}}$ by applying Prop. 5.10. The graph $\mathcal{G}$ possesses two almost equitable bipartitions π_1 and π_2 which are illustrated in Fig. 5.3 and 5.4, respectively. Applying Prop. 5.7 yields the corresponding eigenvalues to be $\lambda_1 = 3$ and $\lambda_2 = 3$ which are characterized by π_1 and π_2, respectively. Introducing the characteristic matrix P^{π_1} and P^{π_2} the corresponding eigenvectors are given by

$$v_1 = \begin{pmatrix} 1 & 0 \\ 1 & 0 \\ 1 & 0 \\ 0 & 1 \\ 1 & 0 \\ 0 & 1 \end{pmatrix} \begin{pmatrix} -3 \\ 1 \end{pmatrix} \quad \text{and} \quad v_2 = \begin{pmatrix} 1 & 0 \\ 1 & 0 \\ 0 & 1 \\ 0 & 1 \\ 1 & 0 \\ 1 & 0 \end{pmatrix} \begin{pmatrix} -3 \\ 1 \end{pmatrix}.$$

As $v_1 \neq v_2$ the eigenvalue $\lambda = 3$ has geometric multiplicity greater than one. Hence, the dynamical system (5.3) is uncontrollable as discussed in Prop. 5.2. The uncontrollable eigenvector is given by $v^{\bar{c}} = v_1 + \alpha v_2$ where we set $\alpha = \frac{1}{3}$ in order to zeroize the last entry of $v^{\bar{c}}$. Hence, we have $v^{\bar{c}} = [-1,-1,1,2,-1,0]^\intercal$ which explains the uncontrollable state $x^{\bar{c}} = v^{\bar{c}\intercal}\bar{x}$.

5.4.2 Non-Trivial AEP of the Quotient Graph

When inspecting the almost equitable partition of a quotient graph $\mathcal{G}/\pi$, further occurrences of uncontrollable subspaces can be affected by leader-cell-invariant almost equitable partition of an almost equitable partition of a graph which are not trivial. Note that $\mathcal{G}/\pi$ is generally directed

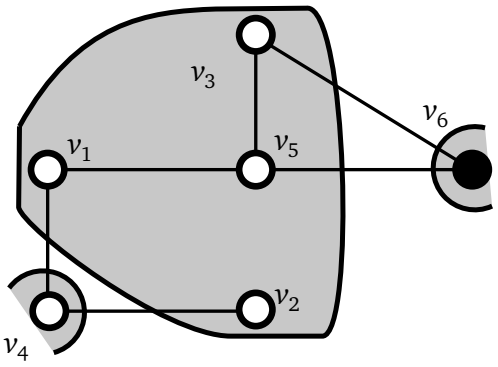

Figure 5.3: The leader is denoted as • and the almost equitable partition π_1 is denoted by the gray enclosures around the nodes. Here, $\pi_1 = \{\{v_4, v_6\}, \{v_1, v_2, v_3, v_5\}\}$ is an almost equitable bipartition which reveals the eigenvalue $\lambda_1 = 3$.

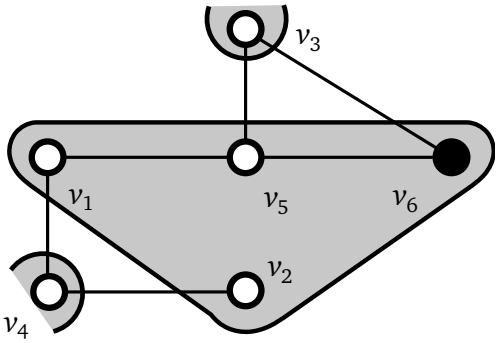

Figure 5.4: The leader is denoted as • and the almost equitable partition π_2 is denoted by the gray enclosures around the nodes. Here, $\pi_2 = \{\{v_3, v_4\}, \{v_1, v_2, v_5, v_6\}\}$ is an almost equitable bipartition which reveals the eigenvalue $\lambda_2 = 3$.

and weighted but can in particular be undirected and unweighted. Consequently, AEPs are also defined for $\mathcal{G}/\pi$. To formally state our result we first define the leader-cell-invariant almost equitable partition ρ of an almost equitable partition π. A leader-cell-invariant AEP ρ is then defined as

$$\rho^{-1}(\rho(C_k)) = C_k \text{ where } v_{N+1} \in C_k,$$

where the cell C_k contains the leader node v_k and the cell C_k is in a singleton cell. When inspecting the leader-cell-invariant AEP ρ of a quotient graph $\mathcal{G}/\pi$, uncontrollable subspaces can be induced as formally stated in the following.

Proposition 5.11. *Let $\mathcal{G}$ be an undirected graph and let $\pi = \{C_1, C_2, \dots, C_k\}$ be an almost equitable partition of $\mathcal{G}$. If the maximal leader-cell-invariant almost equitable partition $\rho = \{S_1, S_2, \dots, S_l\}$ of the quotient graph $\mathcal{G}/\pi$ is not trivial and $\mathcal{G}/\pi$ is undirected, then the controlled consensus protocol* (5.3) *is uncontrollable.*

Proof. The characteristic matrices P^π and $\bar{P}^\rho$ are defined as in Prop. 5.3. As ρ is non-trivial we know that $\bar{P}^\rho \neq \emptyset$. By a repeated application of Prop. 5.3 for we know that a Laplacian eigenvector is given by $v = P^\pi \bar{P}^\rho z$, where z is an eigenvector of the Laplacian of $\mathcal{G}/\pi/\rho$. Furthermore, since $\bar{P}^\rho$ is leader-cell-invariant and not trivial, the jth row of $\bar{P}^\rho$ is zero. Since $\mathcal{G}/\pi$ is undirected, $\bar{P}^\rho$ can be used to computed both left and right eigenvector. Due to the structure of the characteristic matrix P^π the zero row propagates also for the $N+1$th entry in the eigenvector of L. Hence, (5.3) is uncontrollable which follows from Proposition 5.1. □

The next example shows how Prop. 5.11 can be used to account for uncontrollable subspaces which are not covered by leader-invariant maximal almost equitable partitions.

Example 5.3. Consider the graph $\mathcal{G}$ depicted on the left hand side in Fig. 5.5 which has a trivial leader-invariant AEP. However, the uncontrollable subspace can be computed as $x^{\bar{c}} = x_4 + x_1 - x_2 - x_3$. We can explain $x^{\bar{c}}$ by applying Prop. 5.11. The graph $\mathcal{G}$ has an almost equitable 3-partition given by $\pi = \{\{v_1, v_4\}, \{v_2, v_3\}, \{v_5, v_6\}\}$ of which the characteristic matrix P^π and the generalized Laplacian L^π are given by

$$P^\pi = \begin{pmatrix} 1 & 0 & 0 \\ 0 & 1 & 0 \\ 0 & 1 & 0 \\ 1 & 0 & 0 \\ 0 & 0 & 1 \\ 0 & 0 & 1 \end{pmatrix} \text{ and } L^\pi = \begin{pmatrix} 1 & 0 & -1 \\ 0 & 1 & -1 \\ -1 & -1 & 2 \end{pmatrix}.$$

The quotient graph $\mathcal{G}/\pi$ is depicted on the right hand side of Fig. 5.5. The quotient graph $\mathcal{G}/\pi$ has a non-trivial leader-cell-invariant partition $\rho = \{\{C_1, C_2\}, \{C_3\}\}$. Hence, the matrix $\bar{P}^\rho$ for the quotient graph $\mathcal{G}/\pi$ is given by $\bar{P}^{\bar{\rho}} = e_1 - e_2$ and $z = 1$ where due to Prop. 5.3 the vector $\bar{P}^{\bar{\rho}}$ is an eigenvector of L^π. A recursive application of Prop. 5.3 yields an eigenvector $v^{\bar{c}}$ of the graph Laplacian L given by

$$v^{\bar{c}} = P^\pi P^{\bar{\rho}} z = e_1 + e_4 - e_2 - e_3,$$

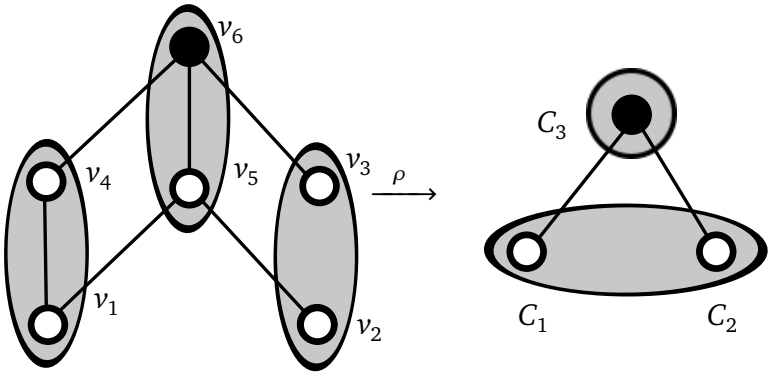

Figure 5.5: The leader is denoted as • and the almost equitable partitions π and ρ are denoted by the gray enclosures around the nodes. Here, $\pi = \{\{v_1, v_4\}, \{v_2, v_3\}, \{v_5, v_6\}\} = \{C_1, C_2, C_3\}$ is an almost equitable partition whose quotient graph $\mathcal{G}/\pi$ is depicted on the right side. The maximal leader-cell-invariant almost equitable partition of $\mathcal{G}/\pi$ is nontrivial as $\rho = \{\{C_1, C_2\}, \{C_3\}\}$. Hence, the dynamical system is uncontrollable.

which explains the uncontrollable state $x^{\bar{c}} = v^{\bar{c}\mathsf{T}}\boldsymbol{x}$.

In this section we introduced novel topological conditions which can explain the uncontrollability of a controlled agreement protocol. The last condition presented in this section considers Laplacian eigenvectors which have only zero elements except for $+1$ and -1. In the literature, these eigenvectors are called Faria vectors and we now discuss their relevance for the controlled consensus protocol in detail.

5.5 Uncontrollable Subspace by Faria Vectors

5.5.1 General Faria Vectors in Laplacians

A particular structure of Laplacian eigenvectors is called *Faria* vectors. A Faria vector has only zero entries except for two which are $+1$ and -1, see e.g. [176]. Hence, they can lead to an uncontrollable subspace. A general version of these vectors is first introduced in [175], where eigenvectors are investigated corresponding to an integer eigenvalue. Faria vectors are examined in the context of the multiplicity of integer roots of the characteristic polynomial of the Laplacian L. A Faria vector occurs in a graph if there exists a subset of vertices with the same degree p which have particular neighbors within the subset and particular edges to the remaining nodes. This is formally stated in the following.

Proposition 5.12 ([175])**.** *Let $\mathcal{G}$ be a graph on N vertices and V_p the set of vertices of $\mathcal{G}$ of degree p. If there are vertices $v_1, v_2, \ldots, v_{2r} \in V_p$, such that $\Gamma(v_j) \cap \Gamma(v_k) = \emptyset, 1 \leq j < k \leq r, \Gamma(v_j) \cap \Gamma(v_k) = \emptyset, r+1 \leq j < k \leq 2r$, and $\Gamma(\{v_1, \ldots, v_r\}) = \Gamma(\{v_{r+1}, \ldots, v_{2r}\})$, then p is an eigenvalue of L with the corresponding Faria eigenvector $v = [v_i]$, where $v_i = 1, i = 1 \ldots r$, $v_i = -1, i = r+1 \ldots 2r$, $v_i = 0, i = 2r+1 \ldots N$.*

In consequence there are Laplacian eigenvectors with 0 entries depending on topological conditions, which can lead to an uncontrollable subspace. However, this theorem is very strict

since all vertices within the set V_p are required to have the same degree p. To obtain a more general version of the previous theorem, we relax the condition that each vertex of V_p requires the same degree p. Therefore we divide the considered vertex set into two equal subsets. Here, we require that each vertex inside one subset is associated with a specific value with respect to its own degree, its neighbors in its own subset and the neighbors in the other subset. This condition is less restrictive in finding Faria eigenvectors.

Theorem 5.1. *Let $\mathcal{G}$ be a graph of N vertices. If there exists a partition π consisting of the three vertex sets $V_1 = \{v_1, \dots, v_r\}$, $V_2 = \{v_{r+1}, \dots, v_{2r}\}$ for some r and $V_\sigma = \mathcal{V} \backslash \{V_1, V_2\} = \{v_{2r+1}, \dots, v_N\}$ and if now*

$$\begin{aligned} &\Gamma_{V_\sigma}(v_j) \cap \Gamma_{V_\sigma}(v_k) = \emptyset \qquad 1 \leq j < k \leq r, \\ &\Gamma_{V_\sigma}(v_j) \cap \Gamma_{V_\sigma}(v_k) = \emptyset \qquad r+1 \leq j < k \leq 2r, \end{aligned} \tag{5.12}$$

and

$$\Gamma_{V_\sigma}(V_1) = \Gamma_{V_\sigma}(V_2), \tag{5.13}$$

and

$$\begin{aligned} &\exists p \in \mathbb{N}, \\ &\quad p = \deg(v_j) - \deg_\pi(v_j, V_1) + \deg_\pi(v_j, V_2) \qquad 1 \leq j \leq r, \\ &\quad p = \deg(v_j) - \deg_\pi(v_j, V_2) + \deg_\pi(v_j, V_1) \qquad r+1 \leq j \leq 2r, \end{aligned} \tag{5.14}$$

then p is an integer eigenvalue of L with the associated eigenvector $v = [v_i]$, where $v_i = 1$ for $i \in \{1, \dots, r\}$, $v_i = -1$ for $i \in \{r+1, \dots, 2r\}$, $v_i = 0$ for $i \in \{2r+1, \dots, N\}$.

Proof. For a given r the vertices of $\mathcal{G}$ can be relabeled in the following way. Let $V_1 = \{v_1, \dots, v_r\}$ be the first r vertices and $V_2 = \{v_{r+1}, \dots, v_{2r}\}$ be the next r vertices. The adjacent vertices of both V_1 and V_2 are ordered afterward. The remaining nodes are arbitrarily and thus the Laplacian L is given by:

$$L = \left[\begin{array}{ccc|ccc|c|c} \deg(v_1) & & \Psi_1 & & & & & \\ & \ddots & & & \Omega & & \Xi & 0 \\ \Psi_1^\intercal & & \deg(v_r) & & & & & \\ \hline & & & \deg(v_{r+1}) & & \Psi_2 & & \\ & \Omega^\intercal & & & \ddots & & \Pi & 0 \\ & & & \Psi_2^\intercal & & \deg(v_{2r}) & & \\ \hline & \Xi^\intercal & & & \Pi^\intercal & & \star & \star \\ \hline & 0 & & & 0 & & \star & \star \end{array}\right],$$

where due to (5.12) the rows of Π are linearly independent. The same fact is applicable for Ξ. However, since both sets V_1 and V_2 have the same set of neighbors due to (5.13), the row space of Π is equivalent to Ξ. The sum of each row in the strictly upper triangular matrices Ψ_1 and Ψ_2 is $\deg_\pi(v_j, V_1)$ and $\deg_\pi(v_j, V_2)$, respectively. The sum of each row in Ω and $\Omega^\intercal$ is $\deg_\pi(v_j, V_2)$ and $\deg_\pi(v_j, V_1)$, respectively. Since p is equal for vertices in V_1, V_2, p is an eigenvalue of L with the corresponding eigenvector $v = [v_i]$, $v_i = 1, i = 1 \dots r$, $v_i = -1, i = r+1 \dots 2r$, $v_i = 0, i =$

$2r+1 \dots n$. □

Theorem 5.1 provides a characterization of Laplacian eigenvectors with $0, -1, +1$ entries based on the topological conditions (5.12)-(5.14). It should be noted that Faria eigenvectors can only occur if the Laplacian has at least one integer eigenvalue constraining the class of graphs for which the method is suitable. We now define the set of eigenvalues $\sigma(L^{\text{Faria}})$ of Laplacian eigenvalues characterized by Theorem 5.1 as

$$\sigma(L^{\text{Faria}}) = \{p |\ p \in \sigma(A^{\bar{c}}) \cap p \text{ as defined in Theorem } 5.1\}.$$

For the controlled consensus problem we arrive at the following observations.

5.5.2 Faria Vectors in Controlled Consensus Protocols

If the leader node is selected among the nodes of $V_\sigma = \{v_{2r+1}, \dots, v_N\}$, the Faria eigenvector of the Laplacian has a zero entry at the leader position. It follows from Proposition 5.1, that under this leader the eigenmode associated with this Faria vector is uncontrollable. Note that analogously to Proposition 5.1 the Faria eigenvector is given as $\nu = \left[\nu_A^\intercal, 0\right]^\intercal$ where ν_A is also an eigenvector of A. Hence, the Faria vector ν describes one uncontrollable direction $x^{\bar{c}} = \nu_A^\intercal x$ which is asymptotically stable, $\lim_{t\to\infty} x^{\bar{c}}(t) = 0$. Since the Faria vector is constructed as $\nu = [\nu_i]$, $\nu_i = 1, i \in V_1$, $\nu_i = -1, i \in V_2$ an equality constraint appears for $t \to \infty$ as

$$\lim_{t\to\infty} \sum_{i\in V_1} x_i(t) - \sum_{i\in V_2} x_i(t) = 0.$$

If Faria vectors exist in a controlled agreement problem, they lead to equality conditions for the final states x^f of the leader-follower network. Besides characterizing the uncontrollable subspace, condition (5.14) provides us with the corresponding eigenvalue p. Note that through the decomposition of (A, B) from $-L$ in (5.2), the eigenvalue of A and $-L$ is $-p$. Hence, the equation of motion of the uncontrollable state characterized by a Faria vector ν is given by $e^{-pt}\nu_A^\intercal x_0$ where p and ν_A arise from topological properties. If we know all eigenvalues of the uncontrollable system, we can further conclude about the convergence rate within the uncontrollable subspace.

Corollary 5.1. *If the uncontrollable subspace is completely characterized by Faria vectors, the rate of convergence within the uncontrollable subspace is bounded by the smallest integer eigenvalue p_{min} associated with the characterizing Faria eigenvector.*

Proof. The dynamics of the uncontrollable subsystems are given as $\dot{x}^{\bar{c}} = A^{\bar{c}} x^{\bar{c}}$ and we use the positive definite $V = \frac{1}{2} x^{\bar{c}\intercal} x^{\bar{c}}$ as Lyapunov function candidate for the uncontrollable dynamics. Hence, $\dot{V} = \frac{1}{2}(\dot{x}^{\bar{c}\intercal} x^{\bar{c}} + x^{\bar{c}\intercal} \dot{x}^{\bar{c}}) = \frac{1}{2} x^{\bar{c}\intercal}(A^{\bar{c}\intercal} + A^{\bar{c}}) x^{\bar{c}} \leq \lambda_{\max}(A^{\bar{c}}) x^{\bar{c}\intercal} x^{\bar{c}} < 0 \quad \forall x^{\bar{c}} \neq 0$, where $\lambda_{\max}(A^{\hat{c}}) < 0$ is the largest eigenvalue of $A^{\hat{c}}$. The spectra of $A^{\hat{c}}$ and $A^{\hat{c}\intercal}$ are equal, $\sigma(A^{\hat{c}}) = \sigma(A^{\hat{c}\intercal})$, and the inequality $\frac{1}{2} x^{\bar{c}\intercal}(A^{\bar{c}\intercal} + A^{\bar{c}}) x^{\bar{c}} \leq \lambda_{\max}(A^{\bar{c}}) x^{\bar{c}\intercal} x^{\bar{c}}$ follows from the Rayleigh quotient. This proves that V is a valid Lyapunonv function. By assumption the uncontrollable subspace is completely characterized by Faria vectors which have associated eigenvalues p_i, of which the minimal eigenvalue is denoted as $p_{\min}$. These eigenvalues p_i are also the spectra of $-A^{\bar{c}}$ and $\lambda_{\max}(A^{\bar{c}}) = -p_{\min}$. Hence, the uncontrollable states vanish exponentially as $|x^{\bar{c}}(t)| \leq e^{-p_{\min} t} |x^{\bar{c}}(t_0)|$. □

Remark 5.4. The conditions (5.12)- (5.14) from Theorem 5.1 need to be tested as follows. For testing the conditions all possible vertex sets V_1, V_2 for all set cardinalities $r = 1 \dots \text{floor}\left(\frac{N}{2}\right)$ have to be created with $\text{floor}\left(\frac{N}{2}\right)$ being the maximal cardinality to create two vertex sets with equal cardinality. The remaining nodes are collected in V_σ. For the simplest cardinality, $r = 1$, condition (5.12) is always true. In order to find a Faria eigenvector, condition (5.12)- (5.14) have to be evaluated for each vertex set V_1, V_2.

Remark 5.5. Due to the duality of controllability and observability, the obtained results can be applied to the output node. Consider the consensus equation (5.2) and select an output node y resulting in the decomposition

$$\begin{aligned} \dot{x} &= Ax, \\ y &= B^\intercal x, \end{aligned} \tag{5.15}$$

where y represent the output nodes. Then the question is, whether the full system state can be reconstructed based on the observations at the output node. As a consequence on our results on the controllability we arrive at the following consideration here. The system (5.15) is unobservable if L has a Faria eigenvector and an output node belongs to the set V_σ of this Faria eigenvector.

Faria Vectors and Multiple Leaders

LEPs are only valid for single-leader consensus networks. An uncontrollable subspace characterized by Faria vectors can also occur for multiple leaders. The argumentation straightforwardly extends the single leader problem. In case of M leaders, the LTI system (5.2) is resized as $A \in \mathbb{R}^{(N+1-M)\times(N+1-M)}$ and $B \in \mathbb{R}^{(N+1-M)\times M}$. The description of uncontrollable subspaces described by Faria vectors builds on Proposition 5.1 and this theorem is also valid for multiple leaders and enhances as follows: If the $N-M$th entries are 0s in any eigenvector of L the associated eigenmode is uncontrollable. Consequently, the satisfaction of the conditions within the follower nodes in Theorem 5.1 leads to an uncontrollable subspace characterized by Faria vectors. Based on the previous characterization we can provide a design guideline for selecting the leaders.

Design Guideline for Multiple Leaders

As 0 entries in the Laplacian eigenvector at the leader index lead to an uncontrollable subspace and Faria eigenvector do only have $0, -1, +1$ entries, we are also able to interpret this in the context of leader-selection.

Corollary 5.2. *If a Faria vector is present as an eigenvector of the Laplacian L at least one input of* (5.3) *has to be chosen among the set V_1 and V_2 to avoid an uncontrollable subspace.*

Proof. We know from Proposition 5.1 that the corresponding system motion is uncontrollable if the Laplacian eigenvector has a 0 entry at the leader position From Theorem 5.1 we know that the vertices of V_1, V_2 have $+1/-1$ entries in the eigenvector. So when picking one leader among the two sets V_1, V_2 we avoid the 0 entry in the Laplacian eigenvector at the position of the leader. □

Example 5.4. Consider the graph in Fig. 5.1. If we choose the leader nodes as $\mathcal{V}_l = \{v_4, v_6\}$ then the uncontrollable subspace $x^{\bar{c}} = x_5 + x_3 - x_1 - x_2$ remains uncontrollable despite more inputs. In contrast by choosing the leader set as $\mathcal{V}_l = \{v_1, v_6\}$ we have direct access to $x^{\bar{c}}$ by agent 1 and the system is then completely controllable.

Faria Vectors and the Edge Principle

Since the entries of Faria vectors can only take the values $-1, +1, 0$ the edge principle is of interest here

Theorem 5.2 ([176])**.** *Let λ be an eigenvalue of L associated with the eigenvector v. If $v[i] = v[j]$, then λ is an eigenvalue of $L(\mathcal{G}^\star)$ associated with v, where $\mathcal{G}^\star$ is the graph obtained from $\mathcal{G}$ by deleting or adding $e = \{v_i, v_j\}$, depending on whether or not it is an edge of $\mathcal{G}$.*

Here it follows that we can add or remove edges connecting nodes within the sets V_1 and V_2, respectively, from the graph without effecting the uncontrollable subspace $x_{\bar{c}}$. Note that adding or removing edges can alter the LEP $\pi^\star$ and is hence not straightforwardly applicable.

Example 5.5. Note the graph in Fig. 5.1 here as example. Adding the edge $e = \{v_1, v_2\}$ or removing $e = \{v_3, v_5\}$ preserves the eigenvector $v = [-1, -1, 1, 0, 1, 0]$ and its corresponding uncontrollable space.

Note that the indistinct occurrence of LEP/Faria vectors is described in Remark 5.6.

5.6 Numerical Investigations

In this section the presented conditions for uncontrollable subspaces in controlled consensus protocol are evaluated. In the first subsection optimal control is applied to demonstrate the influence of uncontrollable subspaces in networks, while in the next subsection all non-isomorphic networks with $N = 2 \dots 8$ followers are generated to analyze the occurence of LEPs, Faria vectors, and other uncontrollable subspaces in a empirical way. Finally the influence of the number of vertices, the number of edges, and the edge probability on the uncontrollable subspaces is investigated for larger networks.

5.6.1 Open-loop Leader Input

To validate the statements about Faria vectors and LEP numerically we consider the graph depicted in Fig. 5.6. However, the structure of this graph also reveals two sets with equal cardinality which satisfy the Faria condition in Theorem 5.1. Here, $V_1 = \{v_2, v_3\}, V_2 = \{v_4, v_6\}, p = 2$ results in an equality constraint for the states and gives $x_1^{\bar{c}} = x_6 + x_4 - x_2 - x_3$. Furthermore $V_1 = \{v_1\}, V_2 = \{v_5\}, p = 3$ satisfies the Faria conditions. Here, the uncontrollable subspace $x_2^{\bar{c}} = x_1 - x_5$ can also be characterized by the LEP. Based on numerical investigations we observe the following.

Remark 5.6. Uncontrollable subspaces characterized by Faria vectors and uncontrollable subspaces by the clustering of an LEP can be equal and are no distinct sets. The coincidence of Faria vectors and LEPs can be straightforwardly explained by comparing Prop. 5.9 and Theorem 5.1.

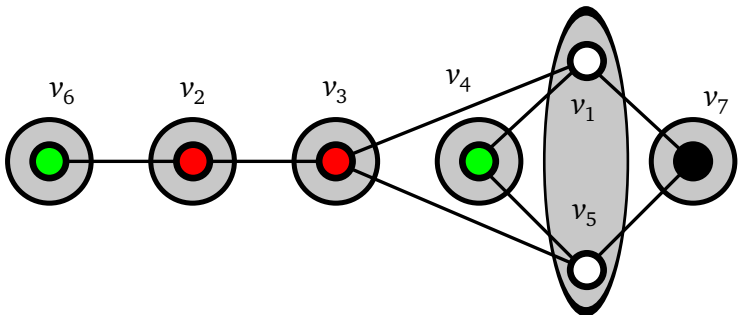

Figure 5.6: The leader is denoted as • and the partition π_l^* is denoted by the gray enclosures around the nodes. We obtain that $\pi_l^\star = \{\{v_1, v_5\}, \{v_2\}, \{v_3\}, \{v_4\}, \{v_6\}, \{v_7\}\}$ is not trivial, but $|\pi_l^\star| - 1 \neq \text{rank}(Q)$. Here, $x_1^{\bar{c}} = x_6 + x_4 - x_2 - x_3$ is uncontrollable and is described by Faria vectors due to the partitions V_1, V_2. The signs of the elements in $x^{\bar{c}}$ are denoted by •/•.

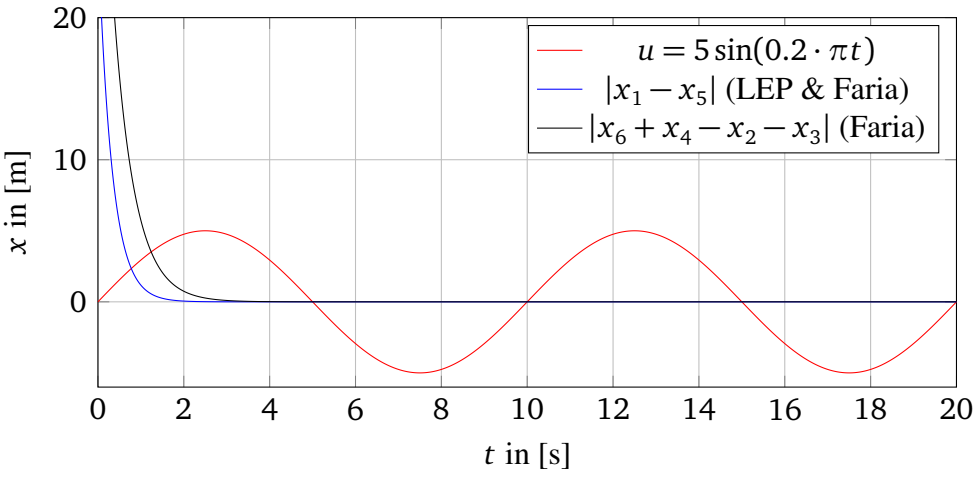

Figure 5.7: Though the system is excited, the uncontrollable subspace characterized by LEP & Faria vanishes.

We excite the system (5.3) with a sinusoidal signal $u(t) = 5\sin(0.2 \cdot \pi t)$. We observe that both uncontrollable subspaces converge as illustrated in in Fig 5.7: $\lim_{t\to\infty}(x_1(t) - x_2(t)) = 0$ and $\lim_{t\to\infty}\left(x_6(t) + x_4(t) - x_2(t) - x_3(t)\right) = 0$.

Often it is necessary to drive the controllable system states from an initial to a final configuration with an open-loop control input. To drive the controllable states from an initial $x^c(t_0)$ to a final configuration $x^c(t_f)$ within a finite time horizon t_f, we can directly apply the open-loop input

$$u_{[0,t_f]}(t) = -B^{c\,T} e^{A^{c\,T}(t_f - t)} W_s^{-1}\left(e^{A^c t_f} x^c(t_0) - x^c(t_f)\right),$$

with the Grammian matrix $W_s = \int_0^{t_f} e^{A^c \tau} B^c B^{c\,T} e^{A^{c\,T}\tau} d\tau$. As the uncontrollable subspace is asymptotically stable, the uncontrollable states $x^{\hat{c}}$ are located inside an ϵ-ball after t_f

$$|x^{\hat{c}}(t)| = |e^{A^{\hat{c}} t_f}||x^{\hat{c}}(t_0)| \leq e^{\lambda_{\max}(A^{\hat{c}})t_f}|x^{\hat{c}}(t_0)| \leq \epsilon.$$

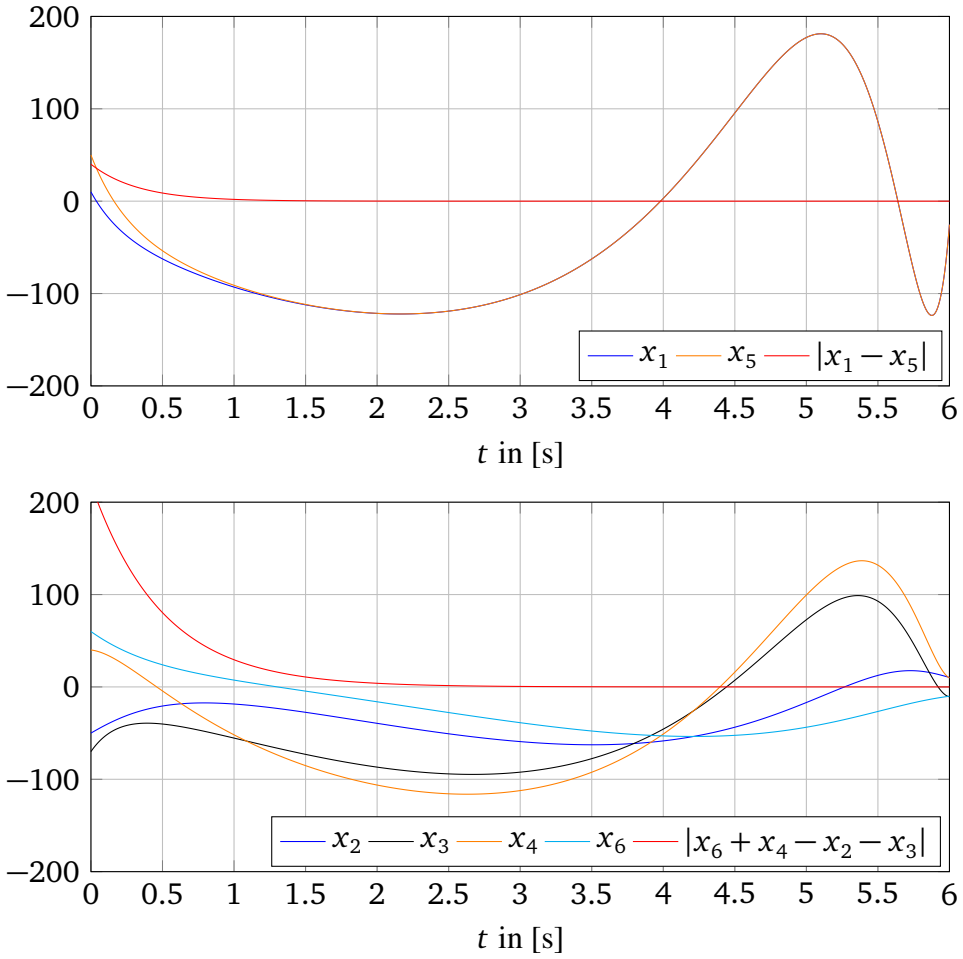

Figure 5.8: Both uncontrollable subspaces $|x_6+x_4-x_2-x_3|$ and $|x_1-x_5|$ are asymptotically stable. Both states x_1 and x_5 eventually evolve equal on the top. The states x_2, x_3, x_4, x_5 remain different in the transition phase for the second uncontrollable subspace.

Hence, the minimal time horizon results in

$$t_f \leq \frac{1}{\lambda_{\max}(A^{\hat{c}})} \log\left(\frac{\epsilon}{|x^{\hat{c}}(t_0)|}\right). \tag{5.16}$$

We want to drive the controllable states of graph in Fig. 5.6 from an initial configuration $x(0) = [10, -50, -70, 40, 50, 60]$ into a final configuration $x(t_f) = [-20, 10, -10, 10, -20, -10]$. The final configuration satisfies both uncontrollable subspaces since $\lim_{t\to\infty} (x_1(t) - x_5(t)) = 0$ and $\lim_{t\to\infty} \big(x_6(t) + x_4(t) - x_2(t) - x_3(t)\big) = 0$. Here, $|x^{\hat{c}}(t_0)| = 223.6$. Although $\{1, 5\}$ can be specified by LEPs, it can also be characterized by Faria vectors. A side effect of Faria vectors is that we can derive the eigenvalues, here $\lambda(A^{\bar{c}}) = (-2, -3)$ and so $\lambda_{\max}(A^{\hat{c}}) = -2$. Due to (5.16) the minimal time t_f to drive the system to a final configuration results as $t_f \leq \frac{1}{\lambda_{\max}(A^{\hat{c}})} \log(\frac{\Delta\epsilon}{|x^{\hat{c}}(t_0)|}) = -\frac{1}{2}\log(\frac{\Delta\epsilon}{220})$. We assume $\Delta\epsilon = 1e^{-2}$ and thus $t_f \leq 4.66$. Fig. 5.8 shows the states that are driven from $x(0)$ to $x(t_f)$.

5.6.2 Graph Size over Uncontrollable Subspace

The major objective of this subsection is to evaluate the quantitative occurrence of uncontrollable subspaces characterized by LEPs, Faria vectors, or Prop. 5.10 for all connected non-isomorphic graphs with for $N+1$ nodes where one node is the anchor/leader node. The set of all undirected and connected graph with $N+1$ vertices and a root is denoted by $\mathbb{G}_{N+1}^{\text{all},\bullet}$. The number of undirected graphs on $N+1$ vertices with an anchor vertex is Sequence A126100 in the OEIS [183]. For $N+1 = 3\dots10$ the cardinality of the sets $\mathbb{G}_{N+1}^{\text{all},\bullet}$ are $3, 11, 58, 407, 4306, 72489, 2111013, 111172234$. To obtain the numerical results in a reasonable amount of time we choose $N+1 \leq 9$ and generate all possible graphs with an anchor node. For larger graphs where $N \geq 9$ the occurrence of uncontrollable subspaces is later discussed based on a generation of random graphs. All non-isomorphic connected undirected graphs with $N+1 = 2\dots9$ nodes are efficiently generated using Nauty/Traces [184]. To obtain all non-isomorphic graphs with a special vertex which is in our scenario the leader the automorphism group of each graph and the corresponding orbits of the group are computed. Then one representative from each different orbit yields a graph with an anchor node[1].

For $N = 2, 3, 4, \dots 8$ there are in total $2\cdot3, 3\cdot11, 4\cdot58, \dots 8\cdot2111013$ different states for all non-isomorphic graphs. We checked controllability for each state in graphs with $N = 2, 3, 4, \dots 8$ followers using (5.4) i.e. for $N = 2$ 6 states have to be checked , for $N = 3$ there are 33 states and so on. The share of the total number of uncontrollable states in the total number of uncontrollable states for each N can be computed by

$$p_{N,\text{Kalman}}(\mathbb{G}_{N+1}^{\text{all},\bullet}) = \sum_{\mathcal{G}\in\mathbb{G}_{N+1}^{\text{all},\bullet}} \frac{|\sigma(A^{\bar{c}}(\mathcal{G}))|}{N|\mathbb{G}_{N+1}^{\text{all},\bullet}|},$$

and is depicted in Fig. 5.9 for $N = 2\dots8$ followers. We observe that for $N = 2, 3, 4, 5$ about a third of all the states is uncontrollable. In our analysis for $N \geq 4$ the share decreases until only 9.4% of all states are uncontrollable for $N = 8$. Though as the total number of states increases as given by the OEIS sequence A126100 and given by the number of followers the absolute number of uncontrollable states increases significantly, i.e. 9.4% of $2111013 \cdot 8$ is in total 1587737 uncontrollable states which is significantly larger than 33% yielding 2 uncontrollable states for $N = 2$. Furthermore, the share of uncontrollable states characterized by LEPs given by Prop. 5.5 and Faria vectors given by Theorem 5.1 is depicted in Fig. 5.9. The major share of uncontrollable subspaces can by characterized by both LEPs and Faria vectors (red) which is defined as

$$p_{N,\text{Faria}\cap\text{LEP}}(\mathbb{G}_{N+1}^{\text{all},\bullet}) = \sum_{\mathcal{G}\in\mathbb{G}_{N+1}^{\text{all},\bullet}} \frac{|\sigma(\bar{L}^{\pi_l^*}) \cap \sigma(L^{\text{Faria})})|}{N|\mathbb{G}_{N+1}^{\text{all},\bullet}|}.$$

The share of uncontrollable subspaces which are only characterized by LEPs is defined as

$$p_{N,\text{LEP}}(\mathbb{G}_{N+1}^{\text{all},\bullet}) = \sum_{\mathcal{G}\in\mathbb{G}_{N+1}^{\text{all},\bullet}} \frac{|\sigma(\bar{L}^{\pi_l^*}) \backslash (\sigma(\bar{L}^{\pi_l^*}) \cap \sigma(L^{\text{Faria})}))|}{N|\mathbb{G}_{N+1}^{\text{all},\bullet}|},$$

[1] The authors thank Gordon Royle and Brendan McKay for their support in this context with nauty.

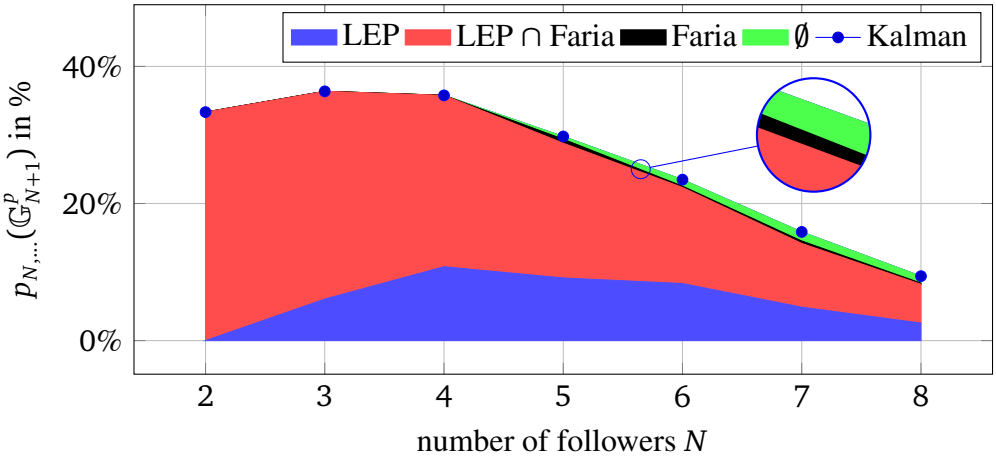

Figure 5.9: All non-isomorphic graphs for $N = 2 \dots 8$ with an additional anchor node are considered to empirically investigate the share of the total number of uncontrollable states described by LEP or Faria in the total number of states. Note here that the plots are stacked for the sake of exposition.

and is less but significant (blue). The share of uncontrollable states only described by Faria vectors (black) for $N > 4$ and is minor.

$$p_{N,\text{Faria}}(\mathbb{G}^{\text{all},\bullet}_{N+1}) = \sum_{\mathcal{G} \in \mathbb{G}^{\text{all},\bullet}_{N+1}} \frac{|\sigma(L^{\text{Faria}})) \backslash (\sigma(\bar{L}^{\pi_l^*}) \cap \sigma(L^{\text{Faria}}))|}{N |\mathbb{G}^{\text{all},\bullet}_{N+1}|}.$$

The remaining uncontrollable subspaces (green) as e.g. proposed by Prop. 5.10 are given by

$$p_{N,\emptyset}(\mathbb{G}^{\text{all},\bullet}_{N+1}) = p_{N,\text{Kalman}} - p_{N,\text{Faria}\cap\text{LEP}} - p_{N,\text{LEP}} - p_{N,\text{Faria}}.$$

Yet though the share of $p_{N,\text{Faria}}$ and $p_{N,\emptyset}$ is quite low there are plenty of those subspaces in total numbers as discussed earlier, e.g. for $N = 8$ we have $p_{8,\text{Faria}} \approx 0.17\%$ and $p_{8,\emptyset} \approx 1\%$ which is in total numbers 30239 and 170829 states.

Furthermore, we are interested in the arithmetic mean of the number of uncontrollable states $\overline{|\sigma(A^{\bar{c}}(\mathbb{G}^{\text{all},\bullet}_{N+1}))|} = \sum_{\mathcal{G} \in \mathbb{G}^{\text{all},\bullet}_{N+1}} \frac{|\sigma(A^{\bar{c}}(\mathcal{G}))|}{|\mathbb{G}^{\text{all},\bullet}_{N+1}|}$ by Kalman and $\overline{|\sigma(\bar{L}^{\pi_l^*}(\mathbb{G}^{\text{all},\bullet}_{N+1}))|} = \sum_{\mathcal{G} \in \mathbb{G}^{\text{all},\bullet}_{i+1}} \frac{|\sigma(\bar{L}^{\pi_l^*})|}{|\mathbb{G}^{\text{all},\bullet}_{N+1}|}$ by LEP and the corresponding standard deviations for controlled consensus networks with all connected graphs $\mathbb{G}^{\text{all},\bullet}_{N+1}$ with $N = 2 \dots 8$ followers. The mean and standard deviation over the number of followers $N = 2 \dots 8$ is depicted in Fig. 5.10. Note that $|\sigma(A^{\bar{c}})| \geq |\sigma(\bar{L}^{\pi_l^*})|$ as specified in Prop. 5.6 and so it also holds for the arithmetic mean as $\overline{|\sigma(A^{\bar{c}})|} \geq \overline{|\sigma(\bar{L}^{\pi_l^*})|}$. In a very naive way the arithmetic mean gives us the expected number of uncontrollable states for a particular graph with N followers. From $N = 2$ to $N = 4$ the arithmetic mean increases and later for $N \geq 5$ the arithmetic mean decreases again. The decrease of the arithmetic mean of $\overline{|\sigma(A^{\bar{c}}(\mathbb{G}^{\text{all},\bullet}_{N+1}))|}$ for increasing N is unexpected here. Naively speaking the expected number of uncontrollable states for a particular graph decreases though the number of states N increases. To explore this phenomena in more detail we investigate larger graphs, i.e. $N \geq 10$ in the next subsection.

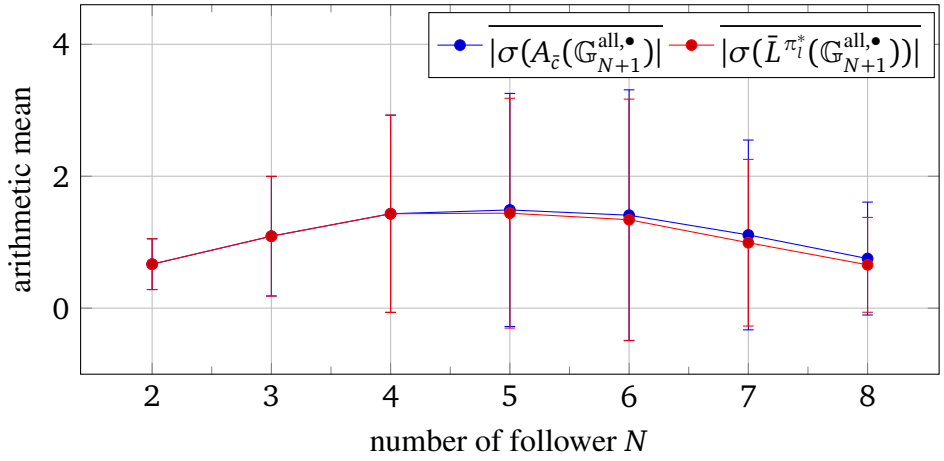

Figure 5.10: For all non-isomorphic graphs with a single anchor node for $N = 2 \dots 8$ the arithmetic mean and the standard deviation of the uncontrollable state.

5.6.3 Uncontrollable Subspaces and Graph Sparsity

The major objective of this section is to numerically evaluate the share of the uncontrollable subspace on the total subspace for graphs with different number of edges. For each $N = 2, 4, 6, \dots 20$ followers and one leader and for each edge probability as $p = 0.1, 0.2, \dots 0.9$ 10000 connected and undirected graphs are randomly generated using Nauty/Traces. Nauty/Traces is a software tool for computing automorphism groups of (di)graphs which come along with efficient generators for (bipartite) graphs, digraphs, and multigraphs in large-scale in a compact format. For further detail see [184]. After generating a particular graph the leader node is selected randomly. We denote the set of 10.000 randomly generated connected graphs with N followers and p edge probability by $\mathbb{G}^p_{N+1}$ where we have $|\mathbb{G}^p_{N+1}| = 10.000$. Note here that the graphs can be isomorphic, so there are in total $20.000, 40.000 \dots 200.000$ states for each $p = 0.1, \dots 0.9$. The share $p_{N,\text{Kalman}}(\mathbb{G}^p_{N+1})$ of the total number of uncontrollable states in the total number of states over the edge probability $p = 0.1, \dots 0.9$ for each N is depicted in Fig. 5.11. We observe here two interesting phenomena.

First, for all connected graphs with $N > 4$ the share of uncontrollable states in the total number of states has two peaks, namely for rather sparse graphs, i.e. $p = 0.1$ and for rather dense graphs, i.e. $p = 0.9$. Note here that the share in dense graphs is always larger than the share in sparse graphs. For graphs with edge probability between $p = 0.1$ and $p = 0.9$ there is a valley in the share.

Second, the more follower there are in the controlled consensus protocol (or equivalently the larger N is), the lower is the valley in the share between $p = 0.1$ and $p = 0.9$. For $N > 14$ the share of uncontrollable states in the total number of states for $p = 0.5$ tends to zero.

Both observations are in line with a very interesting open issue on sparse graph which are obtained from structural controllability analysis: sparser graphs are known to be more difficult to control [185]. However, it remains still open whether leader centrality or degree heterogeneity plays a major role in defining controllability of sparse graphs.

Remark 5.7. Evaluating (5.4) for graphs with $N > 15$ and $N > 40$ vertices we faced numerical issues using MATLAB functions *rank*/*ctrb* and *ctrbf*, respectively. We recommend here to

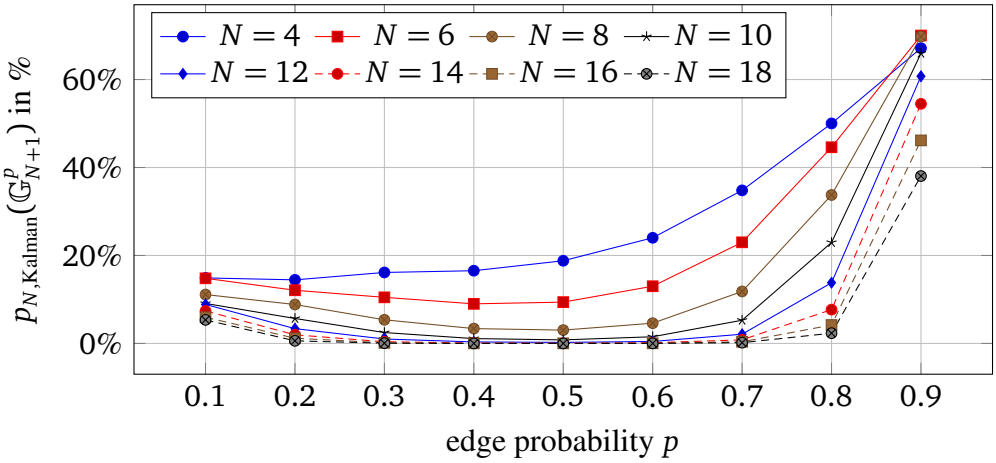

Figure 5.11: 10.000 random and connected graphs with each $N = 4, 6, \ldots, 20$ nodes and with each edge probability ranging from $0.1, \ldots 0.9$ are generated. The share of uncontrollable states in the total states over the edge probability shows two peaks for sparse and dense graphs.

apply the Popov-Belevitch-Hautus (PBH) test when checking for controllability of the controlled consensus protocol. The PBH test requires the calculation of $\text{rank}[\lambda_i I_N - A \mid b] \;\forall\; \lambda_i \in \sigma(A)$.

5.6.4 Uncontrollable Subspaces and LEPs

The major objective of this section is to numerically evaluate how a different number of nodes and a different number of edges affects the number of uncontrollable states. Especially, we are interested how both influence the quantitative difference between the states described by the Kalman condition and by LEPs.

10.000 connected graphs with $N = 49$ followers with the edge size being $|\mathscr{E}| = 1000 \ldots 1200$ are randomly generated using Nauty/Traces [184]. For each edge size $\mathscr{E}$ the set of graphs is denoted by $\mathbb{G}_{50}^{|\mathscr{E}|}$. Note here that the graphs are not necessarily isomorphic and so there are 490.000 states for each edge size in total. The share of the number of uncontrollable states $p_{N,\text{Kalman}}(\mathbb{G}_{50}^{|\mathscr{E}|})$ is plotted over the edge size in Fig. 5.12. It is apparent here that the share $p_{N,\text{Kalman}}(\mathbb{G}_{50}^{|\mathscr{E}|})$ of uncontrollable states increases with the number of edges. This observation confirms the statement in Section 5.6.3. The relative deviation between share $p_{N,\text{Kalman}}(\mathbb{G}_{50}^{|\mathscr{E}|})$ of uncontrollable subspaces characterized by LEPs in the number $p_{N,\text{LEP}}(\mathbb{G}_{50}^{|\mathscr{E}|})$ of subspaces given by the Kalman criterion is defined as $\frac{p_{N,\text{Kalman}}(\mathbb{G}_{50}^{|\mathscr{E}|}) - p_{N,\text{LEP}}(\mathbb{G}_{50}^{|\mathscr{E}|})}{p_{N,\text{Kalman}}(\mathbb{G}_{50}^{|\mathscr{E}|})}$. We observe in Fig. 5.12 that the relative deviation increases from $|E| = 1000$ to $|\mathscr{E}| = 1175$. Especially, here it is relevant to consider Propositions 5.10 and 5.11. The relative deviation drops again when the graph becomes more complete ($|\mathscr{E}| > 1175$).

Furthermore, 10.000 connected graphs with $|\mathscr{E}| = 1765$ edges and the number of follower ranging from $N = 9 \ldots 19$ for each are randomly generated using Nauty/Traces [184]. For each follower size N the set of graphs is denoted by $\mathbb{G}_{N+1}^{|\mathscr{E}|=1765}$. Note here that the graphs are not necessarily isomorphic and so there are $9.000, \ldots, 19.000$ states for the vertex size in total. The share of uncontrollable states $p_{N,\text{Kalman}}(\mathbb{G}_{N+1}^{|\mathscr{E}|=1765})$ is plotted over the number of followers in Fig. 5.13. The relative deviation $\frac{p_{N,\text{Kalman}}(\mathbb{G}_{N+1}^{|\mathscr{E}|=1765}) - p_{N,\text{LEP}}(\mathbb{G}_{N+1}^{|\mathscr{E}|=1765})}{p_{N,\text{Kalman}}(\mathbb{G}_{N+1}^{|\mathscr{E}|=1765})}$ between the uncontrollable

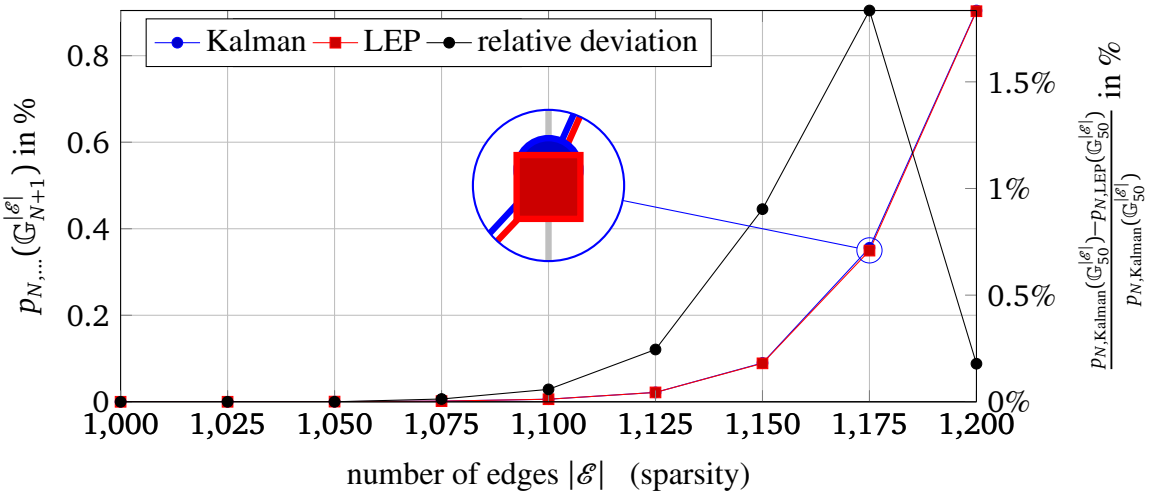

Figure 5.12: 10.000 random and connected graphs with $N = 49$ followers are generated with the edge size being $|\mathscr{E}| = 1000 \dots 1200$. The number of uncontrollable states is plotted over the number of edges. The relative deviation of uncontrollable subspaces not characterized by LEP has a peak at $|\mathscr{E}| = 1175$ (right axis).

subspaces characterized by LEPs from the subspaces given by the Kalman criterion increases with ascending follower number from $N = 9$ to $N = 19$. Especially, here it is relevant to consider Propositions 5.10 and 5.11.

5.7 Experiencing Network Interaction in a Virtual Reality

Leader-follower dynamics in interconnected systems have various application domains in practice and are of great relevance in recent theoretical research. For a relative small network of robotic followers the interaction paradigm was evaluated in Chapter 4. The dominant benefit of leader-follower consensus is considered to be its scalability, i.e. when the number of followers becomes large scale. However, the interaction with a large number of actual and real robots is genuinely hard to realize due to their availability and due to their vulnerability to failures. This section aims to provide a mechanism for interacting with large-scale network of robotic agents in a virtual reality which abandons the disadvantages of actual robots mentioned previously. The application for virtual realities range from consumer gaming experiences to providing simulated environments that could otherwise not be provided to the human operator. The intended idea is to create and maintain an impression with the human operator of a reality around him/her that is actually not physically present. We aim at establishing a system for visualizing the dynamic behavior of *large-scale* interconnected dynamical systems. To provide the human operator with the experience of interaction such a system consists of multiple parts: the first one tracks the motion of the human as input, the second one processes the human input and excites the controlled consensus dynamics based on the human input, and the third step visualizes the interaction in a virtual reality to make the interaction more favorable. To sum up we display the human operator an environment and a network of objects that are not physically present but the human operator can interact with them. The experimental setup is described in the upcoming section.

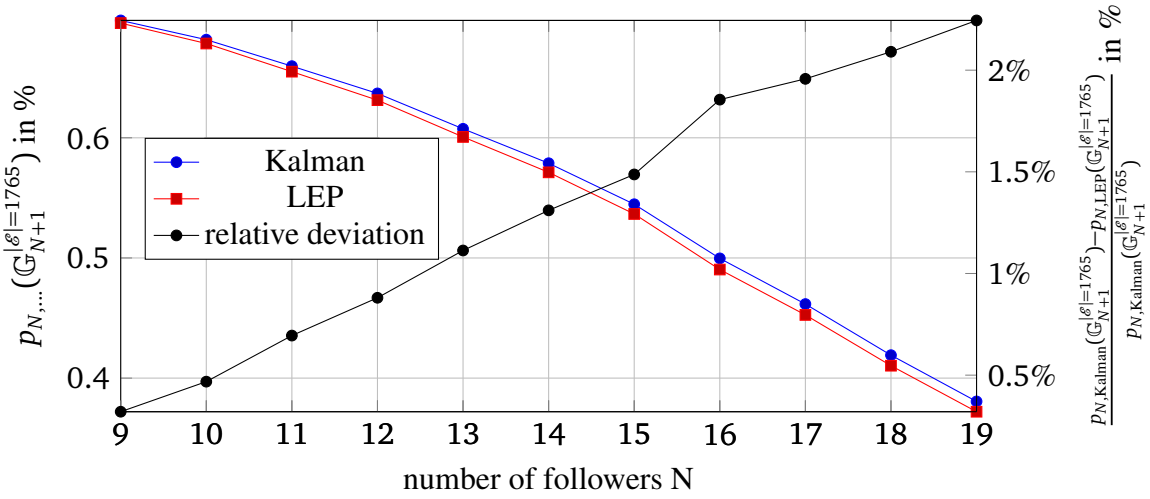

Figure 5.13: 10.000 random and connected graphs are created with $|\mathscr{E}| = 1765$ edges and the number of followers ranging from $N = 9 \ldots 19$. The number of uncontrollable states is plotted over the number of followers. The relative deviation (black) of uncontrollable subspaces not characterized by LEP increases with ascending number of followers N.

5.7.1 Experimental Setup

The objective of this section is to illustrate how the human operator can interact with a network of cooperating agents in order to guide the network with the movement of his/her hand. The setup consists of three parts: the tracking system is mainly a hardware component, the multi-agent system is a software system and the visualization is a combination of both hardware and software. A general overview of the system is depicted in the Fig. 5.14. In the following we clarify the aspects of each part in detail.

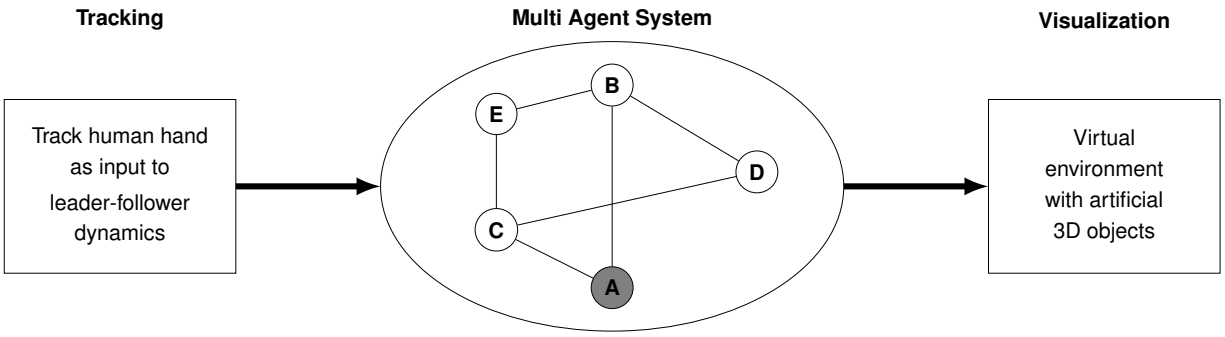

Figure 5.14: Arrangement of different system components. The human hand movement is tracked by a Qualisys Motion Tracker system. Wearing a head-mounted stereo display the human operator perceives an interaction with the network of objects based on his/her arm movement.

Tracking System

To collect the data of the human hand motion , a Qualisys Motion Tracker system is employed. Further details on the motion tracking system can be found in Appendix C. The human operator is equipped with a marker-equipped glove. The motion capture system can track the motion of the glove at a very high accuracy which facilitates to transfer relatively small human inputs to the system dynamics. In order to transmit the motion input data to the multi-agent system simulation a UDP connection is used to transfer the continuous data stream in real-time

Multi-Agent System

To simulate the system dynamics (5.3) in 3D the multi-agent system is implemented in Simulink using MTIDS [186]. MTIDS is a Matlab toolbox for creating and simulating large-scale interconnected systems. Using MTIDS we are able to create individual interacting topology with different agent dynamics. An interface to Simulink is provided which enables an easy and fast integration of the system. Furthermore, MTIDS provides us with the algebraic graph properties such as the Laplacian L and system matrix A which are calculated and provided automatically. To serve the particular purpose of the user experience templates for the three-dimensional consensus protocol are created.

Visualization

After the human motion is tracked and the network is simulated based on the processed motion data in Simulink a visualization is required to provide the operator with an intensive experience To make the interaction with the multi-agent system more realistic the 3D visualization is illustrated on a head-mounted stereo display namely the Oculus Rift depicted in Fig. 5.15. The Oculus Rift features 3 axis gyroscopes, accelerometers and magnetometers with an update rate of 1000Hz. Stereo images are displayed on a 7" display with features a resolution of 1280x800. Fig. 5.17 shows the virtual environment with which the human operator can interact through the motion of his/her hand. This 3D visualization is then displayed to make interacting with the network in a virtual reality possible for seamless human-network interaction. The leader node which directly follows the motion of the human hand is highlighted in red color. Note that the following agents are illustrated by objects of different shape and color. The interaction topolgy is depicted by solid lines. To increase the impression of surround vision while compensating for the lack of a third dimension on the head-mounted display, a black underground is drawn beneath the scene.

While displaying a graphic on a computer monitor one only needs a single image, for stereo vision two images are required. Note here that both graphics have to be projected by an appropriate perspective transformation in order to display one plane on the Oculus Rift. The method of projecting two images is called image rectification. Image rectification is used to create a 3D impression when wearing a head-mounted display. Without that image rectification the regarded image is distorted as explained in Fig. 5.16 on the left hand side. On the right hand side the view after a image rectification is shown. Based on an established computer graphics method, a perspective transformation matrix rectifies the view for the human operator. Using a motion-tracking system and a head-mount stereo display we are able to provide the user a swarm interaction experience in an easy and uncomplicated manner.

Figure 5.15: Head-mounted stereo display Oculus Rift.

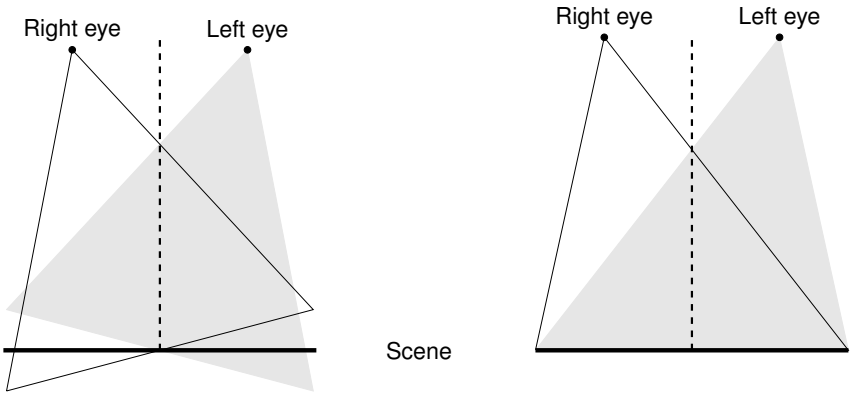

Figure 5.16: Stereo vision without image rectification yields a distorted image (left). With image rectification there is no distortion (right).

5.8 Summary

In this chapter we provide a novel approach to characterize the uncontrollable subspace of a controlled consensus problem based on topological properties. Section 5.3 outlines the controllability questions for controlled consensus protocol and exposes the most relevant results based on algebraic graph theory. It is based on the knowledge that almost equitable partitions are closely related to the Laplacian eigenvectors and here zero entries in the eigenvectors of the Laplacian result in an uncontrollable subspace of the controlled consensus protocol. The close relation of almost equitable partitions and Laplacian eigenvectors is analyzed here in detail. The role of generalized almost equitable partitions for characterizing the uncontrollable subspace of the controlled consensus problem is exposed in Section 5.4. We reveal several novel topological conditions for describing the uncontrollable subspace. In 5.5 we discuss that the Laplacian eigenvectors with 0s can be characterized e.g. by Faria vectors which arise from particular adjacency relations of two equal vertex sets and lead to equality constraints. The proposed approach complements the existing one based on leader-invariant almost equitable partitions (LEPs). In Section 5.6 we verify that uncontrollable subspaces for examples of graphs that are previously defined in the literature can now be identified by the condition provided in this chapter. Furthermore, extensive numerical investigations considering graphs with different sizes and connectivities evidence the

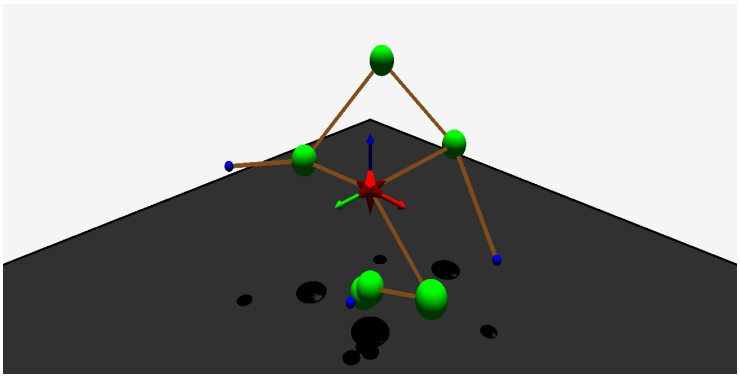

Figure 5.17: Single view visualization of the multi-agent system. Each agent is a object of different color and shape. The interaction topology is depicted by brown, solid lines.

relevance of our results. Section 5.7 completes the chapter with the introduction of a new concept of a virtual reality through which a human operator can interact with a large-scale network in an easy and uncomplicated manner. Wearing a head-mounted stereo display the human operator can conveniently and freely lead a virtual network of various followers with the movement of his/her hand and so experience the feeling of human-network interaction.

6

Conclusions and Outlook

The interaction and cooperation of robots with humans and among each other is an essential prerequisite for the acceptance of robotic assistances in our society. The guidance of a cooperative robotic manipulation task by a human operator encompasses relevant application domains such as manufacturing, construction, agriculture and forestry, service robotics, search and rescue but also cooperative aerial and underwater manipulation. A convenient interface of the human operator to multiple cooperative robotic helpers is realized by means of a pertinent system synthesis: (i) distributed robot control which facilitates robot autonomy in cooperative manipulation tasks, (ii) a human-robot-team interaction mechanism by which multiple robots can be simultaneously and efficiently controlled, and (iii) a system analysis of the interaction topology which characterizes the influence of the human input on the following robotic agents from a system-theoretic point of view.

In order to control multiple robots distributedly in a cooperative robotic manipulation task, Chapter 3 presented a novel LQR-like optimal control design of a control law which drives a formation of interconnected robots from an initial configuration to a desired final configuration. An important novel property is the inclusion of the formation rigidity as penalty term into the cost functional, thus combining the two research directions of formation control and advanced nonlinear robot dynamics. The resulting cost functional includes biquadratic terms. Two iterative algorithms, the first based on gradient descent, the second on a quasi-Newton method, are presented to solve the optimal control problem and derive the feedback matrix. The presented algorithms are validated in numerical simulations and experiments. Furthermore, a second control approach based on cooperative dynamic movement primitives (DMPs) is presented. A cooperation feedback term based on an artificial potential field for formation control is introduced into the original DMP formulation. The equilibria analysis provides desired and undesired equilibria, however, the undesired equilibria turn out to be of no practical relevance. The effectiveness and quality of both proposed controllers with respect to disturbances is successfully demonstrated in experiments.

When a human operator issues commands to a number of robots simultaneously, several challenges of human-swarm interaction are acknowledged. A distributed control law and a feedback strategy for a robot team guided by a single human in a cooperative manipulation task, which makes use of a formation-based paradigm, is presented in Chapter 4. By analyzing the system properties of such a human-robot formation control we deduce that a human-to-all connection in the underlying interaction topology is beneficial for a successful manipulation task execution. The effectiveness and quality of the human-driven set-point generator based on a virtual and artificial robot formation for a cooperative robotic manipulation task is successfully demonstrated in experiments and in a user study.

By significantly increasing the number of robotic followers, it is shown that the interaction topology of the underlying communication network literally plays a dominant role in the characterization of the human influence on particular robots. The influence of the human operator on particular robotic followers is denoted by the system theoretical property of controllability. In Chapter 5 a novel approach is presented to describe the uncontrollable subspace of a controlled consensus problem based on topological properties. It is based on the knowledge that particular partitions called *almost equitable partitions* are closely related to the Laplacian eigenvectors and that zero entries in Laplacian eigenvectors lead to uncontrollable subspaces of the controlled consensus protocol. These eigenvectors with 0s can be characterized, e.g. by Faria vectors which arise from particular adjacency relations of two equal vertex sets and lead to equality constraints. The proposed approach complements the existing one based on leader-invariant almost equitable partitions (LEPs). We verify these uncontrollable subspaces for counterexamples of graphs that are previously defined in the literature. Furthermore, extensive numerical investigations considering graphs with different sizes and connectivities evidence the relevance of our results.

This thesis addressed relevant steps towards rendering the guidance of multiple cooperating robots by a single human operator possible in order to fulfill a challenging and collective objective.

6.1 Outlook

Human-robot interaction has the ultimate goal of a seamless interaction between the robots and a human operator. Further research should close the gap between theory and praxis and it should facilitate the humans to solve ambitious issues better, safer, and faster. The guidance mechanism, which is presented in the thesis at hand, of a cooperative manipulation task by a single human operator further elaborates the development in this area towards an efficient but also stable system. State-of-the-art methods in the context of cooperative manipulation are considered and new dimensions are introduced in the guidance of multiple robots with the leader-follower interaction framework for cooperative manipulation. Although relevant issues regarding the control design were addressed in this thesis, the placement of a cooperative human-guided robotic manipulation task in daily life requires further research.

Distributed control for flexible objects

The proposed distributed control schemes, which allow for successful and proven cooperative robotic manipulation, consider multiple robots *rigidly* grasping a *rigid* object. Considering a non-rigid grasp or a flexible manipulated object or both opens up a new dimension of challenges.

First, a consistent dynamical system model is required for the interaction dynamics. We assume, that a hybrid formulation of the system dynamics can provide possible solutions to model the contact of the manipulators with the object for different grasp types. Furthermore, we suggest that flexible objects should be incorporated in the multi-robot interaction dynamics by exploiting the results of object impedance control. This extension can further increase the applicability of our proposed controllers by exhibiting their robustness in different situations including also aerial or underwater cooperative manipulation.

Adjustable team control for a single human

An architecture for team control allows humans to control other robotic agents but the human should also to receive feedback cues from the serving agents. The development of a higher level control architecture for the heterogeneous team of human and robots is essential for a seamless human-robot interaction which facilitates different modes of operation in the proposed supervisory control. A major challenge in the development of such an architecture is to what extend the notification and guidance of a human operator can be effectively accomplished. In order to obtain fundamental insights into the appropriate allocation of roles, the development of a system theoretical input-output model of the human operator is considered to be a first step towards finally installing an entire supervisory control architecture. These are necessary intermediate steps in applying robots in real-world challenges where complex tasks need to be conducted during an interactive session.

Degree of controllability for networks

Detached from the cooperative manipulation task, there exist situations in which a network of agents has to be conducted by a single input and in which it is then necessary to control not only the collective behavior of the robots but to individually address subgroups. In such a situation the yes-no question of controllability, which answers if the input can guide specific robots independently from each other, is often helpful but not sufficient. Often the responsible system design engineer additionally wonders, how much effort or energy is necessary in order to issue commands to specific robots. A substantially equivalent question from a control theoretic point of view here is how close one particular state to uncontrollability is. Defining a degree of controllability for human network interaction is already a very though and challenging task when control theoretic results are contemplated. Extending the topological controllability discussion of leader-follower networks in terms of a degree of controllability gives rise to a complete new research question.

We are confident that more relevant results can be made in the near future and that the guidance of multiple robots for achieving a cooperative task will some day be applied in space missions and in large-scale hazardous and dangerous operations.

A

Linear Algebra

Modeling and control of a group of robot manipulators and the interaction of a human with a network of following robotic agents requires an extensive use of matrices and vectors.

Definitions

A matrix of dimension $(m \times n)$ where m and n are positive integers is defined as an array arranged into m rows and n columns as

$$A \in \mathbb{R}^{m \times n} \Leftrightarrow A = \left[a_{ij}\right]_{\substack{i=1,\dots m, \\ j=1,\dots n}} = \begin{bmatrix} a_{11} & \dots & a_{1n} \\ \vdots & & \vdots \\ a_{m1} & \dots & a_{mn} \end{bmatrix}, a_{ij} \in \mathbb{R}.$$

A matrix is said to be square if $m = n$. A matrix A is called a diagonal matrix if $a_{ij} = 0$ for $i \neq j$, i.e. $A = \mathrm{diag}(a_{11}, a_{22}, \dots, a_{nn})$. If a diagonal matrix has only unit entries on the diagonal, i.e. $a_{ii} = 1$, the matrix is called identity matrix and is denoted by I_n. A matrix is said to be a null matrix if all elements are zero and it is denoted by 0. Transposition is a basic matrix operation which is given by

$$C = A^{\intercal} \Rightarrow c_{ij} = a_{ji},$$

where $()^{\intercal}$ is an operation which interchanges the rows and the columns of a matrix. If $A = A^{\intercal}$, then a matrix is said to be symmetric. The rank of a matrix A is denoted by $\mathrm{rank}(A)$ and is said to be the dimension of the space spanned by its columns or its rows. A matrix is said to be full rank if $\mathrm{rank}(A) = \min(m, n)$. A square matrix is said to be invertible if there is a matrix $A^{-1} \in \mathbb{R}^{n \times n}$ such that

$$A^{-1}A = AA^{-1} = I_n.$$

A matrix is said to be orthogonal if $A^\intercal = A^{-1}$. The Woodbury identity which can be used to calculate the inverse of a matrix is known in different variations such as

$$(A+CBC^\intercal)^{-1} = A^{-1} - A^{-1}C(B^{-1}+C^\intercal A^{-1}C)^{-1}C^\intercal A^{-1},$$
$$(A+UBV)^{-1} = A^{-1} - A^{-1}U(B^{-1}+VA^{-1}U)^{-1}VA^{-1}.$$

A set of Searle identities which are employed throughout this thesis is given by

$$(I_n + A^{-1})^{-1} = A(A+I_n)^{-1},$$
$$(A+BB^\intercal)^{-1}B = A^{-1}B(I_n + B^\intercal A^{-1}B)^{-1},$$
$$(I_n + AB)^{-1} = I_n - A(I_n+BA)^{-1}B.$$

For a general matrix $A \in \mathbb{R}^{m\times n}$, which is not necessarily square, the pseudo inverse $A^\dagger$ of a matrix A is defined as a matrix that satisfies

$$\begin{aligned} AA^\dagger A &= A, \\ A^\dagger AA^\dagger &= A, \\ AA^\dagger &\quad \text{is symmetric}, \\ A^\dagger A &\quad \text{is symmetric}. \end{aligned}$$

If A is full-rank, then

$$A^\dagger = \begin{cases} A^{-1}, & \text{if } m = n \\ (A^\intercal A)^{-1}A^\intercal & \text{if } m > n \\ A^\intercal(AA^\intercal)^{-1} & \text{if } m < n. \end{cases}$$

A vector $\boldsymbol{a} \in \mathbb{R}^m$ is a special case of a matrix where only a single column is present. The scalar product of two vectors $\boldsymbol{a}$ and $\boldsymbol{b}$ is defined as $c = \boldsymbol{a}^\intercal\boldsymbol{b}$. Two vectors $\boldsymbol{a}$ and $\boldsymbol{b}$ are orthogonal if $\boldsymbol{a}^\intercal\boldsymbol{b} = 0$. The 2-norm of a vector is defined as $\|\boldsymbol{a}\| = \sqrt{\boldsymbol{a}^\intercal\boldsymbol{a}}$. The cross product of two vectors $\boldsymbol{a}$ and $\boldsymbol{b}$ in the Euclidean space is given by

$$\boldsymbol{a} \times \boldsymbol{b} = S(\boldsymbol{a})\boldsymbol{b} = \begin{bmatrix} a_2b_3 - a_3b_2 \\ a_3b_1 - a_1b_3 \\ a_1b_2 - a_2b_1 \end{bmatrix},$$

where the matrix operator $S(\boldsymbol{a})$ is expressed as a skew-symmetric matrix given by

$$S(\boldsymbol{a}) = \begin{bmatrix} 0 & -a_3 & a_2 \\ a_3 & 0 & -a_1 \\ -a_2 & a_1 & 0 \end{bmatrix}.$$

The following properties hold:

$$\begin{aligned} \boldsymbol{a} \times \boldsymbol{b} &= S(\boldsymbol{a})\boldsymbol{b} = -S(\boldsymbol{b})\boldsymbol{a}, \\ S(\boldsymbol{a})\boldsymbol{a} &= S(\boldsymbol{a})^\intercal \boldsymbol{a} = \boldsymbol{0}, \\ S(\boldsymbol{a})S(\boldsymbol{b}) &= \boldsymbol{a}\boldsymbol{b}^\intercal - \boldsymbol{a}^\intercal \boldsymbol{b} I_3. \end{aligned}$$

Linear Transformations

The linear transformation between the vector $\boldsymbol{x} \in \mathscr{X}$, where $\mathscr{X}$ is a vector space of dimension m, and $\boldsymbol{y} \in \mathscr{Y}$, where $\mathscr{Y}$ is a vector space of dimension n, is given by

$$\boldsymbol{y} = A\boldsymbol{x},$$

where $A \in \mathbb{R}^{m \times n}$. The range of the transformation is defined as the subspace

$$\text{range}(A) = \{\, \boldsymbol{y} : \boldsymbol{y} = A\boldsymbol{x}, \boldsymbol{x} \in \mathscr{X} \} \subseteq \mathscr{Y},$$

which is spanned by the linearly independent columns of the matrix A. Hence, we have $\dim(\text{range}(A)) = \text{rank}(A)$. Moreover, the null space of the linear transformation is the subspace defined as

$$\ker(A) = \{\boldsymbol{x} : A\boldsymbol{x} = \boldsymbol{0}, \boldsymbol{x} \in \mathscr{X}\} \subseteq \mathscr{X}.$$

Assume that we have a matrix $A \in \mathbb{R}^{m \times n}$ then $\dim(\text{range}(A)) + \dim(\ker(A)) = n$ always holds. Both range and null space are subspaces which are orthogonal to each other from which can conclude the following:

$$\ker(A) = \text{range}(A^\intercal)^\perp \quad \text{and} \quad \text{range}(A) = \ker(A^\intercal)^\perp,$$

where $(\cdot)^\perp$ denotes the orthogonal complement. The *invariant subspace* of a linear mapping $T : \mathscr{X} \to \mathscr{X}$ from some vector space $\mathscr{X}$ to itself is a subspace $\mathscr{Y}$ of $\mathscr{X}$ that is preserved by T, i.e. $T(\mathscr{W}) \subseteq \mathscr{W}$.

Eigenvalues and Eigenvectors

The eigenvalues λ_i and eigenvectors $\boldsymbol{v}_i$ of a matrix $A \in \mathbb{R}^{n \times n}$ satisfy

$$A\boldsymbol{v}_i = \lambda_i \boldsymbol{v}_i.$$

If the matrix A is symmetric, then all eigenvalues are real. The matrix V formed by the vectors $\boldsymbol{v}_i$ is full rank and forms a basis of the n-dimensional subspace. Moreover, the transformation matrix V indicates a similar transformation as $D = V^{-1}AV$ where D is a diagonal matrix so that $D = \text{diag}(\lambda_1, \ldots, \lambda_N)$.

The characteristic polynomial of the matrix A is defined as $\det(A - \lambda I_n) = 0$ where

$$p(\lambda) = \det(A - \lambda I_n),$$

is commonly denoted as the characteristic equation. The Cayley-Hamilton theorem says that every matrix satisfies its own characteristic equation, i.e. $p(A) = 0$.

The following theorem taken from [121, p. 9.5.1] relates the eigenvalues of a symmetric matrix to its principal matrix. It is a generalized version of the Cauchy interlacing theorem.

Theorem A.1 ([121]). *Let A be a real symmetric $n \times n$ matrix and let R be an $n \times m$ matrix such that $R^\intercal R = I_m$. Set B equal to $R^\intercal AR$ and let $\boldsymbol{v}_1, \ldots, \boldsymbol{v}_m$ be an orthogonal set of eigenvectors of B such that $B\boldsymbol{v}_i = \theta_i(B)\boldsymbol{v}_i$. Then:*

(a) The eigenvalues of B interlace the eigenvalues of A.

(b) If $\theta_i(B) = \theta_i(A)$, then there is an eigenvector $\mathbf{y}$ of B with eigenvalue $\theta_i(B)$ such that $R\mathbf{y}$ is an eigenvector of A with eigenvalue $\theta_i(A)$.

(c) If $\theta_i(B) = \theta_i(A)$ for $i = 1, \ldots, l$, then $R\boldsymbol{v}_i$ is an eigenvector for A with eigenvalues $\theta_i(A)$ for $i = 1, \ldots, l$.

(d) If the interlacing is tight, then $AR = RB$.

Eigenvalues and eigenvectors are not defined for non-square matrix $A \in \mathbb{R}^{n \times m}$ where $n \neq m$. However, a similar and more general principle for non-square matrices is found in singular value decomposition (SVD) and it is defined as

$$A = UDV^\intercal,$$

where $U \in \mathbb{R}^{n \times n}$ are the eigenvectors of $AA^\intercal$ and $V \in \mathbb{R}^{m \times m}$ are the eigenvectors of $A^\intercal A$. Furthermore, D results as $D = \sqrt{\text{diag}(\text{eig}(AA^\intercal))}$ and the elements of D are called singular values.

Factorizations

QR factorization states that a matrix $A \in \mathbb{R}^{m \times n}$ can be factored into the product of an upper triangular matrix $R \in \mathbb{R}^{m \times n}$ and an orthogonal matrix $Q \in \mathbb{R}^{m \times m}$:

$$A = QR.$$

QR factorization is widely used in solving least square problems and there exist several methods to compute the factorization which are mostly based on Householder or Givens transformations.

The intersection of subspaces is a recurring problem in linear algebra. Let $A \in \mathbb{R}^{m \times n}$ and $B \in \mathbb{R}^{p \times n}$ be given, and consider the problem of determining an orthonormal basis $\text{range}(A) \cap \text{range}(B)$ which is solved by following algorithm found in [156].

Algorithm 3.
1. Compute the QR factorization $A = Q_A R_A$ and $B = Q_B R_B$.
2. $C = Q_A^\intercal Q_B$.
3. Compute the SVD: $Y^\intercal C Z = \text{diag}(\cos(\theta_k))$.
4. $Q_A Y(:, 1:q) = \left[f_1 | \ldots | f_q\right]$.
5. $Q_B Z(:, 1:q) = \left[g_1 | \ldots | g_q\right]$.

6. Find the index s such that $1 = \cos(\theta_1) = \ldots = \cos(\theta_s) > \cos(\theta_{s+1})$.
7. Then $\text{range}(A) \cap \text{range}(B) = \text{span}\{f_1, \ldots, f_s\} = \text{span}\{g_1, \ldots, g_s\}$.

B

Graph Theory

We assume the interaction of a team of robots or agents with each other through a sensing or communication network or by a composition of both. It is convenient to characterize the interaction model among the robots or agents by directed and undirected graphs. Suppose that the team is composed of N robots or agents. A *directed graph* $\mathcal{G} = (\mathcal{V}, \mathcal{E})$ of order N is defined as a pair $(\mathcal{V}, \mathcal{E})$ where $\mathcal{V} = \{ v_1, v_2, \dots v_N\}$ is a finite and nonempty vertex set and $\mathcal{E} \subseteq \mathcal{V} \times \mathcal{V}$ is the edge set of ordered pair of nodes. Self-edges or loops (v_i, v_i) are not allowed. If in a directed graph there is an edge (v_i, v_j) then the agent j receives information from agent i but not necessarily conversely. In contrast the pairs of vertices in an undirected graph are unordered i.e. the edge (v_i, v_j) denotes that agents i and j can receive information from each other. Note here that an undirected graph can be regarded as a special case of a directed graph where each edge (v_i, v_j) of the undirected one resembles two edges (v_i, v_j) and (v_j, v_i) of the directed one. If there is a (directed) path between every pair of distinct vertices then the $\mathcal{G}$ is called (strongly) connected. A *weighted* graph assigns a weight to every edge in the graph. The adjacency matrix A of a directed graph encodes the neighborhood relationship according to

$$[A]_{i,j} = \begin{cases} a_{ij} & \text{if } (i,j) \in \mathcal{E} \\ 0 & \text{if } (i,j) \notin \mathcal{E}, \end{cases}$$

where $a_{ij} \in \mathbb{R}^+$ is a positive weight and a_{ij} denotes the weights of the edge $(v_j, v_i) \in \mathcal{E}$. If weights are irrelevant then we set a_{ij} equal to 1 if $(v_j, v_i) \in \mathcal{E}$. For an undirected graph the adjacency matrix A is defined similarly and we always have $a_{ij} = a_{ji}$. Hence, A is symmetric for undirected graphs. We define the in-degree and out-degree of node v_i as $\sum_{j=1}^{N} a_{ij}$ and $\sum_{j=1}^{N} a_{ji}$. For an undirected graph both in-degree and out-degree are equal and are generally denoted as degree. Let the degree matrix D of an undirected graph be a diagonal matrix where the ith entry on the

diagonal is given by its degree:

$$[D]_{i,i} = \sum_{j=1}^{N} a_{ij}.$$

Finally, we defined the matrix L [121] given by

$$L = D - A.$$

To associate the matrices L, D, A with a graph $\mathcal{G}$ we can also write $L(\mathcal{G}), D(\mathcal{G}), A(\mathcal{G})$. For an undirected graph, we have $L = L^{\intercal}$, L is positive definite and L is called the Laplacian matrix. For a directed graph L is called *directed* Laplacian matrix. Note that the rows of L always sum up to zero, i.e. we have $L\mathbf{1} = 0$. Hence, 0 is always an eigenvalue of L with corresponding eigenvector $\mathbf{1}$. For an undirected graph, $\lambda_i(L)$ is the ith eigenvalue of L and the eigenvalues can be ordered as

$$0 = \lambda_1(L) \leq \lambda_2(L) \leq \ldots \leq \lambda_N(L),$$

where $\lambda_1(L) = 0$. In general $\lambda_2(L)$ is called algebraic connectivity. Note that $\mathcal{G}$ is connected if and only if $\lambda_2(L) > 0$. The algebraic connectivity $\lambda_2(L)$ is considered to be a measure for the convergence rate of the consensus algorithm.

Graph theory has a strong relationship to abstract algebra, especially when we consider the symmetry structures in a graph and their associated equitable partitions. An automorphism of a graph $\mathcal{G} = (\mathcal{V}, \mathcal{E})$ is defined as a permutation ψ of $\mathcal{V}$ such that

$$(\psi(v_i), \psi(v_j)) \in \mathcal{E} \Leftrightarrow (v_i, v_j) \in \mathcal{E}.$$

All possible automorphisms ψ of $\mathcal{G}$ is denoted as the automorphism group of $\mathcal{G}$. A permutation matrix Ψ can be defined for each automorphism as

$$[\Psi]_{i,j} = \begin{cases} 1 & \text{if } \psi(v_i) \in j \\ 0 & \text{otherwise,} \end{cases}.$$

Then ψ is an automorphism of $\mathcal{G}$ if and only if

$$\Psi A(\mathcal{G}) = A(\mathcal{G})\Psi.$$

We define a cell C to be a subset of the verstex set $\mathcal{V}$. A partition π of a graph is an apportioning of the vertex set $\mathcal{V}$ into different cells C as $\pi = \{C_1, \ldots C_p\}$. The cardinality of π is denoted by p. A p-partition $\pi = \{C_1, \ldots C_p\}$ of $\mathcal{V}$ is called *equitable* if for all i, j every vertex in C_j has the equal number of neighbors in C_i. The N-partition $\pi^* = \{\{v_1\}, \{v_2\}, \ldots, \{v_N\}\}$ is the *trivial* equitable partition. Generally, equitable partitions can be acquired from the automorphism groups of a graph. The characteristic vector $\boldsymbol{p}_i \in \mathbb{R}^n$ of the cell C_i of a partition π features 1s in the entries corresponding to C_i and 0s otherwise. The characteristic matrix $P \in \mathbb{R}^{n \times r}$ is a matrix with the vectors p_i forming its columns. It is known that π is equitable if and only if P is $A(\mathcal{G})$-invariant, i.e.$A(\mathcal{G})\mathcal{R}(P) \subseteq \mathcal{R}(P)$.

C

Experimental Setups

Six DoF Mobile Manipulator 1

The human-sized robotic platform shown in Fig. C.1 consists of a four-wheeled omni-directional mobile platform used for repositioning the robot and two identical commercially available KUKA LWR (light-weight robot) 4+ manipulators. Desired angular movements for desired movements in task space are computed by an instantaneous inverse kinematics. For measuring resultant forces independent of the configuration during the cooperative manipulation task, a 6 DoF force/torque sensor (*JR3*) is attached to each wrist. As end-effectors, Schunk PG70 two-finger parallel grippers are used for simple grasping and object pushing with the fingers. Lithium-ion polymer batteries power the system for long periods without recharging and for expanding the reachable workspace.

For computational power, the robot carries two KUKA control boxes, one for each manipulator and a single PC. The PC consists of an *Intel Core i7 920* running at 2.66 GHz executing control schemes, implemented in *MATLAB/Simulink* and executed on the *PREEMPT-RT* using *Matlab's Real-Time Workshop*. It also ensures real-time control of the mobile platform and a synchronized data management utilizing the *KogmoRTDB* real-time database [187]. In order to operate the KUKA LWRs we use *Fast Research Interface* (FRI), which allows user control and status monitoring of the manipulators based on UDP protocol. This software package is integrated in the real-time robot control framework [188]. All low-level control algorithms runs at a frequency of 1 kHz. The robot is equipped with a wireless router in the 5GHz band for inter-robot communication where a UDP protocol is then employed to transmit data between the robots.

Six DoF Mobile Manipulator 2

The human-sized robot as depicted in Fig. C.2 consists of a four-wheeled omni-directional mobile platform (f) which offers workspace extension and a roughly human-like maneuverability and

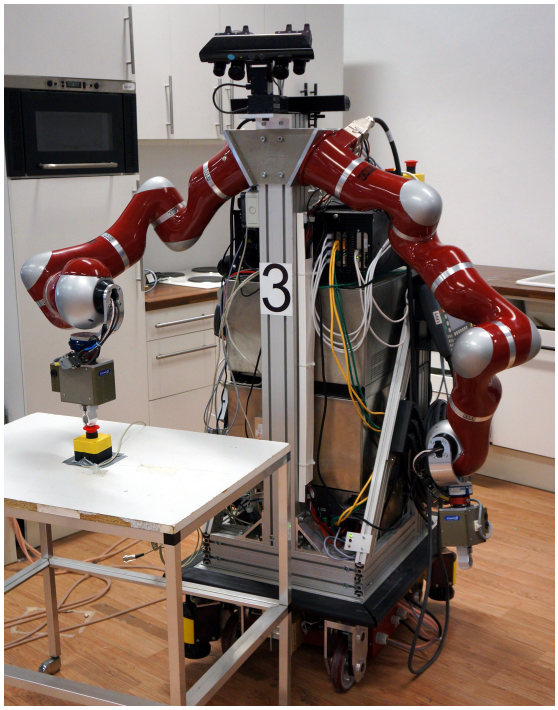

Figure C.1: The robotic platform consisting of two KUKA LWR 4+ manipulators equipped with two-finger grippers and an omni-directional mobile platform.

smooth motion [189]. Two identical anthropomorphic 7-degrees-of-freedom (DoF) arms (c) running with incremental encoders to capture the joint angles are front-mounted on the top of the a rigid torso to provide a human-like working space [77]. Mounted onto a JR3 wrench sensor, the manipulator is equipped with a Schunk PG70 two-finger parallel gripper (a) which enables a tight grasp of the object and allows force/torque sensing in order to enable force feedback control. Lithium-ion polymer batteries(e) mounted at the omni-directional platform power the system and increase its autonomy. More detailed information on the robot used can be found in [190].

The robotic system carries three PCs (d) for computational power. The first is an *Intel Core i7 920* running at 2.66 GHz executing high-level reasoning tasks exploiting the multi-thread *OpenMP* library. The entire manipulator control scheme is implemented in *MATLAB/Simulink* and executed on the *PREEMT-RT* using *Matlab's Real-Time Workshop* on a second PC. An appropriate interface is embedded to a high-level software control framework [191]. The individual low-level control loops run at a frequency of 1 kHz. The third PC is identical to the first and ensures real-time control of the mobile platform and a synchronized data management utilizing the *KogmoRTDB* real-time database [187] available at [192] and the *PREEMPT_RT Linux* real-time kernel patch [193]. For inter-robot data exchange a wireless router in the 5GHz band is attached to the robot. Data packets are transmitted between the robots over an UDP protocol

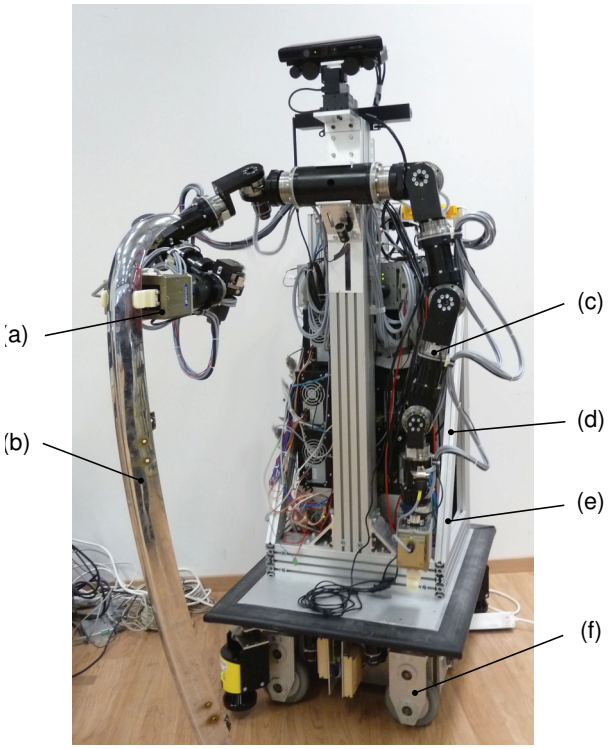

Figure C.2: The human-sized mobile robot is equipped with anthropomorphic manipulators each featuring two-finger grippers and with an omni-directional mobile platform.

Motion Capture System

Active-Marker Based Tracking

For the experiment described in Section 2.5, camera bars of the system *VisualEyez II VZ4000 (PTI PhoeniX Technologies)* are used. The camera bars are mounted overhead at a height of approximately 3m above the work space to be tracked, with the cameras facing downwards normally and centered around the workspace. The object which needs to be tracked is equipped with active markers, which are infrared LEDs of high-power and wide-angle type. For capturing the motion the flash of the active markers is triggered by a wireless target control module in order to uniquely identify the three-dimensional position of the manipulated object. A proprietary software package *VZSoft* for interfacing the motion capture system and gathering motion data runs on a *Microsoft Windows*-based personal computer. The real-time interface of the system provides data at a frequency of 30Hz for on-line processing through a network connection. In addition, the motion data are simultaneously stored at a frequency of 200Hz for off-line analysis.

Passive-Marker Based Tracking

For most experiments a motion capture system is utilized which consists of 21 networked cameras, one *Oqus 3+* and 20 *Oqus 4* (*Qualisys*). The cameras are mounted at ceiling height approximately 3m over the work space which needs to be tracked. All cameras are distributed on a square-shaped frame of approximately 20m x 10m centered around the working space and aligned in order to maximize both the overlapping of the fields of view of each camera and the volume available

Figure C.3: Qualisys Motion Tracker camera.

Figure C.4: Glove equipped with tracking markers.

for tracking. The tracking system is calibrated prior to each experiment by a manual calibration routine yielding an approximate accuracy of < 3mm. Ball-shaped reflective markers are attached to each robot and the object. In order to form a unique geometrical shape at least four markers are rigidly attached for a unique object identification. The motion capture system can be interfaced via the software suite *Qualisys Track Manager (QTM)* which runs on a *Microsoft Windows*-based personal computer. QTM provides capture data in six-dimensional object coordinates at a frequency of 300Hz through the real-time interface for on-line processing. All data, which is low-passed filtered using a 25-point moving average FIR filter at a sampling rate of 1 kHz, are made available to the robot at low latency through a network connection. A camera is depicted in Fig C.3 and a marker-equipped glove is depicted in Fig C.4.

Wearable Haptic Device

The vibrotactile wristband was developed at PERCRO lab to effectively deliver haptic stimuli at the operator's wrist and to provide the operator with vibrotactile cues. The vibrotactile wristband consists of a band of stretchy fabric in order to ensure user comfort as depicted in Fig. C.5. It is equipped with four vibratory pads which which are located at the center of the dorsal (top), ventral (bottom/palm), inner and outer lateral sides of the wrist. The minimum distance between any two vibratory pads is about 4 cm for ensuring a reliable subjects' spatial detection [194]. The motors in the vibratory pads are actuated at a maximum frequency of 180Hz, which is less than the maximum stimulation of skin mechanoreceptors of the human hands (250 Hz) [195].

The architecture of the on-board electronics is composed of a custom-designed circuit board with a micro controller *PIC18LF2431* from the Microchip PIC®family, a 2.4 GHz Bluetooth Class 1 module for wireless communication, a lithium-polymer battery, and a USB Battery Charger. While the rotation frequency of the motor vibrations was kept at a constant value, the activation frequency (or pulsing period), the duty cycle, and the duration of the vibratory signal can be used to generate desired wave patterns.

Figure C.5: The vibrotactile wristband consisting of a band of stretchy fabric in order to ensure user comfort.

Bibliography

[9] S Fujii and S Kurono. “Coordinated computer control of a pair of manipulators.” In: *Industrial Robot* (1975), pp. 155–161.

[10] Eiji Nakano, Shotaro Ozaki, Tatsuzo Ishida, and Ichiro Kato. “Cooperational control of the anthropomorphous manipulator MELARM.” In: *Proc. 4th Int. Symp. Industrial Robots*. 1974, pp. 251–260.

[11] Antti J Koivo and George A Bekey. “Report of workshop on coordinated multiple robot manipulators-planning, control, and applications.” In: *IEEE journal of robotics and automation* 4.1 (1988), pp. 91–93.

[12] P Dauchez and R Zapata. “Co-ordinated control of two cooperative manipulators: the use of a kinematic model.” In: *Proc. 15th Int. Symp. Ind. Robots (Tokyo 1985) pp*. 1985, pp. 641–648.

[13] N Harris McClamroch. “Singular systems of differential equations as dynamic models for constrained robot systems.” In: *Robotics and Automation. Proceedings. 1986 IEEE International Conference on*. Vol. 3. IEEE. 1986, pp. 21–28.

[14] TJ Tarn, AK Bejczy, and X Yun. “New nonlinear control algorithms for multiple robot arms.” In: *Aerospace and Electronic Systems, IEEE Transactions on* 24.5 (1988), pp. 571–583.

[15] Masaru Uchiyama and Pierre Dauchez. “A symmetric hybrid position/force control scheme for the coordination of two robots.” In: *Robotics and Automation, 1988. Proceedings., 1988 IEEE International Conference on*. IEEE. 1988, pp. 350–356.

[16] Masaru Uchiyama and Pierre Dauchez. “Symmetric kinematic formulation and non-master/slave coordinated control of two-arm robots.” In: *Advanced Robotics* 7.4 (1992), pp. 361–383.

[17] Ian D Walker, Robert A Freeman, and Steven I Marcus. “Analysis of motion and internal loading of objects grasped by multiple cooperating manipulators.” In: *The International journal of robotics research* 10.4 (1991), pp. 396–409.

[18] Robert G Bonitz and Tien C Hsia. “Force decomposition in cooperating manipulators using the theory of metric spaces and generalized inverses.” In: *Robotics and Automation, 1994. Proceedings., 1994 IEEE International Conference on*. IEEE. 1994, pp. 1521–1527.

[19] Martin Buss, Bdeki Hashimoto, and John B Moore. “Dextrous hand grasping force optimization.” In: *Robotics and Automation, IEEE Transactions on* 12.3 (1996), pp. 406–418.

[20] David Williams and Oussama Khatib. “The virtual linkage: A model for internal forces in multi-grasp manipulation.” In: *IEEE Int. Conf. on Robotics and Automation*. IEEE. 1993, pp. 1025–1030.

[21] John T Wen and Kenneth Kreutz-Delgado. “Motion and force control of multiple robotic manipulators.” In: *Automatica* 28.4 (1992), pp. 729–743.

[22] Yan-Ru Hu, Andrew A Goldenberg, and Chin Zhou. “Motion and force control of coordinated robots during constrained motion tasks.” In: *The International journal of robotics research* 14.4 (1995), pp. 351–365.

[23] Yun-Hui Liu and Suguru Arimoto. “Decentralized adaptive and nonadaptive position/force controllers for redundant manipulators in cooperations.” In: *The International Journal of Robotics Research* 17.3 (1998), pp. 232–247.

[24] Greg R Luecke and Kien Wee Lai. “A joint error-feedback approach to internal force regulation in cooperating manipulator systems.” In: *Journal of Robotic Systems* 14.9 (1997), pp. 631–648.

[25] Fabrizio Caccavale, Pasquale Chiacchio, and Stefano Chiaverini. “Stability analysis of a joint space control law for a two-manipulator system.” In: *Automatic Control, IEEE Transactions on* 44.1 (1999), pp. 85–88.

[26] T. Flash and N. Hogan. “The coordination of arm movements: An experimentally confirmed mathematical model.” In: *J. Neurosci.* 5 (1985), pp. 1688–1703.

[27] H Bruhm, J Deisenroth, and P Schädler. “On the design and simulation-based validation of an active compliance law for multi-arm robots.” In: *Robotics and Autonomous Systems* 5.4 (1989), pp. 307–321.

[28] S. Schneider and R. Cannon. “Object Impedance Control for Cooperative Manipulation: Theory and Experimental Results.” In: *IEEE Trans. Robot. Automat.* 8.3 (1992), pp. 383–394.

[29] Jérôme Szewczyk, Guillaume Morel, and Philippe Bidaud. “Distributed impedance control of multiple robot systems.” In: *Robotics and Automation, 1997. Proceedings., 1997 IEEE International Conference on*. Vol. 2. IEEE. 1997, pp. 1801–1806.

[30] S. Erhart and S. Hirche. “Model and analysis of the interaction dynamics in cooperative manipulation tasks.” In: *Manuscript submitted for publication* (2015).

[31] Oussama Khatib, K Yokoi, K Chang, D Ruspini, R Holmberg, A Casal, A Baader, et al. “Force strategies for cooperative tasks in multiple mobile manipulation systems.” In: *International Symposium on Robotics Research*. Vol. 7. 1996, pp. 333–342.

[32] T. Sugar and Vijay Kumar. “Multiple cooperating mobile manipulators.” In: *Robotics and Automation, 1999. Proceedings. 1999 IEEE International Conference on*. Vol. 2. May. IEEE, 1999, pp. 1538–1543. url: `http://ieeexplore.ieee.org/xpls/abs%5C_all.jsp?arnumber=772578`.

[33] Herbert G Tanner, Ali Jadbabaie, and George J Pappas. “Stable flocking of mobile agents, Part I: Fixed topology.” In: *Decision and Control, 42nd IEEE Conference on*. 2003.

[34] Herbert G Tanner, Kostas J Kyriakopoulos, and NJ Krikelis. “Modeling of multiple mobile manipulators handling a common deformable object.” In: *Journal of Robotic Systems* 15.11 (1998), pp. 599–623.

[35] Kazuhiro Kosuge, Tomohiro Oosumi, Manabu Satou, Kunihiko Chiba, and Koji Takeo. “Transportation of a single object by two decentralized-controlled nonholonomic mobile robots.” In: *Robotics and Automation, 1998 IEEE International Conference on*. 1998.

[36] Bruce Randall Donald, James Jennings, and Daniela Rus. “Information invariants for distributed manipulation.” In: *The International Journal of Robotics Research* 16.5 (1997), pp. 673–702.

[37] J Spletzer, Aveek K Das, Rafael Fierro, Camillo J Taylor, Vijay Kumar, and James P Ostrowski. “Cooperative localization and control for multi-robot manipulation.” In: *Intelligent Robots and Systems, 2001. Proceedings. 2001 IEEE/RSJ International Conference on*. Vol. 2. IEEE. 2001, pp. 631–636.

[38] C Ronald Kube and Hong Zhang. “Task modelling in collective robotics.” In: *Robot colonies*. Springer, 1997, pp. 53–72.

[39] Chin Pei Tang. “Design and Control Framework for Cooperative Mobile Robot Collectives.” PhD thesis. Citeseer, 2009.

[40] Herbert G Tanner, Savvas G Loizou, and Kostas J Kyriakopoulos. “Nonholonomic navigation and control of cooperating mobile manipulators.” In: *Robotics and Automation, IEEE Transactions on* 19.1 (2003), pp. 53–64.

[41] Christoph Borst, Christian Ott, Thomas Wimböck, Bernhard Brunner, Franziska Zacharias, Berthold Bäuml, Ulrich Hillenbrand, Sami Haddadin, Alin Albu-Schaeffer, and Gerd Hirzinger. “A humanoid upper body system for two-handed manipulation.” In: *Robotics and Automation, 2007 IEEE International Conference on*. IEEE. 2007, pp. 2766–2767.

[42] Thomas Wimböck, Christian Ott, Alin Albu-Schäffer, and Gerd Hirzinger. “Comparison of object-level grasp controllers for dynamic dexterous manipulation.” In: *The International Journal of Robotics Research* 31.1 (2012), pp. 3–23.

[43] Chien-Chern Cheah, Chao Liu, and JJJE Slotine. “Adaptive Jacobian tracking control of robots with uncertainties in kinematic, dynamic and actuator models.” In: *Automatic Control, IEEE Transactions on* 51.6 (2006), pp. 1024–1029.

[44] Kazuhiro Kosuge, Hiromu Kakuya, and Yasuhisa Hirata. “Control algorithm of dual arms mobile robot for cooperative works with human.” In: *Systems, Man, and Cybernetics, 2001 IEEE International Conference on*. Vol. 5. IEEE. 2001, pp. 3223–3228.

[45] Farhad Aghili. “Self-tuning cooperative control of manipulators with position/orientation uncertainties in the closed-kinematic loop.” In: *Intelligent Robots and Systems (IROS), 2011 IEEE/RSJ International Conference on*. IEEE. 2011, pp. 4187–4193.

[46] Long Jin and Yunong Zhang. “G2-type SRMPC scheme for synchronous manipulation of two redundant robot arms.” In: *Cybernetics, IEEE Transactions on* 45.2 (2015), pp. 153–164.

[47] Petter Ögren, Christian Smith, Yiannis Karayiannidis, and Danica Kragic. “A Multi Objective Control Approach to Online Dual Arm Manipulation.” In: *SyRoCo*. 2012, pp. 747–752.

[48] Antonio Petitti, Antonio Franchi, Donato Di Paola, and Alessandro Rizzo. “Decentralized Motion Control for Cooperative Manipulation with a Team of Networked Mobile Manipulators.” In: *2016 IEEE International Conference on Robotics & Automation*. 2016.

[49] Antonio Franchi, Antonio Petitti, and Alessandro Rizzo. “Distributed estimation of the inertial parameters of an unknown load via multi-robot manipulation.” In: *Proceedings of the IEEE 53nd Annual Conference on Decision and Control (CDC)*. 2014.

[50] Antonio Franchi, Antonio Petitti, and Alessandro Rizzo. “Decentralized parameter estimation and observation for cooperative mobile manipulation of an unknown load using noisy measurements.” In: *Robotics and Automation (ICRA), 2015 IEEE International Conference on*. IEEE. 2015, pp. 5517–5522.

[51] Paul S Schenker, Terry L Huntsberger, Paolo Pirjanian, Eric T Baumgartner, and Eddie Tunstel. “Planetary rover developments supporting mars exploration, sample return and future human-robotic colonization.” In: *Autonomous Robots* 14.2-3 (2003), pp. 103–126.

[52] Javier Alonso-Mora, Ross Knepper, Roland Siegwart, and Daniela Rus. “Local motion planning for collaborative multi-robot manipulation of deformable objects.” In: *Robotics and Automation (ICRA), 2015 IEEE International Conference on*. IEEE. 2015, pp. 5495–5502.

[53] Y. Hirata, Y. Kume, Zhi-Dong Wang, and K. Kosuge. “Decentralized Control of Multiple Mobile Manipulators based on Virtual 3-D Caster Motion for Handling an Object in Cooperation with a Human.” In: *Proc. IEEE ICRA*. Vol. 1. 2003, 938–943 vol.1.

[54] Oussama Khatib, Kazu Yokoi, K Chang, Diego Ruspini, Robert Holmberg, and Arancha Casal. “Vehicle/arm coordination and multiple mobile manipulator decentralized

cooperation." In: *Intelligent Robots and Systems, IEEE/RSJ International Conference on*. 1996.

[55] Bruce Donald, Larry Gariepy, and Daniela Rus. "Distributed manipulation of multiple objects using ropes." In: *Robotics and Automation, 2000. Proceedings. ICRA'00. IEEE International Conference on*. Vol. 1. IEEE. 2000, pp. 450–457.

[56] Dongjun Lee and Mark W Spong. "Bilateral teleoperation of multiple cooperative robots over delayed communication networks: theory." In: *Robotics and Automation, 2005. ICRA 2005. Proceedings of the 2005 IEEE International Conference on*. IEEE. 2005, pp. 360–365.

[57] Dongjun Lee, Oscar Martinez-Palafox, and Mark W Spong. "Bilateral teleoperation of multiple cooperative robots over delayed communication networks: Application." In: *Robotics and Automation, 2005. ICRA 2005. Proceedings of the 2005 IEEE International Conference on*. IEEE. 2005, pp. 366–371.

[58] Glenn D White, Rajankumar M Bhatt, Chin Pei Tang, and Venkat N Krovi. "Experimental evaluation of dynamic redundancy resolution in a nonholonomic wheeled mobile manipulator." In: *Mechatronics, IEEE/ASME Transactions on* 14.3 (2009), pp. 349–357.

[59] Rajankumar M Bhatt, Chin Pei Tang, and Venkat N Krovi. "Formation optimization for a fleet of wheeled mobile robots—A geometric approach." In: *Robotics and Autonomous Systems* 57.1 (2009), pp. 102–120.

[60] Milan D Djurovic and Miomir K Vukobratovic. "A contribution to dynamic modeling of cooperative manipulation." In: *Mechanism and Machine Theory* 25.4 (1990), pp. 407–415.

[61] Xiaoping Yun and Vijay R Kumar. "An approach to simultaneous control of trajectory and interaction forces in dual-arm configurations." In: *Robotics and Automation, IEEE Transactions on* 7.5 (1991), pp. 618–625.

[62] Jorge Gudiño-Lau and Marco A Arteaga. "Dynamic model and simulation of cooperative robots: a case study." In: *Robotica* 23.05 (2005), pp. 615–624.

[63] AJ Koivo and MA Unseren. "Reduced order model and decoupled control architecture for two manipulators holding a rigid object." In: *Journal of dynamic systems, measurement, and control* 113.4 (1991), pp. 646–654.

[64] Bruno Siciliano, Lorenzo Sciavicco, Luigi Villani, and Giuseppe Oriolo. *Robotics: modelling, planning and control*. Springer Science & Business Media, 2010.

[65] Roy Featherstone and D Orin. "Chapter 2: Dynamics." In: *Springer handbook of robotics. New York: Springer* (2008).

[66] Mark W Spong, Seth Hutchinson, and M Vidyasagar. *Robot modeling and control. 2006*.

[67] Fabrizio Caccavale, Pasquale Chiacchio, Alessandro Marino, and Luigi Villani. "Six-DOF impedance control of dual-arm cooperative manipulators." In: *Mechatronics, IEEE/ASME Transactions on* 13.5 (2008), pp. 576–586.

[68] Neville Hogan. “Impedance control: An approach to manipulation: Part II—Implementation.” In: *Journal of dynamic systems, measurement, and control* 107.1 (1985), pp. 8–16.

[69] Hassan K Khalil and JW Grizzle. *Nonlinear systems*. Vol. 3. Prentice hall New Jersey, 1996.

[70] Oussama Khatib. “Mobile manipulation: The robotic assistant.” In: *Robotics and Autonomous Systems* 26.2 (1999), pp. 175–183.

[71] Jindong Tan, Ning Xi, and Yuechao Wang. “Integrated task planning and control for mobile manipulators.” In: *The International Journal of Robotics Research* 22.5 (2003), pp. 337–354.

[72] Alexander Imanuel Mörtl et al. “Design of Interactive Motor Behaviors for Close Joint Action of Humans and Robots.” PhD thesis. München, Technische Universität München, Diss., 2014, 2014.

[73] Fabrizio Caccavale and Masaru Uchiyama. “Cooperative manipulators.” In: *Springer Handbook of Robotics*. Springer, 2008, pp. 701–718.

[74] Kazuhiro Kosuge, Kentaro Kamei, and Takashi Nammoto. “Coordinated motion control of dual manipulators for handling a rigid object with non-negligible deformation.” In: *Robotics and Automation (ICRA), 2014 IEEE International Conference on*. IEEE. 2014, pp. 5145–5151.

[75] S. Erhart and S. Hirche. “Load distribution in cooperative manipulation tasks.” In: *Manuscript submitted for publication*. 2014.

[76] Firdaus E Udwadia and Robert E Kalaba. “A new perspective on constrained motion.” In: *Proceedings: Mathematical and Physical Sciences* (1992), pp. 407–410.

[77] B. Stanczyk and M. Buss. “Development of a Telerobotic System for Exploration of Hazardous Environments.” In: *Proc. IEEE/RSJ IROS*. 2004, pp. 2532–2537.

[78] Rainer Bischoff and Johannes Kurth. “The kuka-dlr lightweight robot arm-a new reference platform for robotics research and manufacturing.” In: *Robotics (ISR)* (2010).

[79] Julie A Adams, Ruzena Bajcsy, Jana Kosecka, Vijay Kumar, Robert Mandelbaum, Max Mintz, R Paul, Curtis Wang, Yoshio Yamamoto, and Xiaoping Yun. “Cooperative material handling by human and robotic agents: Module development and system synthesis.” In: *Intelligent Robots and Systems 95.’Human Robot Interaction and Cooperative Robots’, Proceedings. 1995 IEEE/RSJ International Conference on*. Vol. 1. IEEE. 1995, pp. 200–205.

[80] Jerome Szewczyk, Frederic Plumet, and Philippe Bidaud. “Planning and controlling cooperating robots through distributed impedance.” In: *Journal of Robotic Systems* 19.6 (2002), pp. 283–297.

[81] Thomas G Sugar and Vijay Kumar. “Control of cooperating mobile manipulators.” In: *Robotics and Automation, IEEE Transactions on* (2002).

[82] Jaydev P Desai and Vijay Kumar. “Motion planning for cooperating mobile manipulators.” In: *Journal of Robotic Systems* (1999).

[83] Tucker Balch and Ronald C Arkin. “Behavior-based formation control for multirobot teams.” In: *Robotics and Automation, IEEE Transactions on* 14.6 (1998), pp. 926–939.

[84] Lynne E Parker. “ALLIANCE: An architecture for fault tolerant multirobot cooperation.” In: *Robotics and Automation, IEEE Transactions on* 14.2 (1998), pp. 220–240.

[85] Magnus Egerstedt and Xiaoming Hu. “Formation constrained multi-agent control.” In: *IEEE Trans. Robot. Autom* 17.6 (2001), pp. 947–951.

[86] Magnus Egerstedt, Simone Martini, Ming Cao, Kanat Camlibel, and Antonio Bicchi. “Interacting with networks: How does structure relate to controllability in single-leader, consensus networks?” In: *Control Systems, IEEE* (2012).

[87] Tolga Eren, Peter N Belhumeur, Brian DO Anderson, and A Stephen Morse. “A framework for maintaining formations based on rigidity.” In: *Proceedings of the 15th IFAC World Congress, Barcelona, Spain*. 2002, pp. 2752–2757.

[88] M Cao, AS Morse, C Yu, BDO Anderson, and S Dasgupta. “Maintaining a directed, triangular formation of mobile autonomous agents.” In: *Communications in Information and Systems* 11.1 (2011), p. 1.

[89] Kwang-Kyo Oh, Myoung-Chul Park, and Hyo-Sung Ahn. “A survey of multi-agent formation control.” In: *Automatica* (2014).

[90] Mehran Mesbahi and Magnus Egerstedt. *Graph theoretic methods in multiagent networks*. Princeton University Press, 2010.

[91] Wei Ren and Yongcan Cao. *Distributed coordination of multi-agent networks: emergent problems, models, and issues*. Springer Science & Business Media, 2010.

[92] Jaydev P Desai, James P Ostrowski, and Vijay Kumar. “Modeling and control of formations of nonholonomic mobile robots.” In: *Robotics and Automation, IEEE Transactions on* 17.6 (2001), pp. 905–908.

[93] M Anthony Lewis and Kar-Han Tan. “High precision formation control of mobile robots using virtual structures.” In: *Autonomous Robots* 4.4 (1997), pp. 387–403.

[94] Naomi Ehrich Leonard and Edward Fiorelli. “Virtual leaders, artificial potentials and coordinated control of groups.” In: *Decision and Control, 2001. Proceedings of the 40th IEEE Conference on*. Vol. 3. IEEE. 2001, pp. 2968–2973.

[95] Petter Ogren, Edward Fiorelli, and Naomi E Leonard. “Formations with a mission: Stable coordination of vehicle group maneuvers.” In: *Symposium on mathematical theory of networks and systems*. 2002, p. 15.

[96] Petter Ögren, Magnus Egerstedt, and Xiaoming Hu. "A control Lyapunov function approach to multi-agent coordination." In: *Decision and Control, 2001. Proceedings of the 40th IEEE Conference on*. Vol. 2. IEEE. 2001, pp. 1150–1155.

[97] Michael Steinegger, Benjamin Passenberg, Marion Leibold, and Martin Buss. "Trajectory planning for manipulators based on the optimal concatenation of LQ control primitives." In: *Decision and Control and European Control Conference (CDC-ECC), 2011 50th IEEE Conference on*. 2011.

[98] Martin Lawitzky, Melanie Kimmel, Peter Ritzer, and Sandra Hirche. "Trajectory Generation under the Least Action Principle for Physical Human-Robot Cooperation." In: *Proceedings of the IEEE International Conference on Robotics and Automation (ICRA)*. 2013.

[99] Auke Jan Ijspeert, Jun Nakanishi, and Stefan Schaal. "Learning rhythmic movements by demonstration using nonlinear oscillators." In: *IEEE International Conference on Intelligent Robots and Systems*. 2002.

[100] Stefan Schaal. "Dynamic movement primitives-a framework for motor control in humans and humanoid robotics." In: *2nd International Symposium on Adaptive Motion of Animals and Machines*. 2003.

[101] A. Gams, B. Nemec, L. Zlajpah, M. Wachter, A. Ijspeert, T. Asfour, and A. Ude. "Modulation of motor primitives using force feedback: Interaction with the environment and bimanual tasks." In: *Intelligent Robots and Systems, IEEE International Conference on*. 2013.

[102] Antonio Franchi, Cristian Secchi, Hyoung Il Son, Heinrich H Bulthoff, and Paolo Robuffo Giordano. "Bilateral teleoperation of groups of mobile robots with time-varying topology." In: *Robotics, IEEE Transactions on* 28.5 (2012), pp. 1019–1033.

[103] Thomas Schmickl, Ronald Thenius, Christoph Moslinger, Jon Timmis, Andy Tyrrell, Mark Read, James Hilder, Jose Halloy, Alexandre Campo, Cesare Stefanini, et al. "CoCoRo–The Self-Aware Underwater Swarm." In: *Self-Adaptive and Self-Organizing Systems Workshops (SASOW), 2011 Fifth IEEE Conference on*. IEEE. 2011, pp. 120–126.

[104] Yuichi Kobayashi, Kyouji Otsubo, and Shigeyuki Hosoe. "Design of decentralized capturing behavior by multiple mobile robots." In: *Distributed Intelligent Systems: Collective Intelligence and Its Applications, 2006. DIS 2006. IEEE Workshop on*. IEEE. 2006, pp. 13–18.

[105] Aveek K Das, Rafael Fierro, Vijay Kumar, James P Ostrowski, John Spletzer, and Camillo J Taylor. "A vision-based formation control framework." In: *Robotics and Automation, IEEE Transactions on* 18.5 (2002), pp. 813–825.

[106] Mauro Franceschelli and Andrea Gasparri. "On agreement problems with gossip algorithms in absence of common reference frames." In: *Robotics and Automation (ICRA), 2010 IEEE International Conference on*. IEEE. 2010, pp. 4481–4486.

[107] Magnus Egerstedt and Xiaoming Hu. “A hybrid control approach to action coordination for mobile robots.” In: *Automatica* 38.1 (2002), pp. 125–130.

[108] Robin Ritz, Mark W Muller, Markus Hehn, and Raffaello D’Andrea. “Cooperative quadrocopter ball throwing and catching.” In: *Intelligent Robots and Systems (IROS), 2012 IEEE/RSJ International Conference on*. IEEE. 2012, pp. 4972–4978.

[109] Shervin Nouyan and Marco Dorigo. “Chain based path formation in swarms of robots.” In: *Ant Colony Optimization and Swarm Intelligence*. Springer, 2006, pp. 120–131.

[110] F. Deroo, M. Ulbrich, B. D. O. Anderson, and S. Hirche. “Accelerated iterative distributed controller synthesis with a Barzilai-Borwein step size.” In: *Proc. IEEE/CSS CDC*. 2012, pp. 4864–4870.

[111] J. Nocedal and S. J. Wright. *Numerical Optimization*. 2nd. Springer, 2006.

[112] J. Barzilai and J. M. Borwein. “Two-point step size gradient methods.” In: *IMA Journal of Numerical Analysis* 8.1 (1988), pp. 141–148.

[113] D. P. Bertsekas. *Nonlinear Programming*. Athena Scientific, Belmont, MA, 1999.

[114] Auke Jan Ijspeert, Jun Nakanishi, and Stefan Schaal. “Movement imitation with nonlinear dynamical systems in humanoid robots.” In: *Robotics and Automation, IEEE International Conference on*. 2002.

[115] Ales Ude, Andrej Gams, Tamim Asfour, and Jun Morimoto. “Task-specific generalization of discrete and periodic dynamic movement primitives.” In: *Robotics, IEEE Transactions on* 26.5 (2010), pp. 800–815.

[116] Sethu Vijayakumar and Stefan Schaal. “Locally weighted projection regression: An O (n) algorithm for incremental real time learning in high dimensional space.” In: *Proceedings of the Seventeenth International Conference on Machine Learning*. 2000.

[117] Stefan Schaal, Peyman Mohajerian, and Auke Ijspeert. “Dynamics systems vs. optimal control - a unifying view.” In: *Progress in brain research* (2007).

[118] Brian DO Anderson, Changbin Yu, Baris Fidan, and Julien M Hendrickx. “Rigid graph control architectures for autonomous formations.” In: *Control Systems, IEEE* (2008).

[119] Jack B Kuipers. *Quaternions and rotation sequences*. Vol. 66. Princeton university press Princeton, 1999.

[120] Meng Ji and Magnus Egerstedt. “Distributed coordination control of multiagent systems while preserving connectedness.” In: *Robotics, IEEE Transactions on* 23.4 (2007), pp. 693–703.

[121] Christopher David Godsil, Gordon Royle, and CD Godsil. *Algebraic graph theory*. Vol. 8. Springer New York, 2001.

[122] Oussama Khatib. “Real-time obstacle avoidance for manipulators and mobile robots.” In: *The international journal of robotics research* 5.1 (1986), pp. 90–98.

[123] Raja Parasuraman, Thomas B Sheridan, and Christopher D Wickens. “A model for types and levels of human interaction with automation.” In: *Systems, Man and Cybernetics, Part A: Systems and Humans, IEEE Transactions on* 30.3 (2000), pp. 286–297.

[124] Matteo Diana, J-P de la Croix, and Magnus Egerstedt. “Deformable-medium affordances for interacting with multi-robot systems.” In: *Intelligent Robots and Systems (IROS), 2013 IEEE/RSJ International Conference on*. IEEE. 2013, pp. 5252–5257.

[125] Woojin Chung, Myoungkuk Park, Kwanghyun Yoo, Jae Il Roh, and Jongsuk Choi. “Backward-motion control of a mobile robot with n passive off-hooked trailers.” In: *Journal of mechanical science and technology* 25.11 (2011), pp. 2895–2905.

[126] Antonio Franchi, Paolo Robuffo Giordano, Cristian Secchi, Hyoung Il Son, and Heinrich H Bülthoff. “A passivity-based decentralized approach for the bilateral teleoperation of a group of UAVs with switching topology.” In: *Robotics and Automation (ICRA), 2011 IEEE International Conference on*. IEEE. 2011, pp. 898–905.

[127] Dongjun Lee, Antonio Franchi, Paolo Robuffo Giordano, Hyoung Il Son, and Heinrich H Bülthoff. “Haptic teleoperation of multiple unmanned aerial vehicles over the internet.” In: *Robotics and automation (icra), 2011 ieee international conference on*. IEEE. 2011, pp. 1341–1347.

[128] Luca Consolini, Fabio Morbidi, Domenico Prattichizzo, and Mario Tosques. “Leader–follower formation control of nonholonomic mobile robots with input constraints.” In: *Automatica* 44.5 (2008), pp. 1343–1349.

[129] Stefano Scheggi, Marco Aggravi, Fabio Morbidi, and Domenico Prattichizzo. “Cooperative human-robot haptic navigation.” In: *Robotics and Automation (ICRA), 2014 IEEE International Conference on*. IEEE. 2014, pp. 2693–2698.

[130] Stefano Scheggi, Fabio Morbidi, and Domenico Prattichizzo. “Human-robot formation control via visual and vibrotactile haptic feedback.” In: *Haptics, IEEE Transactions on* 7.4 (2014), pp. 499–511.

[131] Nora Ayanian, Andrew Spielberg, Matthew Arbesfeld, Jason Strauss, and Daniela Rus. “Controlling a team of robots with a single input.” In: *Robotics and Automation (ICRA), 2014 IEEE International Conference on*. IEEE. 2014, pp. 1755–1762.

[132] Gaëtan Podevijn, Rehan O’Grady, Youssef SG Nashed, and Marco Dorigo. “Gesturing at subswarms: Towards direct human control of robot swarms.” In: *Towards Autonomous Robotic Systems*. Springer, 2014, pp. 390–403.

[133] Manuele Brambilla, Eliseo Ferrante, Mauro Birattari, and Marco Dorigo. “Swarm robotics: a review from the swarm engineering perspective.” In: *Swarm Intelligence* 7.1 (2013), pp. 1–41.

[134] Magnus Egerstedt, Jean-Pierre de la Croix, Hiroaki Kawashima, and Peter Kingston. "Interacting with Networks of Mobile Agents." In: *Large-Scale Networks in Engineering and Life Sciences*. Springer, 2014, pp. 199–224.

[135] Carlos I Aldana, Emmanuel Nuno, and Luis Basanez. "Leader-follower Pose Consensus for Heterogeneous Robot Networks with Variable Time-Delays." In: *World Congress*. Vol. 19. 1. 2014, pp. 6674–6679.

[136] Emmanuel Nuno, Ioannis Sarras, and Luis Basanez. "Consensus in networks of nonidentical Euler–Lagrange systems using P+ d controllers." In: *Robotics, IEEE Transactions on* 29.6 (2013), pp. 1503–1508.

[137] Tina Setter, Alex Fouraker, Hiroaki Kawashima, and Magnus Egerstedt. "Haptic Interactions With Multi-Robot Swarms Using Manipulability." In: *Journal of Human-Robot Interaction* 4.1 (2015), pp. 60–74.

[138] Jean-Pierre de la Croix and Magnus Egerstedt. "Controllability Characterizations of Leader-Based Swarm Interactions." In: *AAAI Fall Symposium: Human Control of Bioinspired Swarms*. 2012.

[139] W.S. Kim, F. Tendick, S.R. Ellis, and L.W. Stark. "A comparison of position and rate control for telemanipulations with consideration of manipulator system dynamics." In: *Robotics and Automation, IEEE Journal of* 3.5 (Oct. 1987), pp. 426–436. issn: 0882-4967. doi: 10.1109/JRA.1987.1087117.

[140] Christopher D Wickens. *Engineering psychology and human performance* . HarperCollins Publishers, 1992.

[141] Sebastian Erhart and Sandra Hirche. "Adaptive force/velocity control for multi-robot cooperative manipulation under uncertain kinematic parameters." In: *Intelligent Robots and Systems (IROS), 2013 IEEE/RSJ International Conference on*. IEEE. 2013, pp. 307–314.

[142] Kyong-Sok Chang, Robert Holmberg, and Oussama Khatib. "The augmented object model: Cooperative manipulation and parallel mechanism dynamics." In: *Robotics and Automation, 2000. Proceedings. ICRA'00. IEEE International Conference on*. Vol. 1. IEEE. 2000, pp. 470–475.

[143] Peng Song and Vijay Kumar. "A potential field based approach to multi-robot manipulation." In: *Robotics and Automation, 2002. Proceedings. ICRA'02. IEEE International Conference on*. Vol. 2. IEEE. 2002, pp. 1217–1222.

[144] Guilherme AS Pereira, Mario FM Campos, and Vijay Kumar. "Decentralized algorithms for multi-robot manipulation via caging." In: *The International Journal of Robotics Research* 23.7-8 (2004), pp. 783–795.

[145] Kyoung-Hwan Jo and Jihong Lee. "Multi-robot cooperative localization with optimally fused information of odometer and GPS." In: *Control, Automation and Systems, 2007. ICCAS'07. International Conference on*. IEEE. 2007, pp. 601–605.

[146] Stanley Schneider, Robert H Cannon Jr, et al. "Object impedance control for cooperative manipulation: Theory and experimental results." In: *Robotics and Automation, IEEE Transactions on* 8.3 (1992), pp. 383–394.

[147] Jawad Nagi, Alessandro Giusti, Luca M Gambardella, and Gianni A Di Caro. "Human-swarm interaction using spatial gestures." In: *Intelligent Robots and Systems (IROS 2014), 2014 IEEE/RSJ International Conference on*. IEEE. 2014, pp. 3834–3841.

[148] Amir M Naghsh, Jeremi Gancet, Andry Tanoto, and Chris Roast. "Analysis and design of human-robot swarm interaction in firefighting." In: *Robot and Human Interactive Communication, 2008. RO-MAN 2008. The 17th IEEE International Symposium on*. IEEE. 2008, pp. 255–260.

[149] Gaëtan Podevijn, Rehan O'Grady, Youssef SG Nashed, and Marco Dorigo. "Gesturing at subswarms: Towards direct human control of robot swarms." In: *Towards Autonomous Robotic Systems*. Springer, 2013, pp. 390–403.

[150] A. Debruyn. "Human-Swarm Interaction: An Escorting Robot Swarm that Diverts a Human away from Dangers one cannot perceive." M.Sc. Thesis in Computer Science Engineering. Belgium: Université Libre de Bruxelles, 2015.

[151] J Nagi, H Ngo, LM Gambardella, and Gianni A Di Caro. "Wisdom of the swarm for cooperative decision-making in human-swarm interaction." In: *Robotics and Automation (ICRA), 2015 IEEE International Conference on*. IEEE. 2015, pp. 1802–1808.

[152] Ghazaleh Pour Sadrollah, Jan Carlo Barca, Jens Eliasson, and Asad I Khan. "A Distributed Framework and Consensus Middle-Ware for Human Swarm Interaction." In: ().

[153] Carlos I Aldana, Eduardo Romero, Emmanuel Nuño, and Luis Basañez. "Pose consensus in networks of heterogeneous robots with variable time delays." In: *International Journal of Robust and Nonlinear Control* (2014).

[154] Simone Martini, Magnus Egerstedt, and Antonio Bicchi. "Controllability analysis of multi-agent systems using relaxed equitable partitions." In: *Int. J. Syst. Contr. Comm.* 2.1 (2010), pp. 100–121.

[155] Maria Isabel Garcia Planas, Jose Luis Dominguez Garcia, and Laurence Emilie Um. "Sufficient conditions for controllability and observability of serial and parallel concatenated linear systems." In: (2014).

[156] Gene H Golub and Charles F Van Loan. *Matrix computations*. Vol. 3. JHU Press, 2012.

[157] Herbert G Tanner, George J Pappas, and Vijay Kumar. "Leader-to-formation stability." In: *Robotics and Automation, IEEE Transactions on* 20.3 (2004), pp. 443–455.

[158] Edwin G Johnsen and William R Corliss. *Human factors applications in teleoperator design and operation*. Wiley-Interscience New York, 1971.

[159] Lynette A Jones and Nadine B Sarter. “Tactile displays: Guidance for their design and application.” In: *Human Factors: The Journal of the Human Factors and Ergonomics Society* 50.1 (2008), pp. 90–111.

[160] Reza Olfati-Saber, J Alex Fax, and Richard M Murray. “Consensus and cooperation in networked multi-agent systems.” In: *Proceedings of the IEEE* 95.1 (2007), pp. 215–233.

[161] Javad Ghaderi and R Srikant. “Opinion dynamics in social networks: A local interaction game with stubborn agents.” In: *American Control Conference (ACC), 2013*. IEEE. 2013, pp. 1982–1987.

[162] Herbert G Tanner. “On the controllability of nearest neighbor interconnections.” In: *Proc. IEEE CDC*. IEEE. 2004, pp. 2467–2472.

[163] Meng Ji and M Egersted. “A graph-theoretic characterization of controllability for multi-agent systems.” In: *Proc. ACC*. 2007, pp. 4588–4593.

[164] Shuo Zhang, M Kanat Camlibel, and Ming Cao. “Controllability of diffusively-coupled multi-agent systems with general and distance regular coupling topologies.” In: *Proc. IEEE CDC*. IEEE. 2011, pp. 759–764.

[165] Amirreza Rahmani, Meng Ji, Mehran Mesbahi, and Magnus Egerstedt. “Controllability of multi-agent systems from a graph-theoretic perspective.” In: *SIAM Journal on Control and Optimization* 48.1 (2009), pp. 162–186.

[166] Hiroki Yamamoto and Koji Tsumura. “Optimal controlling node problem for multi-agent systems via Alt-PageRank.” In: *Proc. SICE*. 2011, pp. 1350–1354.

[167] Fu Lin, Makan Fardad, and Mihailo R Jovanović. “Algorithms for leader selection in large dynamical networks: Noise-corrupted leaders.” In: *Decision and Control and European Control Conference (CDC-ECC), 2011 50th IEEE Conference on*. IEEE. 2011, pp. 2932–2937.

[168] Hitoshi Kawashima and Magnus Egerstedt. “Leader selection via the manipulability of leader-follower networks.” In: *American Control Conference (ACC), 2012*. IEEE. 2012, pp. 6053–6058.

[169] Mohsen Zamani and Hai Lin. “Structural controllability of multi-agent systems.” In: *American Control Conference, 2009. ACC’09.* IEEE. 2009, pp. 5743–5748.

[170] Shuo Zhang, Ming Cao, and M Kanat Camlibel. “Upper and lower bounds for controllable subspaces of networks of diffusively coupled agents.” In: *Automatic Control, IEEE Transactions on* 59.3 (2014), pp. 745–750.

[171] Simone Martini, Magnus Egerstedt, and Antonio Bicchi. “Controllability decompositions of networked systems through quotient graphs.” In: *Proc. IEEE CDC*. 2008, pp. 5244–5249.

[172] Domingos M Cardoso, Charles Delorme, and Paula Rama. “Laplacian eigenvectors and eigenvalues and almost equitable partitions.” In: *European journal of combinatorics* 28.3 (2007), pp. 665–673.

[173] Cesar O Aguilar and Bahman Gharesifard. “Graph controllability classes for the laplacian leader-follower dynamics.” In: *Automatic Control, IEEE Transactions on* 60.6 (2015), pp. 1611–1623.

[174] MK Camlibel, S Zhang, and M Cao. “Comments on ’Controllability analysis of multi–agent systems using relaxed equitable partitions’.” In: *Int. J. Syst. Contr. Comm.* 4.1 (2012), pp. 72–75.

[175] Isabel Faria. “Multiplicity of integer roots of polynomials of graphs.” In: *Linear algebra and its applications* 229 (1995), pp. 15–35.

[176] Russell Merris. “Laplacian graph eigenvectors.” In: *Linear algebra and its applications* 278.1 (1998), pp. 221–236.

[177] Bo Liu, Tianguang Chu, Long Wang, and Guangming Xie. “Controllability of a leader–follower dynamic network with switching topology.” In: *IEEE Transactions on Automatic Control* 53.4 (2008), pp. 1009–1013.

[178] Zhijian Ji, Zidong Wang, Hai Lin, and Zhen Wang. “Controllability of multi-agent systems with time-delay in state and switching topology.” In: *International Journal of Control* 83.2 (2010), pp. 371–386.

[179] Darina Goldin and Jorg Raisch. “Controllability of second order leader-follower systems.” In: *IFAC Proceedings Volumes* 43.19 (2010), pp. 233–238.

[180] Fangcui Jiang, Long Wang, Guangming Xie, Zhijian Ji, and Yingmin Jia. “On the controllability of multiple dynamic agents with fixed topology.” In: *Proc. ACC*. 2009, pp. 5665–5670.

[181] Meng Ji, Abubakr Muhammad, and Magnus Egerstedt. “Leader-based multi-agent coordination: Controllability and optimal control.” In: *Proc. ACC*. 2006, pp. 1358–1363.

[182] Cesar O Aguilar and Bahman Gharesifard. “On almost equitable partitions and network controllability.” In: ().

[183] Neil JA Sloane et al. *The on-line encyclopedia of integer sequences*. 2003.

[184] Brendan D McKay and Adolfo Piperno. “Practical graph isomorphism, II.” In: *Journal of Symbolic Computation* 60 (2014), pp. 94–112.

[185] Yang-Yu Liu, Jean-Jacques Slotine, and Albert-László Barabási. “Controllability of complex networks.” In: *Nature* 473.7346 (2011), p. 167.

[186] Frederik Deroo and Sandra Hirche. “A MATLAB Toolbox for Large-Scale Networked Systems.” In: *at-Automatisierungstechnik Methoden und Anwendungen der Steuerungs-, Regelungs-und Informationstechnik* 61.7 (2013), pp. 506–514.

[187] M. Goebl and G. Färber. "A Real-Time-capable Hard- and Software Architecture for Joint Image and Knowledge Processing in Cognitive Automobiles." In: *Proc. IEEE IV*. 2007, pp. 734–740.

[188] Daniel Althoff, Omiros Kourakos, Martin Lawitzky, A. Mörtl, M. Rambow, F. Rohrmüller, D. Brščić, D. Wollherr, S. Hirche, and M. Buss. "An architecture for real-time control in multi-robot systems." In: *Human Centered Robot Systems* (2009), pp. 43–52.

[189] U. Hanebeck, N. Saldic, and G. Schmidt. "A Modular Wheel System for Mobile Robot Applications." In: *Proc. IEEE/RSJ IROS*. 1999, pp. 17–22.

[190] D. Brscic, M. Eggers, F. Rohrmüller, O. Kourakos, S. Sosnowski, D. Althoff, M. Lawitzky, A. Mörtl, M. Rambow, V. Koropouli, J.R. Medina, X. Zang, W. Wang, D. Wollherr, K. Kühnlenz, C. Mayer, T. Kruse, A. Kirsch, J. Blume, A. Bannat, T. Rehrl, F. Wallhoff, T. Lorenz, P. Basili, C. Lenz, T. Röder, G. Panin, W. Maier, S. Hirche, M. Buss, M. Beetz, B. Radig, A. Schubö, S. Glasauer, A. Knoll, and E. Steinbach. *Multi Joint Action in CoTeSys - Setup and Challenges*. Tech. rep. Technische Universität München and Ludwig-Maximilians-Universität München, 2010.

[191] Matthias Rambow, Florian Rohrmüller, Omiros Kourakos, Drazen Brščic, Dirk Wollherr, Sandra Hirche, and Martin Buss. "A Framework for Information Distribution, Task Execution and Decision Making in Multi-Robot Systems." In: *IEICE transactions on information and systems* 93.6 (2010), pp. 1352–1360. issn: 0916-8532. doi: 10.1587/transinf.E93.D.1352.

[192] M. Goebl. *KogMo-RTDB - Real-time Database for Cognitive Automobiles*. 2011. url: http://www.kogmo-rtdb.de.

[193] The Preempt RT community. *Real-Time Linux Wiki*. 2011. url: http://rt.wiki.kernel.org.

[194] F Gemperle, T Hirsch, A Goode, J Pearce, D Siewiorek, and A Smailigic. *Wearable Vibro-Tactile Display*. Tech. rep. Carnegie Mellon Wearable Group, Carnegie Mellon University, 2003.

[195] Myoung-Jong Yoon and Kee-Ho Yu. "Psychophysical experiment of vibrotactile pattern perception by human fingertip." In: *Neural Systems and Rehabilitation Engineering, IEEE Transactions on* 16.2 (2008), pp. 171–177.

Author's Publications

[1] Sebastian Erhart, Dominik Sieber, and Sandra Hirche. "An impedance-based control architecture for multi-robot cooperative dual-arm mobile manipulation." In: *Intelligent Robots and Systems (IROS), 2013 IEEE/RSJ International Conference on*. IEEE. 2013, pp. 315–322.

[2] Dominik Sieber, Frederik Deroo, and Sandra Hirche. “Iterative optimal feedback control design under relaxed rigidity constraints for multi-robot cooperative manipulation.” In: *Decision and Control (CDC), 2013 IEEE 52nd Annual Conference on*. IEEE. 2013, pp. 971–976.

[3] Dominik Sieber, Frederik Deroo, and Sandra Hirche. “Formation-based approach for multi-robot cooperative manipulation based on optimal control design.” In: *Intelligent Robots and Systems (IROS), 2013 IEEE/RSJ International Conference on*. IEEE. 2013, pp. 5227–5233.

[4] Jonas Umlauft, Dominik Sieber, and Sandra Hirche. “Dynamic Movement Primitives for cooperative manipulation and synchronized motions.” In: *Robotics and Automation (ICRA), 2014 IEEE International Conference on*. IEEE. 2014, pp. 766–771.

[5] Dominik Sieber, Selma Music, and Sandra Hirche. “Multi-robot manipulation controlled by a human with haptic feedback.” In: *IEEE/RSJ International Conference on Intelligent Robots and Systems (IROS)*. 2015.

[6] Dominik Sieber and Sandra Hirche. “Cooperative Robotic Manipulation Task Guided By A Single Human.” In: *IEEE Transactions on Control Systems Technology* (2018).

[7] Dominik Sieber and Sandra Hirche. “Uncontrollability in consensus networks.” In: *Asian Journal of Control* (in prep.).

[8] Dominik Sieber and Sandra Hirche. “Uncontrollability of controlled consensus networks characterized by Faria vectors.” In: *Control Conference (ECC), 2014 European*. IEEE. 2014, pp. 196–201.

[196] José Ramón Medina, Dominik Sieber, and Sandra Hirche. “Risk-sensitive interaction control in uncertain manipulation tasks.” In: *Robotics and Automation (ICRA), 2013 IEEE International Conference on*. IEEE. 2013, pp. 502–507.

[197] Dominik Sieber, Markus Wiedemann, and Sandra Hirche. *Towards Robot Whole-Body Collision Avoidance Using Distributed Sensing*. Poster. 2012.

[198] Sebastian Erhart, Dominik Sieber, Thomas Nierhoff, Timo Fritzsch, Kolja Kühnlenz, and Sandra Hirche. *Cognitive Cooperative Mobile Multi-Robot Manipulation, Proc. 5th International Conference on Cognitive Systems*. Poster. 2012.